ENGINEERING EVALUATION OF POST-LIQUEFACTION RESIDUAL STRENGTH

(VOLUME 2, PART 1: APPENDIX A)

by

Joseph P. Weber, Raymond B. Seed, Robb E. S. Moss, Juan M. Pestana,
Chukwuebuka Nweke, Tonguc T. Deger and Khaled Chowdhury

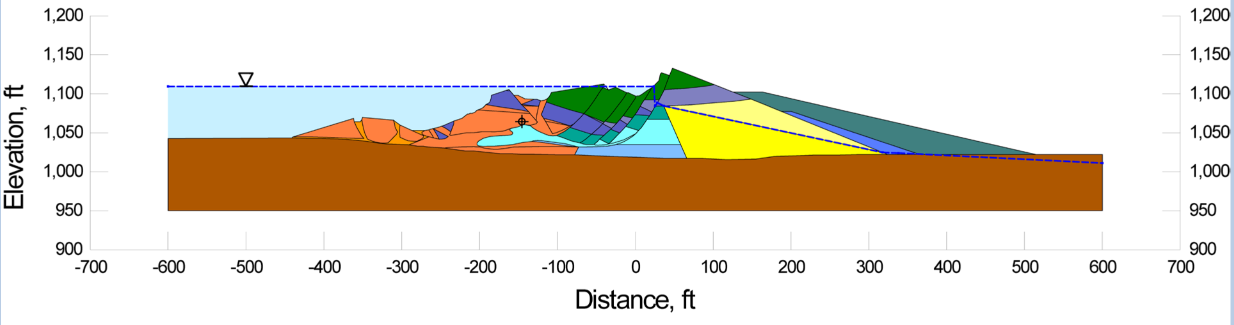

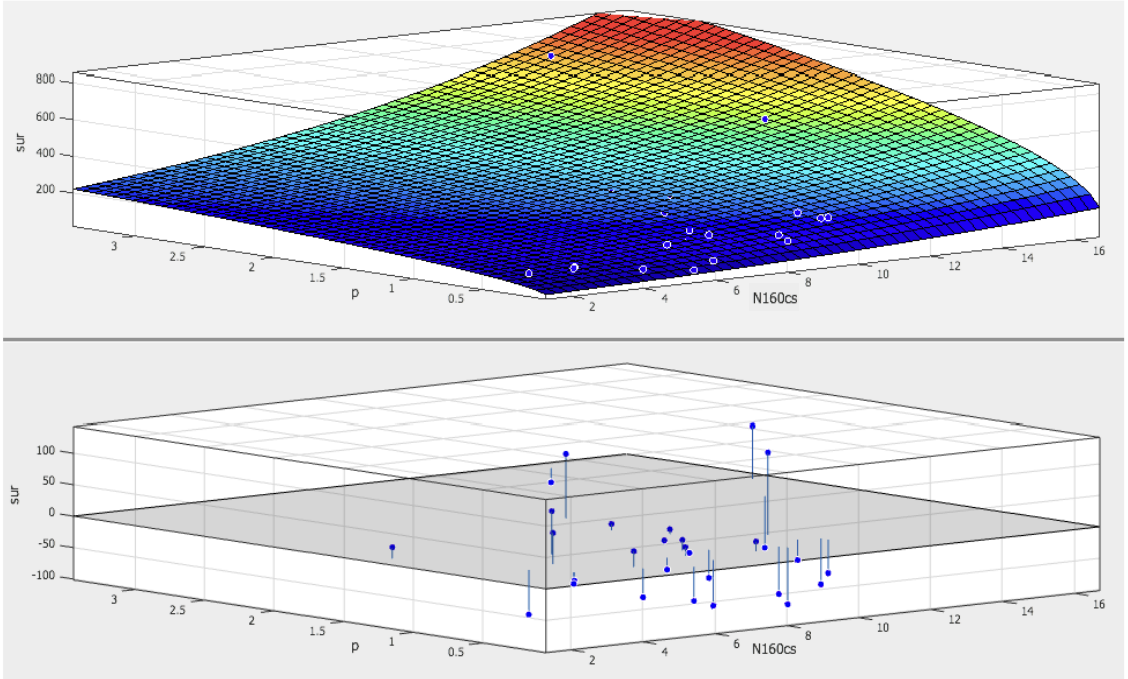

Geotechnical Research Report No. UCB/GT/22-01
Department of Civil and Environmental Engineering
University of California at Berkeley

August 2022

Appendix A:

Back-Analyses of Class A and Class C Liquefaction Failure Case Histories

Class A Case Histories:

Class C Case History:

A.1 North Dike of Wachusett Dam (Massachusetts, USA; 1907)

A.1.1 Brief Summary of Case History Characteristics

Name of Structure	Wachusett Dam
Location of Structure	Massachusetts, USA
Type of Structure	Poorly compacted earthen dam
Date of Failure	April 11, 1907
Nature of Failure	Non-seismic, during initial reservoir filling
Approx. Maximum Slope Height	88 ft.

A.1.2 Introduction and Description of Failure

The best description and summary of field data regarding the failure of the North Dike of Wachusett Dam is presented by Olson et al. (2000), and the description here is based largely on Olson et al. (2000) and Olson (2001). GZA GeoEnvironmental (1991) performed geotechnical studies of the dam to investigate seismic stability of the North Dike, and Haley & Aldrich (1984a,b) also performed geotechnical studies of the North Dike.

Construction of the dike began in 1898 with the excavation of cut-off trenches in the foundation. Backfilling of these cut-off trenches occurred in 1900 and 1901. These cut-off trenches were not involved in the failure. Construction of the main dike embankment began in 1902, and fill placement for the North Dike was completed in 1904, approximately three years prior to the slope failure.

A slope failure occurred on the upstream side of the North Dike embankment on April 11, 1907, during initial filling of the reservoir. Figures A.1.1 and A.1.2 show pre-failure and post-failure cross-sections through the failure zone (Olson et al, 2000). The failure was centered over the former river channel, at the location of the maximum height embankment section where the dam reached a height of approximately 24.4 m (80 ft). The reservoir had risen to an elevation approximately 40 feet below the crest of the embankment when the failure occurred. The zone of likely "jetting" shown in Figure A.1.2 refers to "jetting" that was performed during the post-failure slope repair to try to inter-mix (and knit) the repair fill and the slope scarp. This "jetting" occurred after the failure, and is not pertinent to the back-analyses of the failure.

Olson et al. postulate that the cause of the failure was reduction in effective stress along the base of the failure mass due to increasing buoyancy as the reservoir filled, while there was a commensurate (but lesser) reduction in driving shear stresses along this failure surface as much of the embankment fill remained above the reservoir level. It is suggested here that a more likely cause would have been wetting-induced "collapse" of the very loose, cohesionless soils comprising the upstream shell. As discussed a bit later, saturation (wetting) was employed to "compact" the similar downstream shell fill materials, and this was observed to produce volumetric reductions of

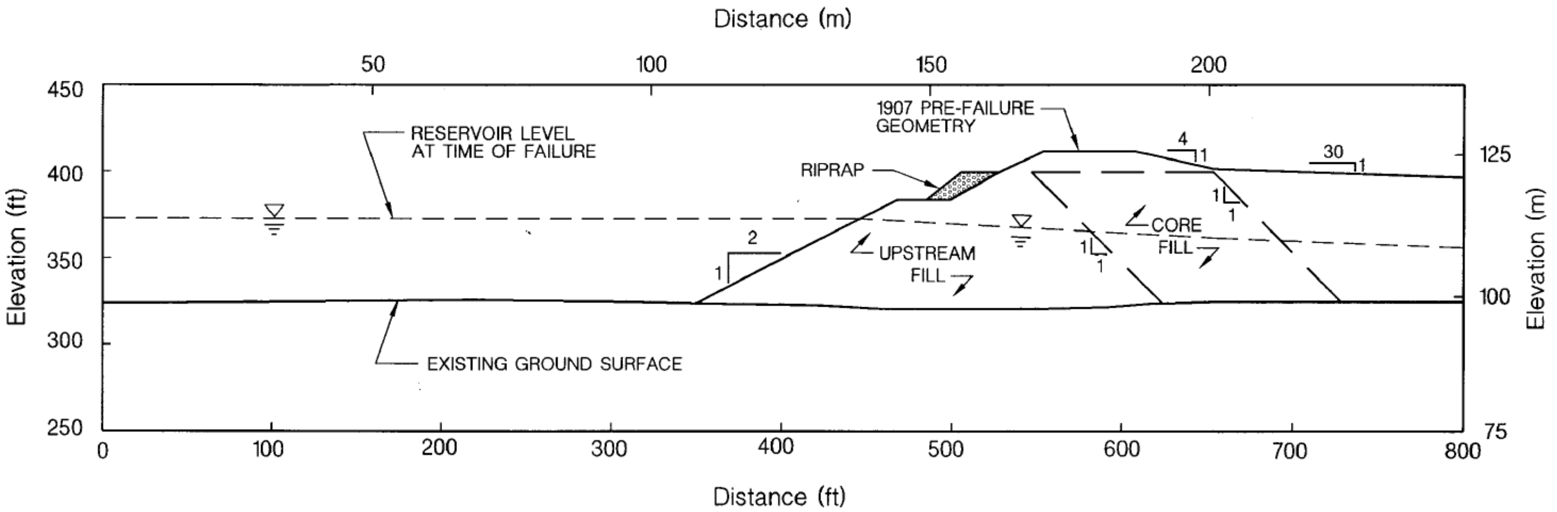

Figure A.1.1: Pre-failure cross-section of the North Dike of Wachusett Dam at Station 23+20 (from Olson et. al, 2000).

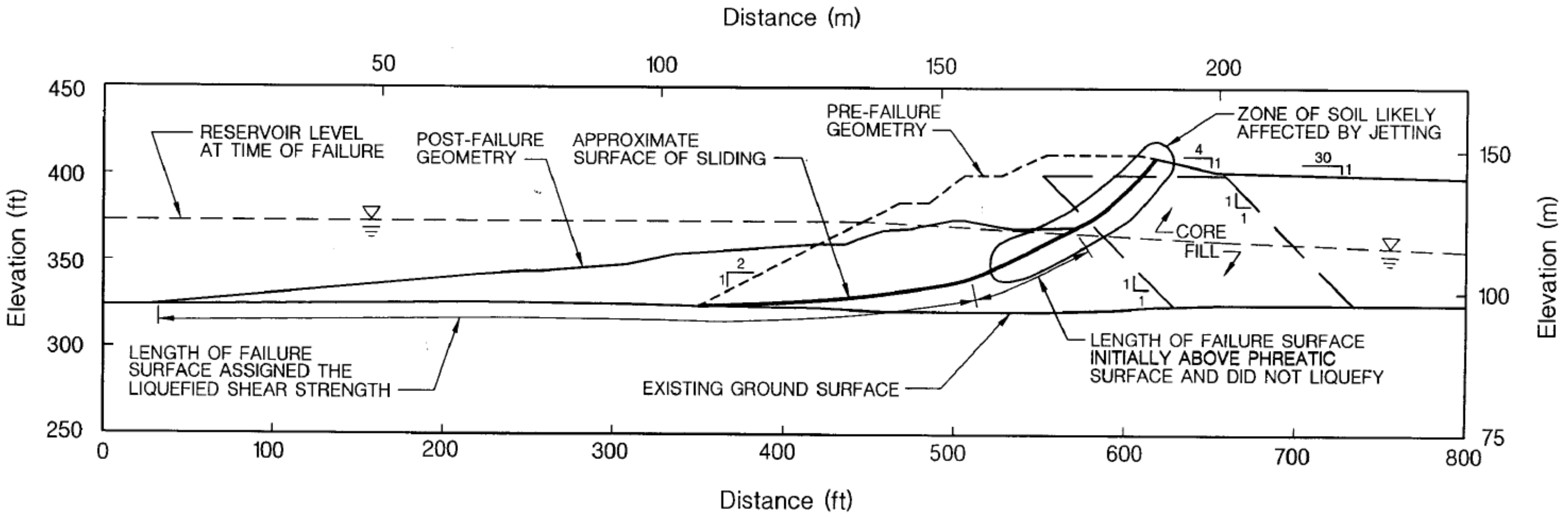

Figure A.1.2: Post-failure cross-section of the North Dike of Wachusett Dam at Station 23+20, showing the approximate location of the apparent sliding surface (from Olson et. al, 2000).

approximately 6% to 12% as each lift was saturated. No similar "saturation" was applied during placement of lifts of the upstream shell, and so there is a high likelihood that significant wetting-collapse would have occurred as the reservoir was filled for the first time. Regardless of the actual details of the triggering of the failure, the ensuing flow-type failure can be safely judged to have been initiated "statically", with no cyclic or dynamic triggering forces. As shown in Figures A.1.1 and A.1.2, movements of the failure mass into the reservoir were large.

The failed zone of the Dike was rebuilt in 1907, and the reservoir was re-filled without incident.

Foundation soils beneath the dike are comprised mainly of dense to very dense sands, gravels and non-plastic silts. A large portion of the fill soils for the embankment's shell zones consisted of fine sands, which were spoils from the excavation of the cut-off trenches into these foundation soils. Materials for the core were also stripped from the reservoir, and consisted of sandy silt to silty sand.

As shown in Figure A.1.1, the core was approximately 100 feet in width, with slopes of 1:1 towards the upstream direction on both the upstream and downstream sides of the core zone. The core soils were placed in lifts of approximately 6 inches, and were rolled by horse drawn carts. No direct measurements of the resulting unit weights of the core materials were made during construction, but more recent investigations indicate that current unit weights are on the order of 120 to 130 lbs/ft^3.

The downstream shell consists of sand to silty sand, with some gravel. As shown in Figure A.1.1, the downstream face has a slope of 4:1 near the crest, but the rest of the downstream face is sloped at 30:1 towards Coachlace Pond. The downstream shell soils were reportedly placed in approximately 7 to 8 foot lifts, and were "compacted" by flooding with water. Approximately 6 to 12 inches of settlement was observed following saturation of each lift. Further details of the downstream shell zone are not pertinent to these current analyses, as the downstream shell zone was not involved in the failure.

The upstream shell also consists of sand to silty sand with some gravel. Fines contents were low, typically on the order of approximately 5% to 10%, though some soils had somewhat higher fractions of largely non-plastic fines. Unlike the downstream shell, the upstream shell received neither compaction nor flooding with water during construction. As a result, the upstream shell was in a very loose condition, and likely prone to some degree of volumetric "collapse" upon initial wetting during the first filling of the reservoir. The slope of the upstream face was relatively steep at 2:1, with a bench near the crest, and with riprap on the upstream face above this bench.

A.1.3 Initial Yield Stress Analyses

Figure A.1.3(a) shows the cross-section used for back-analyses of the post-liquefaction initial yield strength $S_{r,yield}$ that would be required within the liquefied upstream shell materials to produce a calculated Factor of Safety equal to 1.0. This is not the actual post-liquefaction strength, but it proves to be useful in developing a number of charts and relationships for these overall studies.

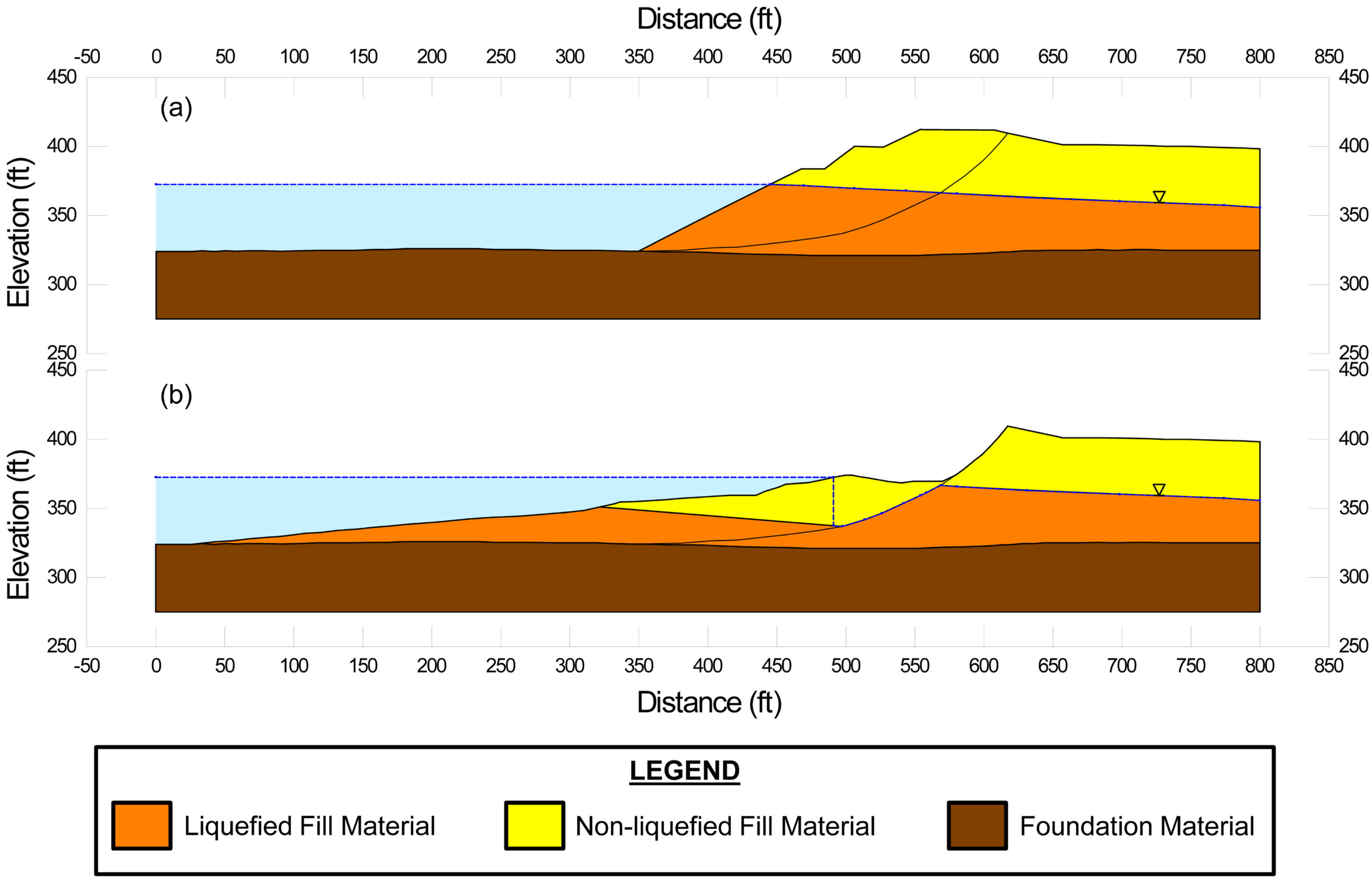

Figure A.1.3: Wachusett Dam at Station 23+20: (a) Pre-failure geometry and best-estimate failure surface for initial yield stress analyses, and (b) post-failure geometry and best-estimate failure surface for post-failure residual geometry analyses.

Figure A.1.3(a) also shows the best estimate failure surface. The failure surface is relatively well constrained at the back heel by the observable failure scarp. The precise location of the failure surface at the base of the failure is uncertain, but the most critical failure surfaces in terms of lowest Factor of Safety for a given value of strength within the liquefied shell fill materials are those that go right to the bottom of the fill. The potential depths are then constrained by the very dense foundation soils. Additional analyses were performed, varying this failure surface; the shape at the lower back heel was varied, and the failure surface was allowed to occur at various elevations slightly above the base of the shell fill. These variations were performed to evaluate sensitivity of the resulting calculated values of $S_{r,yield}$.

Shear strength of the non-saturated, loose sand to silty sand shell and crest fill materials was modeled as frictional, with $Ø' = 30°$. Unit weights of non-saturated shell and crest fills were taken as 111 lbs/ft^3. Shear strength of the moderately compacted, non-saturated sandy silt to silty sand of the upper "core" zone through which part of the failure surface passes was modeled with $Ø' = 30°$. A unit weight of 111 lbs/ft^3 was modeled for these non-saturated "core" materials. The saturated unit weight of the liquefied silty sands was modeled as 123 lbs/ft^3.

The saturated portions of the upstream shell were considered to be potentially liquefiable, and shear strengths of portions of potentially liquefied failure surfaces were modeled with post-liquefaction yield strength $S_{r,yield}$. $S_{r,yield}$ was modeled as uniform along any potential failure surface, and the calculation of the value of $S_{r,yield}$ was the primary objective of these analyses.

Permeabilities of the upstream shell zone were relatively high, and permeabilities of the siltier core zone are lower than those of the upstream shell. Accordingly, it is assumed that the phreatic surface on the upstream side of the core equilibrated relatively rapidly with reservoir elevation increase during the first filling in 1907. The phreatic surface within the core zone, and further downstream, during this first reservoir filling cannot be estimated with similar confidence, but this is not important because the failure occurred to the upstream side of the potentially saturated portions of the core.

For the best estimate geometry, conditions, and failure surface described above and shown in Figure A.1.3, the resulting value of post-liquefaction yield strength was found to be $S_{r,yield}$= 829 lbs/ft^2. Sensitivity analyses were then performed, varying the details and location (at depth) of the failure surface, unit weights, and friction angles for the non-liquefied upper crest and non-liquefied upper core zones. These analyses suggested that there was little likelihood that this failure would have proceeded in an incrementally progressive manner, and so this failure was modeled only as a monolithic event, with the full eventual sliding mass beginning to move largely coherently at the inception of failure. The resulting range of values of $S_{r,yield}$ for combinations of modeling assumptions and details considered to be reasonable was found to be $S_{r,yield} \approx 752$ to 909 lbs/ft^2.

Olson (2001) also performed back-analyses to determine $S_{r,yield}$. Failure surfaces analyzed were similar. Olson reported values of $S_{r,yield} \approx 37.6$ to 41.9 kPa (784 to 875 lbs/ft^2).

A.1.4 Residual Strength Analyses Based on Residual Geometry

The calculation of the "apparent" post-liquefaction strength ($S_{r,resid/geom}$) required to produce a calculated Factor of Safety equal to 1.0 based on residual geometry is illustrated in Figure A.1.3(b). This figure shows the phreatic surface, and the failure surface, used to calculate the best-estimate value of $S_{r,resid/geom}$, based on the best estimate modeling parameters as described in the previous section. An additional detail here is the shear strength modeled at the base of the portion of the upstream toe of the embankment that traveled out into the reservoir. This was the first filling of the reservoir, so there were no loose reservoir sediments accumulated yet at the upstream toe. There may have been some hydroplaning, however, as the embankment materials moved rapidly into the reservoir. The incremental inertial analyses presented in Section A.1.5 that follows indicate that the maximum velocity was on the order of approximately 14.3 ft/sec, and the velocity during most of the run-in was lower. As discussed, it is not possible to fully accurately determine the degree of hydroplaning that would have occurred. The best estimate analysis of $S_{r,resid/geom}$ was performed assuming that shear strength at the base of the embankment materials that entered into the reservoir was 100% of $S_{r,resid/geom}$. The resulting best estimate calculated value of "apparent" post-liquefaction strength based on post-failure residual geometry was $S_{r,resid/geom} \approx 81$ lbs/ft^2.

Variations were then made in parameters, and in location of the pre-failure phreatic surface, as was described in the preceding section in order to evaluate uncertainty or variability. Varying degrees of potential hydroplaning were also modeled, with the average shear strength at the base of the portion of the failure mass that entered the reservoir being modeled as varying from a low of 20% of $S_{r,resid/geom}$ to a high of 100% of $S_{r,resid/geom}$. Considering ranges of variations in modeling details and parameters considered to be reasonable, the resulting likely range of post-liquefaction strength required to provide a calculated Factor of Safety equal to 1.0 based on residual geometry was considered to be $S_{r,resid/geom} \approx 71$ to 87 lbs/ft^2.

Olson (2001) also calculated post-liquefaction strength required to produce a calculated Factor of Safety equal to 1.0 based on residual geometry, and reported a best estimate value of $S_{r,resid/geom} \approx 3.8$ kPA (79 lbs/ft^2). No range was reported.

A.1.5 Incremental Momentum Back-Analyses and Overall Estimates of S_r

Incremental inertial back-analyses were performed using the same sets of properties and geometries (including failure surfaces and phreatic surfaces) as described in the previous sections.

Figure A.1.4 shows the best-estimate progressive incremental inertial analysis, showing the five stages of geometry evolution modeled as the failure proceeds. Figure A.1.5 shows the associated calculations of (1) acceleration vs. time, (2) velocity vs. time, and (3) displacement of the overall center of gravity vs. time. The resulting best estimate value of post-liquefaction strength was $S_r = 294$ lbs/ft^2.

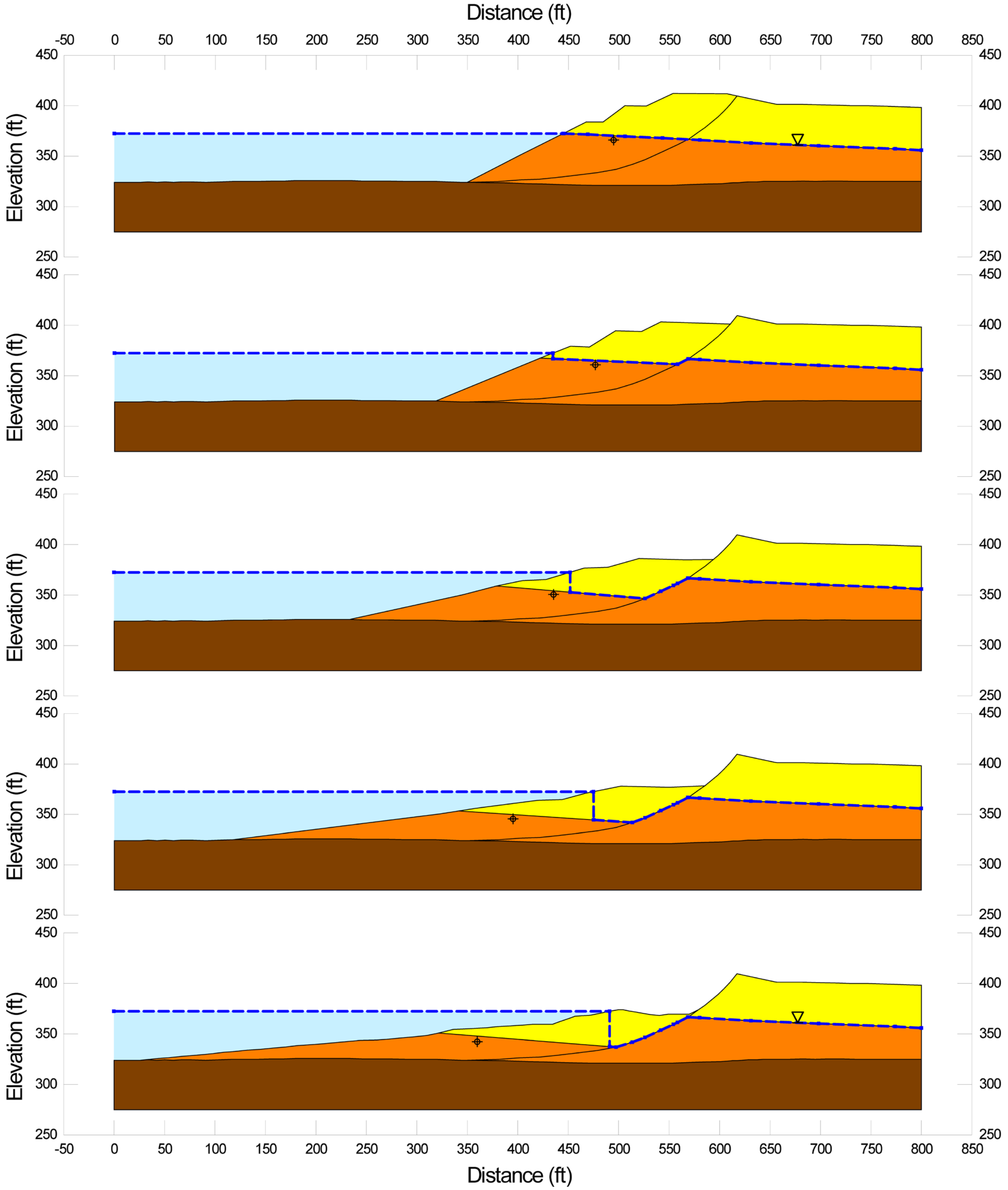

Figure A.1.4: Incremental momentum analysis of the failure of the North Dike of the Wachusett Dam, showing progressive evolution of cross-section geometry modeled.

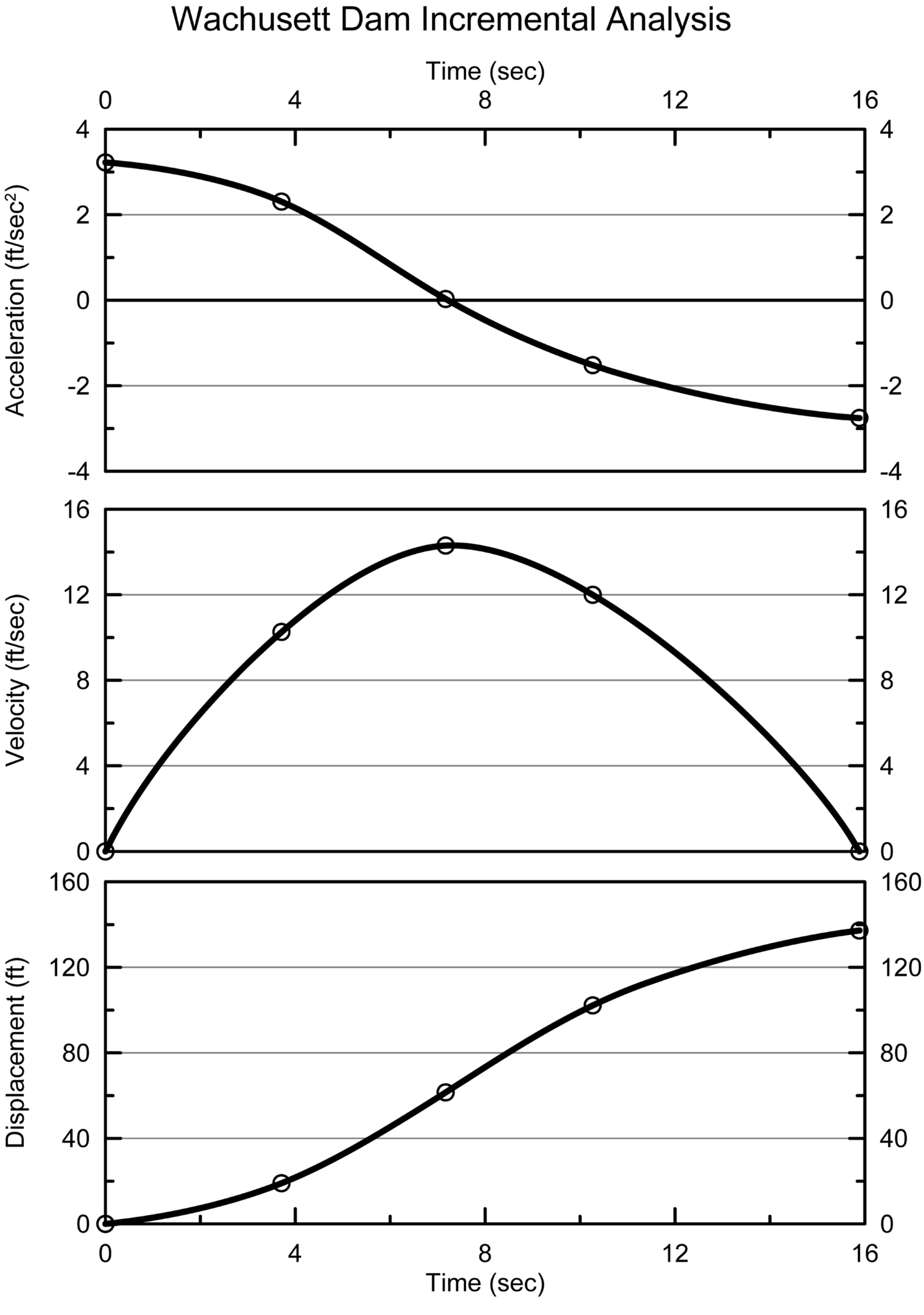

Figure A.1.5: Incremental momentum analysis of the failure of the North Dike of the Wachusett Dam, showing progressive evolution of: (1) acceleration vs. time, (2) velocity vs. time, and (3) displacement vs. time of the overall center of gravity of the failure mass.

The main sources of uncertainty, or variability, in back-calculated values of S_r were (1) frictional strengths of the non-liquefied embankment fill materials, (2) degree of potential hydroplaning as the failure mass entered into the reservoir, (3) the precise location and shape of the failure plane at depth, and (4) unit weights.

Based on all analyses performed, and the considerations discussed, the overall best estimate value of post-liquefaction strength for the failure of the North Dike of Wachusett Dam was judged to be $S_r \approx 294$ lbs/ft^2, with a likely range of $S_r \approx 236$ to 360 lbs/ft^2. Based on the factors contributing to uncertainty or variance for this case history, it was the judgment of the investigation team that this range represented approximately ± 2 standard deviations. This range of variance is not symmetrical about the best estimate value, so minor further adjustments were made to produce a representative estimate of S_r suitable for regression analyses.

Overall, based on an assumed normal distribution, it was judged that the (mean and median) best estimate of post-liquefaction strength for this case history is

$$\overline{S_r} = 294 \text{ lbs/ft}^2$$

and that the best estimate of standard deviation of mean overall post-liquefaction strength is

$$\sigma_{\overline{S}} = 31 \text{ lbs/ft}^2$$

Wachusett Dam was more recently developed as a case history than most of the other cases considered in these studies, and it has not been back-analyzed by many investigators. Olson (2001) and Olson and Stark (2002) present one set of results, and Wang (2003) and Kramer (2008) present a second set of results. Interestingly, both the Olson/Stark and Wang/Kramer efforts specifically account analytically for momentum effects. Olson (2001) and Olson and Stark (2002), reported a best estimate value of $S_r = 16.0$ kPa (335 lbs/ft^2), based on their inertial displacement analyses that considered kinetics, and a range of $S_r = 10.4$ to 19.1 kPa (217 to 400 lbs/ft^2). Wang (2003) and Wang and Kramer (2008) employed their zero inertial force (ZIF) method to incorporate inertial effects in their back-analyses of this failure, and they developed estimates of both mean (best estimate) $\overline{S_r} = 348.0$ lbs/ft^2 as well as the associated standard deviation $\sigma_{\overline{S}} = 74.8$ lbs/ft^2. The details of their analyses, and the cross-sections and failure mass assumptions employed, are not presented and so cannot be checked.

This is an unusually well-defined case history, and these three sets of back-analyses that analytically incorporate momentum effects are all in reasonably good agreement.

A.1.6 Evaluation of Initial Effective Vertical Stress

Average initial (pre-failure) effective vertical stress was assessed for the liquefied zones of each of the failure surface shown in Figure A.1.3. Additional sensitivity analyses were then performed for reasonable ranges of variations in (1) the location of the phreatic surface, (2) unit weights, and (3) the precise location of the overall failure surface in order to evaluate uncertainty or variance.

The resulting best estimate of average pre-failure effective stress within the liquefied materials controlling the failure was then $\sigma_{vo}' \approx 3{,}142$ lbs/ft^2, with a reasonable range of $\sigma_{vo}' \approx 2{,}886$ to 3,414 lbs/ft^2. This range is slightly non-symmetric about the median value, and this range was judged by the engineering team to represent approximately ± 2 standard deviations. Overall, the best characterization of initial (pre-failure) average effective vertical stress was then taken to be represented by a mean value of

$$\overline{\sigma'_{vo}} \approx 3{,}142 \text{ lbs/ft}^2$$

and with a standard deviation of

$$\sigma_{\overline{\sigma}} \approx 132 \text{ lbs/ft}^2$$

An estimate of representative σ_{vo}' was also calculated by Olson and Stark (2001, 2002) and these are shown in Table A.1.1(c). Olson (2001) and Olson and Stark (2002) report average initial effective vertical stresses of approximately $\sigma_{vo}' \approx 3{,}158$ lbs/ft^2. Average initial vertical effective stresses were not directly reported by Wang (2003) and Kramer (2008), but they were published more recently in the publication by Kramer and Wang (2015). As discussed in Section 2.3.8.1(a), the approach taken by Wang (2003) to evaluation of σ_{vo}' for his nine "primary" case histories (this is one of those nine) is not clearly explained, and it is also poorly documented. Wang's value of $\sigma_{vo}' = 2{,}558$ lbs/ft^2 is in fair agreement with the values of Olson (2001) and these current studies, but this is not considered a very rigorous check here. Agreement between Olson's independently back-calculated value, and the value developed in these current studies, is excellent.

A.1.7 Evaluation of $N_{1,60,CS}$

The field investigations reported by GZA Environmental (1991) and by Haley & Aldrich (1984a,b) included six SPT borings at the reconstructed failure section at Station 23+20. These are shown in Figure A.1.6. All of the borings were advanced by rotary wash boring, and a donut hammer with rope and cathead was used to drive the SPT samplers. The SPT hammer energy ratio was taken to be approximately 45%, as was used by Olson et al. (2000) and Olson (2001) in their back-analysis of this case history. Thirty of the SPT's were performed in the upstream shell materials involved in the 1907 flow failure. Thirteen of these were performed near to the apparent shear failure surface, and these are shown with open circles in Figure A.1.6. A source of uncertainty, therefore, is how to weight the SPT blowcounts apparently "near" the failure surface vs. the rest of the SPT blowcounts in the upstream shell material. In these current studies, equal weighting was given to the thirteen blowcounts near the failure zone vs. the full ensemble of blowcounts in the upstream shell materials (assuming that variation is random, and that blowcounts might be distributed differently at nearby locations).

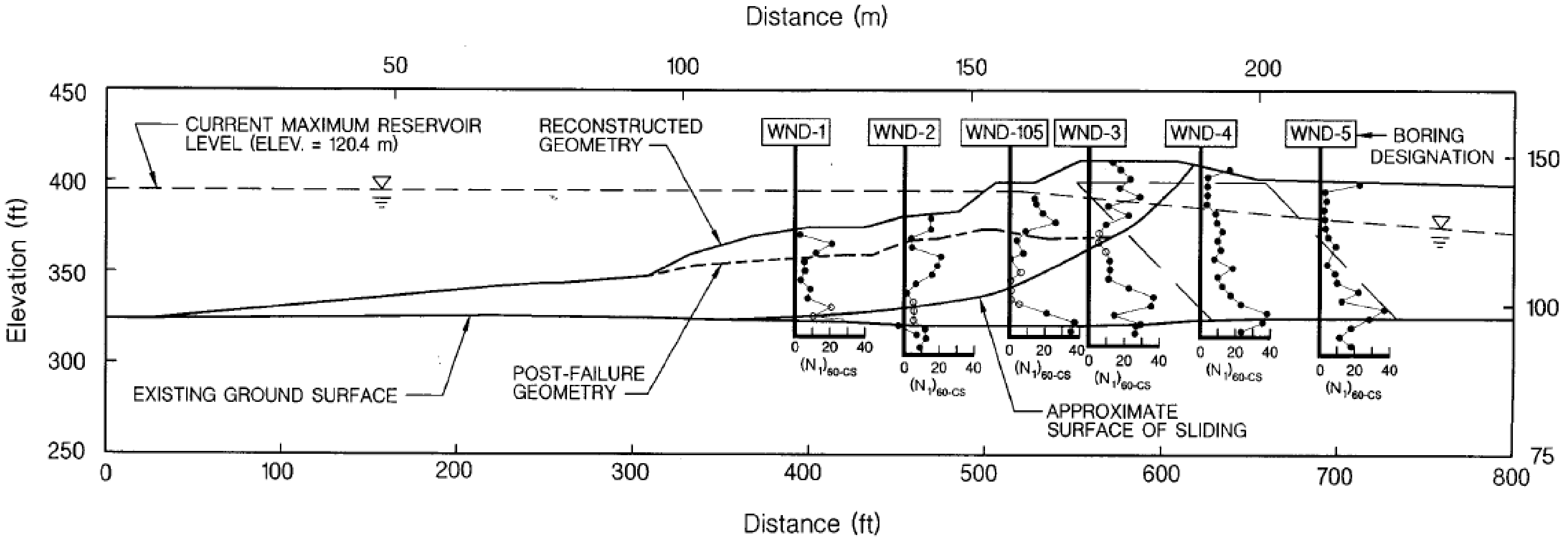

Figure A.1.6: Reconstructed cross-section of the North Dike of Wachusett Dam showing the locations and results of recent standard penetration tests (from Olson et al., 2001).

Corrections for effective overburden stress (C_N) were made using the relationships proposed by Deger (2014), as presented and discussed in Appendix C. Corrections for fines content were made using the relationship proposed by Cetin et al. (2018a,b), and a representative fines content of approximately 5% to 10%; resulting in a null to minor fines adjustment. The resulting median $N_{1,60,CS}$ value for the thirteen SPT tests near to the failure surface was found to be approximately 8 blows/ft, and the median value for the full ensemble of SPT blowcounts (including the thirteen near the failure surface) was found to be approximately 7.5 blows/ft. The resulting best estimate median $\overline{N_{1,60,CS}}$ value for these current studies is then taken as $\overline{N_{1,60,CS}} \approx 7.5$ blows/ft. Variance of $\overline{N_{1,60,CS}}$ was estimated primarily on the basis of the perceived uncertainties associated with the (1) the use of blowcounts from within the failure zone, (2) likely increases in blowcounts over time since the failure (the fill had been only recently placed at the time of the failure), and the perceived high level of variability among the SPT data available. It appears unlikely that jetting of the interface between the failure scarp and the repair fill would have significantly adversely affected these SPT data. Considering all of these, the representation of uncertainty in the representative median value of $\overline{N_{1,60,CS}}$ was taken as $\sigma_{\overline{N}} \approx 1.7$ blows/ft.

Table A.1.1(b) shows values of representative $N_{1,60}$ or $N_{1,60,CS}$ values developed by two other teams of investigators, and variance or standard deviations in these representative values if available. Olson and Stark (2001, 2002) developed an estimated representative value of $N_{1,60} = 7$ blows/ft, but for this case history they proposed no range. Wang (2003) and Kramer (2008) jointly developed a representative value of $\overline{N_{1,60,CS}} = 7.3$ blows/ft, and their estimated standard deviation of that overall mean value for this case history was $\sigma_{\overline{N}} = 1.8$ blows/ft. Details of the development of this interpretation by Wang and Kramer are not presented. Overall agreement between the three independent assessments of representative $\overline{N_{1,60,CS}}$ values is excellent, and variance or uncertainty in $\overline{N_{1,60,CS}}$ appears to be relatively low.

A.1.8 Additional Indices from the Back-Analyses

A number of additional results, and indices, can be extracted from the analyses performed. Some of these are useful in developing some of the over-arching relationships and figures presented in the main text of this report. These values are presented in Table A.1.2.

Table A.1.1: Representative values for the North Dike of Wachusett Dam case history of: (a) post-liquefaction strength (S_r), (b) initial vertical effective stress (σ_{vo}'), and (c) $N_{1,60,CS}$ developed by various investigation teams, and estimates of variance in each of these indices when available.

(a) Post-Liquefaction Strength:	
Olson (2001) and Olson and Stark (2002)	S_r = 335 psf, and range = 217 to 399 psf
Wang (2003) and Kramer (2008)	$\overline{S_r}$ = 348.0 psf, and $\sigma_{\bar{S}}$ = 74.8 psf
This Study	$\overline{S_r}$ = 294 psf and $\sigma_{\bar{S}}$ = 31 psf
(b) Representative $N_{1,60}$ or $N_{1,60,CS}$ Value:	
Olson (2001) and Olson and Stark (2002)	$N_{1,60}$ = 7 bpf
Wang (2003) and Kramer (2008)	$\overline{N_{1,60,CS}}$ = 7.3 bpf, and $\sigma_{\bar{N}}$ = 1.9 bpf
This Study	$\overline{N_{1,60,CS}}$ = 7.5 bpf, and $\sigma_{\bar{N}}$ = 1.6 bpf
(c) Representative Initial Vertical Effective Stress:	
Olson (2001) and Olson and Stark (2002)	σ_{vo}' ≈ 3,158 psf, with no range provided.
Wang (2003) and Kramer (2008)	Value of σ_{vo}' ≈ 2,558 psf is poorly documented, and so is considered useful only as an approximate comparison. (See Section 2.3.8.1, and Table 2.3.)
This Study	$\overline{\sigma'_{vo}}$ = 3,142 psf, and $\sigma_{\bar{\sigma}}$ = 132 psf

Table A.1.2: Additional results and indices from the analyses of the North Dike of Wachusett Dam failure case history.

Maximum distance traveled by the center of gravity of the overall failure mass	137.3 ft.
Initial post-liquefaction Factor of Safety prior to displacement initiation, and based on best estimate value of S_r	FS = 0.47
Final post-liquefaction Factor of Safety at final (residual) post-failure geometry, and based on best estimate value of S_r	FS = 3.43

A.2 Fort Peck Dam (Montana, USA; 1938)

A.2.1 Brief Summary of Case History Characteristics

Name of Structure	Fort Peck Dam
Location of Structure	Montana, USA; Missouri River
Type of Structure	Hydraulic Fill Dam
Date of Failure	September 22, 1938
Nature of Failure	Static, During Construction
Approx. Maximum Slope Height	196 ft.

A.2.2 Introduction

The Fort Peck Dam embankment failed during construction on September 22, 1938. This failure was well-investigated, and details of the initial failure, investigations of that failure, and the repair (reconstruction) operations are well documented by the U.S Army Corps of Engineers (1939), Middlebrooks (1942), Casagrande (1965, 1976), Marcuson and Krinitsky (1976), and Marcuson et al. (1978). This case has also been studied by numerous teams investigating post-liquefaction strengths, as will be discussed in the Sections that follow.

The dam is located on the Missouri River, in northeastern Montana. The dam is a hydraulic fill structure, with a maximum height of 250 ft. (76.3 m) above the original river bed, and a crest length of approximately 10,580 ft. There is an additional dike, extending west of the main dam, with a crest length of approximately 10,450 ft. The main dam was constructed by traditional hydraulic fill methods; with starter dikes, and with dredged materials being deposited from both the upstream and downstream sides to develop relatively cohesionless "shells" and a central "puddle core" of finer materials near the center.

Dredging operations began on October 13, 1934. Nearly four years later, on the morning of September 22, 1938, hydraulic fill placement of the dam embankment section was nearing full design crest height. The reservoir was also partially filled, and at the time of failure was on the lower third of the upstream face of the dam. On the morning of September 22, settlements of as much as 1.5 feet were noted at the top of the upstream face near the right abutment (east abutment). At about 1:15 in the afternoon, a major slide occurred in the upstream slope at the right abutment, as shown in Figures A.2.1 through A.2.4.

Casagrande (1965) summarized observations of the failure as it occurred: "The movement began by a bulging out of the western portion of the affected upstream slope with simultaneous subsidence of the core pool. Then a transverse crack developed at the western end which widened rapidly into a deep gap while the moving portion of the slope started to swing in a rotational movement as if hinged at the abutment. Through this gap the core pool drained with enormous speed. The western portion which was moving out faster and further, broke into several large blocks and came to rest in the fan-shaped pattern seen in the aerial photographs."

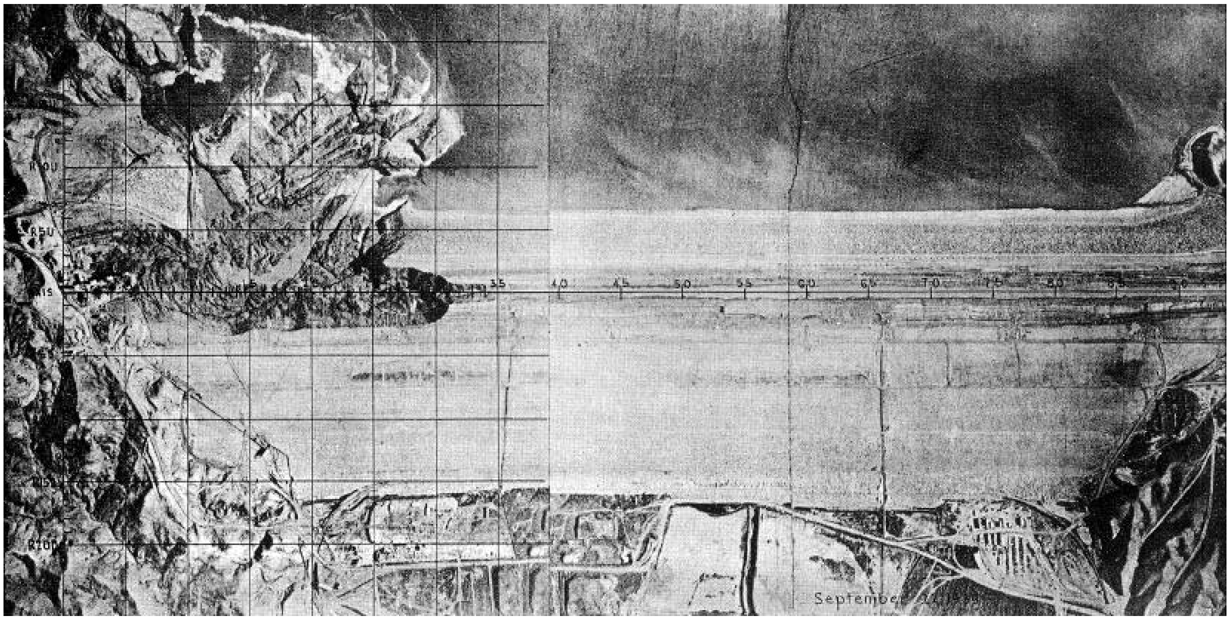

Figure A.2.1: Aerial view of post failure geometry. (U.S. Army Corps of Engineers, 1939)

Figure A.2.2: Enlarged aerial photo from Figure A.2.1 showing failure at the east end of the dam. (from http://www.midrivers.com/~rafter/lake/)

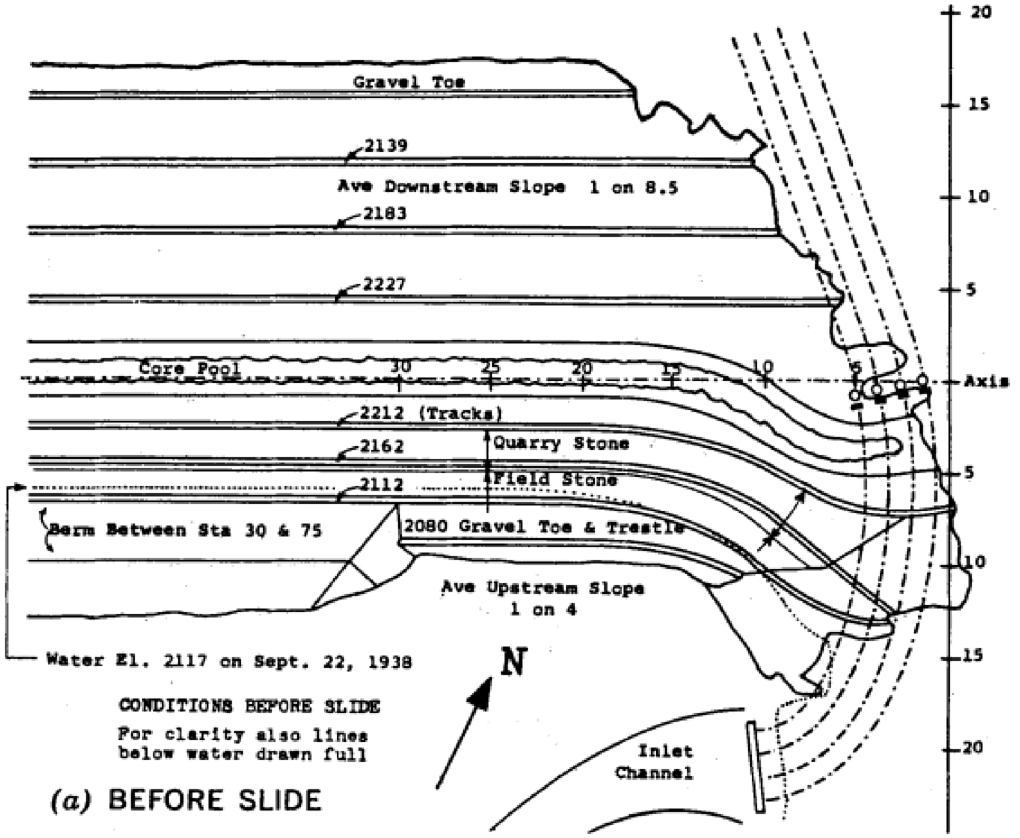

(a) BEFORE SLIDE

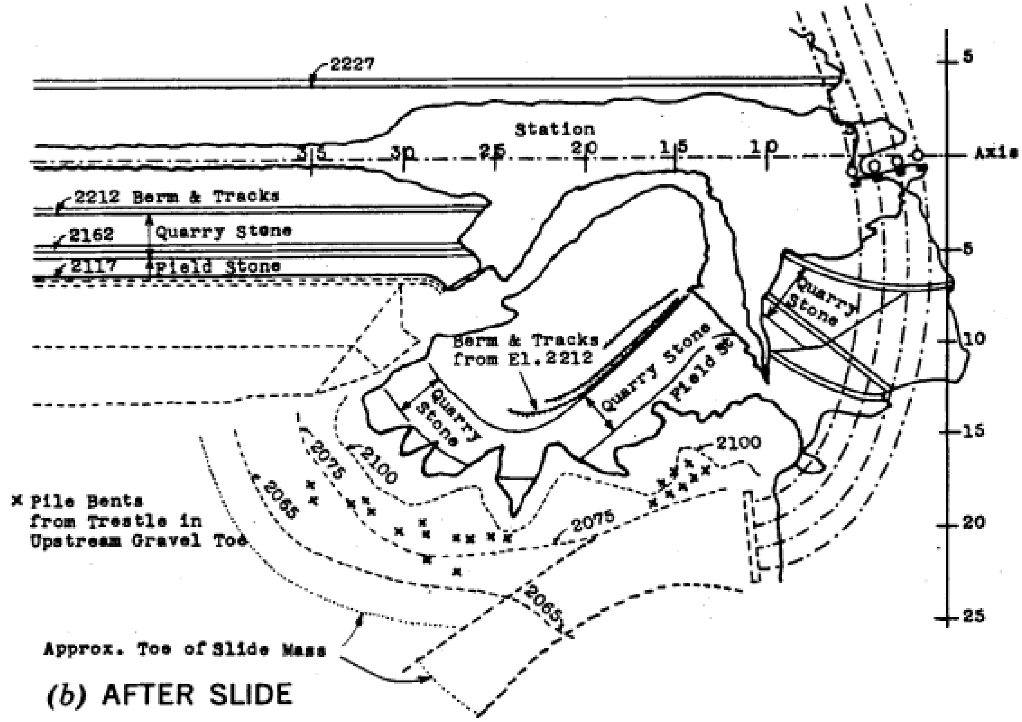

(b) AFTER SLIDE

Figure A.2.3: (a) Pre-failure and (b) post-failure plan views of the east end of Fort Peck Dam, showing locations of identifiable elements and structures that can be tracked from inception of failure to final resting position. (Casagrande, 1965)

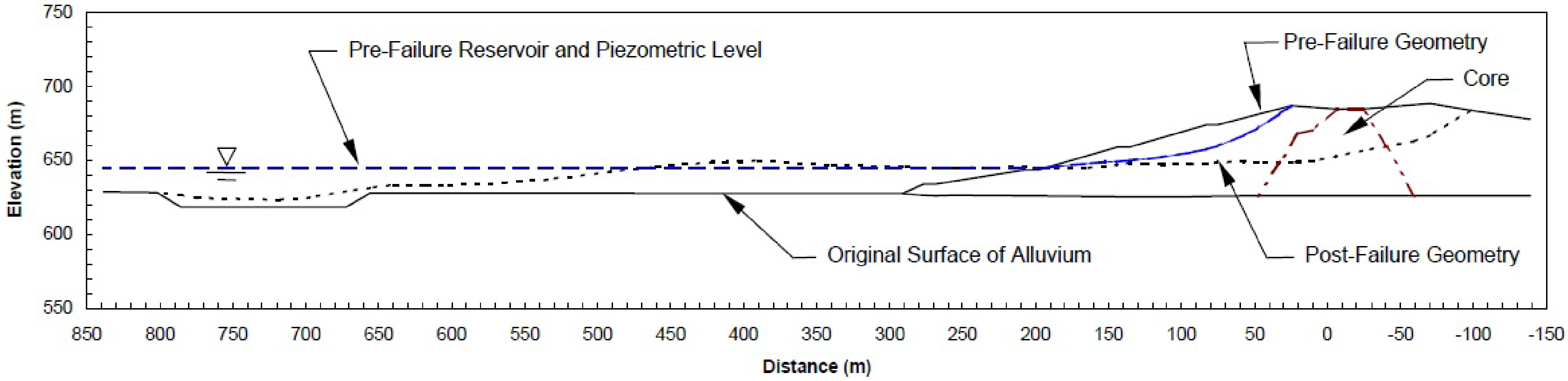

Figure A.2.4: Pre-failure and post-failure cross-section geometry of Fort Peck Dam. (from Olson, 2001; after Middlebrooks, 1942 and Casagrande, 1965)

Casagrande also summarized his initial observations upon visiting the site; noting that large, intact blocks of the embankment travelled "like floating islands in a mass of thoroughly disturbed materials". He also noted that the materials between the intact blocks were "dangerously quick", and that numerous sand boils were still actively discharging both sand and water ten days after the failure.

Following the initial investigations, a debate arose as to the actual cause of the failure. This debate can largely be tracked in Middlebrooks (1942) and in the associated follow-on Discussions in the ASCE Journal. A Board of Consultants was formed to determine the cause of this failure, and their majority conclusion was that the failure had been triggered by sliding along weak, nearly horizontal beds of Bearpaw Shale within the upper foundation. A few Board members had dissenting opinions, and felt that the initial movement may have been initiated by slippage along the shale beds, but that this, in turn, had triggered liquefaction of the overlying loose, saturated embankment shell and core materials (Gilboy, 1942; Casagrande, 1965). Gilboy summarized the expert panel minority view nicely as "liquefaction was triggered by shear failure in the shale, and the great magnitude of the failure was principally due to liquefaction."

Soil liquefaction was not very well understood at the time of the failure, and this debate was in part a product of the era; and so the majority opinion of the original Board of Consultants was that the shale beds were the principal culprits. Casagrande (1965) went on to better justify the alternate view that this was a liquefaction-induced flow failure, and his arguments and data were eventually compelling. As a result, this failure has been one of the most studied case histories for purposes of engineering evaluation of post-liquefaction strengths.

A.2.3 Geology and Site Conditions

Fort Peck Dam was constructed by hydraulic fill placement of local river sands and other alluvial soils (Casagrande, 1965). Most of the surficial clay deposits were removed prior to placement of base cutoff sheet piles and embankment fill. The remaining foundation alluvial deposits consist of alternating and interbedded layers of gravels, sands and clays, as can be seen in Figure A.2.5, which has an exaggerated vertical scale. Also shown in Figure A.2.5 is the contact between the site's alluvium and the underlying Bearpaw clay-shale deposit, which consists of layers of shale interbedded with thin layers of bentonite (Casagrande, 1965; Marcuson and Krinitzsky, 1976).

An extensive site investigation was performed at the Fort Peck Dam site as part of the static and seismic stability studies reported in Marcuson and Krinitzsky (1976). Figure A.2.6 shows a cross-section of the repaired and completed dam, and the locations of a number of the SPT borings performed as part of these studies. A number of rotary wash borings with SPT measurements were performed, and these will be discussed in more detail in the Sections that follow. Figure A.2.6 also shows the zonation developed by the USACE at station 42+00, based on these borings as well as previous cross-sections from the original failure investigations. This mid-1970's site investigation also included a limited number of Dutch cone soundings, but only one of the soundings penetrated into the sandy hydraulic fill materials of the dam shells.

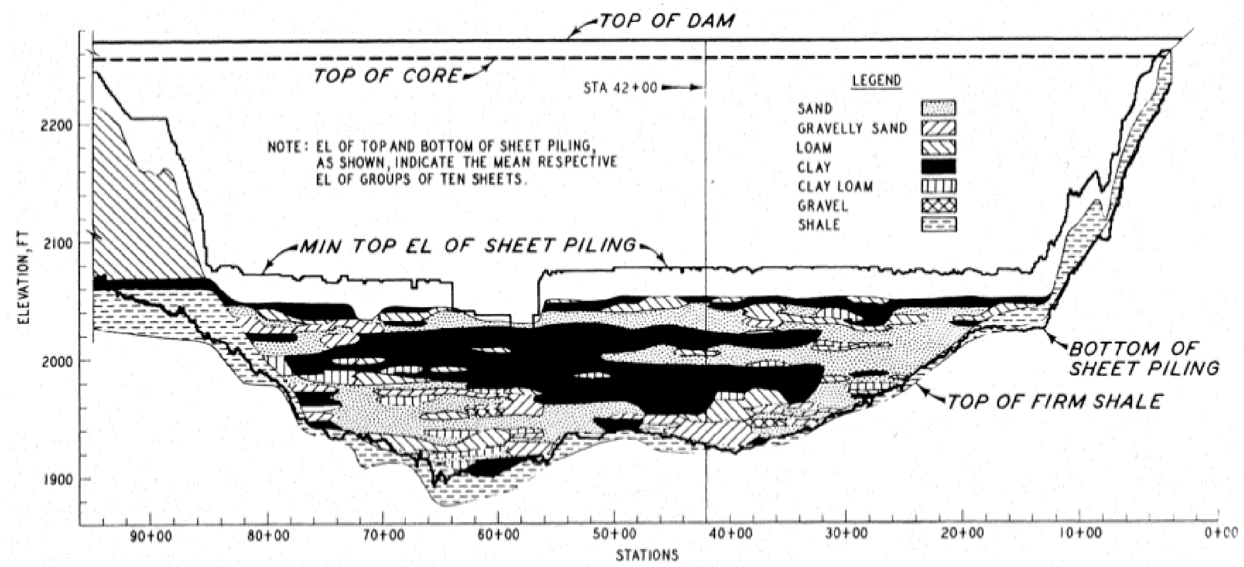

Figure A.2.5: Foundation site conditions at Fort Peck Dam. (Marcuson and Krinitzsky, 1976).

A.2.4 Evaluation of Representative Post-Liquefaction Residual Strength

A.2.4(a) Initial Yield Stress Analyses

The pre-failure and post-failure cross-sections utilized for back analyses were based in large part on the cross-sections presented in Casagrande (1965), as presented in Figure A.2.7. Figure A.2.8(a) shows the pre-failure cross-section geometry modelled as the best estimate case. This figure also shows the best estimate failure surface for these initial yield stress analyses. Initial yield stress ($S_{r,yield}$) is defined as the theoretical post-liquefaction strength within liquefiable materials on the eventual failure surface that would be necessary to develop a calculated Factor of Safety equal to 1.0 for the pre-failure geometry.

The unit weights of the hydraulic fill materials at the time of failure above and below the phreatic surface were estimated considering the recent time since placement, the nature of the hydraulic fill materials that comprised the dam, the values used by other investigators, and data developed by available field studies. Conventional Mohr-Coulomb type shear strength parameters were estimated for non-liquefied soils on a similar basis. Table A.2.1 summarizes the best estimate material properties employed for these analyses. Additional analyses were performed, varying these properties, to investigate sensitivity of resulting calculated post-liquefaction residual strengths.

The principal stratigraphy shown in Figure A.2.8(a) is separated into three main layers: (1) the foundation strata, (2) the liquefied hydraulic fill zones, and (3) non-liquefied hydraulic fill. The location of the interface between the foundation strata and liquefied embankment soils is primarily based on the results of SPT tests and the geologic cross section presented in Marcuson and Krinitzsky (1976) at station 42+00. The interface between the liquefied and non-liquefied

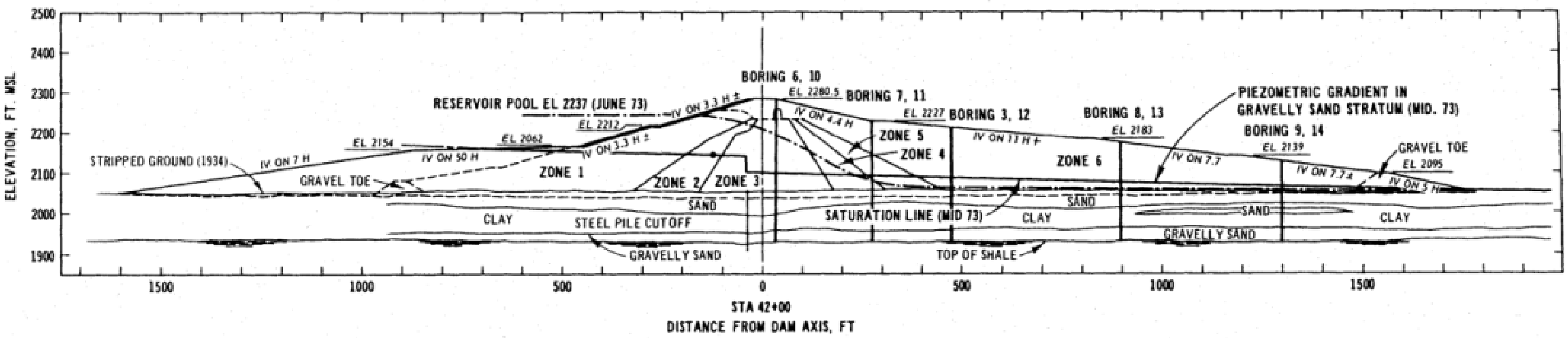

Zone	Elevation (ft)	Average D_{10} (mm)	Average Clay Content (%)
1 and 6	Below 2100	> 0.1	< 3
1 and 6	2100 – 2180	> 0.1	< 5
1 and 6	Above 2180	> 0.05	< 8
2 and 5	Below 2255	> 0.005	< 10
3	Below 2200	< 0.005	> 10 & < 30
3	Above 2200	< 0.01	< 30
4	Below 2255	Same as Zone 3 or Zone 5	
Sand Plugs	Below 2180	< 0.1	< 20
Above Sand Plugs	2180 - 2255	< 0.01	< 30

Figure A.2.6: Fort Peck Dam cross-section at Station 42+00. (Marcuson and Krinitzsky, 1976).

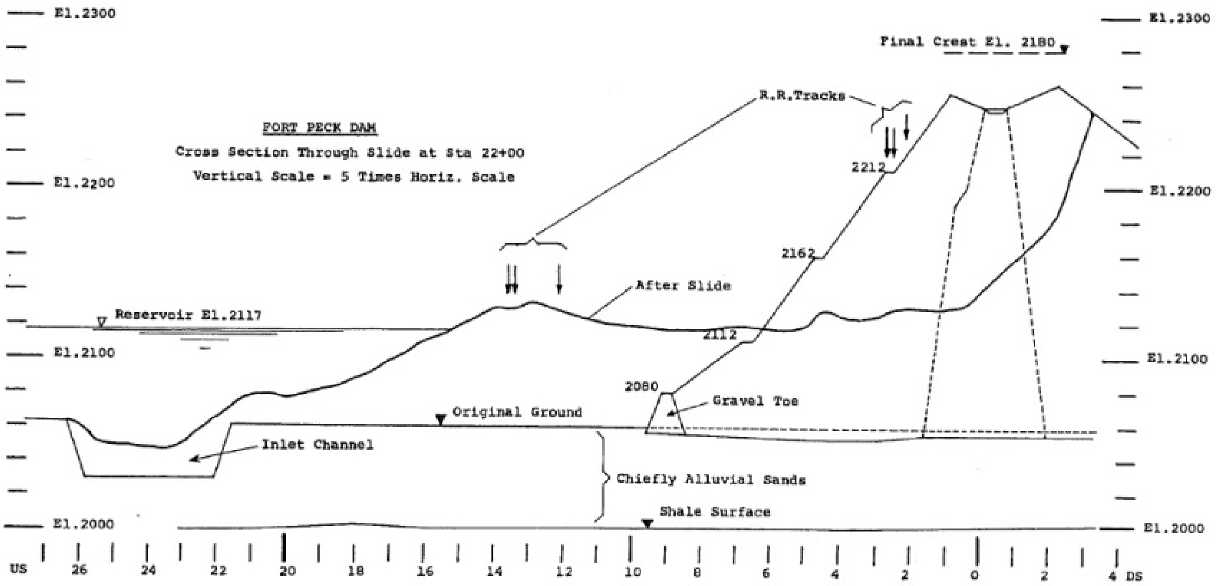

Figure A.2.7: Pre-failure and post-failure geometry of Fort Peck Dam at Station 22+00, with significant vertical scale exaggeration. (Casagrande, 1965).

Table A.2.1: Best estimate material properties for back-analyses of the failure.

Material	Unit Wt.	Mohr-Coulomb Strength Properties	
		Cohesion	Phi
Foundation	125 pcf	c′ = 0	Ø′ = 35°
Liquefied Hydraulic Fill	122 pcf	S_r = Back-Analyzed	Ø′ = 0
Non-Liquefied Hydraulic Fill	115 pcf	c′ = 0	Ø′ = 30

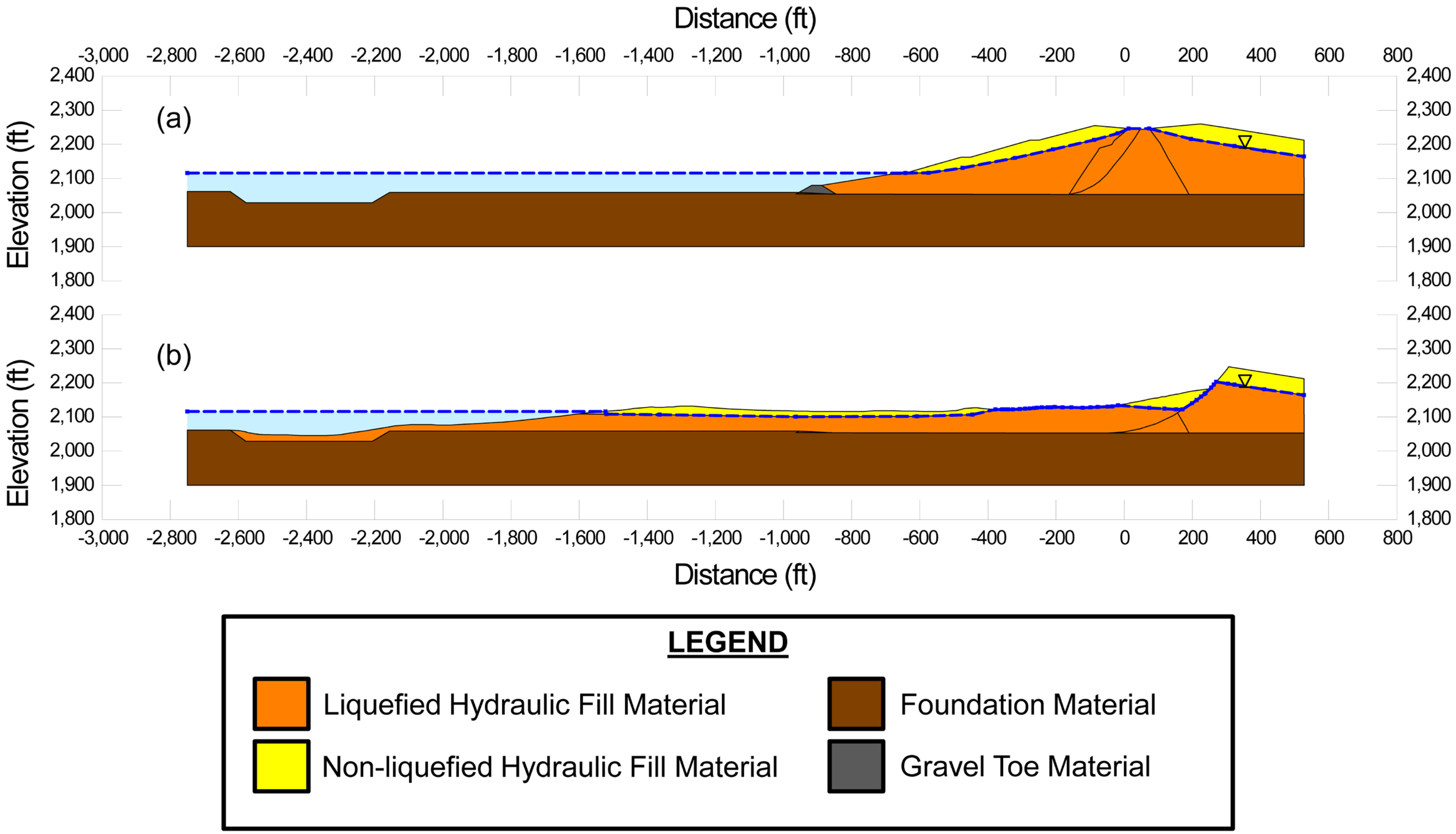

Figure A.2.8: Fort Peck Dam: (a) Pre-failure geometry and best-estimate failure surface for initial yield stress analyses, and (b) post-failure geometry and best-estimate failure surface for post-failure residual geometry analyses.

hydraulic fill material is based on the assumed phreatic surfaces on the upstream and downstream sides of the rising embankment fill. The locations of these phreatic surfaces are based on knowledge of the water level within the reservoir and the approximate elevation of the puddle core pool where material was actively being hydraulically placed at the time of the failure. With the control points at the upstream toe and the crest known, a phreatic surface was assumed in the relatively recently placed hydraulic fill. Resulting calculated post-liquefaction strengths were found not to be very sensitive to the phreatic surface modelled here, as the principal failure occurred at depth.

Conditions within the central "puddle core" and transition zones are complicated, and represent a challenge with regard to back-analyses of the post-liquefaction strength of the hydraulic fill materials of the upstream shell. Hydraulic fill was deposited from rail lines along the upstream and downstream edges of the rising fill, and was contained within starter dykes at the upstream and downstream sides. As a result, coarser materials tended to settle nearer the upstream and downstream faces, while finer soils tended to settle more slowly, and thus to propagate towards the center of the rising dam. The intent was to construct an embankment with a naturally transitioning gradation from coarser, free draining sandy shells towards a more clayey "puddle core".

In actuality, the result was more randomly variable and poorly controlled, with layers and lenses of coarser and finer soils interlayered together in a complex manner. Nine of the SPT borings from the 1976 stability studies provide the best available basis for characterization of the hydraulic fill materials comprising the dam. These 1976 stability studies were focused mainly on the potentially "liquefiable" coarser sands and silty sands of the shell zones, and only two of these nine borings penetrated the central "puddle core" and/or the adjacent "transition" zones. These two borings are presented in Figures A.2.9 and A.2.10. Boring No. 6 (shown in Figure A.2.9) was performed through the center of the "puddle core", as shown in the cross-section of Figure A.2.6. A second boring (Boring No. 10) was co-located at the same central core location, but it was performed for installation of a piezometer and was not carried to full depth and was not performed or logged as an SPT boring. Boring No. 7 (shown in Figure A.2.10) was performed through the downstream edge of the downstream side "transition" zone, as also shown in the cross-section of Figure A.2.6. Close examination of Borings No's. 6 and 7 show that layers and lenses of relatively clean sandy soils, with variable silt and clay content, extend right through the central "puddle core", while clayey and silty layers can also extend away from the central puddle core zone and across the adjacent "transition" zones and likely into the "shells".

As shown in Figures A.2.8(a) and A.2.8(b), the main failure surface passes through the lower portion of the central puddle core region as well as both the upstream and downstream transition regions. The apparent initial (smaller) failure surface nearer to the face of the dam passes through the upper portions of the central puddle core zone as well. Modeling of conditions, and shear strengths, across the central "puddle core" and "transition" embankment region is thus an important issue in back-analyses of the 1938 slope failure. Different approaches have been taken by different investigation teams and analysts. In these current studies, it was considered that some fraction of the sandier materials in the central "puddle core" were likely to perform as potentially liquefiable hydraulic fill soils, and that conditions were even more "mixed" in the even more variable adjacent transition zones. As a best estimate case, it was considered that a considerable

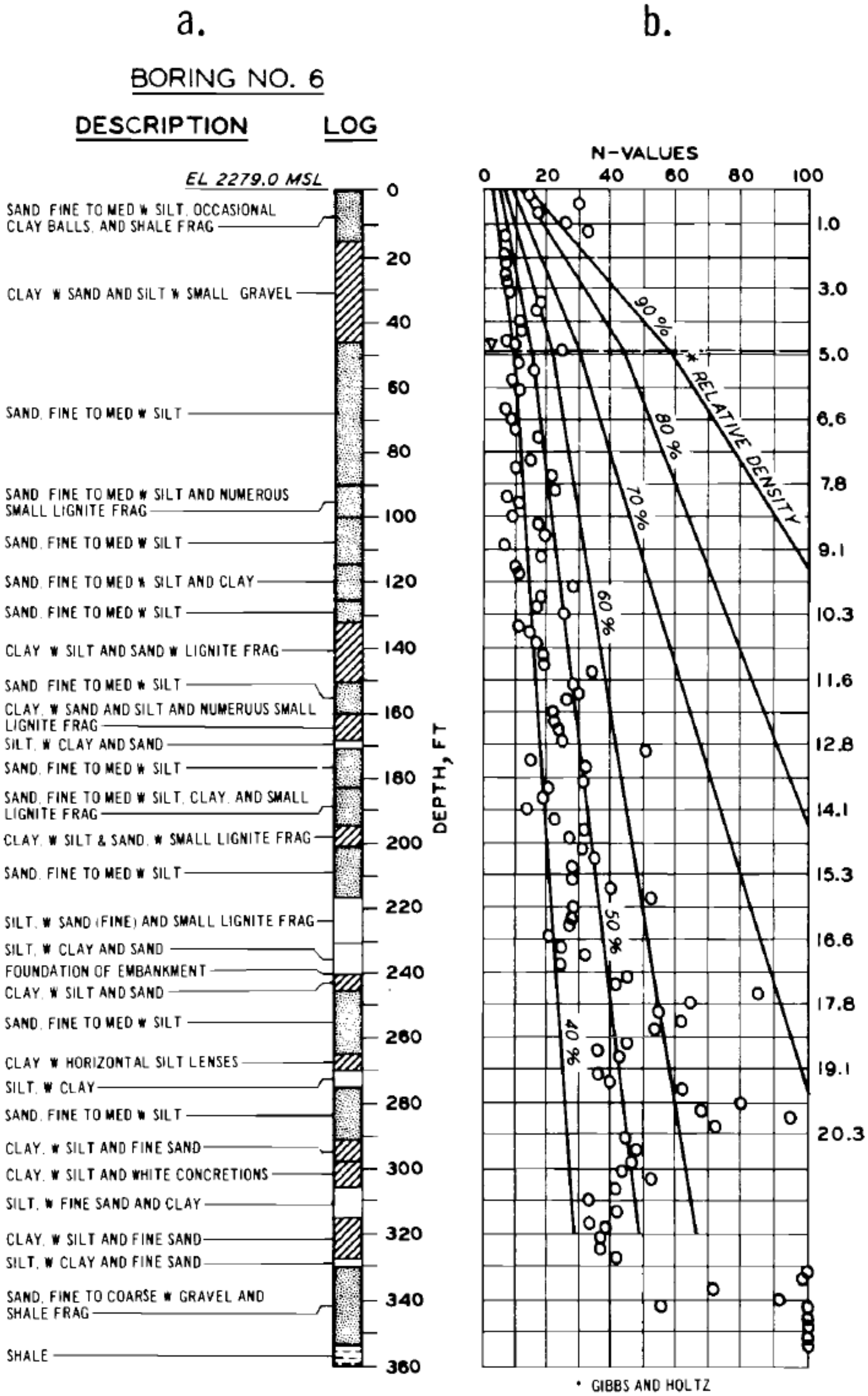

Figure A.2.9: Boring No. 6 through the central puddle core zone of Fort Peck Dam. (Marcuson and Krinitzsky, 1976)

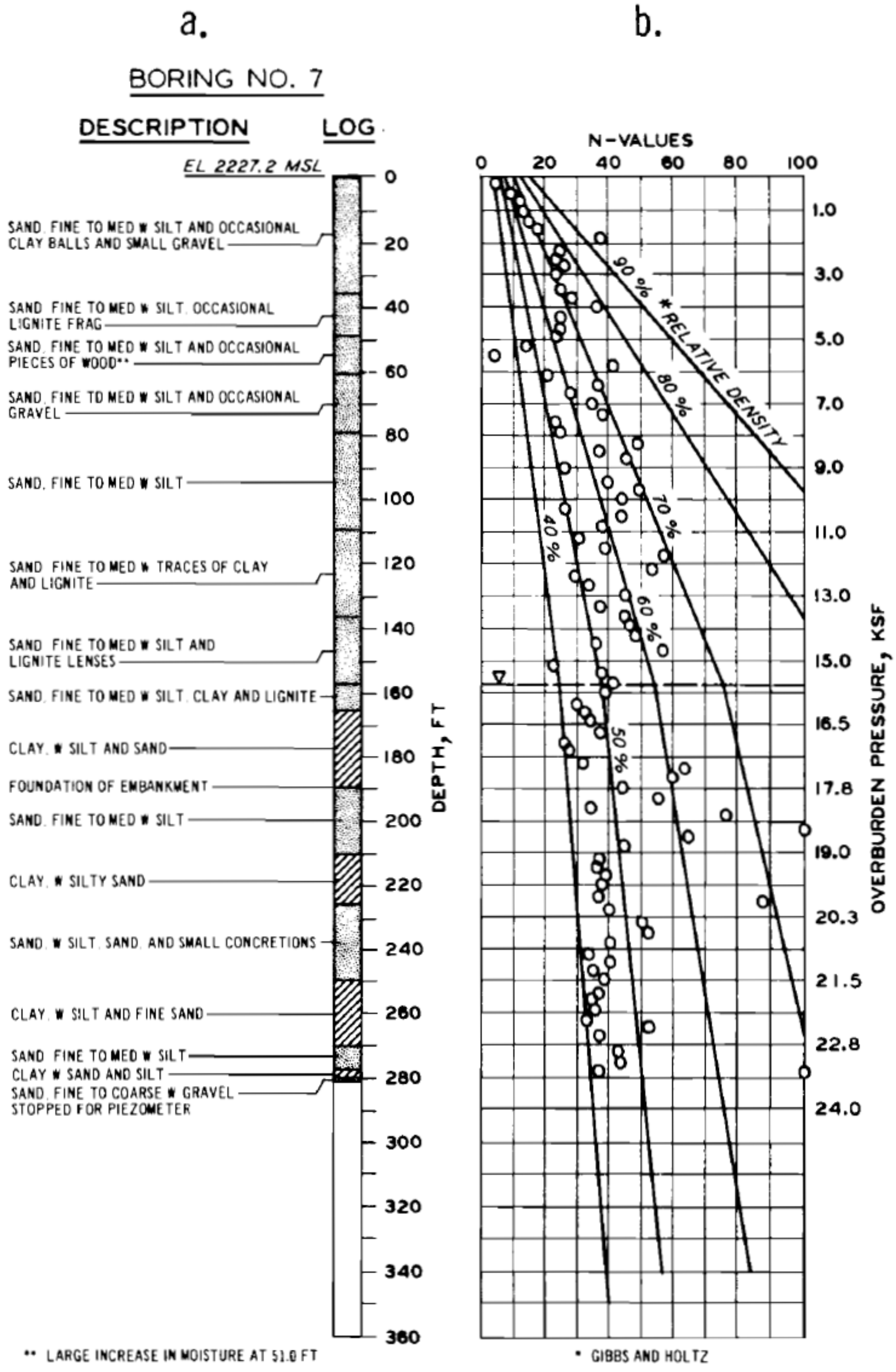

Figure A.2.10: Boring No. 7 through the upstream transition zone of Fort Peck Dam. (Marcuson and Krinitzsky, 1976) majority of the failure surface passing through the central "puddle core" zone shown in Figures A.2.5 through A.2.7 would pass through soils that would behave as clay-dominated materials with regard to undrained shear strength, and that only a small fraction of any potential failure surface would pass through soils that would behave as classically "liquefiable" sandy and silty soils. Similarly, it was assumed that a majority (but not all) of the transition zones would be best modeled as being comprised of soils likely to behave in a more classically "liquefiable" manner.

In this current study, the central puddle core zone materials were modeled as "clayey" soils with undrained residual strength $S_{u,r}$, and the adjacent transition zones were modeled as being comprised of potentially liquefiable hydraulic fill materials with post-liquefaction strength S_r. It is clear that cohesive, clayey soils occur into the transition zones, and that more cohesionless soils extend into the core zone, and this simplified modeling is intended to accomplish some "averaging" across this complicated region.

The lowest of the central puddle core and transition fill materials had been in place for a bit less than four years when the 1938 slope failure occurred. As a result, it was assumed that these primarily clayey soils in the central region of the embankment were likely underconsolidated to varying degrees. It is also noted, however, that largely horizontal layers and lenses of coarser, more free-draining sandy and silty soils would have helped to promote lateral drainage and would have accelerated consolidation of the more clayey materials to some degree. It is difficult to make a precise estimate of the undrained shear strength, and especially the large-strain undrained residual shear strength, of the clayey soils in this central embankment region. More recent testing data is of little assistance here, as multiple decades had passed and these soils had consolidated and gained strength over that period. As a best estimate scenario, it was assumed that these partially under consolidated soils would have an S_u/P ratio of approximately 0.1 to 0.18, and that they would also have significant sensitivity due to their loose (underconsolidated) condition. Sensitivity ratios of approximately 3 to 5 were assumed for these soils which were not likely flocculated (as they were freshwater deposited), but which were likely strongly contractive when sheared. This leads to a residual strength ratio in the range of $S_{u,r}/P \approx 0.02$ to 0.06 for these clayey soils. A value of $S_{u,r}/P$ of 0.04 was taken as the best estimate case, and additional analyses were performed exploring the likely range (upper and lower bounds) with $S_{u,r}/P = 0.02$ and $S_{u,r}/P = 0.06$ to study the sensitivity of calculated post-liquefaction strengths to these modeled conditions in the central embankment region.

Olson (2001), and Olson and Stark (2002) made a slightly different set of modeling assumptions. They also modeled shear strength across the lower portion of the central "puddle core" as being clay-dominated, with an average shear strength of $S_u \approx 4.8$ kPa (~100.3 lbs/ft^2), regardless of depth or effective overburden stress. They do not explain this choice. Most other investigators do not even describe how they modeled shear strengths across this region, so this is often a "black box" within back-analyses for this particular case history.

Based on the best estimate analysis of the failure scenario shown in Figure A.2.8(a), the resulting best estimate value of average initial yield stress (the value of post-liquefaction $S_{r,yield}$ required to produce a calculated Factor of Safety equal to 1.0 for pre-failure geometry) within the liquefiable hydraulic fill was found to be $S_{r,yield} \approx 2{,}370$ lbs/ft^2 for the smaller initial failure surface shown in Figure A.2.8(a) and $S_{r,yield} \approx 2{,}100$ lbs/ft^2 when the final failure surface shown in Figure A.2.8(b) is imposed on the initial geometry. The representative value was then taken as intermediate between these two at $S_{r,yield} \approx 2{,}235$ lbs/ft^2. Failure surfaces were varied to evaluate sensitivity to modelling assumptions and details. Shear strengths across the central embankment were also varied, as discussed above, to evaluate sensitivity to modelling assumptions and details. Strengths of the non-liquefied embankment soils were also varied. Resulting values of representative $S_{r,yield}$ for variations considered reasonable were on the order of $S_{r,yield} \approx 2{,}023$ to 2,468 lbs/ft^2. Initial yield stress is not intended to represent the operative post-liquefaction strength that controlled the full field failure that occurred, but it is useful in calibrating and checking the more rigorous analyses that will follow, and in development of relationships useful in evaluation of other back-analysis case histories.

Stark and Olson also calculated initial yield stress ($S_{r,yield}$), and they reported a best estimate value of $S_{r,yield}$ = 82.9 kPa (1,731 lbs/ft^2), with a range of $S_{r,yield}$ = 69.9 to 89.6 kPa (1,441 to 1,871 lbs/ft^2), in generally good agreement with the values calculated in these current studies.

A.2.4(b) Residual Strength Analyses Based on Residual Geometry

Similar "static" stability analyses were performed to evaluate the "apparent" shear strength within the liquefiable hydraulic fill (S_r) that would result in a calculated Factor of Safety equal to 1.0 for the post-failure residual geometry of Figure A.2.8(b). Assumptions and modeling details were largely the same as described in the previous Section A.2.4(a), and sensitivity analyses with varying combinations of modeling and parameter details were performed here as well.

An additional modeling detail that affects these analyses is the possible occurrence of hydroplaning as the toe of the embankment failure mass enters rapidly into the reservoir, or the possibility of the failure mass being borne along upon weak reservoir sediments of even lower strength than the liquefied embankment materials as the toe of the embankment failure mass enters rapidly into the reservoir. As this was the first filling of the reservoir, it is assumed that there were not yet any significant deposits of loose, weak reservoir sediments accumulated. The question of hydroplaning is a more interesting one. The incremental momentum and displacement analyses described in Section A.2.4(c), which follows, show that peak translational velocities were momentarily as high as approximately 30 feet per second and more at the toe; a rate at which some degree of hydroplaning could occur (see Section 4.2.1). Scale model experiments for soil masses entering into water indicate, however, that hydroplaning seldom occurs over a distance beneath the base of materials entering the reservoir of more than about ten times the thickness of the entering soil thickness (see Section 4.2.1). In these studies, it was assumed that hydroplaning had negligible effect on the residual condition, because the shear strengths at the base of the forward tip of the materials that entered farthest into the reservoir were not modeled as contributing to overall stability of the larger failure mass farther upslope. Hydroplaning will be discussed again in the incremental momentum and displacements analyses described in Section A.2.4(c), which follows.

The full length of the potential failure plane at the base of the residual slide mass was not used to calculate $S_{r,resid/geom}$ because if the extended extreme toe section of the displaced slide mass developed significant resistance to translation, then the failure plane would have risen upwards to daylight through the very thin residual deposits of material at the final toe. Accordingly, the failure surface was assumed to "daylight" at a downstream station of approximately -1,800 feet in Figure A.2.8(b).

Based on the modeling conditions and assumptions described above, the resulting best estimate value of the post-liquefaction shear strength required for FS = 1.0 with residual geometry is $S_{r,resid/geom} \approx 174$ lbs/ft^2. The approximate range, based on reasonable variations in parameters and modeling details, is $S_{r,resid/geom} \approx 150$ to 202 lbs/ft^2.

Olson (2001) also calculated $S_{r,resid/geom}$ for this case history, and reports a best estimate value of $S_{r,resid/geom} \approx 3.8$ kPa (79 lbs/ft^2), and a range of $S_{r,resid/geom} \approx 0.7$ to 15.1 kPa (15 to 315 lbs/ft^2). These values are in good agreement with the values calculated by the current studies, except that Olson's lower bound is much lower. Olson's lower bound value appears to be very low, and insufficient details are presented so this cannot be examined in further detail.

Overall, it was judged that there was good agreement between the two sets of analyses, despite differences in analysis and modeling details and choices made by the two investigation teams.

A.2.4(c) Incremental Momentum and Displacement Analyses and Overall Evaluation of Post-Liquefaction strength

Full incremental momentum and displacement analyses were performed using similar modeling assumptions and details as described in the preceding Sections. Figure A.2.11 shows the best estimate case analysis. It is difficult to see in detail, owing to the scale of the overall problem and the very large lateral displacements that accrue. But it is useful to see the progression of the increments in a single consecutive sequence. This figure is then repeated in six enlarged increment figures in Figure A.2.12 so that more detail can be seen. In these enlarged figures, the progressive locations of the overall center of mass of the active failure mass are also shown.

The modeled stratigraphy, phreatic surface, and failure progression can be seen in Figures A.2.11 and A.2.12. Figure A.2.13 then shows (1) acceleration vs. time, (2) velocity vs. time and (3) displacement vs. time for the center of gravity of the failure mass of Figures A.2.11 and A.2.12.

A total of six cross-sections were used for the progression of the failure mass, due to the very large displacements that accrue, and also due to the potential complexity of this progression. Based on eye witness reports, as well as the post-failure geometry observed, the initial failure surface (first time step) passes through the front edge of the modeled puddle core. By the second step, the failure surface is then modeled to progress to the larger assumed eventual maximum failure surface. This is a slightly progressive development of failure, and it serves to provide for the separation observed at the "crest" section of the residual geometry.

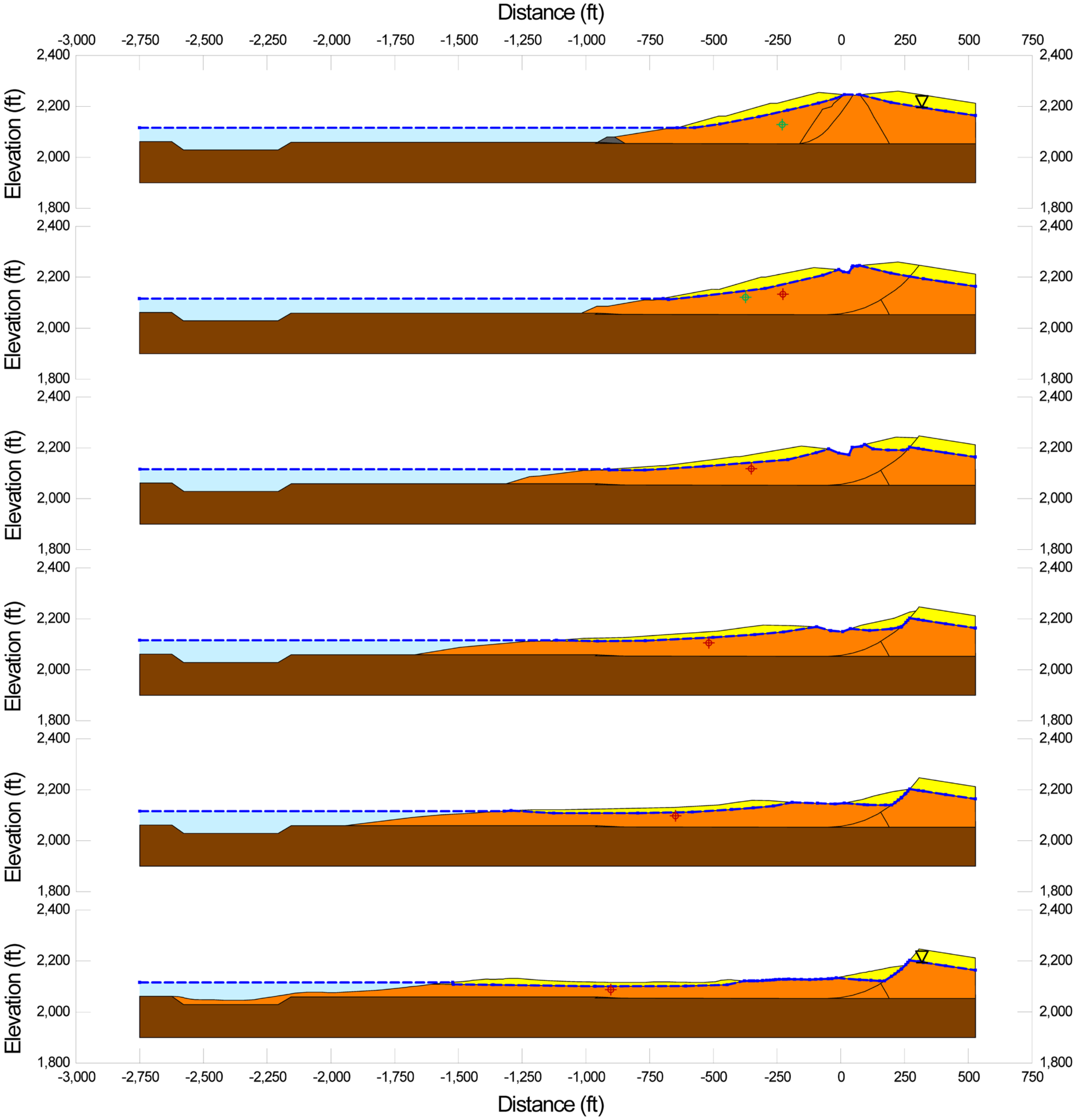

Figure A.2.11: Incremental displacement stages for the incremental momentum and displacement analyses for the best estimate scenario for Fort Peck Dam.

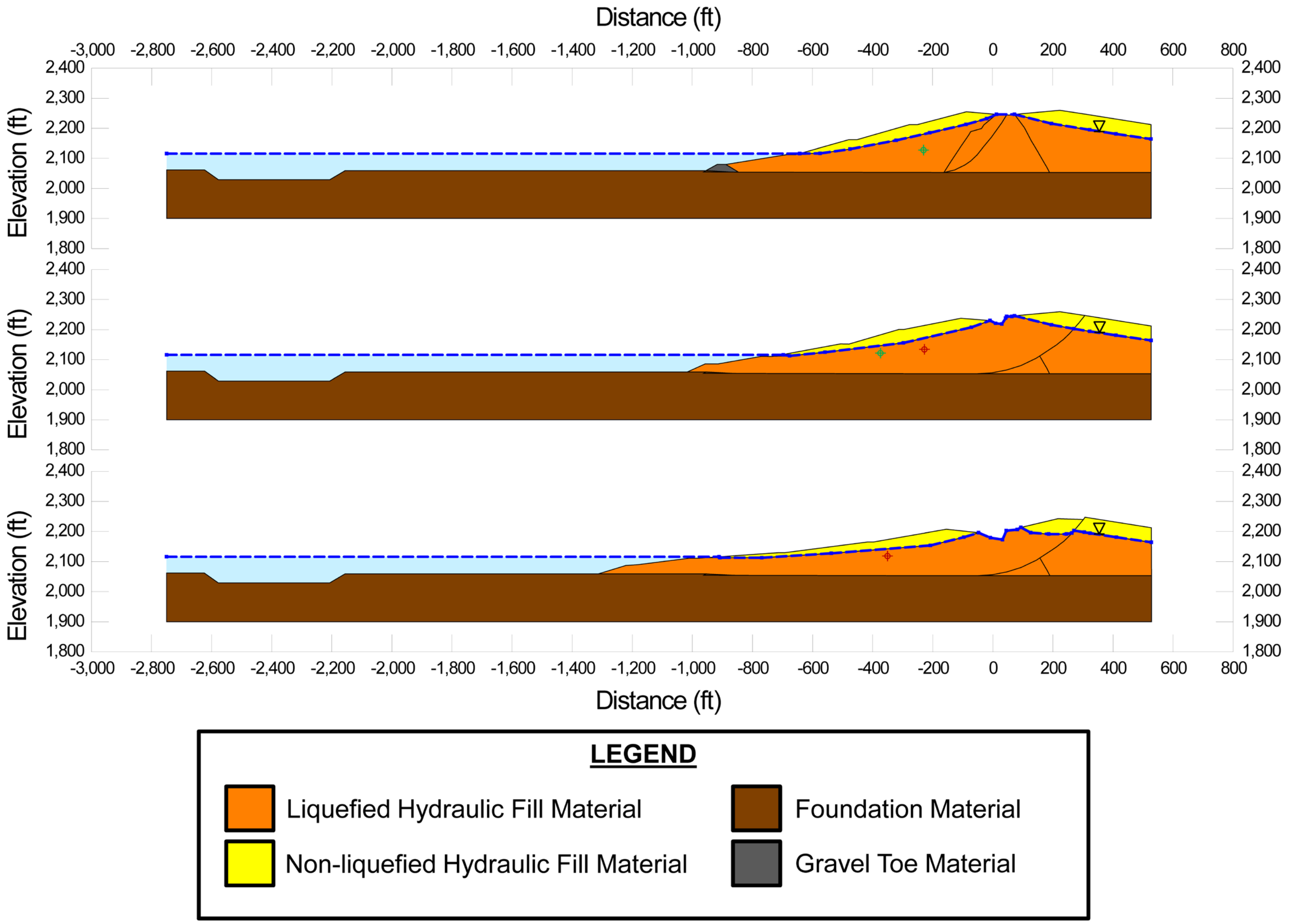

Figure A.2.12: Enlarged view of the incremental displacement stages for the incremental momentum and displacement analyses of Fort Peck Dam from Figure A.2.12 (first three incremental stages).

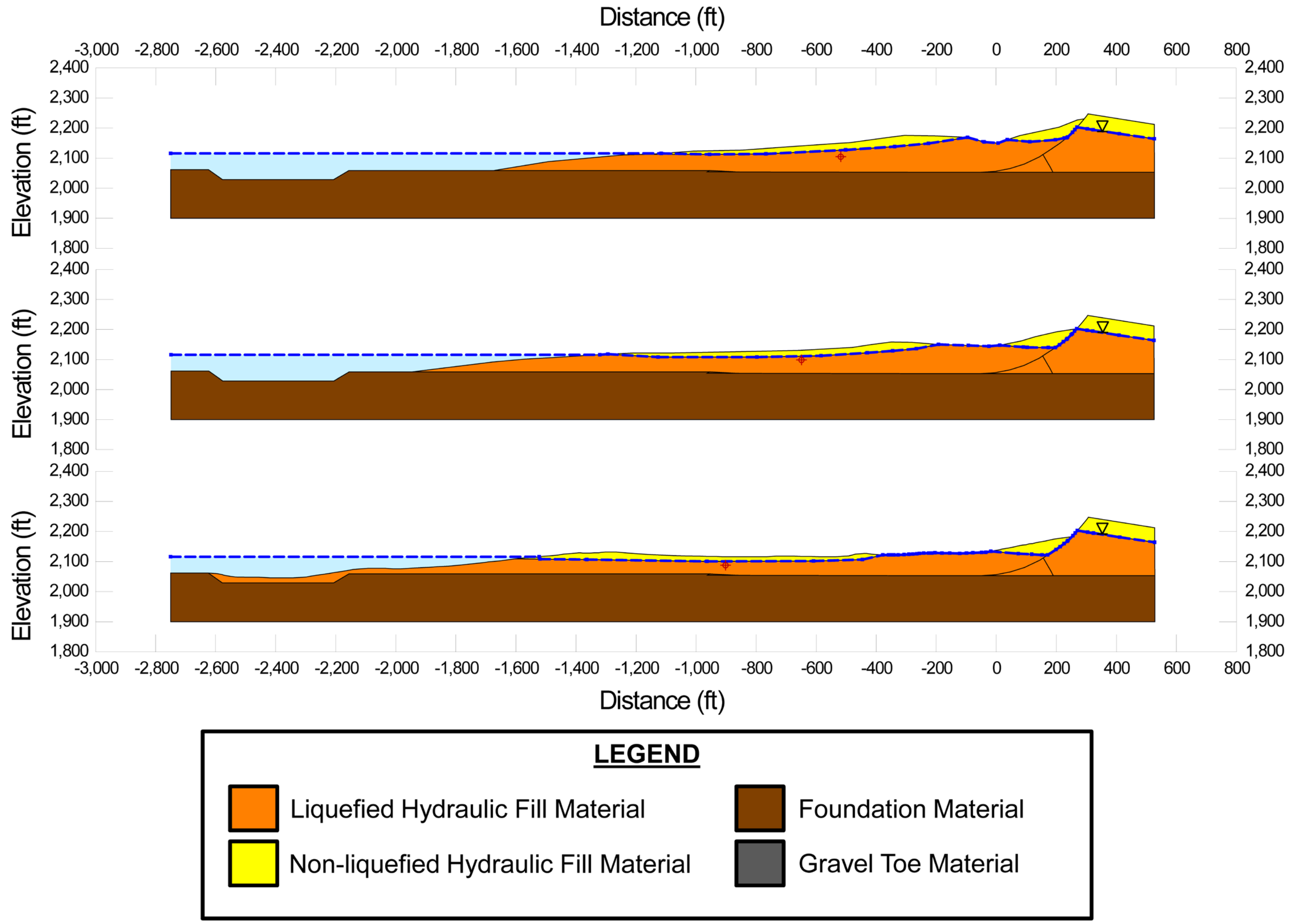

Figure A.2.12 (cont'd): Enlarged view of the incremental displacement stages for the incremental momentum and displacement analyses of Fort Peck Dam from Figure A.2.11 (additional three stages to completion).

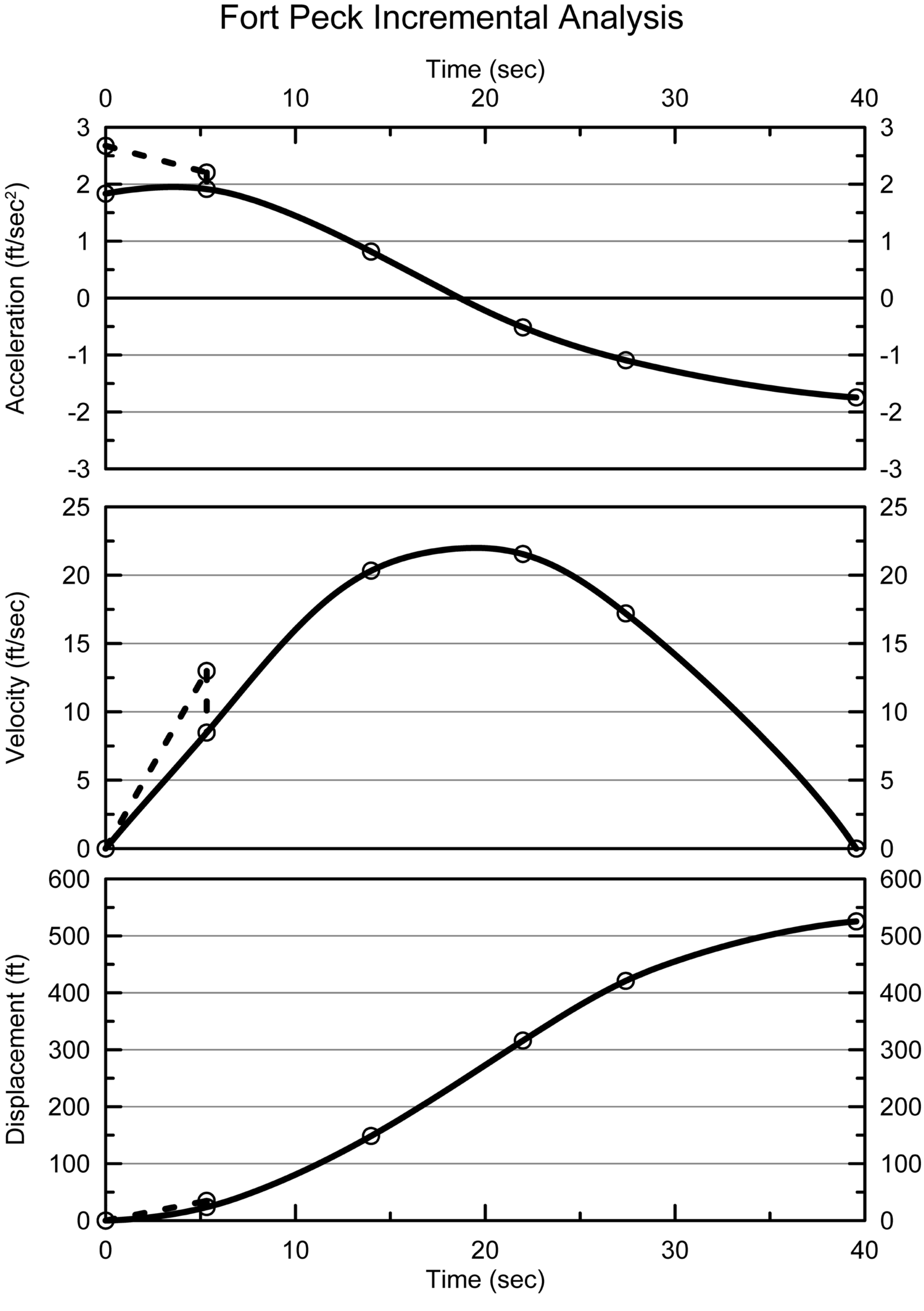

Figure A.2.13: Calculated development of (1) acceleration vs. time, (2) velocity vs. time and (3) displacement vs. time for the incremental momentum and displacement analyses of Figures A.2.11 and A.2.12.

This can be seen most clearly in the enlarged sequence of evolving cross-sections of Figure A.2.12. In this enlarged figure, centers of gravity have been added to the figure. The green cross-hairs of the first cross section are the initial position of the center of gravity delineated by the initial failure surface passing near to the front of the upstream crest. In the second figure, this initial failure mass has progressed, and the center of gravity has moved towards the reservoir. At this second stage, the failure mass of the eventual overall larger full failure along the most downstream back heel scarp begins to move. The red cross-hairs show the location of the new (combined) centers of gravity of the initial failure mass and the incremental additional mass. In the subsequent figures (stages), this center of gravity of the overall failure mass then moves towards the reservoir as the overall failure mass translates and elongates towards the upstream side.

Shear strengths for the “clayey” soils within the central puddle core zone are modeled with $S_{u,r}/P = 0.04$, and the shear strength assigned to the adjacent “transition” zones was the post-liquefaction strength S_r. Post-liquefaction strength (S_r) in the liquefied hydraulic fill soils of the shell and transition zones was iteratively adjusted until a value was found such that the final overall displacement agreed with the observed field displacement.

The failure occurred during first filling of the reservoir, so there were no significant accumulations of soft, weak reservoir sediments. The velocities calculated suggest that some degree of hydroplaning may have occurred as the toe of the embankment entered rapidly into the reservoir (see Section 4.2.1 of the main report). But the assumption that entrapment of fluids beneath the advancing front would occur over a lateral dimension of less than 10 times the thickness of the entering soils, coupled with the relatively flat pre-failure slope of the toe and increasing thinning of the toe failure “tip”, suggest that hydroplaning would have likely been localized near to the advancing tip. For the best estimate case illustrated in Figures A.2.11 through A.2.13, it was assumed that hydroplaning would reduce the shear strength (S_r) at the base of the portion of the overall failure mass that entered into the reservoir and eventually moved farther upstream that lateral Station -1,800 feet in Figures A.2.11 and A.2.12 because embankment soils that eventually traveled farther upstream than this continued to thin and spread far beyond the more nearly coherent toe of the remainder of the failure mass. Even if hydroplaning had not occurred beneath these extreme toe materials, it would not have been possible for these extremely thin toe failure materials to provide significant resistance to movements of the failure materials farther to the right (farther upstream), and the failure surface would have “daylighted” upwards to the surface at about downstream Station -1,800 feet. So negligible shear strength was modeled for materials that passed farther downstream than lateral Station -1,800 feet from the crest centerline.

The resulting back-calculated post-liquefaction strength of the liquefied hydraulic fill that was calculated based on this particular combination of “best estimate” conditions is $S_r = 762$ lbs/ft^2.

A number of variations in parameters were analyzed to investigate variability and sensitivity with regard to calculated post-liquefaction strengths. The shear strengths of the cohesive clayey soils in the central puddle core Zone C were modeled with strengths ratios as low as $S_{u,r}/P = 0.02$, and as high as 0.06. Friction angles in the non-liquefied soils above the phreatic surface were increased and decreased by 3°. The maximum average reduction in average shear strength at the base of the portion of the embankment failure mass that entered into the reservoir due to potential hydroplaning was taken as 90%, and the lateral distance upstream of the advancing toe was increased to nearly twice the best estimate scenario, and reduced to zero. Unit weights were varied up and down by several ponds per cubic foot.

Based on combinations of modeled conditions considered to be reasonable, the range of calculated values of representative S_r was found to be $S_r \approx 575$ to 929 lbs/ft^2. It was the judgment of this engineering team that this represented a range corresponding to approximately +/− 1.5 standard deviations. This range was nearly symmetric about the best estimate value of 762 lbs/ft^2, so no significant further adjustments were necessary. Overall, based on an assumed normal distribution, the best estimate (median) value of post-liquefaction strength from these studies was judged to be

$$\overline{S_r} = 762 \text{ lbs/ft}^2$$

with a standard deviation of

$$\sigma_{\overline{S}} = 118 \text{ lbs/ft}^2$$

The best previous studies for cross-comparisons here are those of Davis et al. (1988), Olson (2001) and Wang (2003), all of whom specifically performed analyses incorporating dynamic inertial effects. As shown in Table A.2.2, the results calculated here are just slightly higher than the other investigation teams in this group. The details of Wang's analyses are not presented, but it is noted that his results agree well with this current study. The full details of Davis' analyses are also not presented, but his value is in reasonably good agreement as well. The studies of Davis et al. and of Olson and Stark did not consider hydroplaning and so may be somewhat conservative.

Additional investigators have also analyzed this case, including Lucia (1981), Bryant et al. (1983), Seed (1987), Seed and Harder (1990), and others. The estimated S_r values from these previous studies range from approximately 240 to 599 lbs/ft^2, and serve to demonstrate the considerable variability in previous estimates made. Many of these earlier analyses employed conservative simplified approaches, and it is to be expected that their results would provide generally lower values of S_r.

A.2.5 Evaluation of Representative SPT Penetration Resistance

As part of the seismic stability analyses of Fort Peck Dam in the study reported by Marcuson and Krinitzsky (1976), a total of nine investigative SPT borings were drilled in the dam's crown and downstream slope. It is assumed that these SPT borings provide data largely representative of the upstream side failure zone due to the approximate symmetry of hydraulic fill placement operations prior to the 1938 slope failure. But the upstream face was much flatter in slope than the downsteam face, so that the distance from the line of upstream side hydraulic fill spigots depositing material to the center of the final crest was significantly greater than for the downstream side spigots, so perfect symmetry did not occur.

These investigation borings were performed by the rotary wash method, and SPT were performed at fairly regular intervals. The results of the SPT were filtered to exclude the results from tests performed outside the zone where liquefaction was assumed to have potentially occurred, and also for tests where clay dominated the material tested in an individual test. The remaining tests were corrected to $N_{1,60,CS}$ values based on the corrections and adjustments for equipment, test procedure, rod length, and fines content as per Cetin et al. (2018a,b), and with the effective overburden stress correction (C_N) of Deger (2014).

Table A.2.2: Representative values for the Fort Peck Dam case history of: (a) post-liquefaction strength (S_r), (b) initial vertical effective stress (σ_{vo}'), and (c) $N_{1,60,CS}$ developed by various investigation teams, and estimates of variance in each of these indices when available.

(a) Post-Liquefaction Strength:	
Olson (2001) and Olson and Stark (2002)	S_r = 570 psf, and range = 63 to 211 psf
Wang (2003) and Kramer (2008)	$\bar{S}_r$ = 671.5 psf, and $\sigma_{\bar{S}}$ = 130.1 psf
Davis et al. (1988)	S_r = 701 psf
This Study	$\bar{S}_r$ = 762 psf, and $\sigma_{\bar{S}}$ = 118 psf
(b) Representative $N_{1,60,CS}$ or $N_{1,60}$ Value:	
Olson (2001) and Olson and Stark (2002)	$N_{1,60}$ = 8.5 bpf, and range = 4 to 14 bpf
Wang (2003) and Kramer (2008)	$\overline{N_{1,60,CS}}$ = 15.8 bpf, and $\sigma_{\bar{S}}$ = 0.9 bpf
Poulos (1988)	$N_{1,60}$ = 5.3 blows/ft
This Study	$\overline{N_{1,60,CS}}$ = 12.5 bpf, and $\sigma_{\bar{N}}$ = 2.7 bpf
(c) Representative Initial Vertical Effective Stress:	
Olson (2001) and Olson and Stark (2002)	σ_{vo}' = 7,341 psf, with no range provided.
Wang (2003) and Kramer (2008)	Value of $\sigma_{vo}' \approx$ 7,466 psf is not well documented, and so is considered useful only as an approximate comparison. (See Section 2.3.8.1, and Table 2.3.)
This Study	$\overline{\sigma'_{vo}}$ = 7,258 psf, and $\sigma_{\bar{\sigma}}$ = 687 psf

The resulting corrected SPT data were then binned into sets based on lateral station along the dam's axis and relative distance from the dam's centerline. Materials tended to have higher fines contents near the dam's centerline (beneath the crest), and lower fines contents farther out towards the faces. $N_{1,60}$ blowcounts uncorrected for fines, on the other hand, tended to increase a bit with distance from the centerline.

Borings 1 through 5, plus 8 and 9, were judged to be most likely representative of $N_{1,60,CS}$ values for the sandy hydraulic fill materials of the downstream side shell zone. These were examined to eliminate the few SPT performed in potentially clayey samples. A small number of very high $N_{1,60}$ values (2% of the total number of SPT) were also deleted based on the assumption of gravel having potentially biased the results. The remaining SPT $N_{1,60}$ values were then binned jointly for these 7 borings, and both median and mean $N_{1,60}$ values were determined. The mean value was determined to be 13.7 blows/ft., and the median value was determined to be 13.3 blows/ft. The representative $N_{1,60}$ value was taken to be the median value of $N_{1,60}$ = 13.3 blows/ft. Because the shell materials generally had low fines contents of between 0% to 10%, fines adjustments per Cetin et al. (2018a,b) would increase this representative value by a factor of between 1.00 to 1.08. A factor of 1.04 was applied, and the estimated representative value of fines adjusted penetration resistance was then $N_{1,60,CS} \approx 13.8$ blows/ft.

A single boring (B-7) provided SPT N-values for soils within the downstream transition zone. Similar processing was performed for this boring, including elimination of SPT performed in clayey soils, deletion of spuriously high values (there were none of these), determination of the mean and median values of $N_{1,60}$, and application of fines adjustments. $N_{1,60}$ values were somewhat lower in this transition zone, with a mean of 12.6 blows/ft. and a median of 12.5 blows/ft. The median value was taken as representative. Fines adjustments were higher in the finer soils encountered in the transition zone, and based on typical reported fines contents of between 10% to 30%, the representative value of fines adjusted penetration resistance was $N_{1,60,CS} \approx 14.8$ blows/ft. This value was considered along with the value of 13.8 blows/foot for the sandier shell zones calculated above. Based on approximate weighted averages based on contribution of the downstream shell and the transition zones to the overall failure surface, the representative penetration resistance was taken to be $N_{1,60,CS} = 13.9$ blows/ft.

An additional adjustment was then made to account for likely "ageing" effects over the roughly four decades that elapsed between the date of the failure and the performance of SPT tests in the 1970's. It is known that both cyclic resistance to triggering of liquefaction, and also penetration resistances, increase somewhat over time since placement or since deposition. Quantification of this with regard to SPT penetration resistance is difficult however. There is some research available regarding increases in both SPT N-values and in CPT tip resistances over time, due in large part to the relatively common use of CPT to evaluate ground improvement by means of densification using vibro-densification, deep dynamic compaction, blasting, etc. (e.g.: Skempton, 1986; Schmertmann, 1987; Lewis et al., 2009; etc.). Skempton (1986) proposes an equation for estimation of increase in SPT N-values over time, but this should be considered highly approximate. Over a period from 1 year after placement to 40 years after placement, Skempton's relationship predicts an increase in N-values of approximately 37%, but this should be considered very approximate. Kulhawy and Mayne (1990) propose an alternate relationship, logarithmically linear over time, and this would predict an increase in N-values of approximately 8% over a period from 1 year after placement to 40 years after placement. It is clear that <u>some</u> adjustment should be made here; otherwise the "representative" $N_{1,60,CS}$ value based on the 1970's SPT data would overestimate the representative value at the time of the failure. Values of between 5 to 40 % were considered here. For conservatism in developing relationships between $N_{1,60,CS}$ vs S_r, an adjustment nearer to the low side was made here. In the end an adjustment of 10% was adopted. The representative blowcount of 13.9 blows/ft. from the 1970's SPT data was then reduced by a factor of 1/1.10 to a final best estimate of $\overline{N_{1,60,CS}} \approx 12.6$ blows/ft.

Only one other failure case history back-analyzed by these current studies had similar potential ageing effects, and that was the Wachusett Dam embankment failure. That failure occurred in 1907, and modern SPT investigations were finally performed seven decades later. As described in Section A.1.1, the representative $N_{1,60,CS}$ value for that case (without correction for ageing effects) was found to be $\overline{N_{1,60,CS}} \approx 8.2$ blows/ft, and a similar adjustment of approximately 10% was then made for ageing effects to produce a final estimate of $\overline{N_{1,60,CS}} \approx 7.5$ blows/ft for the fine sand shell materials of the Wachsett Dam which had been loosely placed in thick lifts. Only two case histories among the thirty case histories back-analyzed warranted adjustments for "ageing" effects, and the adjustments applied were relatively minor. These had relatively little effect on the overall predictive correlations eventually developed based on the back-analyses of the full 30 case histories.

Uncertainty, or variance, in the overall average or representative $N_{1,60,CS}$ value was not so much a function of variance in individual contributing N-values. Instead it was a function of (1) perceived differences in localized $N_{1,60,CS}$ values at different locations that did not appear to be consistently correlated with distance from the core, (2) uncertainty with regard to the use of downstream side SPT data to represent upstream side conditions, especially given the non-symmetric geometry of the wider upstream vs. downstream shells, and (3) passage of time (approximately four decades) from the occurrence of the slope failure to the performance of the field SPT investigations of the 1970's. Overall, it was judged that the penetration resistance of the potentially liquefiable hydraulic fill materials of the downstream shell and the transition zones would be suitably modeled with a normal distribution with mean (and median) $N_{1,60,CS}$ = 12.5 blows/ft, and with a standard deviation of $\sigma_{\overline{N}}$ = 2.7 blows/ft.

As shown in Table A.2.2(c), Olson and Stark developed a somewhat lower estimate of $N_{1,60}$ = 8.5 of blows/ft., and range = 4 to 14 blows/ft. Their $N_{1,60}$ values were not adjusted for fines, and so were lower than the fines-adjusted $N_{1,60,CS}$ values of the other studies. Kramer and Wang developed slightly higher estimates of $\overline{N_{1,60,CS}}$ = 15.8 blows/ft, with a lower standard deviation of $\sigma_{\overline{S}}$ = 0.9 blows/ft. They made no adjustment for ageing effects, and their estimate of standard deviation for this case was driven primarily by the variance within the large suite of SPT N-values available, and did not include the factors in the preceding paragraph above and so likely underestimated uncertainty to some degree. Poulos (1988) working with Davis et al. (1988) proposed a best estimate value of 5.3 blows/ft, but this was lower than the values proposed by any other investigators, and it was not intended to represent a mean or median estimate as Poulos took the "representative" value to be a less than median value within the range of blowcounts available based on the observation that failure would tend to pass through the weaker soils within the failure zones. Accordingly, his estimate is not directly comparable with the others and would be expected to be lower. Each of these investigation teams explain the general approach taken, but do not provide much detail with regard to fine points that might have affected their assessments here.

Overall, it is clear that there is significant uncertainty associated with estimation of representative $N_{1,60,CS}$ for this case history. The values of this current study fall fairly centrally within the ranges of values proposed by previous investigators, and appear to be reasonably well supported given the different approaches taken by the previous investigation teams.

A.2.6 Evaluation of Representative Initial Effective Vertical Stress

The overall best estimate value of the average initial effective vertical effective stress on portions of the eventual failure surface that pass through liquefiable materials was calculated to be σ_{vo}' = 7,258 lbs/ft^2, with a range of σ_{vo}' = 6,548 to 7,992 lbs/ft^2 based on variations in parameters, unit weights and phreatic conditions considered to be reasonable. This was judged to represent a variance of approximately +/- 1 standard deviation, and this range was not fully symmetric about the best estimate value so some minor additional adjustment was made to develop the best characterization of

$$\overline{\sigma'_{vo}} = 7{,}258 \text{ lbs/ft}^2$$

and

$$\sigma_{\overline{\sigma}} = 687 \text{ lbs/ft}^2$$

Values for comparison are shown in Table A.2.2. Olson (2001) calculated an average initial vertical effective stress of $\sigma_{vo}' = 7{,}341$ lbs/ft^2, with no range provided. This agrees very closely with the value developed in these current studies. Average initial vertical effective stresses were not directly reported by Wang (2003) and Kramer (2008), but they were published more recently in the publication by Kramer and Wang (2015). As discussed in Section 2.3.8.1(a), the approach taken by Wang (2003) to evaluation of σ_{vo}' for his nine "primary" case histories (this is one of those nine) is not clearly explained, and it is also poorly documented. Wang's value of $\sigma_{vo}' = 7{,}466$ lbs/ft^2 also agrees very closely with the value developed in these current studies. Agreement between the values of (1) Olson and Stark (2001, 2002), (2) Wang and Kramer (2003, 2008) and (3) these current studies is good.

A.2.7 Additional Indices from the Back-Analyses

A number of additional results, and indices, can be extracted from the analyses performed. Some of these are useful in developing some of the over-arching relationships and figures presented in the main text of this report. These values are presented in Table A.2.3 below.

Table A.2.3: Additional results and indices from the back-analyses of the Fort Peck Dam embankment failure case history.

Maximum distance traveled by the center of gravity of the overall failure mass	528 ft.
Initial post-liquefaction Factor of Safety prior to displacement initiation, and based on best estimate value of S_r	FS = 0.43
Final post-liquefaction Factor of Safety at final (residual) post-failure geometry, and based on best estimate value of S_r	FS = 2.63

A.3 Uetsu Line Railway Embankment (Niigata, Japan; 1964)

A.3.1 Brief Summary of Case History Characteristics

Name of Structure	Uetsu Railway Embankment
Location of Structure	Niigata, Japan
Type of Structure	Relatively symmetric railway embankment
Date of Failure	June 16, 1964
Nature of Failure	Seismic, During the 1964 Niigata Earthquake ($M_W = 7.5$)
Approx. Maximum Slope Height	31 ft.

A.3.2 Introduction and Description of Failure

The Uetsu Line railway embankment failed during the Niigata Earthquake of June 16, 1964 ($M_W = 7.5$), and was initially investigated by Yamada (1966). Peak ground accelerations in the vicinity of the failure were estimated to be on the order of 0.2 g.

Figure A.3.1 shows a cross-section of the failure section, showing pre-failure and post-failure geometry (Yamada, 1966). Figure A.3.2(a) shows the interpreted pre-failure cross-section modeled in these studies, and Figure A.3.2(b) shows the post-failure cross-section modeled in these studies. These are based on the cross-section of Figure A.3.1, and they are shown at true (not exaggerated) vertical scale. The embankment crossed a relatively level valley and the slope of the ground adjacent to the railway embankment was on the order of only 1° to 2°. The final (residual, post-failure) slope of the liquefied embankment material that ran out to a distance of approximately 100 meters (~ 330 feet) beyond the initial embankment toe was estimated have been on the order of about 4°

The railway embankment was constructed from poorly compacted or uncompacted clean, loose, fine sand fill. Fines contents were less than 5%. The embankment at the failure location was founded atop a peat layer, as shown in Figure A.3.1, and this was in turn underlain by clays and sands. The liquefied embankment material that ran out past the original toe spread out thinly over the top of the upper (peat) foundation soils, without wrinkling or bulging the underlying soils, indicating that the shear strength of the liquefied embankment soils was apparently lower than that of the upper foundation soils. The phreatic surface at the time of the failure was not known, and it was inferred to have been at or near to the base of the embankment. Given the fine sands, some degree of capillary rise may have contributed to some minor additional saturation above the phreatic surface.

A.3.3 Initial Yield Strength Analyses

Figure A.3.2(a) shows the cross-section used in these studies for the best estimate case back-analyses performed to determine the initial yield stress, defined as the value of the post-

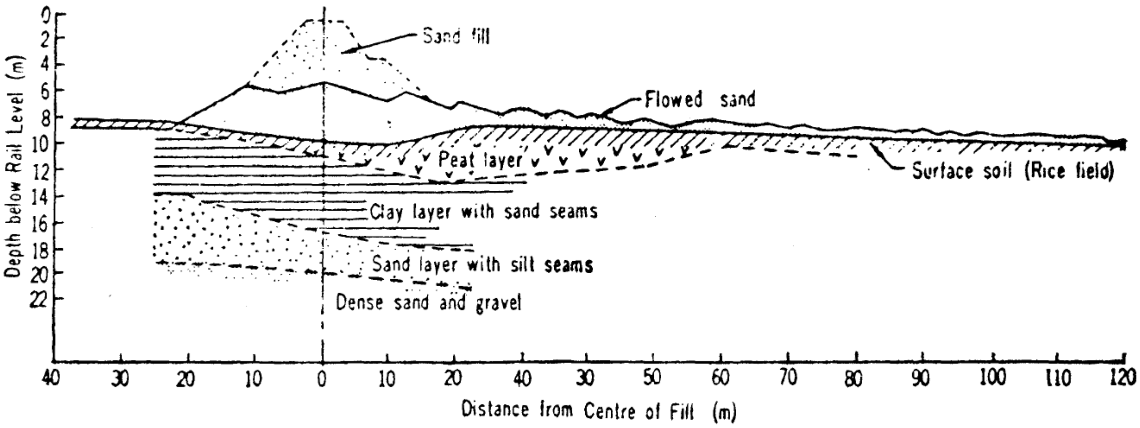

Figure A.3.1: Cross-section of the Uetsu Line railway embankment showing pre-failure and post-failure geometries (from Yamada, 1966)

liquefaction strength $S_{r,yield}$ within the liquefiable saturated lower embankment fill required to produce a calculated Factor of Safety equal to 1.0 for pre-failure geometry.

Based on an eyewitness description, it appears that this failure initiated near the face of the slope and then progressed as an incrementally progressive failure that retrogressed towards the back heel in a series of steps or slices. Based on an assumed phreatic surface that passes approximately through the mid-height of the slope, and exits at the toe, a search was made for the most critical static failure surface assuming liquefaction had been "triggered" in all potentially liquefiable embankment materials below the phreatic surface. This exercise showed that the most critical potential failure surfaces for this set of assumptions would have been for a failure initially closer to the slope face than the final rear scarp shown in Figure A.3.1 and A.3.3(b).

Figure A.3.2(a) shows the most critical failure surface among the potential failure surfaces analyzed (the failure surface requiring the highest value of $S_{r,yield}$ to produce a calculated Factor of Safety of 1.0). Non-saturated embankment sand materials above the phreatic surface were modeled with $Ø' \approx 28°$, and a unit weight of $\gamma_m \approx 114$ lbs/ft^3. Materials below the phreatic surface were considered to liquefy, down to the base of the embankment, and were assigned an undrained post-liquefaction yield strength of $S_{r,yield}$ that was constant along any given failure surface, and a unit weight of $\gamma_s \approx 118$ lbs/ft^3. Results for the most critical initial yield surface shown in Figure A.3.2(a) were $S_{r,yield} = 355$ lbs/ft^2. In these analyses, it was assumed that failure at the toe occurred within the base of the liquefiable embankment fill.

Parameters and geometry were then varied to examine potential variability. The location of the phreatic surface was varied, raising it by up to 0.75 m at the center of the base of the embankment, and lowering it by up to a similar distance. Unit weights were also varied over the ranges considered likely, and the friction angle of non-liquefied material above the phreatic surface was varied from 27° to 30°. Searches were made for the most critical initial failure surface for each combination of assumptions and parameters modeled. Variability was found to be relatively

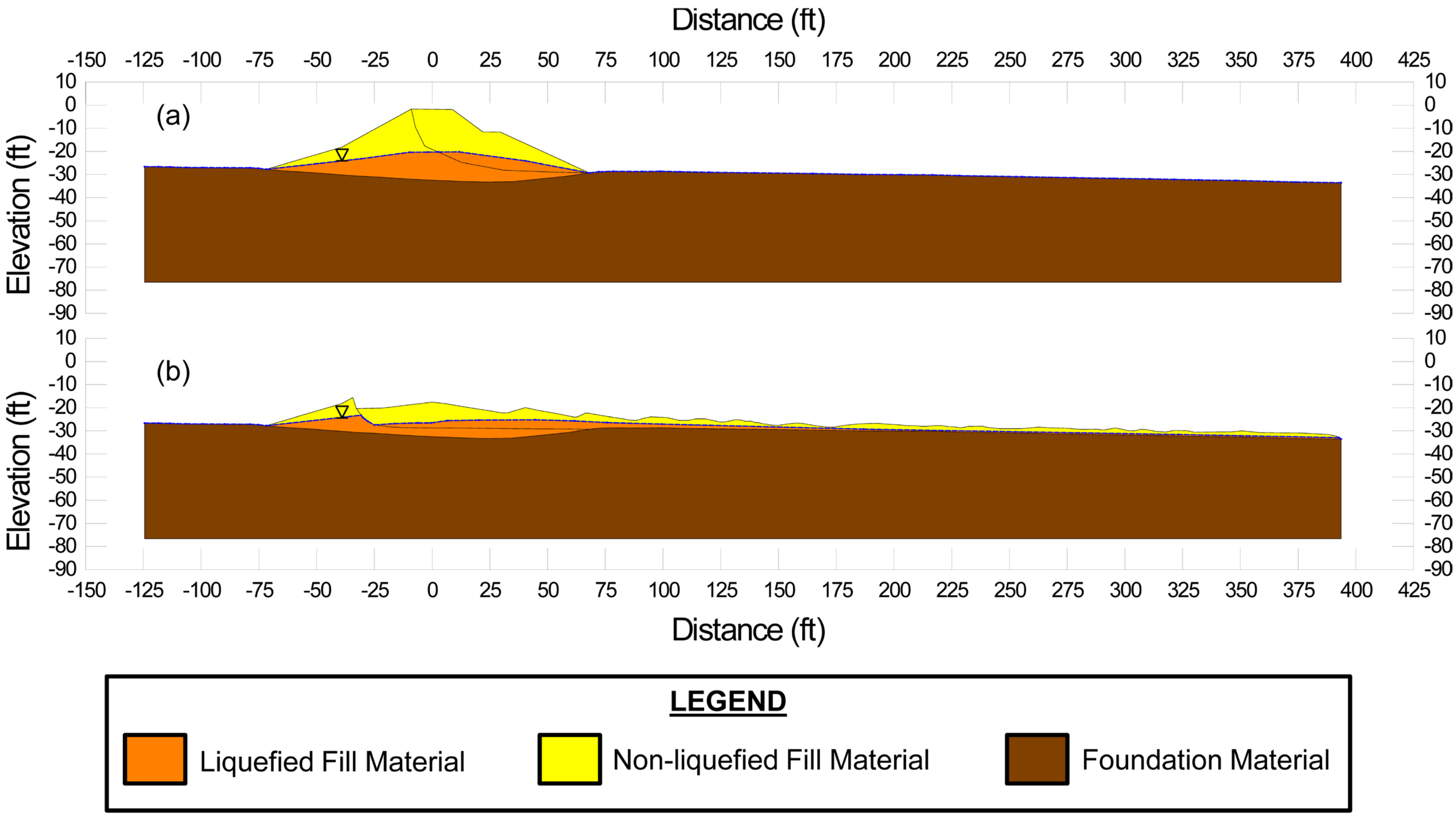

Figure A.3.2: Uetsu Railway Embankment: (a) Pre-failure geometry and best-estimate failure surface for initial yield stress analyses, and (b) post-failure geometry and best-estimate failure surface for post-failure residual geometry analyses.

small, and the resulting range of values of $S_{r,yield}$ for combinations of modeling assumptions and details considered to be reasonable was found to be $S_{r,yield}$ ≈ 317 to 408 lbs/ft^2.

Olson (2001) also performed back-analyses to determine $S_{r,yield}$. Failure surfaces analyzed were generally similar, but varied in close detail. Olson reported a best estimate value of $S_{r,yield}$ ≈ 10.9 kPa (228 lbs/ft^2), and a range of $S_{r,yield}$ ≈ 10.0 to 11.9 kPa (209 to 249 lbs/ft^2).

A.3.4 Residual Strength Analyses Based on Residual Geometry

The calculation of the "apparent" post-liquefaction strength ($S_{r,resid/geom}$) required to produce a calculated Factor of Safety equal to 1.0 based on residual geometry is illustrated in Figure A.3.2(b). This figure shows the phreatic surface, and the failure surface, used to calculate the best-estimate value of $S_{r,resid/geom}$ ≈ 11 lbs/ft^2. Variations were then made in parameters, and in location of the pre-failure phreatic surface, as was described in the preceding section in order to evaluate uncertainty or variability, except that all analyses assumed that the failure surface defining the boundaries of the base of the failure mass as it traveled out past the original toe failed at the interface between the embankment fill and the underlying natural soil. Considering ranges of variations in modeling details and parameters considered to be reasonable, the resulting likely range of post-liquefaction strength required to provide a calculated Factor of Safety equal to 1.0 based on residual geometry was considered to be $S_{r,resid/geom}$ ≈ 7 to 26 lbs/ft^2.

Olson (2001) also calculated post-liquefaction strength required to produce a calculated Factor of Safety equal to 1.0 based on residual geometry, and reported a best estimate value of $S_{r,resid/geom}$ ≈ 0.6 kPa (13 lbs/ft^2), with a range of $S_{r,resid/geom}$ ≈ 0.3 to 1.9 kPa (6 to 40 lbs/ft^2).

A.3.5 Incremental Momentum Back-Analyses and Overall Estimates of S_r

Incremental momentum back-analyses were performed using the same sets of properties and geometries (including failure surfaces and phreatic surfaces) as described in the previous sections. Strengths at the toe, both beneath the original embankment toe, and beneath the toe section as it translated outwards over the peaty marsh deposits, were modeled as 100% of S_r for the liquefiable embankment fill for the case illustrated in Figures A.3.3 and A.3.4. This was, again, based on the observed field geometry after failure which suggested that the base of the liquefied fill had lower strength that the underlying upper foundation soils.

Figure A.3.3 shows the best-estimate progressive incremental momentum analysis, showing the 7 stages of geometry evolution modeled as the failure proceeds. Figure A.3.4 shows the associated calculations of (1) acceleration vs. time, (2) velocity vs. time, and (3) displacement of the overall center of gravity vs. time. For the geometry and phreatic surface shown in Figure A. 3.3, the best estimate value of post-liquefaction strength was S_r = 38 lbs/ft^2.

Failure may have been initiated as an incrementally regressive failure retrogressing in successive "slices" back towards the eventual final rear heel scarp, but given the catastrophically large run out distance, it was assumed that these very loose materials essentially liquefied all at

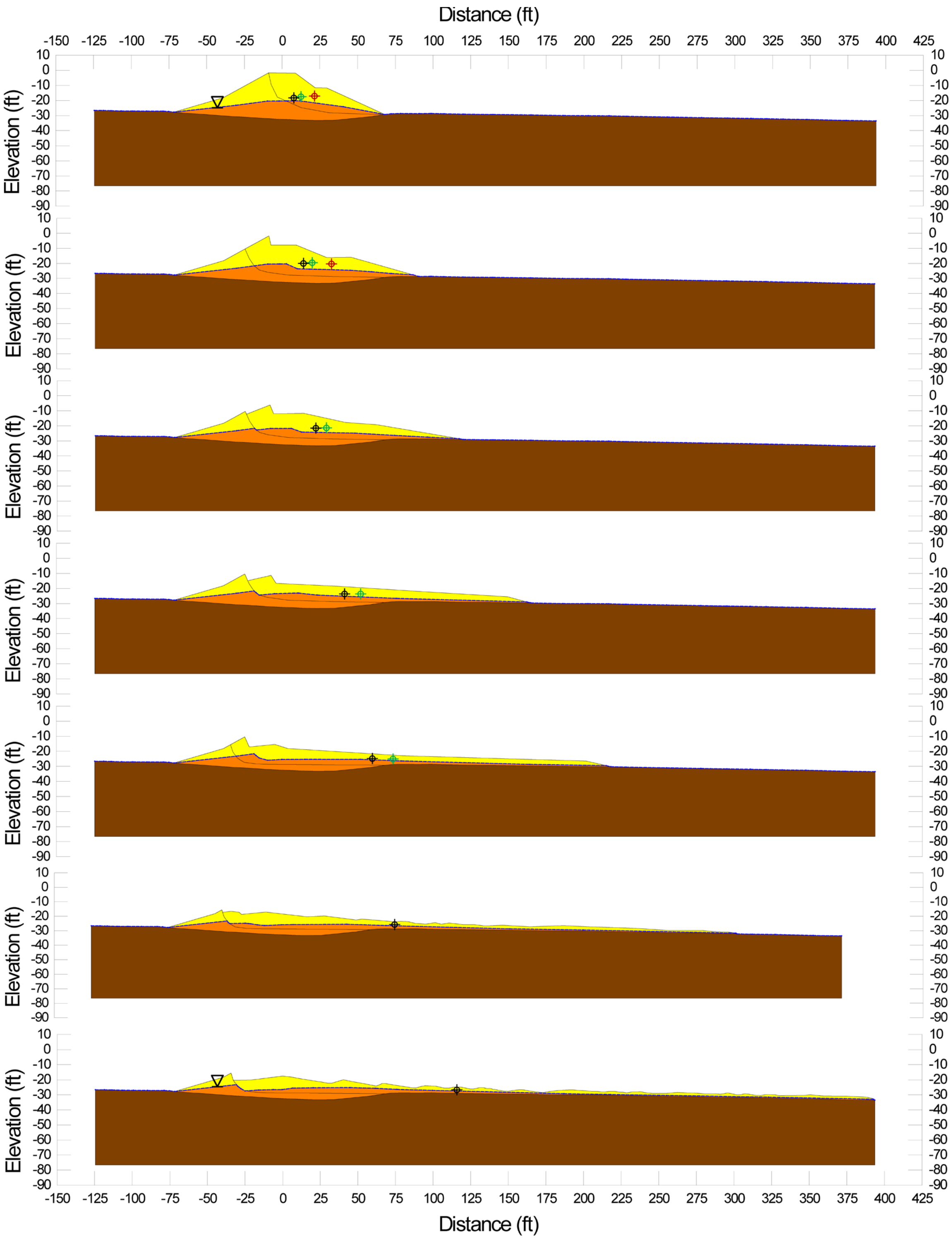

Figure A.3.3: Incremental momentum analysis of the failure of the Uetsu Line Railway Embankment, showing progressive evolution of cross-section geometry modeled.

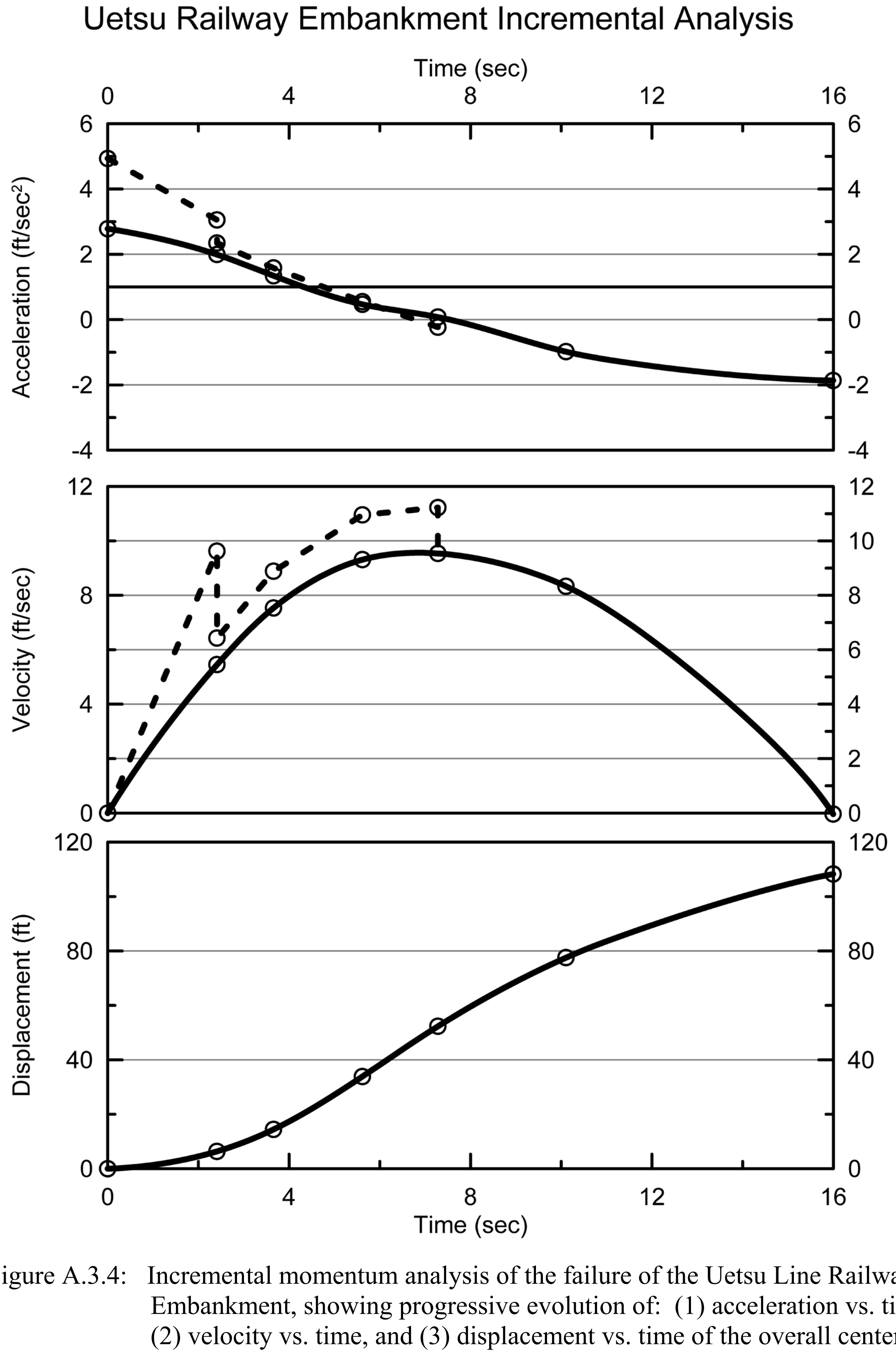

Figure A.3.4: Incremental momentum analysis of the failure of the Uetsu Line Railway Embankment, showing progressive evolution of: (1) acceleration vs. time, (2) velocity vs. time, and (3) displacement vs. time of the overall center of gravity of the failure mass.

once, or nearly so, and the best case analysis shown in Figures A.3.3 and A.3.4 assumes that failure of successive slices initiates rapidly once the slice in front of each successive begins to displace.

The main sources of uncertainty, or variability, in back-calculated values of S_r were (1) the location of the phreatic surface, (2) the rate at which the failure retrogressed progressively towards the back heel in a series of "slices", and the discretization and timing of potentially successive slice initiation, (3) unit weights, (4) frictional strength of the non-saturated upper embankment fill materials, and (5) the precise location of the overall failure surface.

The analysis shown in Figures A.3.3 and A.3.4 neglects cyclic inertial forces, and so may represent a slightly conservative assessment of actual post-liquefaction strength mobilized, but this minor conservatism was neglected.

Based on all analyses performed, and the considerations discussed herein, the overall best estimate value of post-liquefaction strength for the Uetsu Line Railway Embankment failure was judged to be $S_r \approx 38$ lbs/ft^2, with a likely range of $S_r \approx 23$ to 55 lbs/ft^2. Based on the factors contributing to uncertainty or variance for this case history, it was the judgment of the investigation team that this range represented approximately +/− 2 standard deviations. This range of variance is not symmetrical about the best estimate value, so minor further adjustments were made to produce a representative estimate of S_r suitable for regression analyses.

Overall, based on an assumed normal distribution, it was judged that the (mean and median) best estimate of post-liquefaction strength for this case history is

$$\overline{S_r} = 38 \text{ lbs/ft}^2$$

and that the best estimate of standard deviation of mean overall post-liquefaction strength is

$$\sigma_{\overline{S}} = 8 \text{ lbs/ft}^2$$

Estimates of S_r were also reported by several other investigation teams, and two sets of these are shown in Table A. 3.1(a). Olson (2001) and Wang (2003) both performed back-analyses specifically targeting analytical treatment of inertial effects. Olson (2001) and Olson and Stark (2002), reported a best estimate value of $S_r = 1.7$ kPa (35.5 lbs/ft^2), based on their inertial displacement analyses that considered kinetics. Wang (2003) and Wang and Kramer (2008) employed their zero inertial force (ZIF) method to incorporate inertial effects in their back-analyses of this failure, and they also developed estimates of both mean $\overline{S_r} = 43.5$ lbs/ft^2 as well as the associated standard deviation $\sigma_{\overline{S}} = 24.8$ lbs/ft^2. The details of these analyses, and the cross-sections and failure mass assumptions employed, are not presented and so cannot be checked. But this is yet another case history in which the "ZIF" calculations of Wang (2003), which account for inertial effects, produce S_r values in generally good agreement with the results of these current studies.

A.3.6 Evaluation of Initial Effective Vertical Stress

Average initial (pre-failure) effective vertical stress was assessed for the liquefied zones of each of the two failure surfaces (initial and final) shown in Figure A.3.3(a) and (b). The best estimate of the overall average initial vertical effective stress was then taken as the average of these two averages. Reasonable variations were then made in (1) the location of the phreatic surface, (2) unit weights, and (3) the precise location of the overall failure surface.

The resulting best estimate of average pre-failure effective stress within the liquefied materials controlling the failure was then $\sigma_{vo}' \approx 1{,}448$ lbs/ft^2, with a reasonable range of $\sigma_{vo}' \approx 1{,}687$ to $1{,}223$ lbs/ft^2. This range is slightly non-symmetric about the median value, and this range was judged by the engineering team to represent approximately +/− 2 standard deviations. Overall, the best characterization of initial (pre-failure) average effective vertical stress was then taken to be represented by a mean value of

$$\overline{\sigma'_{vo}} \approx 1{,}448 \text{ lbs/ft}^2$$

and with a standard deviation of

$$\sigma_{\bar{\sigma}} \approx 116 \text{ lbs/ft}^2$$

Estimates of σ_{vo}' were also reported by other investigation teams, and two sets of these are shown in Table A.3.1(c). Olson (2001) and Olson and Stark (2002) reported an average pre-failure effective vertical stress of $\sigma_{vo}' = 61.3$ kPa (1,280 lbs/ft^2), in generally good agreement with these current studies. Olson and Stark appear to have developed a slightly lower value of σ_{vo}' due to analysis of a slightly shallower failure surface. Average initial vertical effective stresses were not directly reported by Wang (2003) and Kramer (2008), but they were published more recently in the publication by Kramer and Wang (2015). As discussed in Section 2.3.8.1(a), the approach taken by Wang (2003) to evaluation of σ_{vo}' for his nine "primary" case histories (this is one of those nine) is not clearly explained, and it is also poorly documented. Wang's value of $\sigma_{vo}' = 916$ lbs/ft^2 is significantly lower than the values of Olson (2001) and these current studies, but this is not considered a very rigorous check here and the source of differences between Wang's value and those of Olson (2001) and these current studies cannot be back-tracked. Agreement between Olson's independently back-calculated value, and the value developed in these current studies, is considered good.

A.3.7 Evaluation of $N_{1,60,CS}$

As only Swedish cone soundings were performed within the liquefiable embankment fill materials, inferring equivalent SPT penetration resistances was a challenge. Conversion of these Swedish cone data to equivalent SPT N-values was made using the relationship recommended by Ishihara et al. (1990). There is considerable uncertainty in this relationship, and this is therefore a significant contributor to uncertainty or variability with respect to the median $\overline{N_{1,60,CS}}$ value representative of this material. Corrections for effective overburden stress (C_N) were made using the relationships proposed by Deger (2014), as presented and discussed in Section 4.1.1.

Corrections for fines content were made using the relationship propose by Cetin et al. (2018a,b), and a representative fines content of approximately 20%. The resulting best estimate median $N_{1,60,CS}$ value for these current studies is $\overline{N_{1,60,CS}} \approx 3$ blows/ft. Variance of $\overline{N_{1,60,CS}}$ was estimated primarily on the basis of the perceived uncertainty associated with conversion for Swedish cone penetration resistances to equivalent SPT penetration resistances, and was taken as being represented by a standard deviation of $\sigma_{\overline{N}} \approx 0.8$ blows/ft.

Table A.3.1(b) shows values of representative $N_{1,60}$ or $N_{1,60,CS}$ values developed by two other teams of investigators, and variance or standard deviations in these representative values. Olson and Stark (2001, 2002) developed an estimated representative value of $N_{1,60} = 5.6$ blows/ft, and an estimated range of representative values of $N_{1,60} \approx 2.9$ to 10.7 blows/ft, but did not quantify variance or standard deviation in probabilistic terms. This value is a bit lower than the $N_{1,60,CS}$ value from these current studies because it is uncorrected for fines, and so is not an $N_{1,60,CS}$ value. If a similar fines correction were to be made, the resulting $N_{1,60,CS}$ value of Olson and Stark would be in closer agreement with these current studies. Wang (2003) and Kramer (2008) jointly developed a representative value of $\overline{N_{1,60,CS}} = 5.6$ blows/ft, and their estimated standard deviation of that overall mean value for this case history was $\sigma_{\overline{N}} = 2.2$ blows/ft. Details of the development of this interpretation by Wang and Kramer are not presented, so it is not known why their $\overline{N_{1,60,CS}}$ value is a bit lower than the corresponding value developed in these current studies. As relationships between $N_{1,60,CS}$ and S_r have relatively low slopes, this difference is relatively modest with regard to impact on subsequent development of SPT-based predictive relationships for evaluation of S_r.

A.3.8 Additional Indices from the Back-Analyses

A number of additional results, and indices, can be extracted from the analyses performed. Some of these are useful in developing some of the over-arching relationships and figures presented in the main text of this report. These values are presented in Table A. 3.2;

Table A.3.1: Representative values for the Uetsu Railway Embankment case history of: (a) post-liquefaction strength (S_r), (b) initial vertical effective stress (σ_{vo}'), and (c) $N_{1,60,CS}$ developed by various investigation teams, and estimates of variance in each of these indices when available.

(a) Post-Liquefaction Strength:	
Olson (2001) and Olson and Stark (2002)	S_r = 35.5 psf
Wang (2003) and Kramer (2008)	$\overline{S_r}$ = 43.5 psf, and $\sigma_{\overline{S}}$ = 24.8 psf
This Study	$\overline{S_r}$ = 38 psf and $\sigma_{\overline{S}}$ = 8 psf
(b) Representative $N_{1,60}$ or $N_{1,60,CS}$ Value:	
Olson (2001) and Olso and Stark (2002)	$N_{1,60}$ = 3 bpf
Wang (2003) and Kramer (2008)	$\overline{N_{1,60,CS}}$ = 2.9 bpf, and $\sigma_{\overline{N}}$ = 4.2 bpf
This Study	$\overline{N_{1,60,CS}}$ = 3 bpf, and $\sigma_{\overline{N}}$ = 0.8 bpf
(c) Representative Initial Vertical Effective Stress:	
Olson (2001) and Olson and Stark (2002)	Not reported, but can be inferred from reported S_r/P ratio to be $\overline{\sigma'_{vo}}$ ≈ 1,280 psf. Likely range is not provided.
Wang (2003) and Kramer (2008)	Value of σ_{vo}' ≈ 916 psf is poorly documented, and is considered useful only as an approximate comparison (see Section 2.3.8.1, and Table 2.3.)
This Study	$\overline{\sigma'_{vo}}$ = 1,448 psf, and $\sigma_{\overline{\sigma}}$ = 116 psf

Table A.3.2: Additional results and indices from the analyses of the Uetsu Railway Embankment failure case history.

Maximum distance traveled by the center of gravity of the overall failure mass	108 ft.
Initial post-liquefaction Factor of Safety prior to displacement initiation, and based on best estimate value of S_r	FS = 0.27
Final post-liquefaction Factor of Safety at final (residual) post-failure geometry, and based on best estimate value of S_r	FS = 3.18

A.4 Lower San Fernando Dam (California, USA; 1971)

A.4.1 Brief Summary of Case History Characteristics

Name of Structure	Lower San Fernando Dam
Location of Structure	California, USA
Type of Structure	Hydraulic fill dam
Date of Failure	April 11, 1907
Nature of Failure	Seismic, During 1971 San Fernando Earthquake (M_W = 6.7)
Approx. Maximum Slope Height	141 ft.

A.4.2 Introduction and Description of Failure

The Lower San Fernando Dam (also known as the Lower Van Norman Dam, as it was part of the Van Norman Dam complex) suffered a liquefaction-induced landside on its upstream side as a result of the San Fernando Earthquake of February 9, 1971. Soil liquefaction occurred within the hydraulic fill materials of the upstream side, and the ensuing slide carried a large portion of the embankment, including the crest and most of the upstream side of the dam, back into the reservoir. The toe of the failure mass travelled laterally approximately 150 feet into the reservoir. Crest loss was significant, and perilously little freeboard remained at the lip of the slide scarp to contain the reservoir. Approximately 80,000 people were evacuated from the area downstream while the reservoir was safely lowered over the next three days after the earthquake.

This was a well-studied failure, with significant field investigations immediately after the earthquake, and it has been much investigated and studied since. Seed et al. (1973, 1975) and Lee et al. (1975) documented immediate post-earthquake investigations and studies. Additional studies have subsequently been performed by multiple investigators (e.g. Seed, 1979; Castro et al., 1989; Seed et al., 1989; Vasquez-Herrera and Dobry, 1989, etc.) as this well-documented case history has been used to develop and calibrate new analytical approaches and methods. This is the best-studied and best-documented liquefaction failure case history among the cases considered, and back-analyzed, for these current studies. The level of detail available regarding displacements internally within the embankment dam poses special opportunities with regard to the types of back-analyses performed for these current studies, but it also poses special challenges as very detailed knowledge of internal geometry (within the displaced embankment mass) is available for checking against the displacements analytically modeled.

Figure 4.1 shows two cross-sections through the dam. As part of the post-earthquake investigations, two large trenches were excavated completely through the dam, permitting a thorough inspection and study of the displaced materials at two cross-section near the middle of the dam. Figure 4.1(a) is a post-failure cross-section showing the displaced positions of a number of recognizable and relatively intact "blocks" of the embankment, and the Figure 4.1(b) shows a re-construction of the pre-failure geometry with these blocks returned to their pre-earthquake

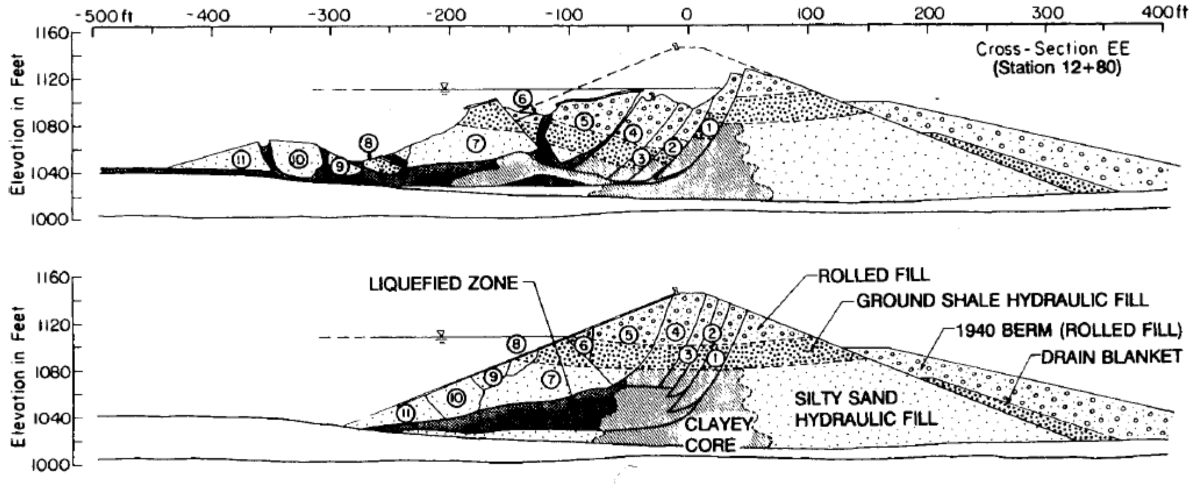

Figure A.4.1: Pre-failure and post-failure cross-sections of the Lower San Fernando Dam (from Castro et al., 1992; after Seed et al., 1973, 1975)

locations. These figures show clearly that the failure was the result of liquefaction-induced loss of strength of sandy and silty hydraulic fill materials within the lower portions of the upstream hydraulic fill zone, with the overlying embankment materials being carried out (or "floated" outwards) as semi-intact blocks atop these underlying liquefied soils.

Construction of the dam began in 1912. Foundation soils consist primarily of stiff clays, with layers of sands and gravels. The foundation sands and gravels are denser than the overlying hydraulic fill, and these foundation units were not involved in the eventual upstream slope failure.

Initial embankment construction was performed by the hydraulic fill method, with starter dikes along the upstream and downstream toes, with hydraulic deposition from pipes along the upstream and downstream toes so that finer soils would travel towards the center of the rising dam and form a clayey "puddled" core. The upstream and downstream shells were raised symmetrically, and both sides were raised in a similar manner and from the same borrow sources. In this manner the initial embankment was eventually comprised of primarily sandy and silty "shells", with a more clayey central "core". Variability of excavated and hydraulically deposited materials, and variability of hydraulic deposition in terms of rate, and in terms of periodic pauses to relocate the pipes through which the materials were being transported and placed, resulted in significant localized variations in material gradation over very small distances, both vertically and laterally within the hydraulic fill embankment. The hydraulic fill zones of the upstream and downstream "shells" were basically striated, or varved, deposits comprised of layers of silts and sands and silty sands with varying fines contents, and these materials periodically penetrated well into the puddled "core" zone, which was otherwise generally comprised mainly of more clayey soils (often clays to sandy clays).

Soils within the lower hydraulic fill zone that liquefied during the earthquake were comprised primarily of variably silty and sandy soils, sometimes with trace amounts of fine gravels. Fines contents varied between approximately 5% to 90%, and most of the fines were low to medium plasticity silts (ML). Figure 2.8 (in Chapter 2 of this report) is a photograph showing the side of one of the two post-earthquake investigation trenches through the failed zone, and it shows these variably layered sandy and silty hydraulic fill materials.

In 1916 the crest was raised by placing ground up shale as a rolled fill at the crest of the hydraulic fill embankment. This ground shale varied in thickness between approximately 15 to 20 feet. Between 1916 to 1930 several additional layers of rolled earth fill (placed and rolled in layers) were placed atop the ground shale to further raise the crest.

A thin drainage blanket was placed on the downstream face of the hydraulic fill in 1929 to 1930, and a downstream side stability berm was placed over this drainage blanket in 1940.

A.4.3 Initial Yield Stress Analyses

Figure A.4.2(a) shows the cross-section used for back-analyses of the post-liquefaction initial yield strength $S_{r,yield}$ that would theoretically be required within the liquefied upstream shell materials to produce a calculated Factor of Safety equal to 1.0. This is not the actual post-liquefaction strength, but it proves to be useful in developing a number of charts and relationships for these overall studies.

Figure A.4.2(a) also shows the best estimate failure surface. This is well-constrained by the post-earthquake investigations and analyses, and by the excellent internal cross-section data available from those critical initial post-failure field studies.

An important question often raised in previous back-analyses is whether (1) the entire slide was initiated largely monolithically, and then dis-aggregated into distinct blocks and slices as it travelled, or (2) the slide initiated progressively, initiating first with the slice nearest the front face, and then retrogressing back towards the eventual back heel of the overall feature as each new slice became unbraced by the partial departure of the slice in front of it. The incremental momentum analyses presented next in Section A.4.4 answer this question, as they found that the final resting positions of the identifiable slices and blocks could not be reasonably achieved unless the slide initiated largely monolithically (en masse) and then disaggregated as it travelled.

As a result, it is the overall basal failure surface that is analyzed for purposes of back-evaluation of $S_{r,yield}$.

Shear strengths of non-liquefied materials are a potentially significant issue here. The shear strengths of the upper ground shale and of the overlying rolled fill materials were modeled with drained shear strengths, with best estimate values of $Ø' = 30$ and 32°, respectively. In parameter sensitivity analyses that followed, this was then varied by ± 3° for the ground shale and ± 5° for the rolled fill. Some shear strength data were available for the clayey "puddle core" zone, and some information on liquidity index as well. To account for the increase in strength in the clayey materials the puddle core zone was split into three zones for the upper middle and lower depth zones. Based on liquidity index based assumption of moderate sensitivity and the results of one lab vane shear test in the puddle core material, shear strength within the "approximate" puddle core zone were modeled as undrained cohesive residual strengths with S_u= 550, 630, and

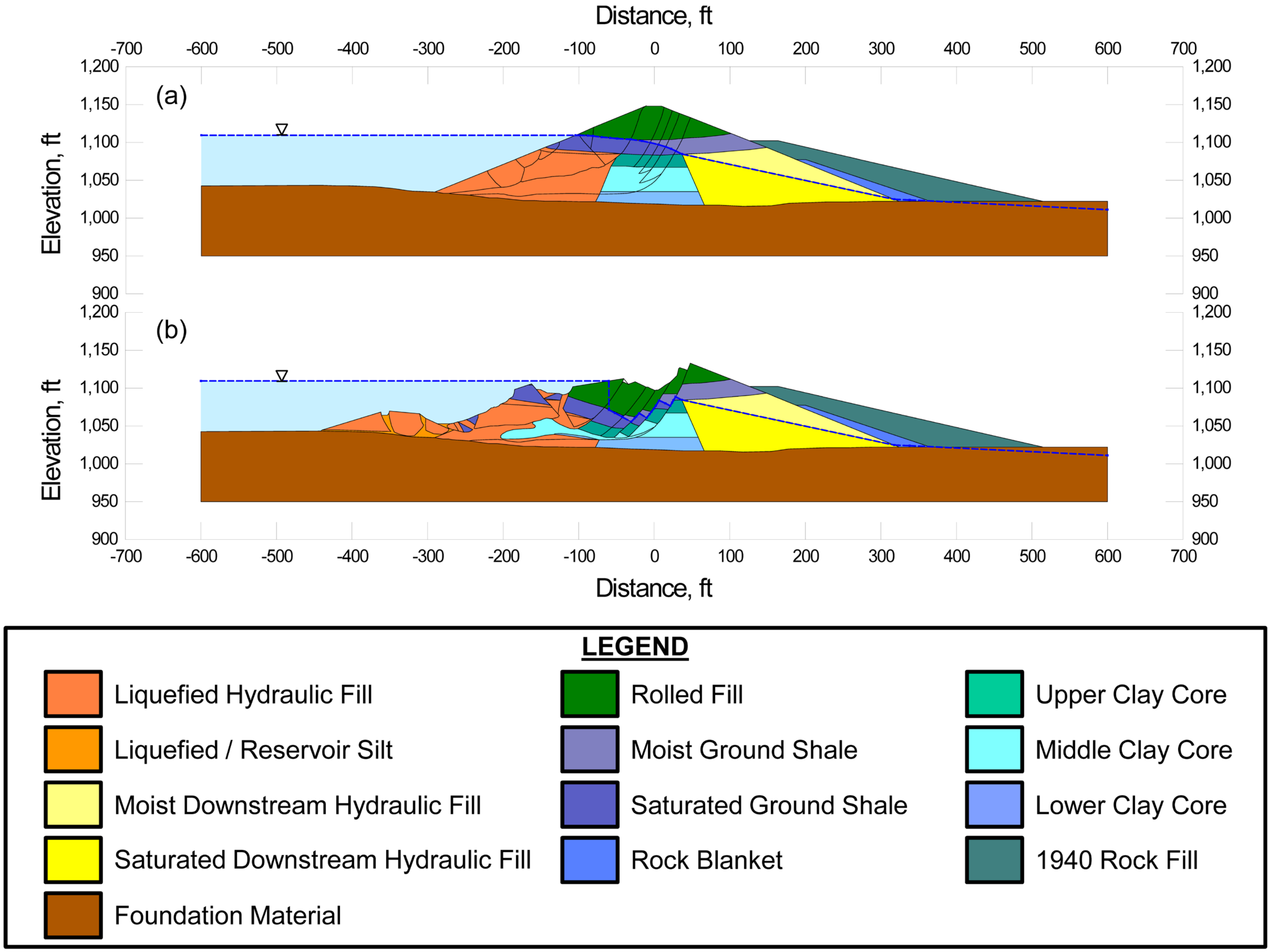

Figure A.4.2: Lower San Fernando Dam: (a) Pre-failure geometry and best-estimate failure surface for initial yield stress analyses, and (b) post-failure geometry and best-estimate failure surface for post-failure residual geometry analyses.

705 lbs/ft^2 for the upper, middle, and lower zones, respectively. These correspond to residual values of $S_{u,r}/P \approx 0.08$, as will be discussed in more detail in Section A.4.5. In parameter sensitivity analyses that followed, these assumed undrained cohesive residual strengths were varied by ± 20%.

Shear strength of the liquefied hydraulic fill materials of the lower portions of the upstream "shell" zone were taken as $S_{r,yield}$, and the back-analyses were then performed to determine $S_{r,yield}$.

Saturated unit weights of the ground shale fill were modeled as γ_s = 126 lbs/ft^3, and non-saturated unit weights were modeled as γ_m = 118 lbs/ft^3. The unit weights of the non-saturated rolled crest fills were modeled as γ_m = 124 lbs/ft^3. An average saturated unit weight of γ_s = 120 lbs/ft^3 was modeled for the clayey "core" zone materials. The average saturated unit weight of the liquefiable sandy and silty hydraulic fill zones in the upstream "shell" zones were modeled as γ_s = 123 lbs/ft^3. These unit weights were then varied, typically by +/- 3 to 5 lbs/ft^3, in subsequent parameter sensitivity studies.

For the best estimate geometry, conditions, and failure surface described above and shown in Figure A.4.2(a), the resulting value of post-liquefaction yield strength was found to be $S_{r,yield}$ = 1,281 lbs/ft^2. Sensitivity analyses were then performed, varying the details and location (at depth) of the failure surface near the base of the upstream hydraulic fill zone, unit weights, and friction angles for the non-liquefied upper crest and non-liquefied upper core zones. The incremental momentum analyses that follow in Section A.4.5 suggested that there was little likelihood that this failure would have proceeded in an incrementally progressive manner, and so this failure was modeled only as a monolithic event, with the full eventual sliding mass beginning to move largely coherently at the inception of failure. The resulting range of values of $S_{r,yield}$ for combinations of modeling assumptions and details considered to be reasonable was found to be $S_{r,yield} \approx$ 1,207 to 1,358 lbs/ft^2.

Olson (2001) did not perform back-analyses to determine $S_{r,yield}$.for this case, so no direct comparisons from previous studies are available.

A.4.4 Residual Strength Analyses Based on Residual Geometry

The calculation of the "apparent" post-liquefaction strength ($S_{r,resid/geom}$) required to produce a calculated Factor of Safety equal to 1.0 based on residual geometry is illustrated in Figure A.4.2(b). This is not the actual post-liquefaction strength, because it neglects momentum effects and thus underestimates the actual value of post-liquefaction S_r, but $S_{r,resid/geom}$ is a useful index for development of a number of relationships in these overall studies. Figure A.4.2(b) shows the post-failure residual geometry, and the failure surface, used to calculate the best-estimate value of $S_{r,resid/geom}$, based on the best estimate modeling parameters as described in the previous section.

An additional detail here is the shear strength modeled at the base of the portion of the upstream toe of the embankment that traveled out into the reservoir. It is known that weak reservoir sediments were in place at the upstream toe prior to the failure, so there may have been some sliding atop these weak sediments as the toe of the failure mass entered into the reservoir, or the failure mass may have "plowed" through these weaker sediments in which case strengths at the base of the toe of the slide mass entering the reservoir may have been essentially the full liquefied strength of the upstream hydraulic fill materials (S_r). Similarly, there may have been some hydroplaning as the toe of the embankment materials moved rapidly into the reservoir. The incremental momentum analyses presented in Section A.4.5 that follows indicate that the maximum velocity was on the order of approximately 7 to 8 ft/sec, and that the velocity during most of the run-in was lower, though the peak velocity at the toe may have briefly been a bit higher than this as the toe also "spread" as it translated laterally. As discussed previously in Section 4.2.2, it is not possible to fully accurately determine the degree of hydroplaning that would have occurred. The observed post-failure residual geometry suggests that the extreme toe of the failure mass did not fully separate itself from the rest of the failure as the overall mass came to rest, but it does appear to have partially separated (or "stretched out") to some degree, suggesting some lower strengths at the base of the materials entering into the reservoir (see Figures A.4.1 and A.4.2(b)).

Taking into account all of these uncertainties, the combined effects of (1) potential hydroplaning, and (2) potential sliding atop weaker reservoir sediments as the toe of the slide mass entered the reservoir were jointly modeled with an assumption that the best estimate strength at the base of the portion of the slide mass entering the reservoir was equal to 50% of the strength (S_r) of the liquefied upstream hydraulic fill materials. Parameter sensitivity studies were then performed, varying this over the range of 25% to 75% of S_r.

The best estimate analysis of $S_{r,resid/geom}$ was performed assuming that shear strength at the base of the embankment materials that entered into the reservoir was 50% of $S_{r,resid/geom}$. The resulting best estimate calculated value of "apparent" post-liquefaction strength based on post-failure residual geometry was $S_{r,resid/geom} \approx 79$ lbs/ft^2.

Variations were then made in parameters, as was described in the preceding section, in order to evaluate uncertainty or variability. Varying degrees of potential hydroplaning were also modeled, with the average shear strength at the base of the portion of the failure mass that entered the reservoir being modeled as varying from a low of 25% of $S_{r,resid/geom}$ to a high of 75% of $S_{r,resid/geom}$. Considering ranges of variations in modeling details and parameters considered to be reasonable, the resulting likely range of post-liquefaction strength required to provide a calculated Factor of Safety equal to 1.0 based on residual geometry was considered to be $S_{r,resid/geom} \approx 36$ to 121 lbs/ft^2.

Olson (2001) also calculated post-liquefaction strength required to produce a calculated Factor of Safety equal to 1.0 based on residual geometry, and reported a best estimate value of $S_{r,resid/geom} \approx 4.8$ kPa (100 lbs/ft^2), with an estimated range of 4.3 to 12.2 kPa (89 to 255 lbs/ft^2).

A.4.5 Incremental Momentum Back-Analyses and Overall Estimates of S_r

Incremental momentum back-analyses were performed using the same sets of properties and geometries (including failure surfaces, and modeling of conditions beneath the portions of the toe of the failure mass that entered into the reservoir) as described in the previous sections.

Shear strengths of the central "clayey" core zone were modeled based on (1) peak $S_u/P \approx 0.20$ to 0.27 based on Plasticity Index, and $S_u/P \approx 0.24$ based on pocket torvane data (Figure A.4.3) from the similar hydraulically placed "puddle core" materials of the adjacent Upper San

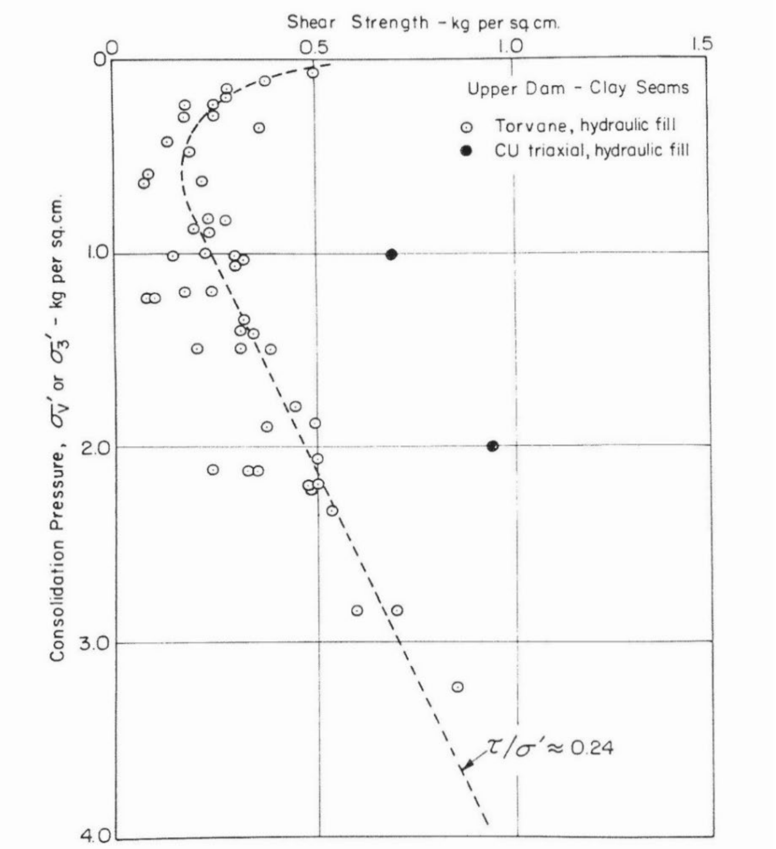

Figure A.4.3: In situ shear strengths of clayey central "puddle core" materials from the Upper San Fernando Dam based on torvane data.

Fernando Dam (See Appendix B, Section B.9), and on (2) sensitivity ≈ 3.4 based on liquidity index and on sensitivity from a laboratory vane shear test on clayey materials from the clayey core zone of the Lower San Fernando dam performed and reported by Castro et al. (1989). Taken together, these values led to the values of post-liquefaction (large strain) strength of these central "clayey" core materials modeled in these current analyses of $S_{u,r}/P \approx 0.24 \div 3.2 = 0.08$. Accordingly, shear strengths in the clayey central "puddle core" materials were modeled based on $S_{u,r}/P = 0.08$. For parameter sensitivity studies, this was subsequently varied by +/- 20%.

Figure 4.2 (in Chapter 4 of the main report text) shows the best-estimate progressive incremental momentum analysis for this case history, showing the seven stages of geometry evolution modeled as the failure proceeds. Figure 4.3 (in Chapter 4) shows the associated calculations of (1) acceleration vs. time, (2) velocity vs. time, and (3) displacement of the overall center of gravity vs. time. Figure A.4.4 (here) repeats Figure 4.2, at larger scale for clarity, as this is a large slide feature with many interesting details. The resulting overall best estimate value of post-liquefaction strength based on these incremental momentum analyses is $S_r = 539$ lbs/ft^2.

An animation of this incremental analysis of the upstream liquefaction induced slide in the Lower San Fernando Dam can be accessed at the following link:

Link: https://www.jweber.sites.lmu.edu/more/lsfd-us/

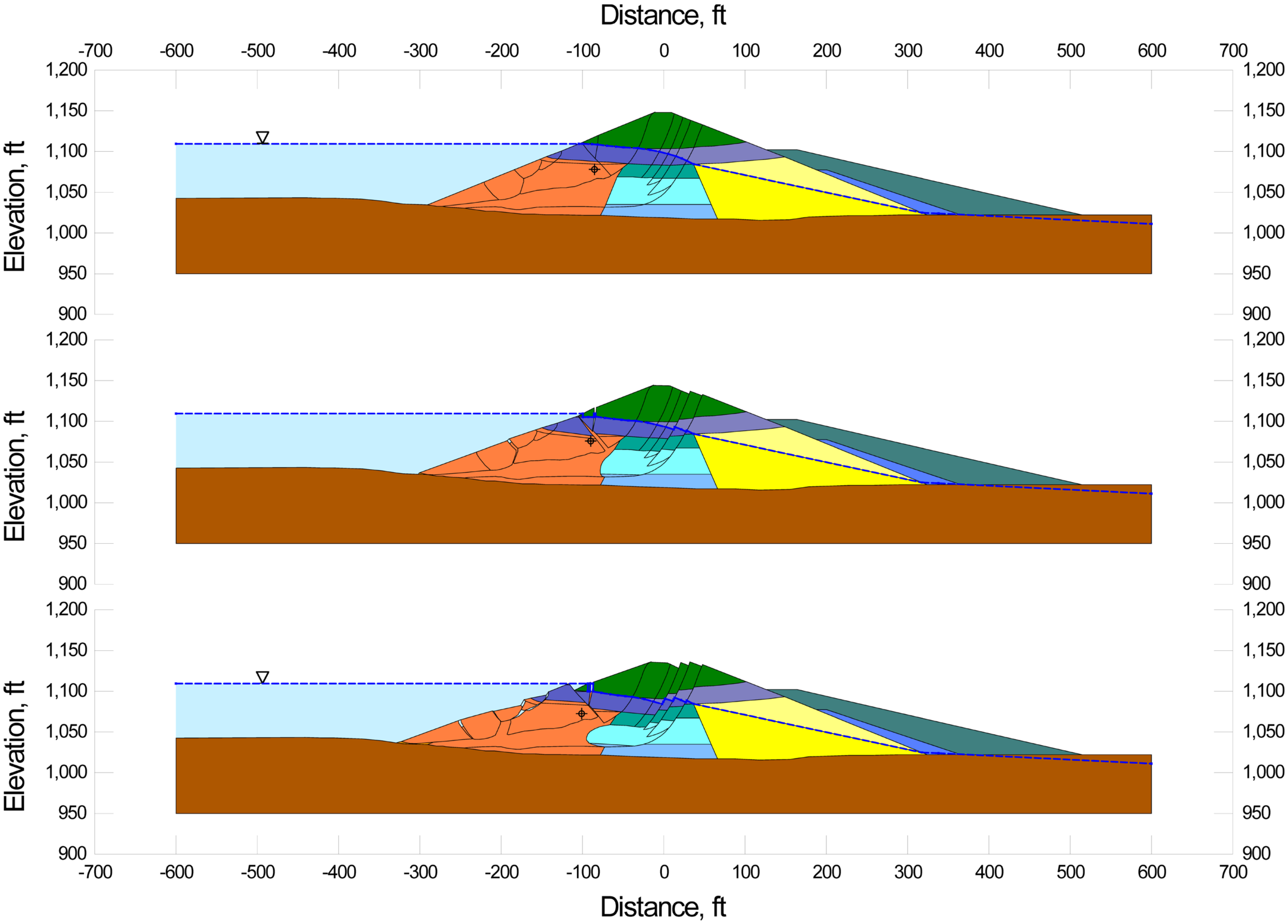

Figure A.4.4: Incremental momentum analysis of the failure of the upstream side of the Lower San Fernando Dam, showing progressive evolution of cross-section geometry as modeled for the best-estimate case.

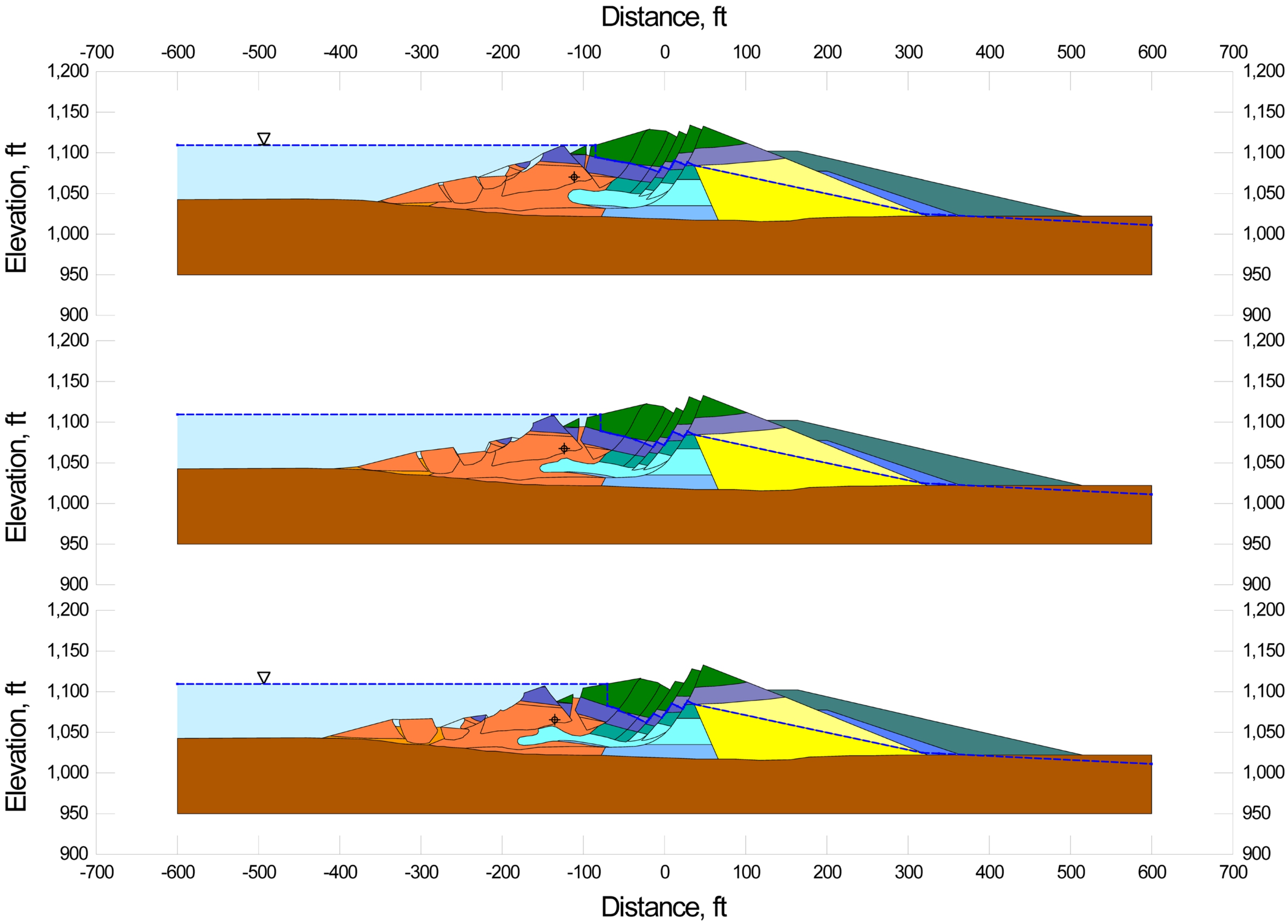

Figure A.4.4(cont'd): Incremental momentum analysis of the failure of the upstream side of the Lower San Fernando Dam, showing progressive evolution of cross-section geometry as modeled for the best-estimate case.

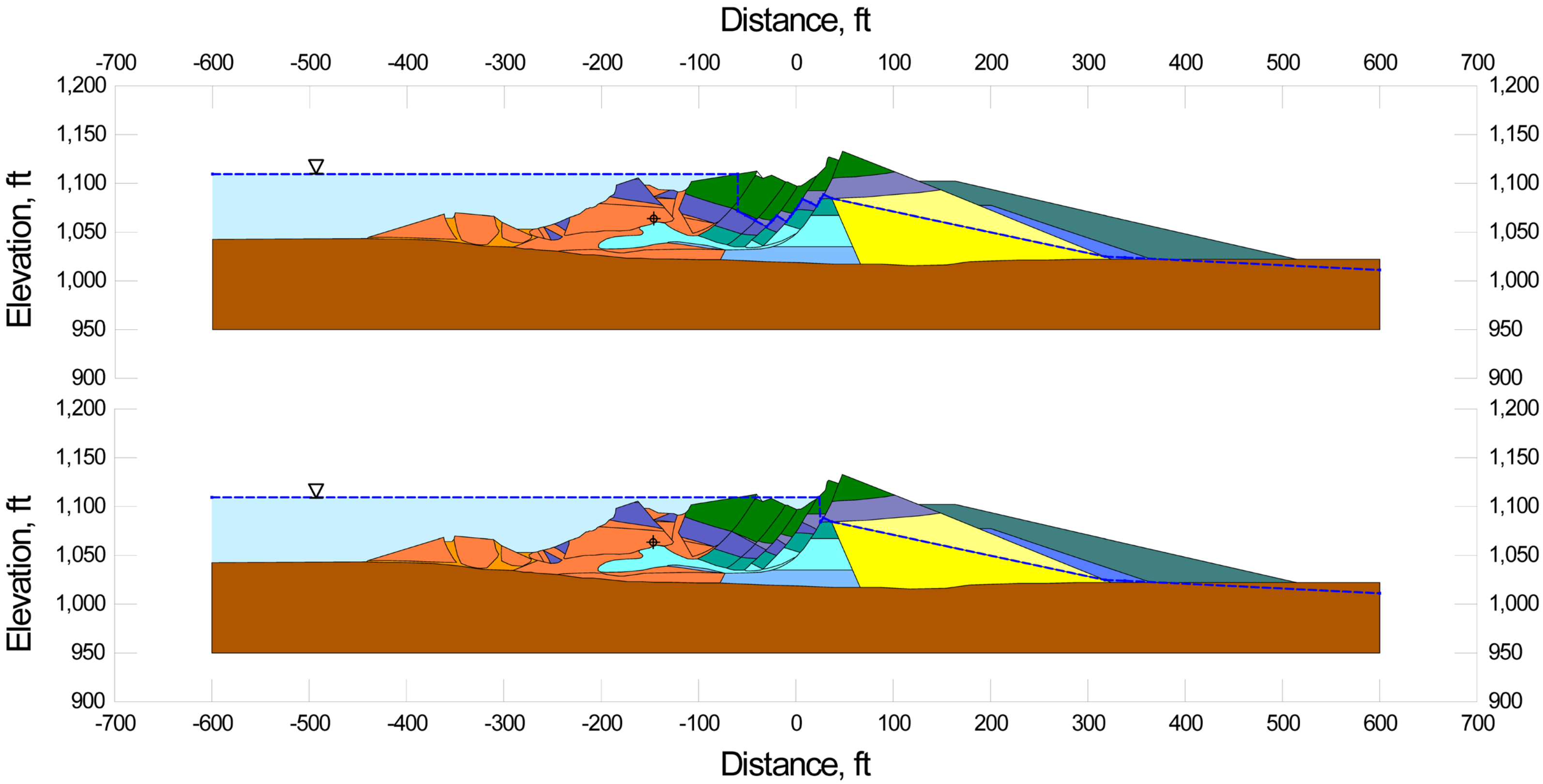

Figure A.4.4(cont'd): Incremental momentum analysis of the failure of the upstream side of the Lower San Fernando Dam, showing progressive evolution of cross-section geometry as modeled for the best-estimate case.

The animation presents a series of composite incremental steps of the analysis of the Lower San Fernando Dam failure, showing (1) the incremental evolution of displaced geometries, (2) the evolution of the displaced location of the center of gravity of the overall failure mass, and (3) incremental evolution of acceleration, velocity and displacement of the center of gravity vs. time. The sequential images of the animation can be "clicked" forward and backward to help engineers better visualize the step-wise progression and mechanics of the incremental momentum analysis, giving the viewer a sense of the motions and of the development of forces and displacements, etc. This can be surprisingly useful, and it can enhance understanding and can also serve as a basis for further tuning of the modeled progression of cross-sections.

The main sources of uncertainty, or variability, in back-calculated values of S_r were: (1) frictional strengths of the non-liquefied embankment fill materials, (2) shear strengths within the clayey "core" zone, (3) potential effects of hydroplaning and/or sliding atop weaker reservoir sediments as the failure mass entered into the reservoir, (4) the precise location and shape of the failure plane at depth near the base of the upstream hydraulic fill "shell", and (5) unit weights.

The exact edges of the "clayey" central core zone are poorly defined, and they are highly irregular due to the stratification resulting from the variability, and the "pauses", in the hydraulic deposition process. This results in silty and sandy "stringers" or strata extending into the clayey core zone, and clayey stringers extending out into the sandy and silty "shell" zones. Shear strengths of the clayey materials (based on $S_{u,r}/P \approx 0.08$) do not differ greatly from those of the hydraulic fill in this vicinity ($S_r/P \approx 0.12$), but they do differ somewhat. For the best estimate case, the edges of the zone modeled as "clayey" material are as shown in Figures A.4.2 and A.4.4.

Based on all analyses performed, and the considerations discussed, the overall best estimate value of post-liquefaction strength for the failure of the upstream slope of the Lower San Fernando Dam was judged to be $S_r \approx 539$ lbs/ft^2, with a likely range of $S_r \approx 447$ to 635 lbs/ft^2. Based on the factors contributing to uncertainty or variance for this case history, it was the judgment of the investigation team that this range represented approximately ± 2 standard deviations. This range of variance is not symmetrical about the best estimate value, so minor further adjustments were made to produce a representative estimate of S_r suitable for regression analyses.

Overall, based on an assumed normal distribution, it was judged that the (mean and median) best estimate of post-liquefaction strength for this case history is

$$\overline{S_r} = 539 \text{ lbs/ft}^2$$

and that the best estimate of standard deviation of mean overall post-liquefaction strength is

$$\sigma_{\overline{S}} = 47 \text{ lbs/ft}^2$$

The Lower San Fernando Dam case history has been either back-analyzed, or used in development of correlations and relationships, by a number of previous investigators. Table A.4.1 presents back-calculated values of S_r from these current studies, as well as from four previous investigations that specifically attempted to account for momentum effects.

Seed and Harder (1990) attempted to account for momentum effects by taking S_r as approximately intermediate (a bit lower than exactly intermediate) between back-calculated values of $S_{r,yield}$ and $S_{r,resid/geom}$, producing and estimated value of $S_r \approx 400$ lbs/ft^2. Based on the apparent large displacements, they may have leaned that estimate a bit to the low side (a bit closer towards $S_{r,resid/geom}$), resulting in a slight underestimation of S_r (see Chapter 4, especially the discussion of Equation 4.2 and Figure 4.7, and the plotting of the Lower San Fernando Dam case history in Figure 4.7). Olson (2001) and Olson and Stark (2002), reported a best estimate value of S_r = 18.7 kPa (390 lbs/ft^2), based on their inertial displacement analyses that considered kinetics, and a range of S_r = 15.8 to 21.8 kPa (330 to 455 lbs/ft^2). Wang (2003) and Wang and Kramer (2008) employed their zero inertial force (ZIF) method to incorporate inertial effects in their back-analyses of this failure, and they developed estimates of both mean $\overline{S_r}$= 484.7 lbs/ft^2 as well as the associated standard deviation $\sigma_{\bar{S}}$ = 111.0 lbs/ft^2. The details of their analyses, and the cross-sections and failure mass assumptions employed, are not presented and so cannot be checked. Davis et al. (1988) calculated $S_r \approx 510$ lbs/ft^2, reportedly based on analyses that specifically included momentum effects, but again the details are not clearly presented and so cannot be checked. The best estimate value of Olson and Stark (2001, 2002) of S_r = 390 lbs/ft^2 is close to that of Seed and Harder (1990), but both values appear to be low. Seed and Harder appear to have taken a low fraction of the average between $S_{r,yield}$ and $S_{r,resid/geom}$ based on the large runout distance observed. Olson and Stark appear to have potentially selected a poor shape for the polynomial path along which their center of gravity slid in their “kinetics” analysis, as shown in Chapter 2, Figure 2.21, and this may have caused some underestimation of S_r. Wang and Kramer (2003, 2008), Davis et al.(1988), and these current studies all provide slightly higher values of back-calculated S_r, and the S_r values developed in these three studies are in generally good agreement.

This is an unusually well-defined case history, and the three sets of back-analyses presented in Table A.4.1 that specifically analytically incorporated inertial effects are all in reasonably good agreement, given the differences in approaches taken in the different back-analyses and the complex challenges involved in back-analyses for this case history as conditions change continuously as the failure progresses, and potential issues including hydroplaning and sliding atop soft reservoir sediments arise.

Additional values of S_r were back-calculated by multiple additional investigators, but some of these evaluations were often not well documented as to their basis and details. Poulos (1988) calculated $S_r \approx 500$ to 1,000 lbs/ft^2, reportedly incorporating momentum effects, but the details of this evaluation are not clearly presented. Castro et al. (1992) proposed a range of $S_r \approx 400$ to 500 lbs/ft^2, also based on analyses that at least approximately accounted for momentum effects.

A.4.6 Evaluation of Initial Effective Vertical Stress

Average initial (pre-failure) effective vertical stress was assessed for the liquefied zones of the failure surface shown in Figure A.4.4. Additional sensitivity analyses were then performed for reasonable ranges of variations in (1) the location of the phreatic surface, (2) unit weights, and (3) the precise location of the overall failure surface in order to evaluate uncertainty or variance.

The resulting best estimate of average pre-failure effective stress within the liquefied materials controlling the failure is $\sigma_{vo}' \approx 3{,}174$ lbs/ft^2, with a reasonable range of $\sigma_{vo}' \approx 2{,}614$ to 3,738 lbs/ft^2. This range is slightly non-symmetric about the median value, and this range was judged by the engineering team to represent approximately ± 2 standard deviations. Overall, the best characterization of initial (pre-failure) average effective vertical stress was then taken to be represented by a mean value of

$$\overline{\sigma'_{vo}} = 3{,}174 \text{ lbs/ft}^2$$

and with a standard deviation of

$$\sigma_{\overline{\sigma}} = 281 \text{ lbs/ft}^2$$

Estimates of σ_{VO}' were also reported by Olson and Stark and by Wang and Kramer, and these are shown in Table A.1.1(c). Olson (2001) and Olson and Stark (2002) report an average initial vertical effective stress on the order of approximately $\sigma_{vo}' = 166.7$ kPa (3,482 lbs/ft^2). Average initial effective overburden stresses were not directly reported by Wang (2003) and Kramer (2008), but they were published more recently in the publication by Kramer and Wang (2015). As discussed in Section 2.3.8.1(a), the approach taken by Wang (2003) to evaluation of σ_{vo}' for his nine "primary" case histories (this is one of those nine) is not clearly explained, and it is also poorly documented. Wang's value of $\sigma_{vo}' = 3{,}538$ lbs/ft^2 is in good agreement with the values of Olson (2001) and these current studies, but this is not considered a very rigorous check here. Overall, agreement between these three teams of investigators is reasonably good for this case history.

A.4.7 Evaluation of $N_{1,60,CS}$

The Lower San Fernando Dam upstream slope failure has been a well-investigated case history. Figure A.4.5 shows a plan view of the borings performed after the failure as part of the 1971 investigation (Seed et al., 1973). Because of the massive upstream slope failure, only two rows of borings (with SPT) on the downstream side provided data pertinent to the sandy and silty hydraulic fill "shell" zones. As a result, analyses of the upstream side slope failure have been based largely on the assumption of symmetry of materials and depositional characteristics of the upstream and downstream shell zones as the hydraulic fill dam was constructed.

Figure A.4.6 shows a compilation of the SPT $N_{1,60}$ values developed and reported by Seed et al., 1988) based on those SPT borings. The hydraulic fill of the shell zones was encountered at elevations of between approximately +1,004 to +1,076 feet in the seven SPT borings that penetrated the downstream hydraulic fill "shell" zone. It was judged that the downstream hydraulic fill could be sub-divided into four zones by elevation as shown, and mean and median values are calculated and presented for each of these four sub-zones. These post-earthquake downstream $N_{1,60}$ values were then subsequently further modified to develop estimates of pre-earthquake representative values for the upstream side hydraulic fill within which the actual failure occurred. Details of the processing of the original N-values to develop $N_{1,60}$ values are presented

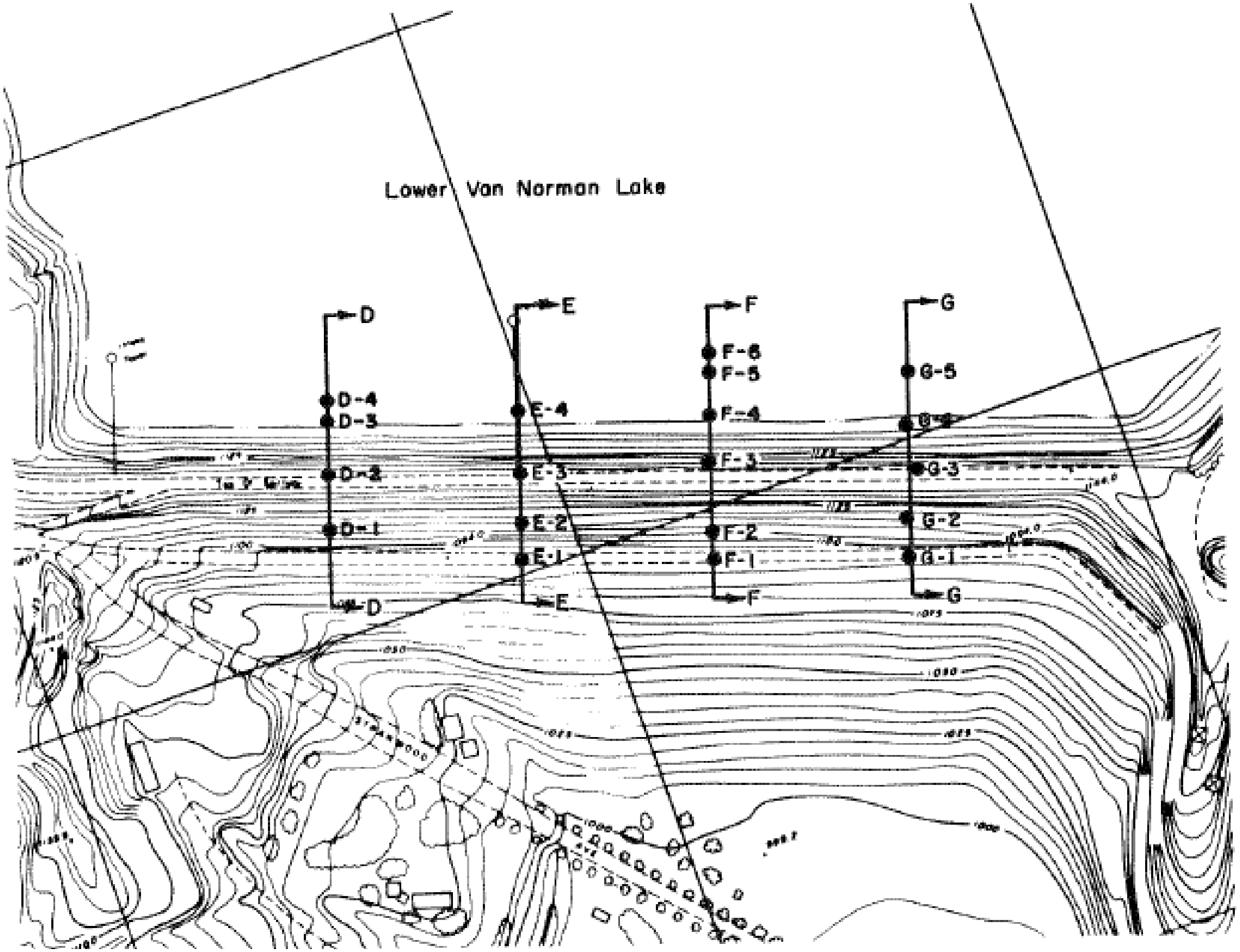

Figure A.4.5: Plan viiew of the Lower San Fernando Dam showing the locations of post-failure SPT borings performed for the 1971 investigation (Seed et al., 1973).

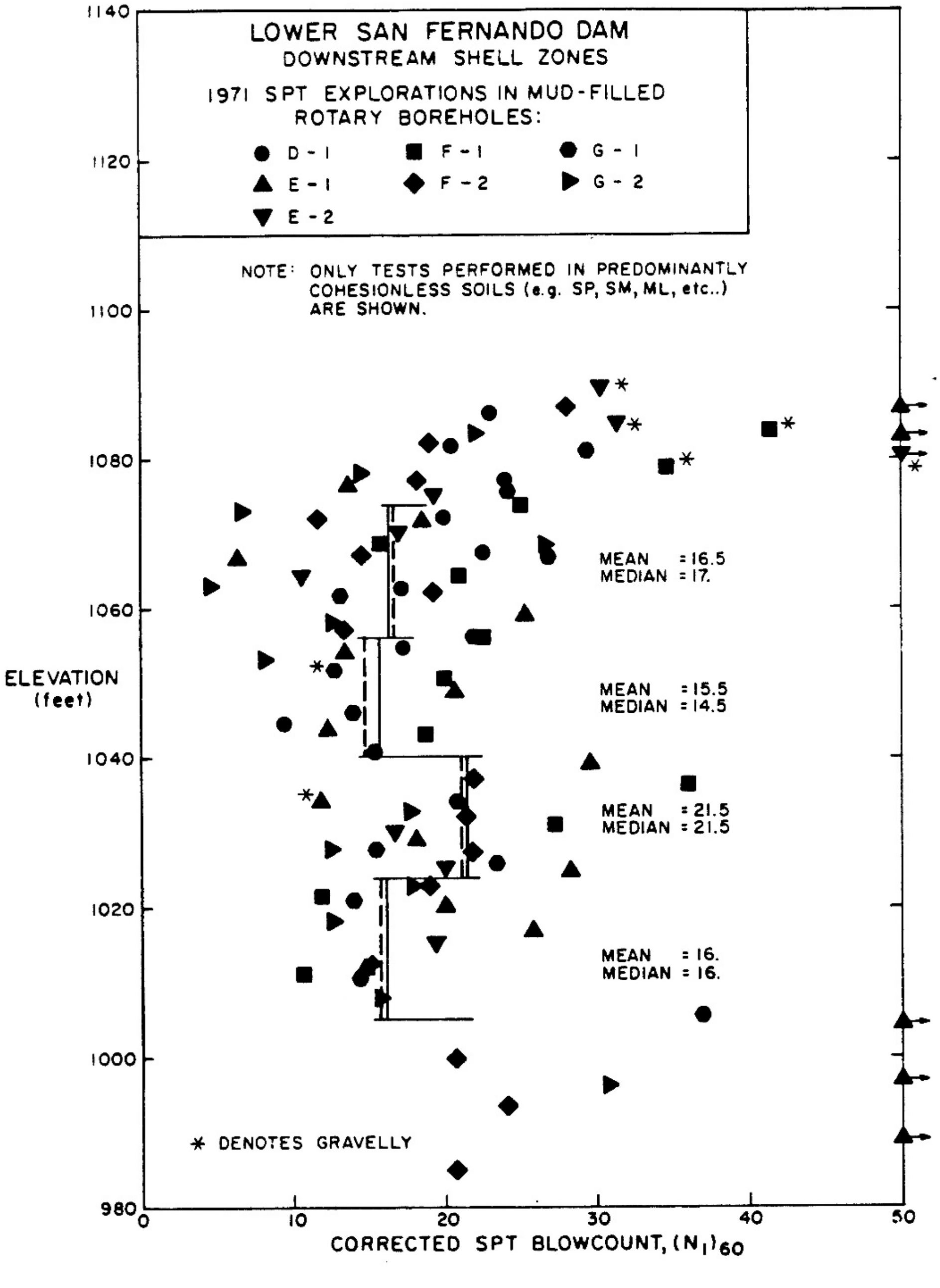

Fig. 4-5 ANALYSES OF SPT DATA FOR COHESIONLESS SOILS IN DOWNSTREAM SHELL - 1971 INVESTIGATION

Figure A.4.6: Summary of overburden and energy and equipment corrected $N_{1,60}$ values as developed and compiled in the 1971 investigation (Seed et al., 1973).

in Seed et al. (1988), and so are the additional adjustments made to develop estimates of pre-earthquake $N_{1,60}$ values for the upstream side hydraulic fill zones.

Figure A.4.7 shows a plan view of the additional borings performed in the subsequent 1985 further investigations of this failure (Castro et al., 1989). By 1985 the dam had been largely re-configured, and only four of the mud-filled rotary wash SPT borings penetrated into the mud-filled rotary wash SPT borings penetrated into the downstream hydraulic fill "shell" zone. Figure A.4.8 shows a summary of the $N_{1,60,CS}$ values from these four additional borings. Hydraulic fill shell zone materials were encountered at elevations of between approximately +998 to +1,076 feet in these borings. It was again judged that the hydraulic fill of the shell zone could be sub-divided into four sub-zones by elevation, based on the SPT data. These zones are shown, and the median and mean values of $N_{1,60,CS}$ developed for each sub-zone are shown in Figure A.4.8. The corrections for energy, equipment and procedures employed to develop these values are presented by Seed et al. (1988). Once again, additional corrections were made to the post-earthquake values measured pre-earthquake conditions in the upstream side hydraulic fill shell zone. These corrections have already been made, and the values shown in Figure A.4.8 are the estimated pre-earthquake values for representation of the upstream shell hydraulic fill zone.

Both the 1971 and the 1986 investigations developed characterizations of the hydraulic fill shell zones that involved largely similar sub-divisions of the shell zones into four sub-layers (by elevation) based on $N_{1,60,CS}$ values, and both developed fairly similar characterizations of each of these four sub-layers. From top to bottom, the second sub-layer (Elev. ~ 1,040 to 1,057 feet) and the fourth and deepest sub-layer (Elev. ~ 1,005 to 1,022 feet) have notably lower $N_{1,60,CS}$ values than the other two, and these are the strata that are suspected to be the principal culprits in the failure that developed (especially the lowest stratum).

Figure A.4.9 shows a compilation of six CPT probes that were passed through the downstream hydraulic fill shell zone as part of the 1985 investigation (Olson, 2001). These show the same pattern, again showing four relatively distinct sub-layers, with the second and fourth sub-layers having lower normalized CPT tip resistances than the other two.

In these current studies, all SPT data obtained in both the 1971 and the 1985 investigations were re-evaluated and re-processed. Figure A.4.10 shows the SPT data from the 11 SPT borings that penetrated into the upstream hydraulic fill shell zone. Energy and equipment and procedural corrections differed for the 1971 and the 1985 field investigations. All corrections applied to measured N-values to develop $N_{1,60,CS}$ values were made according to the procedures and relationships presented in Appendix C. Figure A.4.10 shows the resulting corrected $N_{1,60,CS}$ values.

The resulting corrected blowcounts from Figure A.4.10 were then further examined and processed. The inexplicably high blowcounts ($N_{1,60,CS} > 50$ blows/ft.) were clearly separated from the remainder of the data, and these high values were deleted as "spurious" (likely due to gravel interference). SPT test data and boring logs were carefully reviewed at the apparent base of the downstream side hydraulic fill shell zone. Individual SPT that had been logged as occurring in "foundation" soils were also deleted. In addition, all SPT performed in soils logged as primarily cohesive (CH, CL or SC with high field-estimated fines contents) were also deleted. The remaining SPT data are then presented in Figure A.4.11.

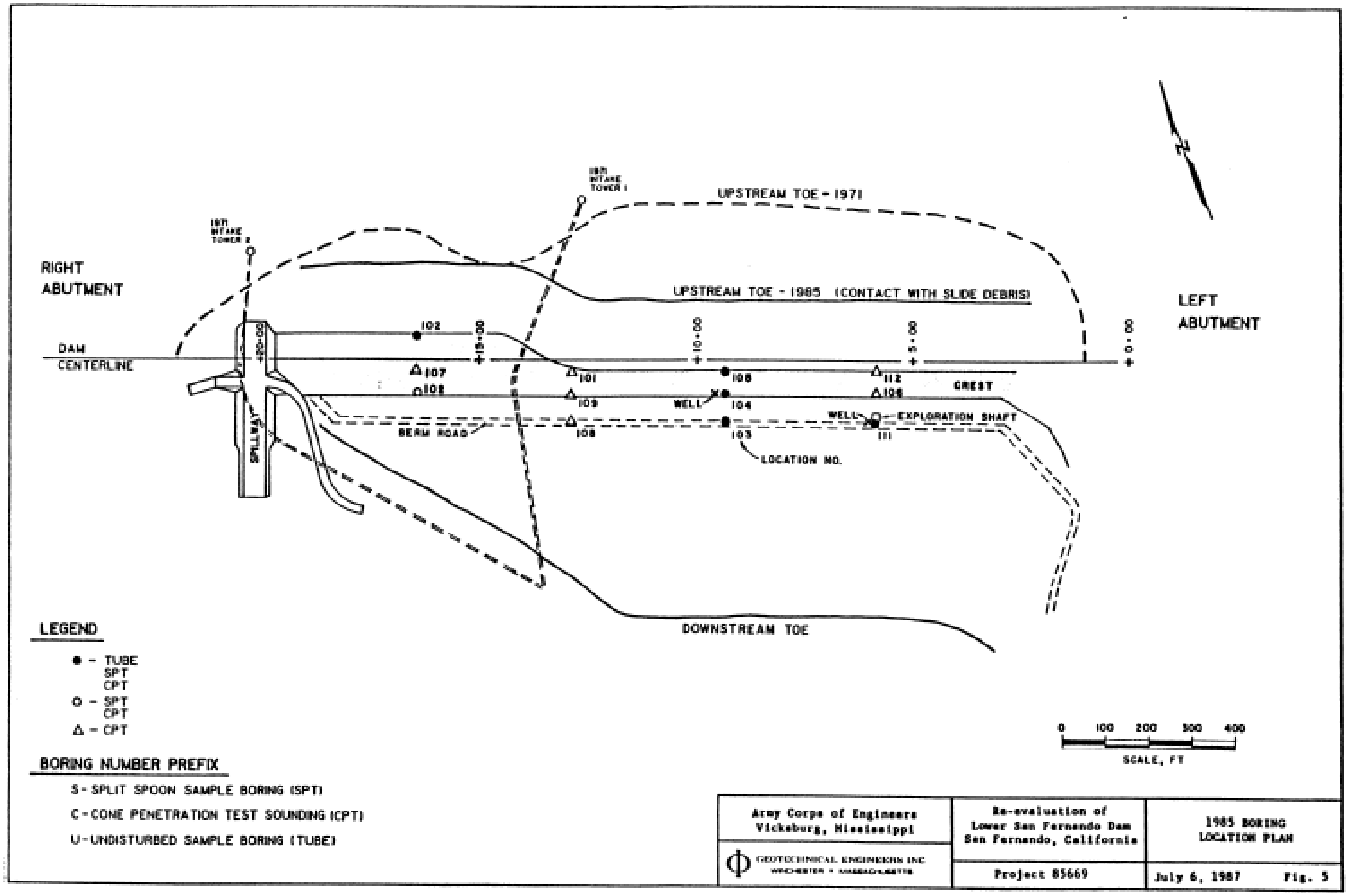

Figure A.4.7: Plan view showing the locations of additional SPT borings performed as part of the 1985 investigation (Castro et al., 1989).

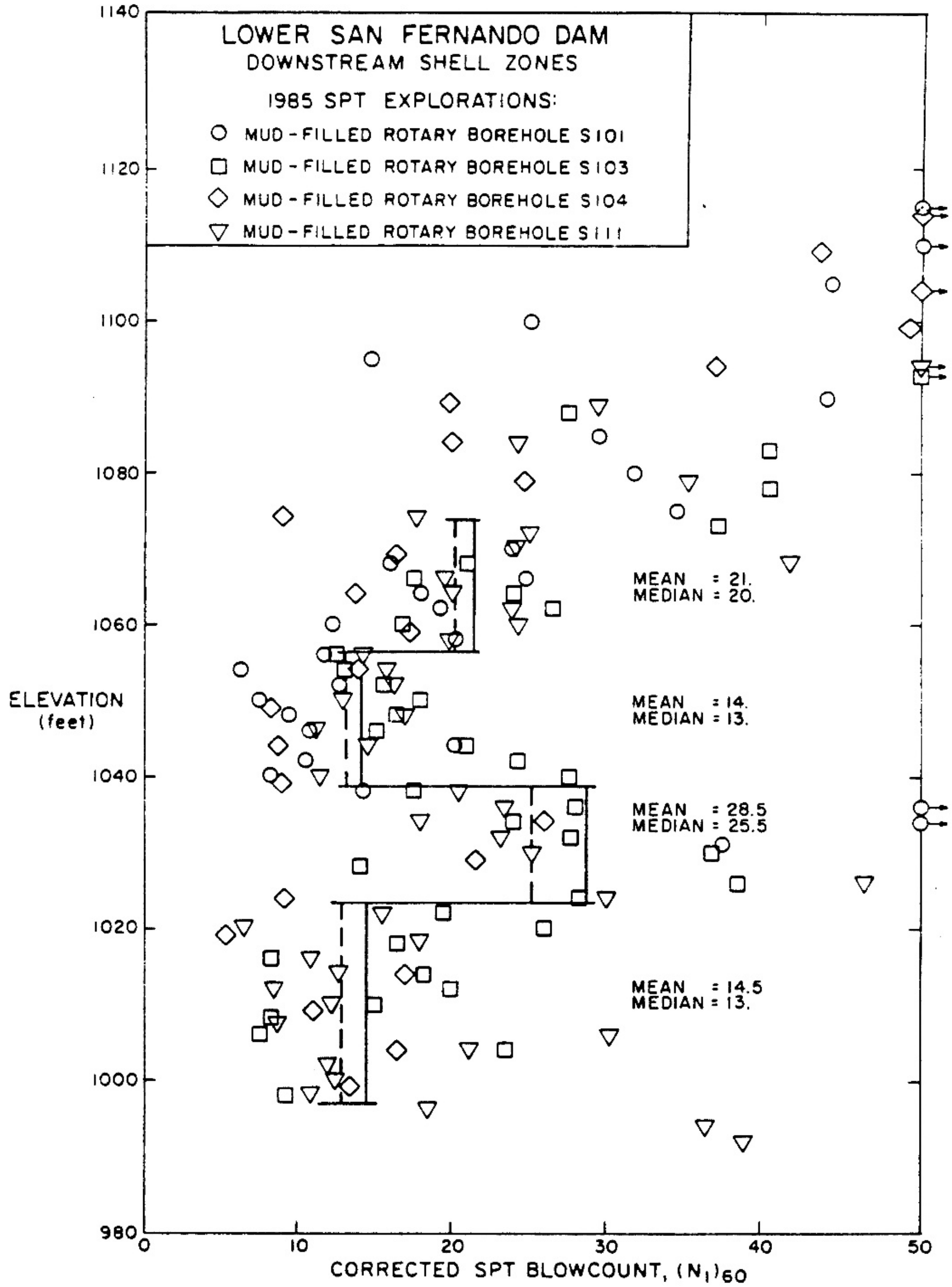

Fig. 4-8 ANALYSES OF SPT DATA FOR BORINGS IN DOWNSTREAM SHELL IN 1985 INVESTIGATION

Figure A.4.8: Summary of overburden and energy and equipment corrected $N_{1,60,CS}$ values as developed and compiled in the 1985 investigation (Seed et al., 1988).

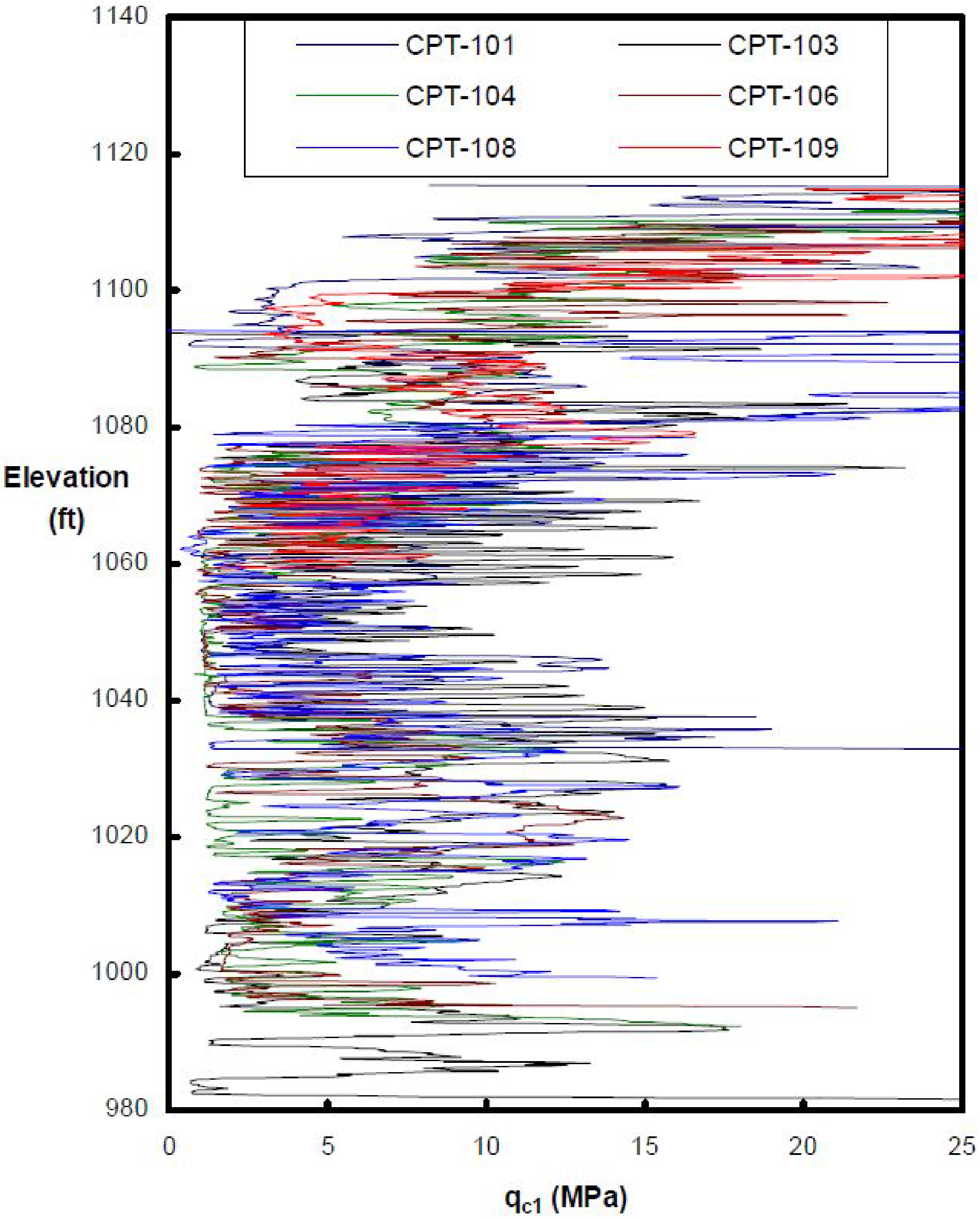

Figure A.4.9: Summary of corrected CPT tip resistance qc1 (MPa) performed through the downstream hydraulic fill "shell" zones as part of the 1985 investigations (Olson, 2001).

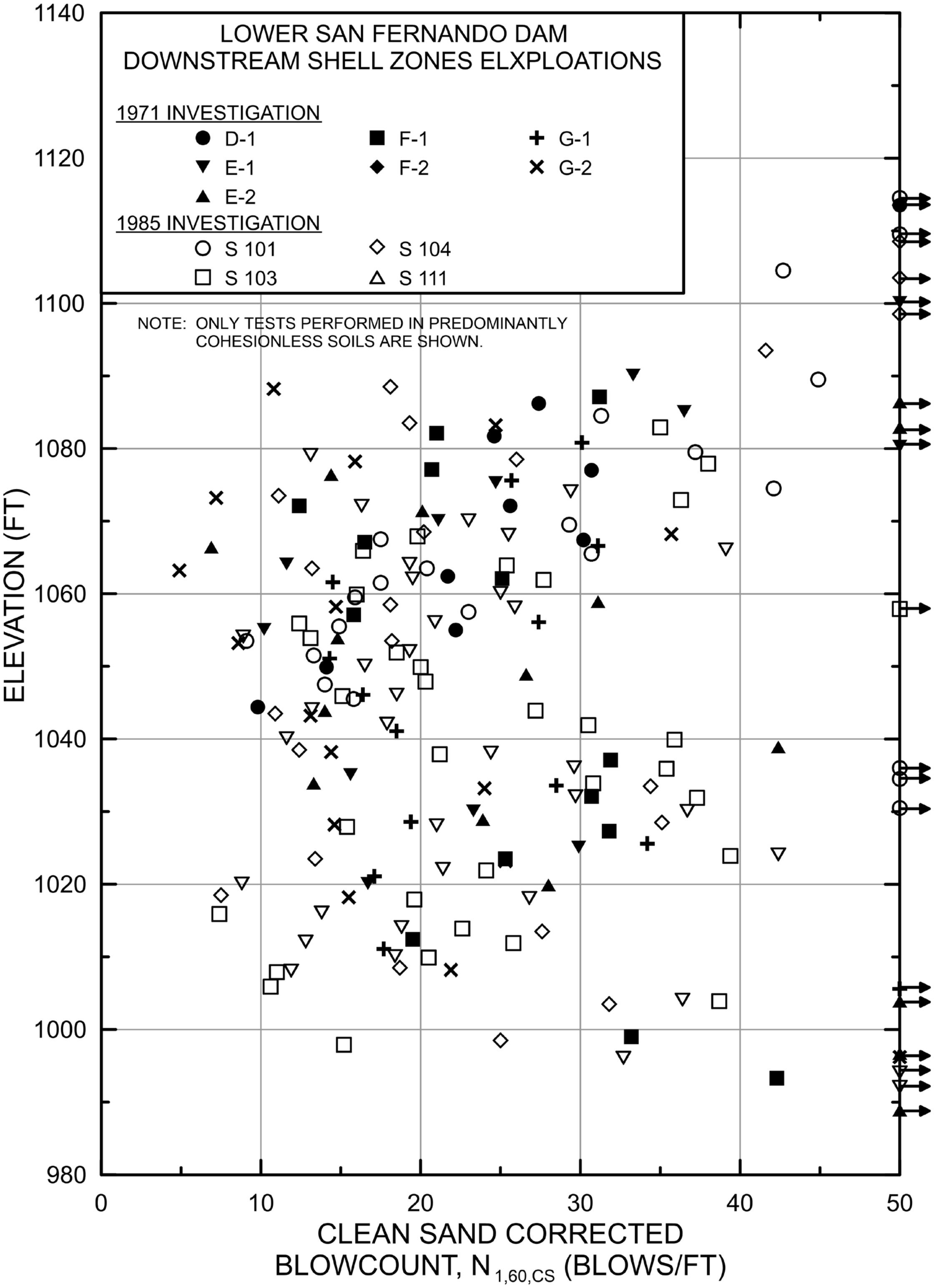

Figure A.4.10: Summary of available data from SPT borings that penetrated through the downstream hydraulic fill zones showing corrected $N_{1,60,CS}$ values as developed for these current studies.

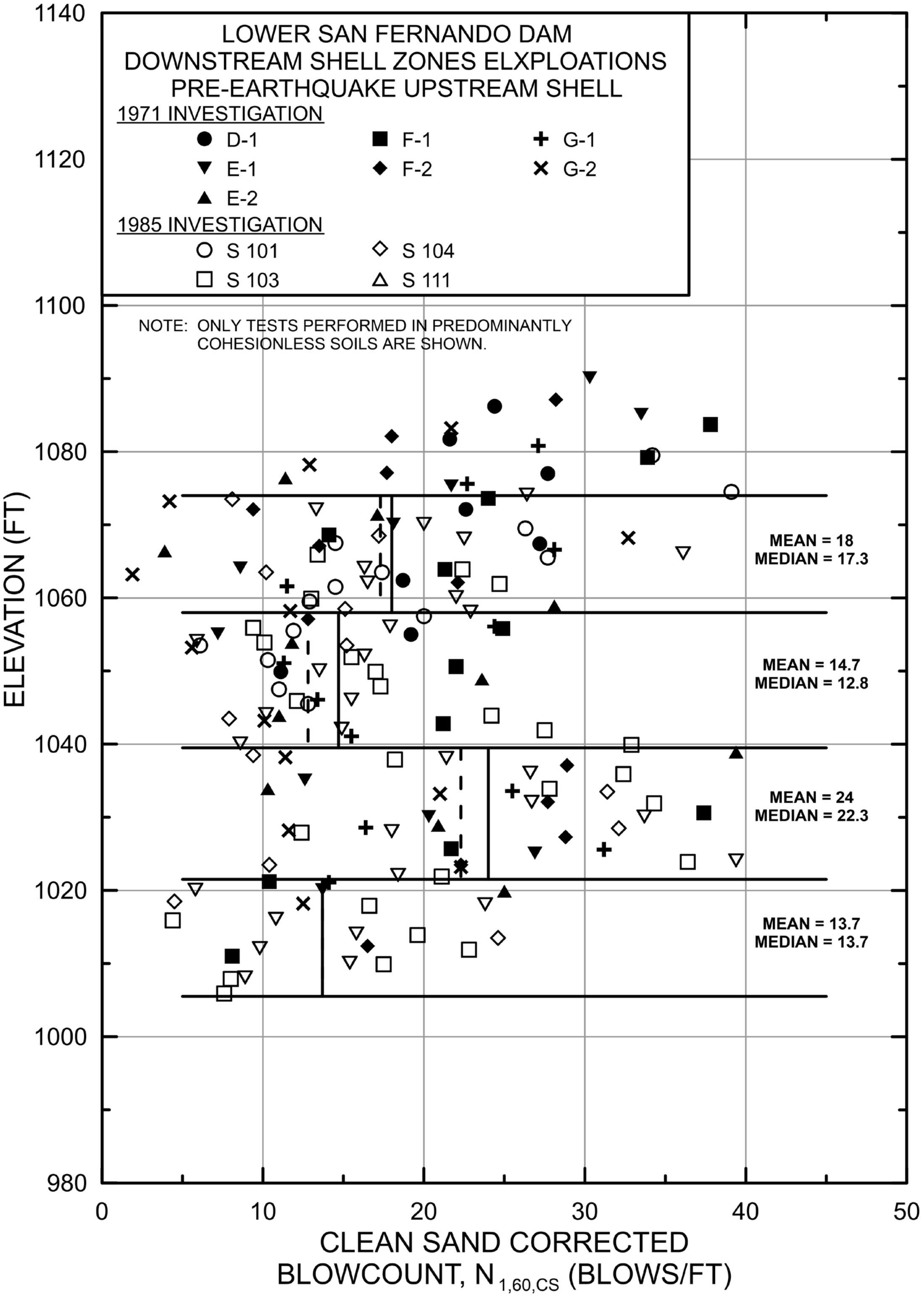

Figure A.4.11: Summary of available SPT data borings that penetrated through the downstream hydraulic fill zones showing corrected $N_{1,60,CS}$ values as adjusted to represent best-estimate values for the upstream side hydraulic fill pre-earthquake conditions.

The values on $N_{1,60,CS}$ presented in Figure A.4.11 have been further adjusted to use the post-earthquake downstream side hydraulic fill shell SPT data to develop estimates of the pre-earthquake upstream side SPT $N_{1,60,CS}$ values. Both the 1971 and the 1985 investigations had made the following two corrections here: (1) Post-earthquake $N_{1,60}$ (or $N_{1,60,CS}$) values were reduced by 2 blows/ft to account for the effects of post-earthquake densification (minus an allowance for disturbance) and (2) the downstream side $N_{1,60}$ (or $N_{1,60,CS}$) values were further reduced by an additional 1 blow/ft. to account for the increased effective overburden stress on the (less buoyant) downstream side. Both of those same adjustments were made in these current studies. Accordingly, the SPT $N_{1,60,CS}$ values carried forward from Figure A.4.10 were each reduced by 3 blows/ft before being re-plotted in Figure A.4.11.

Figure A.4.11 thus shows the best-estimate $N_{1,60,CS}$ characterization for pre-earthquake conditions within the upstream hydraulic fill shell zone. The resulting characterization is very similar to that which resulted previously from the 1971 and the 1985 investigations, and the hydraulic fill shell zone is again characterized as four sub-zones (by elevation) based on the $N_{1,60,CS}$ data. Mean and median values of $N_{1,60,CS}$ are shown for each sub-stratum. Once again, it is the second and the fourth sub-layers that have the lowest $N_{1,60,CS}$ values and that are thus the zones of principal interest. The fourth sub-layer (the deepest) is the zone within which a majority of the upstream failure occurred.

The mean and median $N_{1,60,CS}$ values of sub-layers No's. 2 and 4 are:

Sub-Layer No. 2: Mean $N_{1,60,CS}$ = 14.7 blows/ft and Median $N_{1,60,CS}$ = 12.8 blows/ft.

Sub-Layer No. 4: Mean $N_{1,60,CS}$ = 13.7 blows/ft and Median $N_{1,60,CS}$ = 13.7 blows/ft.

Based on these data, and an assumed Normal distribution, the values selected for characterization of the mean $N_{1,60,CS}$ value for the upstream hydraulic fill in the failure zone, and for the standard deviation of this mean, for the pre-earthquake conditions in the upstream side hydraulic fill shell zone were

$$\overline{N_{1,60,CS}} = 13.5 \text{ blows/ft} \quad \text{and} \quad \sigma_{\overline{N}} = 1.8 \text{ blows/ft.}$$

Table A.4.1(b) shows values of representative $N_{1,60}$ or $N_{1,60,CS}$ values developed by two other teams of investigators, and variance or standard deviations in these representative values if available. Seed and Harder (1990) recommended a representative value of $N_{1,60,CS}$ = 13.5 blows/ft. Olson and Stark (2001, 2002) developed an estimated representative value of $N_{1,60}$ = 11.5 blows/ft, with a range of 5 to 15 blows/ft. This value of Olson and Stark includes no fines adjustment, and that would cause it to be lower than the corresponding $N_{1,60,CS}$ value in these silty sand and sandy silts. Wang (2003) and Kramer (2008) jointly developed a representative value of $\overline{N_{1,60,CS}}$ = 14.5 blows/ft, and their estimated standard deviation of that overall mean value for this case history was $\sigma_{\overline{N}}$ = 1.1 blows/ft. Overall agreement between the three independent assessments of representative $\overline{N_{1,60,CS}}$ values is excellent, with allowance for the lack of a fines adjustment by Olson and Stark, and variance or uncertainty in $\overline{N_{1,60,CS}}$ appears to be relatively low.

A.4.8 Additional Indices from the Back-Analyses

A number of additional results, and indices, can be extracted from the analyses performed. Some of these are useful in developing some of the over-arching relationships and figures presented in the main text of this report. These values are presented in Table A.4.2.

Table A.4.1: Representative values for the Lower San Fernando Dam upstream slope failure case history of: (a) post-liquefaction strength (S_r), (b) initial vertical effective stress (σ_{vo}'), and (c) $N_{1,60,CS}$ developed by various investigation teams, and estimates of variance in each of these indices when available.

(a) Post-Liquefaction Strength:	
Davis et al. (1988)	$S_r \approx 510$ psf
Seed and Harder (1990)	$S_r \approx 400$ psf
Olson (2001) and Olson and Stark (2002)	$S_r = 390$ psf, and range = 330 to 454 psf
Wang (2003) and Kramer (2008)	$\overline{S}_r = 484.7$ psf, and $\sigma_{\overline{S}} = 111.0$ psf
This Study	$\overline{S}_r = 539$ psf and $\sigma_{\overline{S}} = 47$ psf
(b) Representative $N_{1,60}$ or $N_{1,60,CS}$ Value:	
Seed and Harder (1990)	$N_{1,60,CS} \approx 13.5$ bpf
Olson (2001) and Olson and Stark (2002)	$N_{1,60} = 11.5$ bpf, range = 5 to 15 bpf
Wang (2003) and Kramer (2008)	$\overline{N_{1,60,CS}} = 14.5$ bpf, and $\sigma_{\overline{N}} = 1.1$ bpf
This Study	$\overline{N_{1,60,CS}} = 13.5$ bpf, and $\sigma_{\overline{N}} = 1.8$ bpf
(c) Representative Initial Vertical Effective Stress:	
Olson (2001) and Olson and Stark (2002)	$\sigma_{vo}' \approx 3{,}482$ psf. Likely range is not provided.
Wang (2003) and Kramer (2008)	Value of $\sigma_{vo}' \approx 3{,}538$ psf is not well documented, and so is considered useful only as an approximate comparison. (See Section 2.3.8.1, and Table 2.3.)
This Study	$\overline{\sigma'_{vo}} = 3{,}174$ psf, and $\sigma_{\overline{\sigma}} = 281$ psf

Table A.4.2: Additional results and indices from the analyses of the Lower San Fernando Dam upstream slope failure case history.

Maximum distance traveled by the center of gravity of the overall failure mass	63.4 ft.
Initial post-liquefaction Factor of Safety prior to displacement initiation, and based on best estimate value of S_r	FS = 0.60
Final post-liquefaction Factor of Safety at final (residual) post-failure geometry, and based on best estimate value of S_r	FS = 2.22

A.5 Hachiro-Gata Roadway Embankment (Akita, Japan; 1983)

A.5.1 Brief Summary of Case History Characteristics

Name of Structure	Hachiro-Gata Embankment
Location of Structure	Akita, Japan
Type of Structure	Roadway Embankment
Date of Failure	May 26, 1983
Nature of Failure	Seismic, During 1983 Nihon-Kai-Chubu Earthquake (M_L = 7.7)
Approx. Maximum Slope Height	12.7 ft.

A.5.2 Introduction and Description of Failure

The Hachiro-Gata Roadway Embankment failed during Nihon-Kai-Chubu Earthquake of May 26, 1983 (M_L = 7.7), and was investigated by Ohya et al. (1985). Ohya et al. reported a measured peak ground acceleration of 0.168g in the nearby town of Akita.

Figure A.5.1 shows a cross-section through the failure. The roadway approach embankment, which crossed a shallow lake (Hachirogata Lake), was comprised of loose fine sand fill, and it was underlain by layers of medium dense to dense sand and soft clay.

After the failure, an SPT boring and other in situ tests were performed at the toe of the roadway embankment slope, and these are shown in Figure A.5.2 (from Ohya et al., 1985). Results of lab tests performed on samples collected during the site investigation are summarized in Figure A.5.3 (from Ohya et al., 1985). These penetration and laboratory tests reasonably well constrain the key ground conditions at the base of the failure. Construction details are not reported, and it is assumed that the sandy fill was locally sourced, and that it received minimal compaction effort.

Close inspection of the penetration tests shown in Figure A.5.2 shows that the transition from fill to underlying native soils appears to be relatively clearly demarcated by a transition from very low SPT blowcounts within the upper fill to slightly higher penetration resistances in the immediately underlying denser sand. The geometry of the back heel of the final failure surface not as well constrained because the roadway embankment slumped in both directions causing a vertical drop of the roadway and extensional spreading toward each slope. This appears to have been a relatively symmetric failure, and the down-dropped central graben section settled and also pulled apart laterally to some extent. However, a reasonable heel that exits near the center of the roadway can be assumed for the back-analyses. As a result, the approximate location of the overall bounding failure surface is relatively well constrained for this case by this heel scarp, and by the transition to firmer materials at the base of the liquefiable fill. Only the left side of the embankment is analyzed, as the post-failure geometry is better defined on that side. Ohya et al. reported an approximate phreatic surface, which should be fairly well constrained due to the embankment's location within a lake, as shown in Figure A.5.1.

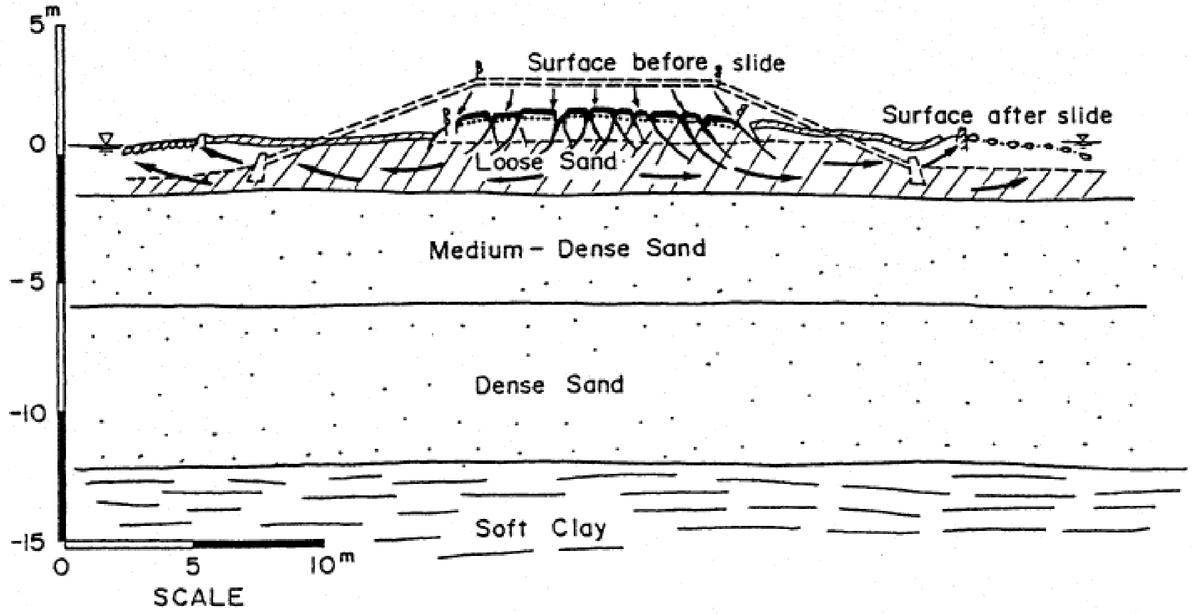

Figure A.5.1: Cross-section through the Hachiro-Gata Roadway Embankment showing pre-failure and post-failure geometry (from Ohya et al, 1985).

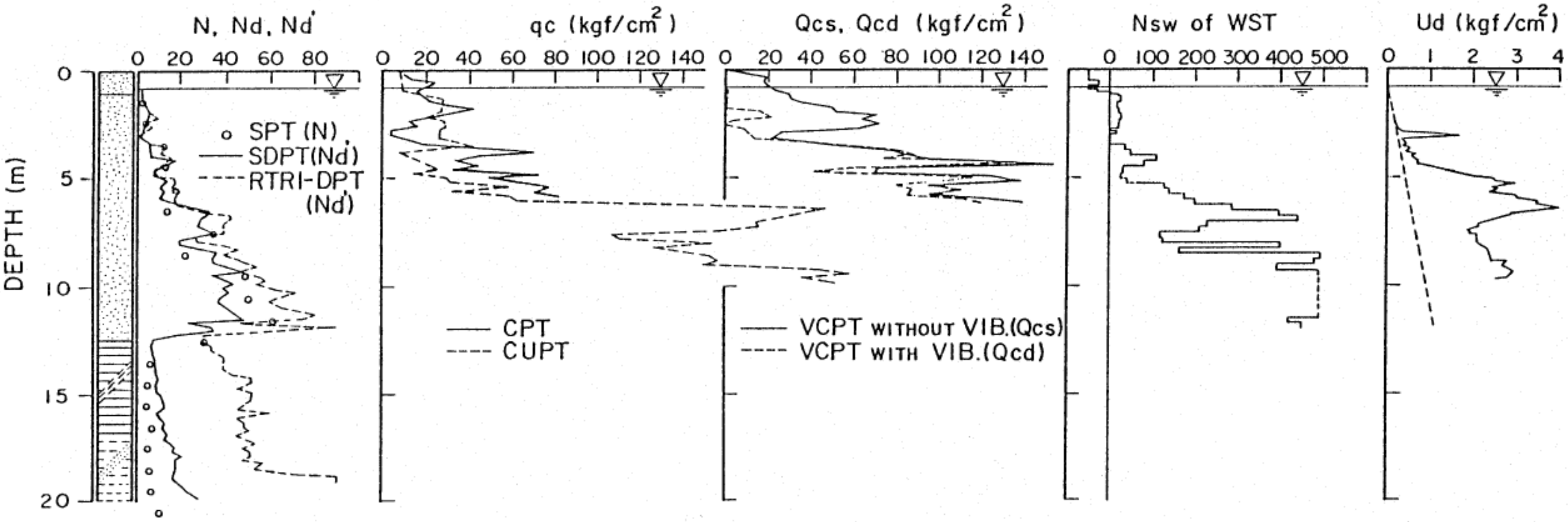

Figure A.5.2: Summary of penetration test results at the Hachiro-Gata Roadway Embankment (from Ohya et al, 1985).

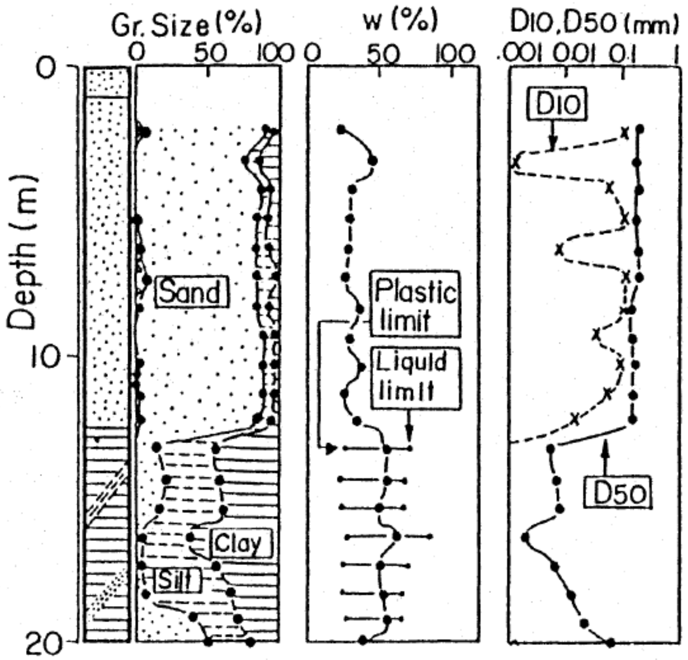

Figure A.5.3: Summary of laboratory tests performed on samples collected during the investigation at the Hachiro-Gata Roadway Embankment (from Ohya et al, 1985).

A.5.3 Initial Yield Strength Analyses

The post failure geometry shown in Figure A.5.1 provides insight as to the potential location of the critical failure surface. While this embankment failed almost symmetrically toward both slopes, the failure toward the left side of Figure A.5.1 was chosen to be analyzed as the post failure geometry is better defined on that side.

The precise location of the initial failure surface at the base of the failure is uncertain, however given the geometry of the failure and the reported stratigraphy the location was fairly well constrained. Based on an assumed phreatic surface that passes approximately through the lower third of the embankment, a search was made for the most critical static failure surface assuming liquefaction had been "triggered" in all potentially liquefiable materials below the phreatic surface. This exercise showed that the most critical potential failure surfaces for this set of assumptions would result in a failure surface exiting near the toe of the slope and reaching to the bottom of the assumed liquefiable layer. The location of the heel of the failure surface is unknown, however the most critical surface was found to exit near the middle to the roadway embankment as shown in Figure A.5.4(a). This result coincides well with the almost symmetrical sliding on each side of the roadway embankment as seen in the post failure geometry. These analyses neglected seismic inertial forces (which were moderate), however, and they also did not account for potentially progressive development of triggering of liquefaction within the slope.

Loose fine sand materials above the phreatic surface were modeled with $Ø' \approx 30°$, and a unit weight of $\gamma_m \approx 115$ lbs/ft^3. Materials below the phreatic surface were considered to liquefy, down to the base of the failure surfaces analyzed, and were assigned an undrained post-liquefaction yield strength of $S_{r,yield}$ that was constant along any given failure surface, and a unit weight of $\gamma_s \approx 122$ lbs/ft^3.

The resulting best-estimated value of $S_{r,yield}$ for the most critical initial failure surface was $S_{r,yield} = 135$ lbs/ft^2.

Parameters and geometry were then varied to examine potential variability. The location of the phreatic surface was varied, raising it by up to 0.5 m (1.5 ft) across the embankment, and lowering it by up to a similar distance. Unit weights were also varied over the ranges considered likely, and the friction angle of non-liquefied material above the phreatic surface was varied from 28° to 36°. The resulting range of values of $S_{r,yield}$ for the most critical initial failure surface was $S_{r,yield} \approx 96$ to 179 lbs/ft^2.

Olson (2001) also performed back-analyses to determine $S_{r,yield}$. Failure surfaces analyzed were similar, but did not extend to the bottom of the loose sand layer. Instead, Olson preferred failure surfaces that remained at some small elevation above the base of the liquefiable stratum. Olson reported values of $S_{r,yield} \approx 4.3$ to 5.3 kPa (90 to 111 lbs/ft^2).

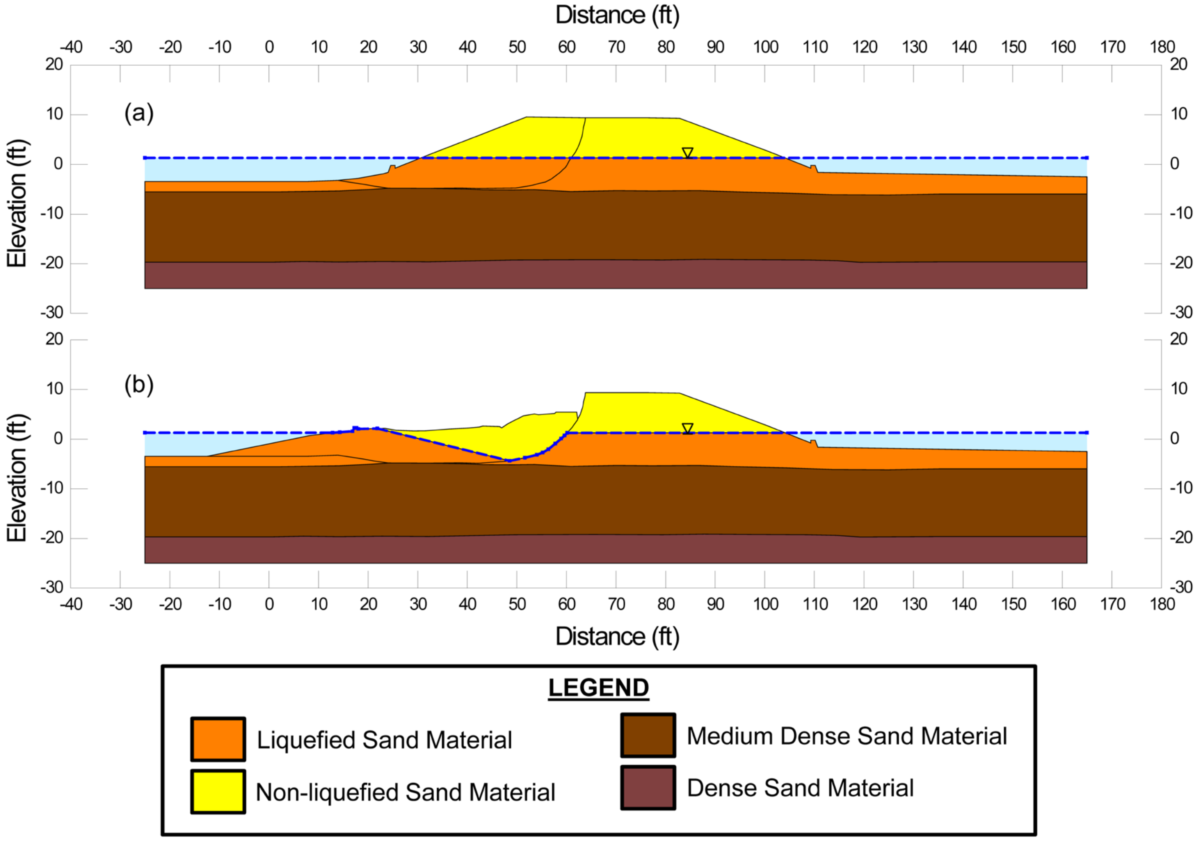

Figure A.5.4: Hachiro-Gata Roadway Embankment cross-sections showing (a) pre-failure geometry of the Hachiro-Gata Embankment and the failure surfaces used for calculation of post-liquefaction initial yield strength $S_{r,yield}$, and (b) post-failure residual geometry and the failure surface used to calculate $S_{r,resid/geom}$.

A.5.4 Residual Strength Analysis Based on Residual Geometry

The calculation of the "apparent" post-liquefaction strength ($S_{r,resid/geom}$) required to produce a calculated Factor of Safety equal to 1.0 based on residual geometry is illustrated in Figure A.5.4(b).

An additional detail here is the shear strength modeled at the base of the portion of the toe of the embankment that traveled out into the lake. The incremental momentum analyses presented in Section A.1.4 that follows indicate that the maximum velocity was on the order of approximately 3.1 ft/sec, and the velocity during most of the run-in was lower. It is not possible to fully accurately determine the degree of hydroplaning that would have occurred or the strength of the sediments on the lake bottom. The best estimate analysis of $S_{r,resid/geom}$ was performed assuming that hydroplaning effects were negligible for this case, and that shear strength at the base of the embankment materials that entered into the reservoir was 100% of $S_{r,resid/geom}$.

This figure shows the phreatic surface, and the failure surface, used to calculate the best-estimate value of $S_{r,resid/geom} \approx 40$ lbs/ft^2. To capture uncertainty or variability, the strengths of the soil at the toe as the embankment material entered the lake was varied to have a strength as low as 50% of $S_{r,resid/geom}$ beneath the portion of the slide mass entering into the lake. Variations were also made in parameters, and in location of the pre-failure phreatic surface, as were described in the preceding section. The resulting likely range of post-liquefaction strength required to provide a calculated Factor of Safety equal to 1.0 based on residual geometry was considered to be $S_{r,resid/geom} \approx 16$ to 58 lbs/ft^2.

Olson (2001) also calculated post-liquefaction strength required to produce a calculated Factor of Safety equal to 1.0 based on residual geometry, and reported a range of $S_{r,resid/geom} \approx 1.1$ to 1.6 kPa (23 to 33 lbs/ft^2), in good agreement with the values calculated in these current studies.

A.5.5 Incremental Momentum Back-Analyses and Overall Estimates of S_r

Incremental momentum back-analyses were performed using the same sets of properties and geometries (including failure surfaces and phreatic surfaces) as described in the previous sections.

Figure A.5.5 shows the best-estimate progressive incremental momentum analysis, showing the five stages of geometry evolution modeled as the failure proceeds. Figure A.5.6 shows the associated calculations of (1) acceleration vs. time, (2) velocity vs. time, and (3) displacement of vs. time for the overall center of gravity. For the geometry and phreatic surface shown in Figure A.5.5, the best estimate value of post-liquefaction strength was $S_r = 68$ lbs/ft^2.

The main sources of uncertainty, or variability, in back-calculated values of S_r were (1) strengths of the materials outside the initial embankment toe as the failure mass entered the lake, (2) unit weights, (3) strengths within the non-liquefied materials, (4) the precise location of the overall failure surface, and (5) the location of the phreatic surface.

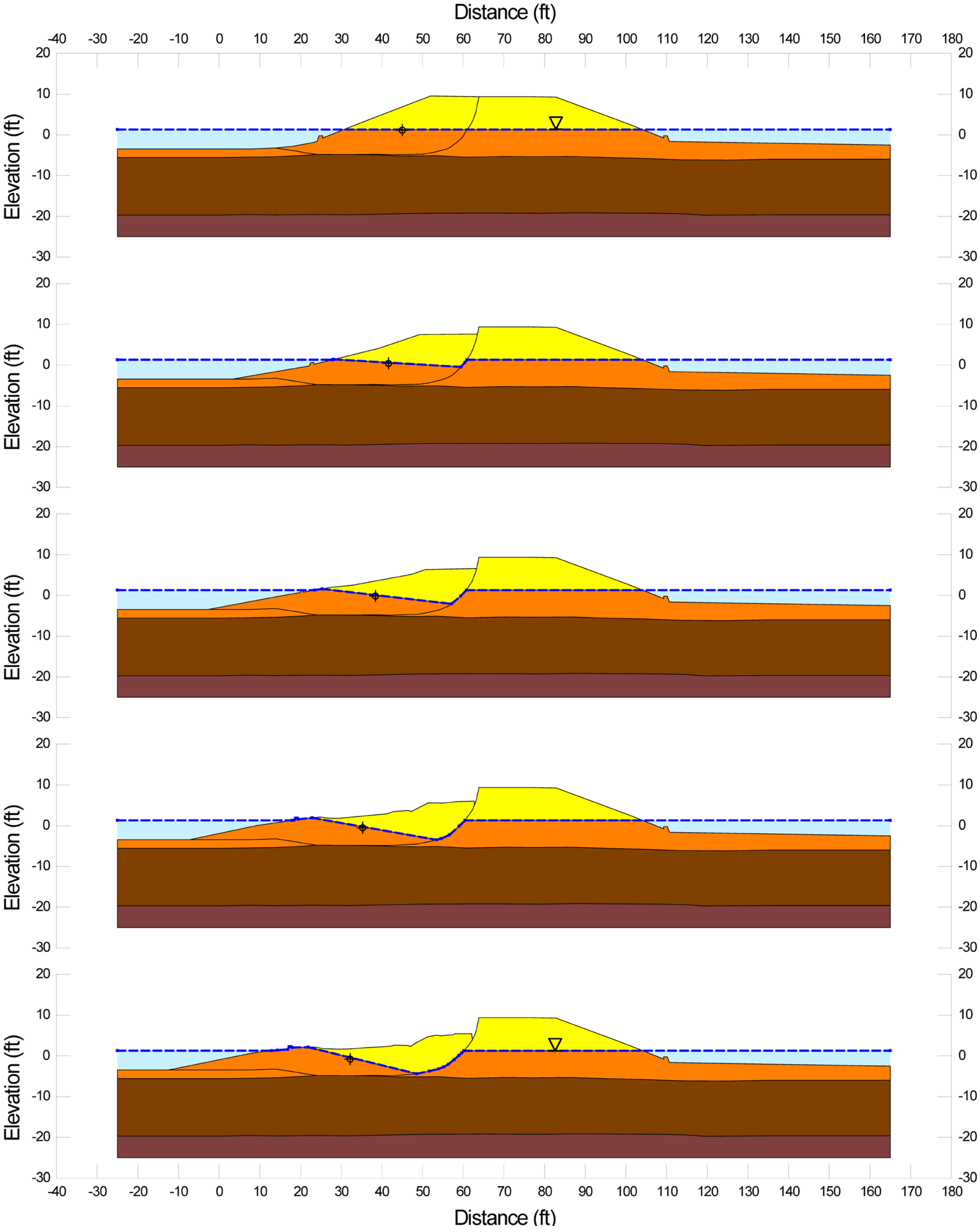

Figure A.5.5: Incremental momentum analysis of the failure of the Hachiro-Gata Embankment, showing the progressive evolution of cross-section geometry modeled.

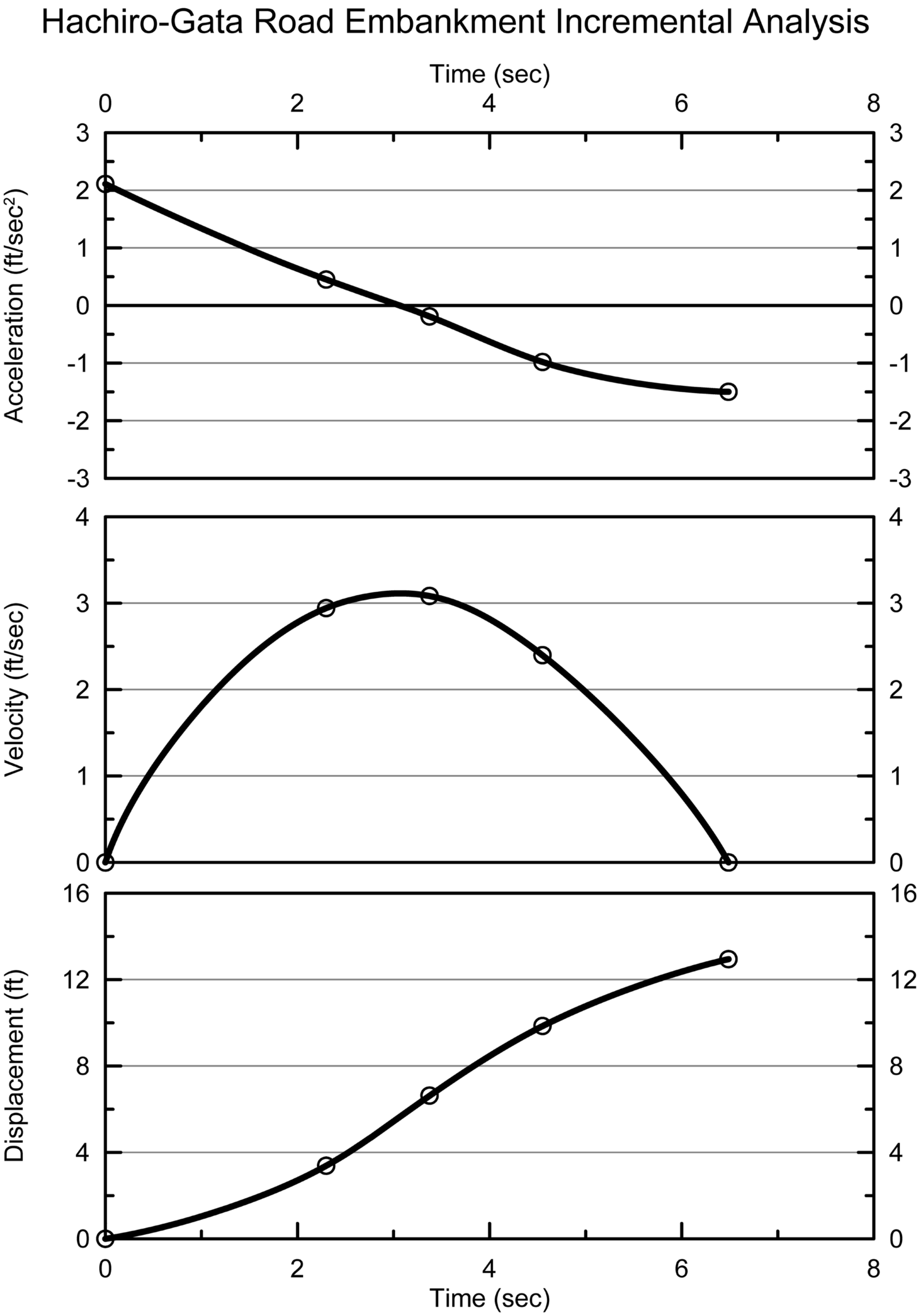

Figure A.5.6: Incremental momentum analysis of the failure of the Hachiro-Gate Embankment, showing progressive evolution of: (1) acceleration vs. time, (2) velocity vs. time, and (3) displacement vs. time of the overall center of gravity.

The analysis shown in Figure A.5.5 neglects cyclic inertial forces, and so may represent a slightly conservative assessment of actual post-liquefaction strength mobilized.

Based on all analyses performed, and the considerations discussed herein, the overall best estimate value of post-liquefaction strength for the Hachiro-Gata Embankment failure was judged to be $S_r \approx 68$ lbs/ft^2, with a likely range of $S_r \approx 45$ to 93 lbs/ft^2. Based on the factors contributing to uncertainty or variance for this case history, it was the judgment of the investigation team that this range represented approximately +/− 2 standard deviations. This range of variance is not quite symmetrical about the best estimate value, so minor further adjustments were made to produce a representative estimate of S_r suitable for regression analyses.

Overall, based on an assumed normal distribution, it was judged that the (mean and median) best estimate of post-liquefaction strength for this case history is

$$S_r = 68 \text{ lbs/ft}^2 \text{ (3.26 kPa)}$$

and that the best estimate of standard deviation of mean overall post-liquefaction strength is

$$\sigma_{\overline{S}} = 12 \text{ lbs/ft}^2 \text{ (0.57 kPa)}$$

Estimates of S_r were also reported by several other investigation teams, and these are shown in Table A.5.1(a). Olson (2001) and Olson and Stark (2002), reported a best estimate value of S_r = 2.0 kPa (42 lbs/ft^2), based on their inertial displacement analyses that considered kinetics, and a range of S_r = 1.0 to 3.2 kPa (21 to 69 lbs/ft^2). Wang (2003) and Wang and Kramer (2008) employed their zero inertial force (ZIF) method to incorporate inertial effects in their back-analyses of this failure, and they also developed estimates of both mean $\overline{S_r} = 65$ lbs/ft^2 as well as the associated standard deviation $\sigma_{\overline{S}} = 24.7$ lbs/ft^2. These other studies each employed different approaches, and different sets of modeling and analysis assumptions. Given these differences in approaches and modeling/analysis judgments, the overall agreement among these three investigations is good.

A.5.6 Evaluation of Initial Effective Vertical Stress

Average initial (pre-failure) effective vertical stress was assessed for the liquefied zones of the failure surface shown in Figure A.5.4(a). Reasonable variations were then made in (1) the location of the phreatic surface, (2) unit weights, and (3) the precise location of the overall failure surface.

The resulting best estimate of average pre-failure effective stress within the liquefied materials controlling the failure was then $\sigma_{vo}' \approx 673$ lbs/ft^2, with a reasonable range of $\sigma_{vo}' \approx 594$ to 758 lbs/ft^2. This range is slightly non-symmetric about the median value, and this range was judged by the engineering team to represent approximately +/− 2 standard deviations. Overall, the best characterization of initial (pre-failure) average effective vertical stress was then taken to be represented by a mean and median value of

$$\overline{\sigma'_{vo}} \approx 673 \text{ lbs/ft}^2 \text{ (32.2 kPa)}$$

with a standard deviation of

$$\sigma_{\overline{\sigma}} \approx 41 \text{ lbs/ft}^2 \text{ (1.96 kPa)}$$

Estimates of σ_{vo}' were also reported by other investigation teams, and these are shown in Table A.13.1(c). Olson (2001) and Olson and Stark (2002) report an average initial vertical effective stress on the order of approximately $\sigma_{vo}' \approx 670$ lbs/ft^2, in excellent agreement with these current studies. Average initial vertical effective stresses were not directly reported by Wang (2003) and Kramer (2008), but they were published more recently in the publication by Kramer and Wang (2015). As discussed in Section 2.3.8.1(a), the approach taken by Wang (2003) to evaluation of σ_{vo}' for his nine "primary" case histories (this is one of those nine) is not clearly explained, and it is also poorly documented. Wang's value of $\sigma_{vo}' = 398$ lbs/ft^2 is significantly lower than the values developed by Olson (2001) and by these current studies. Wang (2003) presents no detailed cross-section for his analyses, so it is not possible to know why his estimated value of σ_{vo}' appears to be so much lower. Agreement between the values calculated by Olson (2001) and these current studies is excellent.

A.5.7 Evaluation of $N_{1,60,CS}$

As shown in Figure A.5.2, only 2 SPT were performed within the liquefiable upper stratum. As a result, lack of numbers of SPT tests is a significant contributor to uncertainty or variability with respect to the median or mean $N_{1,60,CS}$ value representative of this material. Ohya et al. (1985) reported an energy ratio of approximately 68%, and this current study assumes the same. Corrections for effective overburden stress (C_N) were made using the relationships proposed by Deger (2014), as presented and discussed in Appendix C. Corrections for SPT equipment and procedural details, and for fines content, were made based on Cetin et al. (2018a,b). The resulting median $\overline{N_{1,60,CS}}$ value was 6.8 blows/ft.

Variance of $\overline{N_{1,60,CS}}$ within this limited data set was used to calculate the associated variance in the mean (and thus approximately the median) value of $\overline{N_{1,60,CS}}$, but this under-estimated the actual variance or uncertainty. Addition factors significantly affecting variance or uncertainty in the median representative $\overline{N_{1,60,CS}}$ value were (1) lack of numbers of SPT data, and (2) uncertainty as to actual SPT equipment and procedural details. Overall, it was the judgment of the investigation team that SPT penetration resistance could be suitably represented with a representative (median) value of $\overline{N_{1,60,CS}} = 6.8$ blows/ft, and with a standard deviation of the median/representative value of approximately $\sigma_{\overline{N}} = 1.6$ blows/ft.

Table A.5.1(b) shows values of representative $N_{1,60}$ or $N_{1,60,CS}$ values developed by other investigators, and variance or standard deviations in these representative values when available. Olson and Stark (2001, 2002) developed an estimated representative value of $N_{1,60}$ = 4.4 blows/ft, and an estimated range of representative values of $N_{1,60} \approx$ 3.1 to 5.8 blows/ft, but did not quantify variance or standard deviation in probabilistic terms. They applied no fines correction. Wang (2003) and Kramer (2008) jointly developed a representative value of $\overline{N_{1,60,CS}}$ = 5.7 blows/ft, and their estimated standard deviation of that overall mean value for this case history was $\sigma_{\overline{N}}$ = 2.8 blows/ft. The representative $N_{1,60}$ value of Olson and Stark is about 2 to 2.5 blows/ft. lower than the other two sets of values in the table, in part because Olson and Stark did not make a fines correction, which would have served to increase their $N_{1,60}$ values as they became $N_{1,60,CS}$ values in these silty sands.

The investigation teams whose results are presented in Table A.5.1(c) each employed slightly different approaches with regard to corrections for effective overburden stress, fines content, and SPT equipment and procedural details. Given this, the agreement with the value employed in this current study is good. Wride, McRoberts and Robertson (1999) developed a somewhat lower estimate of representative $N_{1,60,CS}$ for this case history, but their approach targeted determination of a more nearly lower bound value, and so is this lower value is to be expected and it is not directly comparable with the other values shown.

Table A.5.1: Representative values for the Hachiro-Gata Roadway Embankment case history of: (a) post-liquefaction strength (S_r), (b) initial vertical effective stress (σ_{vo}'), and (c) $N_{1,60,CS}$ developed by various investigation teams, and estimates of variance in each of these indices when available.

(a) Post-Liquefaction Strength:	
Olson (2001) and Olson and Stark (2002)	S_r = 42 psf, and range = 21 to 69 psf
Wang (2003) and Kramer (2008)	$\overline{S_r}$ = 65 psf, and $\sigma_{\overline{S}}$ = 24.7 psf
This Study	$\overline{S_r}$ = 68 psf, and $\sigma_{\overline{S}}$ = 12 psf
(b) Representative $N_{1,60}$ or $N_{1,60,CS}$ Value:	
Olson (2001) and Olson and Stark (2002)	$N_{1,60}$ = 4.4 bpf, and range = 3.1 to 5.8 bpf
Wang (2003) and Kramer (2008)	$\overline{N_{1,60,CS}}$ = 5.7 bpf, and $\sigma_{\overline{N}}$ = 2.8 bpf
This Study	$\overline{N_{1,60,CS}}$ = 7 bpf, and $\sigma_{\overline{N}}$ = 1.2 bpf
(c) Representative Initial Vertical Effective Stress:	
Olson (2001) and Olson and Stark (2002)	σ_{vo}' = 670 psf, range is not provided.
Wang (2003) and Kramer (2008)	Value of $\sigma_{vo}' \approx$ 398 psf is poorly documented, and so is considered useful only as an approximate comparison. (See Section 2.3.8.1, and Table 2.3.)
This Study	$\overline{\sigma'_{vo}}$ = 673 psf, and $\sigma_{\overline{\sigma}}$ = 41 psf

A.5.8 Other Results and Indices

A number of additional results, and indices, can be extracted from the analyses performed. Some of these are useful in developing some of the over-arching relationships and figures presented in the main text of this report. These values are presented in Table A.5.2.

Table A.5.2: Additional results and indices from the analyses of the Hachiro-Gata Roadway Embankment failure case history.

Maximum distance traveled by the center of gravity of the overall failure mass	12.8 ft.
Initial post-liquefaction Factor of Safety prior to displacement initiation, and based on best estimate value of S_r	FS = 0.55
Final post-liquefaction Factor of Safety at final (residual) post-failure geometry, and based on best estimate value of S_r	FS = 1.66

A.6 La Marquesa Dam Upstream Slope (Chile; 1985)

A.6.1 Brief Summary of Case History Characteristics

Name of Structure	La Marquesa Dam, Upstream Slope
Location of Structure	Chile
Type of Structure	Zoned Earthen Dam
Date of Failure	March 3, 1985
Nature of Failure	Seismic, During 1985 Central Chilean Earthquake (M_S = 7.8)
Approx. Maximum Slope Height	29.2 ft. (U/S side)

A.6.2 Introduction and Description of Failure

The La Marquesa Dam suffered liquefaction-induced slope failures on both its upstream side and its downstream side as a result of the Central Chilean earthquake of March 3, 1985 (M_S = 7.8), and was investigated by de Alba et al. (1987, 1988). This Appendix Section A.6 will deal primarily with the upstream side failure, though both failures are somewhat interactive with each other, and the subsequent Appendix Section A.7 will then deal primarily with the downstream side failure.

The dam is located near the Chilean coast, approximately 65 km west of Santiago. Peak horizontal ground surface accelerations recorded in the general vicinity of the dam during the earthquake were on the order of approximately 0.43 to 0.65 g. (de Alba et al., 1987)

As shown in Figure A.6.1 (from de Alba et al., 1987), the dam suffered liquefaction-induced failures on both the upstream and downstream sides. Displacements were somewhat larger on the upstream side, where the upstream toe foundation soils appeared to have been partially excavated producing a slightly higher slope on the upstream side than on the downstream side. Upstream side displacements were approximately 12 feet vertically at the crest, and approximately 53 feet horizontally at the toe. The downstream side maximum displacements were approximately 9 feet vertically at the crest, and approximately 24 feet horizontally at the toe.

A.6.3 Geology and Site Conditions

Figure A.6.1 shows conditions both before and after the failure (from de Alba et al., 1987). Borings performed before the earthquake, and additional borings performed after the event, showed the dam foundation to consist of a relatively thin layer of silty sand, which was underlain by thicker deposits of sandy clay and clayey sand. The deeper sandy clay and clayey sand materials had higher fines contents, higher plasticity indices, and higher blowcounts and do not appear to have been involved in the two slope failures. It is within the relatively thin, upper (silty sand) foundation stratum that the liquefaction-induced sliding appears to have occurred; though it should be noted that failure through the lower portions of the embankment shells cannot be fully

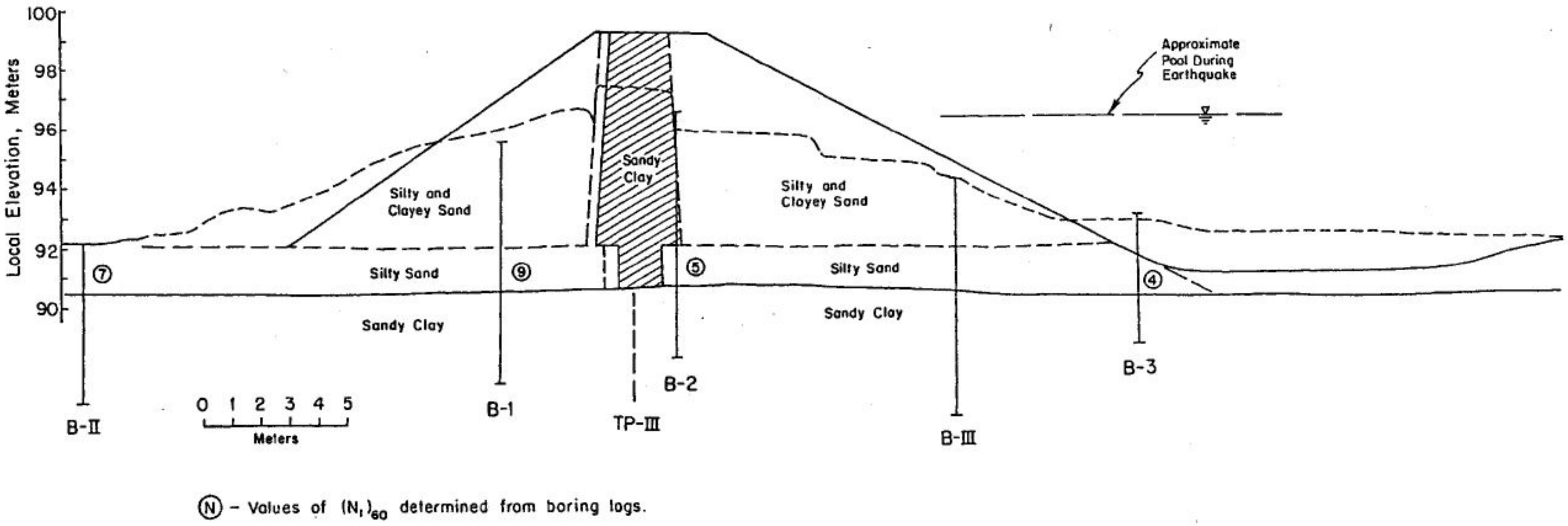

Figure A.6.1: Pre-failure and post-failure cross-sections of the La Marquesa Dam (from de Alba et. al, 1987).

ruled out. This upper foundation stratum of silty sand had estimated fines contents of approximately 20% to 30% beneath the dam, and these soils appear to have been very loose, with very low SPT blowcounts.

Because of the presence of the relatively pervious upper silty sand stratum, a key trench was excavated to extend the central sandy clay core through this upper foundation stratum and this key trench was back-filled with compacted sandy clay core material in order to "key" the core into the lower, less pervious foundation soils.

The embankment fill materials were locally excavated from the valley floor, and from the abutments. The core zone was constructed using the more plastic sandy clays, and the shells were constructed using silty and clayey sands. Details of embankment compaction are not clear, but the embankment fill materials appear to have been very loosely placed, exhibiting SPT $N_{1,60,CS}$ values essentially equal to those of the loose and highly liquefiable underlying materials of the upper (silty sand) foundation stratum.

A.6.4 Initial Yield Stress Analyses

Figures A.6.2(a) and A.6.3(a)shows the cross-sections used for back-analyses of the post-liquefaction initial yield strength $S_{r,yield}$ that would be required within the liquefied upstream shell materials to produce a calculated Factor of Safety equal to 1.0. This is not the actual post-liquefaction strength, but it proves to be useful in developing a number of charts and relationships for these overall studies.

There are two different sets of potential failure surfaces in these two figures, and these correspond to "Scenario A" and "Scenario B". The central core section of the dam suffered some loss of height, as shown in Figures A.6.1 through A.6.3 and A.6.8, and it spread a bit as well becoming a bit wider near its base. As shown in Figure A.6.8, a longitudinal crack occurred roughly along the centerline of the crest, and there was some lateral opening (separation) across the crack as well as some shear displacement across this crest crack. There were significantly greater vertical displacements of the two adjacent shell zones, leaving the core (even with its slightly reduced height) protruding upwards like a horst between the two adjacent down-dropped shell zones.

There were two sets of potential failure mechanisms that could potentially explain these features, and the overall observed post-failure geometries of Figures A.6.1 through A.6.3. The first (Scenario A) involves sliding primarily along the interface between the core zone and the adjacent shell zones, as shown in Figure A.6.2, with some lateral bulging of the core as the level of confinement provided by the adjacent shells reduced somewhat. The second (Scenario B) involves shearing through the lower portions of the core zone, producing both the observed crest settlements of the top of the core zone and also the minor lateral increase in core width, as illustrated in Figure A.6.3. This second Scenario B also serves to directly explain the observed crest crack, and provides a useful explanation for the observed differential vertical displacements across this longitudinal crest crack as well. Overall, it was judged that Scenario B provided a better overall explanation of the observed movements, but that Scenario A could not be completely discounted. Accordingly, both scenarios were modeled and analyzed.

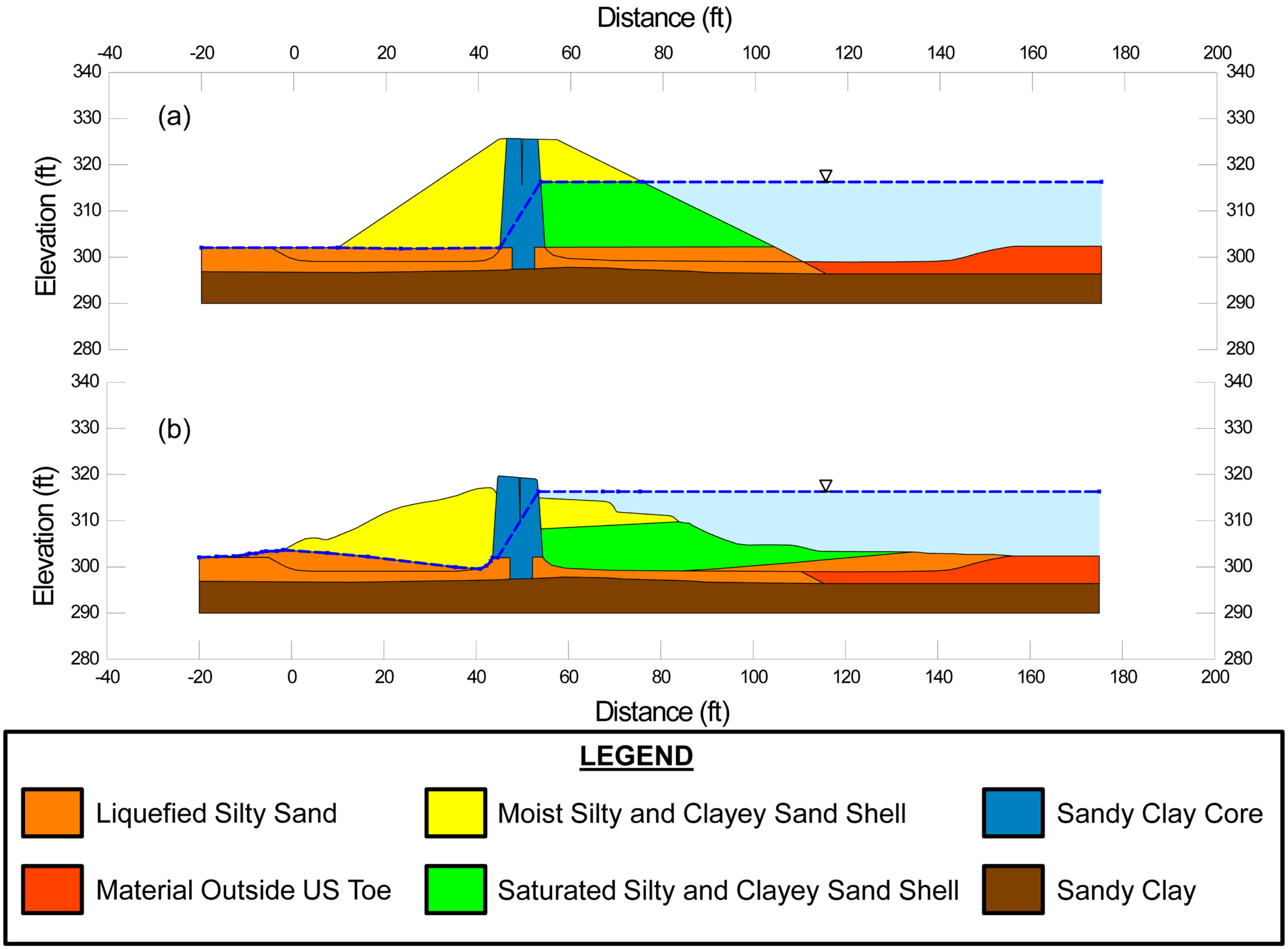

Figure A.6.2: La Marquesa Dam: (a) pre-failure geometry and Scenario A failure surface for initial yield stress analyses, and (b) post-failure geometry and Scenario A failure surface for post-failure residual geometry analyses.

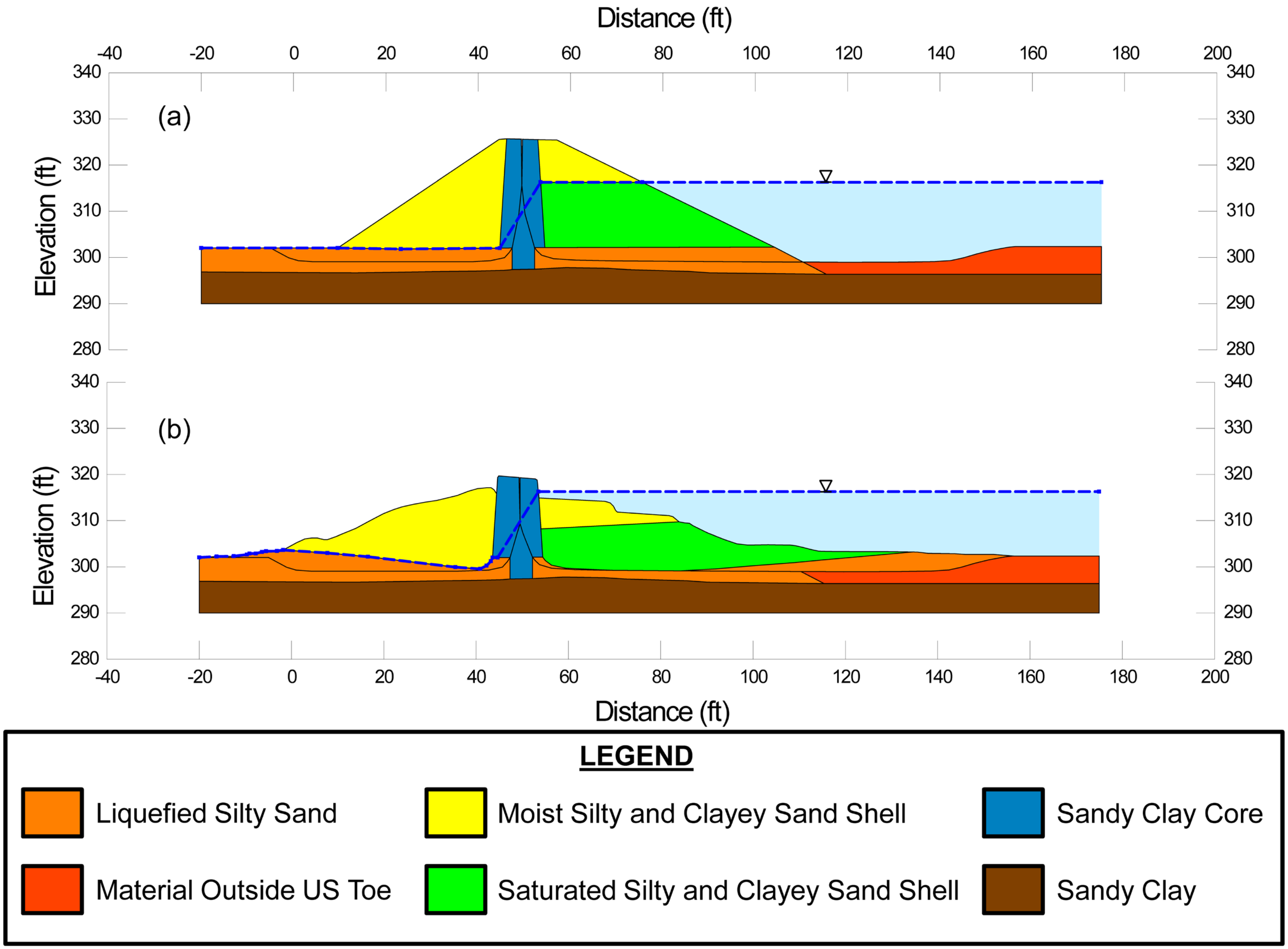

Figure A.6.3: La Marquesa Dam: (a) pre-failure geometry and Scenario B failure surface for initial yield stress analyses, and (b) post-failure geometry and Scenario B failure surface for post-failure residual geometry analyses.

There was no clear differentiation between the SPT blowcounts in the embankment shell zones and those of the underlying upper silty sand foundation stratum, so the embankment shell zone materials (which were of similar provenance) appear to have been placed in a very loose condition.

Shear strengths of non-saturated silty sand materials (above the phreatic surface) in the shell zones were modeled as frictional, with a best estimate value of $Ø' = 30$ °. This was then varied between 26 to 34° in subsequent sensitivity analyses. Shear strengths within the saturated silty sands of both the lower upstream shell and the upper foundation stratum were modeled as S_r, and these current back-analyses were performed in order to determine this value. Shear strengths in the clayey sand core zone were modeled as cohesive, with residual (large displacement) values of $S_{u,r}/P \approx 0.09$ based on very limited data and information. This was then varied between 0.06 and 0.12 in subsequent sensitivity studies. Shears strengths along interfaces between the core and shell zones were considered to be controlled by the lesser of the two available shear strengths. Shear strengths of the nearly vertical cracks/shears at the upper portions of the central core zone (within the core) for Scenario B were modeled as negligible, in part because neither the upstream portion of the embankment nor the downstream portion of the embankment could usefully help to support the other when both were displacing vertically downwards.

Unit weights for the non-saturated shell zones were modeled as $\gamma_m = 120$ lbs/ft^3, and the saturated silty sands of the lower upstream shell and the upper foundation stratum were modeled as $\gamma_s = 125$ lbs/ft^3. These were varied by +/- 5 lbs/ft^3 in subsequent sensitivity studies. Unit weights of the silty clay core materials were modeled as $\gamma_s = 120$ lbs/ft^3 +/- 5 lbs/ft^3.

Based on the cross-sections shown in Figures A.6.2(a) and A.6.3(a), and the properties and parameters described above, the best-estimate value of $S_{r,yield}$ for Scenario A (Figure A.6.2(a)) was 240 lbs/ft^2, and the best-estimate value for Scenario B (Figure A.6.3(a)) was 254 lbs/ft^2. It was judged that Scenario B was more likely to have occurred than Scenario A, because it appears to better explain the overall observed post-failure geometry and cross-section and geometry details. Accordingly, a weighted average value of $S_{r,yield} = 249$ lbs/ft^2 was then selected as the overall best estimate value.

Parameters were next varied, as described previously, and alternate potential failure surfaces were also examined for both Scenarios A and B, including failure surfaces passing within the saturated lower portions of the upstream side embankment shell zone. The two sets of results were again weighted, favoring Scenario B, and the best overall estimate value was $S_{r,yield} \approx 253$ lbs/ft^2, and it was judged that a reasonable range was $S_{r,yield} \approx 227$ to 274 lbs/ft^2.

Olson (2001) was the only other investigator who also performed back-analyses to determine $S_{r,yield}$. Failure surfaces analyzed differed somewhat, and so did some of the parameters and other modeling assumptions. Olson reported a best estimate value of $S_{r,yield} \approx 9.3$ kPa (194 lbs/ft^2) , and a range of $S_{r,yield} \approx 6.7$ to 13.4 kPa (140 to 279 lbs/ft^2).

A.6.5 Residual Strength Analyses Based on Residual Geometry

The calculation of the "apparent" post-liquefaction strength ($S_{r,resid/geom}$) required to produce a calculated Factor of Safety equal to 1.0 based on residual geometry is illustrated in Figures A.6.2(b) and A.6.3(b), again representing Scenarios A and B. Modeling parameters and details are as previously described in the preceding sections.

Based on the cross-sections shown in Figures A.6.2(b) and A.6.3(b), and the properties and parameters described above, the best-estimate value of $S_{r,resid/geom}$ for Scenario A (Figure A.6.2(b)) was 38 lbs/ft^2, and the best-estimate value for Scenario B (Figure A.6.3(b)) was 55 lbs/ft^2. It was again judged that Scenario B was more likely to have occurred than Scenario A, because it appears to better explain the overall observed post-failure geometry and cross-section and geometry details. Accordingly, a weighted average value of $S_{r,resid/geom}$ = 49 lbs/ft^2 was then selected as the overall best estimate value.

Parameters were next varied, as described previously, and alternate potential failure surfaces were also examined for both Scenarios A and B, including failure surfaces passing within the saturated lower portions of the upstream side embankment shell zone. Again weighting the results in favor of Scenario B, it was judged that a reasonable range was $S_{r,resid/geom} \approx 32$ to 68 lbs/ft^2.

Olson (2001) also performed back-analyses to determine $S_{r,resid/geom}$. Failure surfaces analyzed again differed somewhat, and so did some of the parameters and other modeling assumptions. Olson reported a best estimate value of $S_{r,resid/geom} \approx 3.1$ kPa (65 lbs/ft^2) , and a range of $S_{r,resid/geom} \approx 1.9$ to 4.3 kPa (40 to 90 lbs/ft^2).

A.6.6 Incremental Momentum Back-Analyses and Overall Estimates of S_r

Incremental momentum back-analyses were performed using the same sets of properties and geometries (including failure surfaces and phreatic surfaces) as described in the previous sections. Two sets of analyses were again performed, for Scenario A and Scenario B.

Figure A.6.4 shows the best-estimate progressive incremental momentum analysis for Scenario A, showing the five stages of geometry evolution modeled as the failure proceeds. The resulting best estimate value of post-liquefaction strength for Scenario A was S_r = 91 lbs/ft^2.

Figure A.6.5 shows the best-estimate progressive incremental momentum analysis for Scenario B, showing the five stages of geometry evolution modeled as the failure proceeds. Figure A.6.6 shows the associated calculations of (1) acceleration vs. time, (2) velocity vs. time, and (3) displacement of the overall center of gravity vs. time for Scenario B. The resulting best estimate value of post-liquefaction strength was S_r = 106 lbs/ft^2.

Because Scenario B is judged to better explain the full details of the observed field failure, the overall best estimate of post-liquefaction strength based on these incremental momentum back-analyses was weighted in favor of Scenario B (and Figures A.6.5 and A.6.6), and the resulting overall best estimate value is S_r = 101 lbs/ft^2.

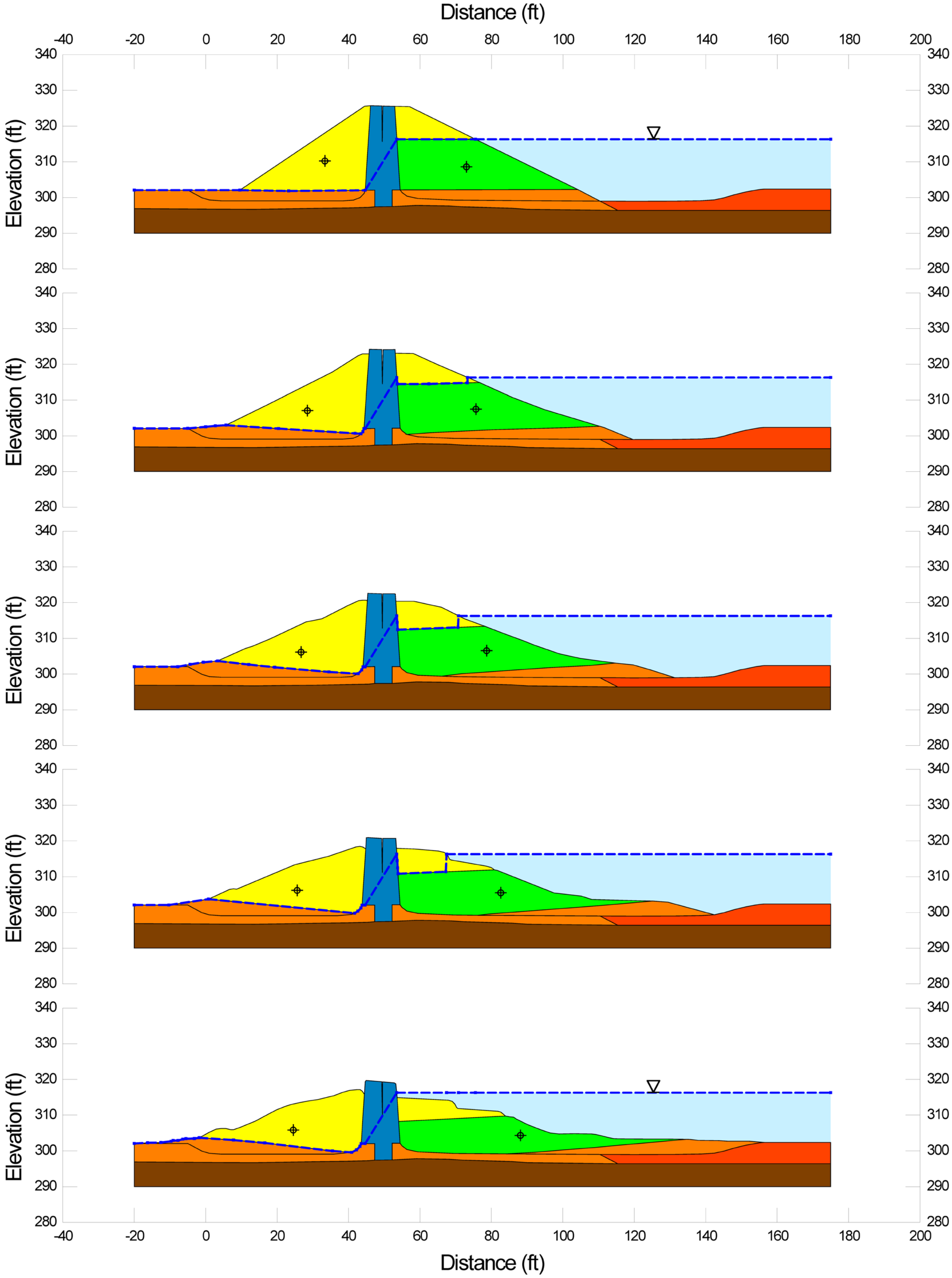

Figure A.6.4: Incremental momentum analysis of the failure of the La Marquesa Dam, showing progressive evolution of cross-section geometry modeled (for Scenario A).

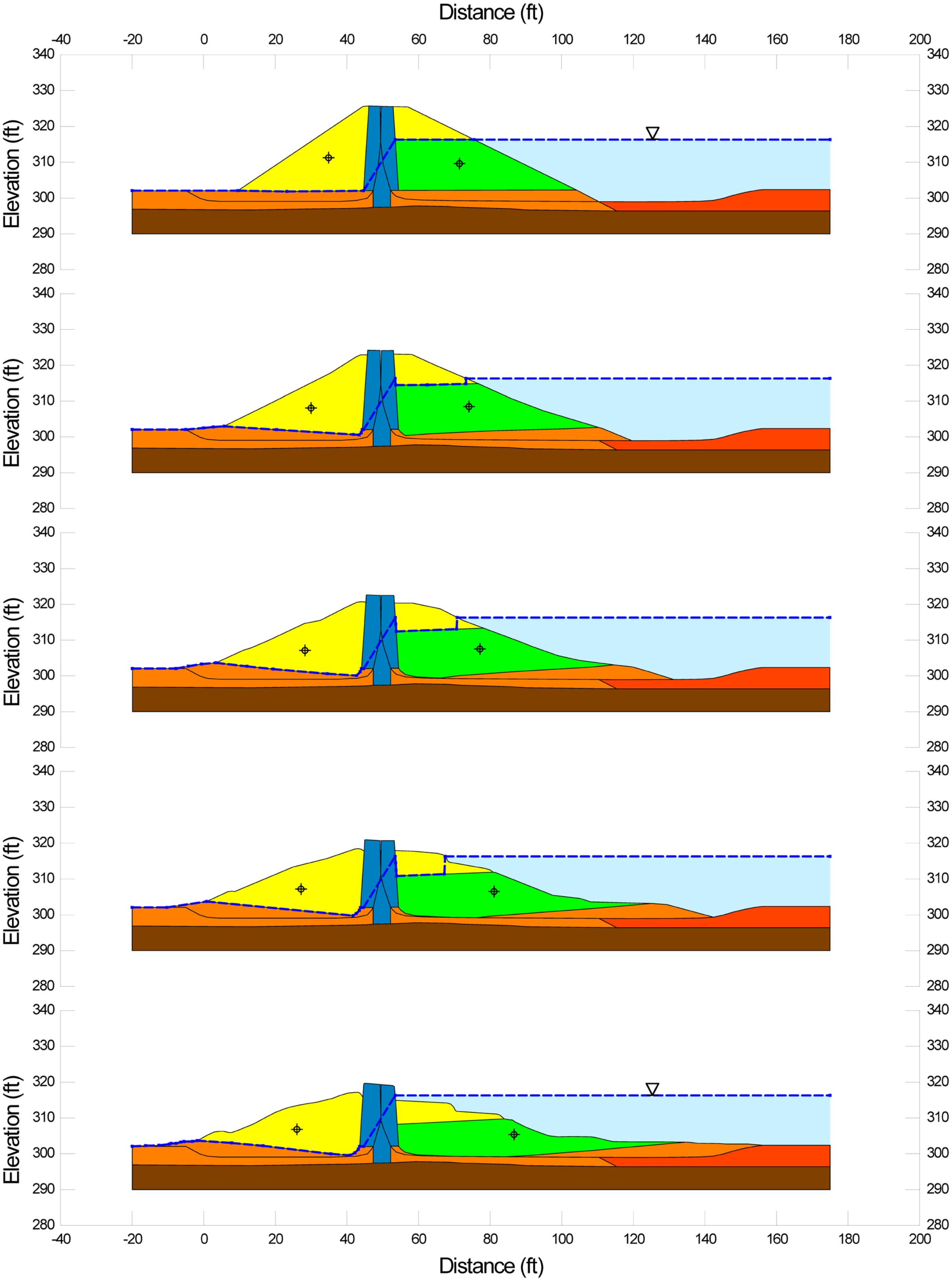

Figure A.6.5: Incremental momentum analysis of the failure of the La Marquesa Dam, showing progressive evolution of cross-section geometry modeled (for Scenario B).

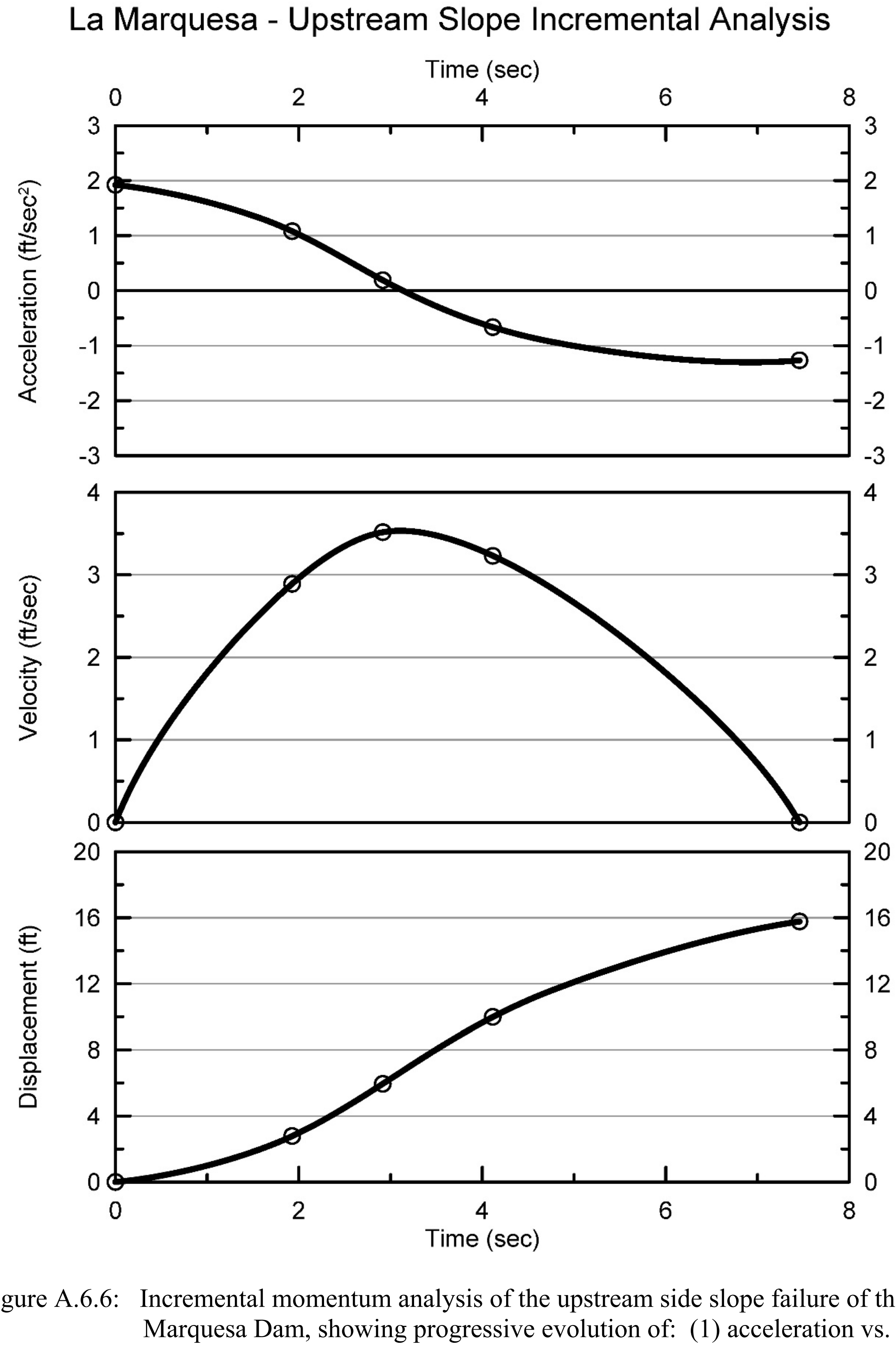

Figure A.6.6: Incremental momentum analysis of the upstream side slope failure of the La Marquesa Dam, showing progressive evolution of: (1) acceleration vs. time, (2) velocity vs. time, and (3) displacement vs. time of the overall center of gravity of the failure mass (for Scenario B).

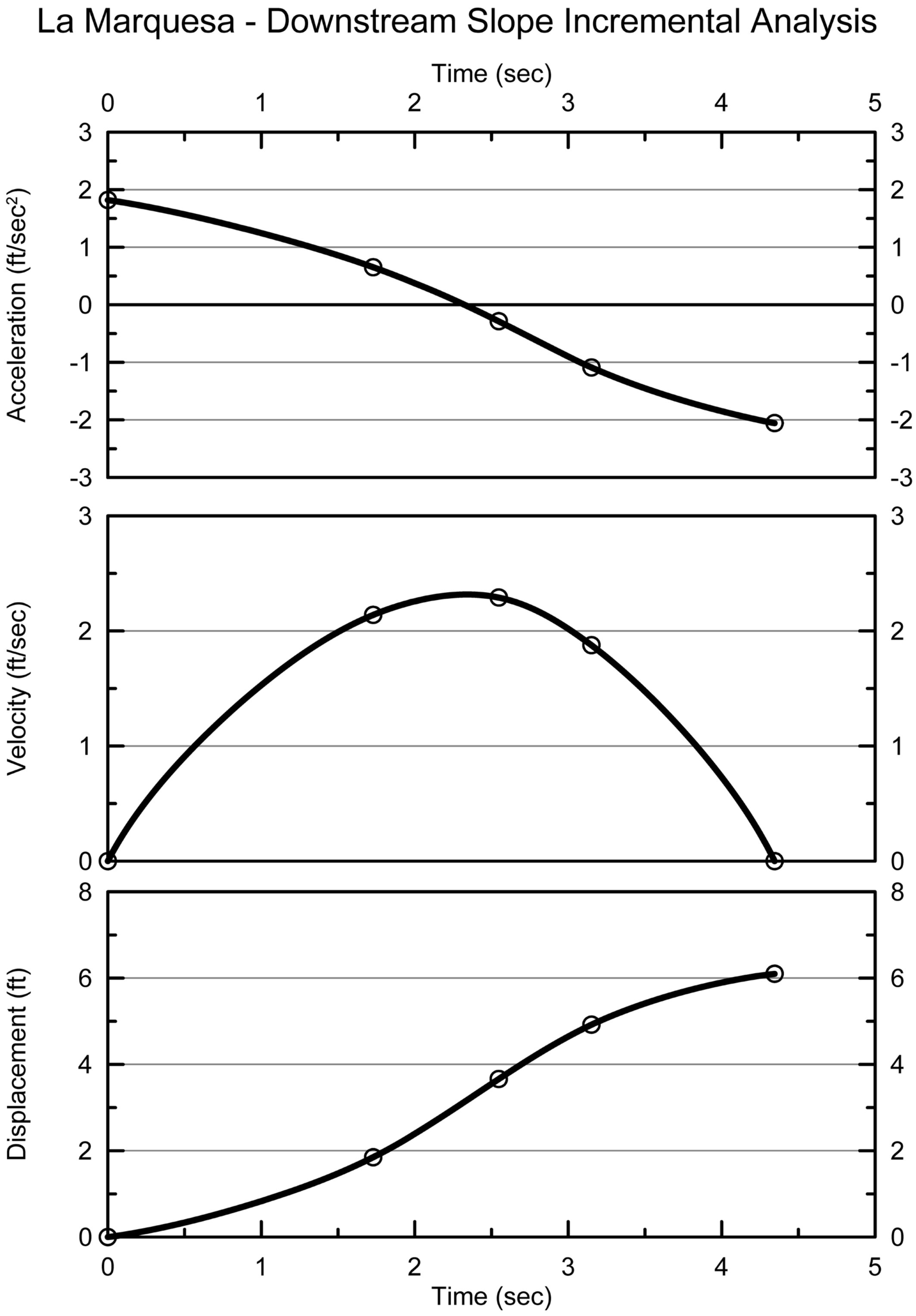

Figure A.6.7: Incremental momentum analysis of the downstream side slope failure of the La Marquesa Dam, showing progressive evolution of: (1) acceleration vs. time, (2) velocity vs. time, and (3) displacement vs. time of the overall center of gravity of the failure mass (for Scenario B).

Parameter sensitivity analyses, including modeling of additional potential failure surfaces considered to be "reasonable/feasible" were then performed to investigate the overall range of post-liquefactions strength values. This range was found to be S_r = 54 to 153 lbs/ft^2. This was judged to represent approximately +/- 1.5 standard deviations. This range of variance is not symmetrical about the best estimate value, so minor further adjustments were made to produce a representative estimate of S_r suitable for regression analyses.

Overall, based on an assumed normal distribution, it was judged that the (mean and median) best estimate of post-liquefaction strength for this case history is

$$\overline{S_r} = 103 \text{ lbs/ft}^2$$

and that the best estimate of standard deviation of mean overall post-liquefaction strength is

$$\sigma_{\overline{S}} = 33 \text{ lbs/ft}^2$$

The La Marquesa Dam upstream slope failure case history has been back-analyzed by a number of previous investigators, but not with back-analysis methods that reasonably accurately incorporate momentum effects. Seed and Harder (1990) reported a value of $S_r \approx 200$ lbs/ft^2, but their back-analyses included a judgmental addition to S_r to account for cyclic inertial effects. Olson (2001) and Olson and Stark (2002) did not apply their "kinetics" method to this case, and so they did not independently develop an estimate of S_r that incorporated momentum effects. Similarly, Wang (2003) and Wang and Kramer (2008) did not employ their zero inertial force (ZIF) method to incorporate inertial effects in back-analyses of this failure, and so they also did not independently develop an estimate of S_r that incorporated momentum effects.

Approximate comparisons can be made to Olson and Stark's (2001, 2002) values of back-calculated values of $S_{r,yield}$ and $S_{r,resid/geom}$ by means of Equation 4.2, as shown in Tables 4.3 and 4.6, but this is not a very rigorous comparison. As shown in Tables 4.3 and 4.6, the resulting inferred value of S_r for $\xi = 0.8$ would be $S_r \approx 104$ lbs/ft^2, in excellent agreement with these current studies. This is the value shown in Table A.6.1.

It appears that the values calculated in these current studies are the first set of back-calculated values of post-liquefaction S_r based on analysis methods that directly incorporate momentum effects.

Finally, it should be noted that this case history is one in which (1) a liquefaction-induced slope failure produced moderate displacements and deformations, and (2) levels and duration of strong shaking were high. This is thus a case in which it may be hypothesized that the values back-calculated in these current studies, even with incorporation of momentum effects, may conservatively underestimate the actual values of S_r to some extent due to the failure to also incorporate cyclic inertial effects during strong shaking. It is not (yet) analytically possible to reliably quantify this additional potential conservatism. Seed and Harder (1990) made a judgmental increase in estimated S_r to account for these cyclic inertial effects, but in these current studies this additional adjustment is not being made.

A.6.7 Evaluation of Initial Effective Vertical Stress

Average initial (pre-failure) effective vertical stress was assessed for the liquefied zones of each of the failure surfaces shown in Figures A.6.2(a) and A.6.3(a). Additional sensitivity analyses were then performed for reasonable ranges of variations in (1) the location of the phreatic surface, (2) unit weights, and (3) the precise location of the overall failure surface in order to evaluate uncertainty or variance.

The resulting best estimate of average pre-failure effective stress within the liquefied materials controlling the failure was then $\sigma_{vo}' \approx 981$ lbs/ft^2, with a reasonable range of $\sigma_{vo}' \approx 771$ to 1,253 lbs/ft^2. This range is slightly non-symmetric about the median value, and this range was judged by the engineering team to represent approximately ± 2 standard deviations. Overall, the best characterization of initial (pre-failure) average effective vertical stress was then taken to be represented by a mean value of

$$\overline{\sigma'_{vo}} \approx 981 \text{ lbs/ft}^2$$

and with a standard deviation of

$$\sigma_{\overline{\sigma}} \approx 134 \text{ lbs/ft}^2$$

An estimate of σ_{vo}' was also calculated by Olson and Stark (2001, 2002) and this is shown in Table A.1.1(c). They reported a weighted average mean value of $\sigma_{vo}' \approx 960$ lbs/ft^2, in excellent agreement with these current studies. Average initial vertical effective stresses were not directly reported by Wang (2003) and Kramer (2008), but they were published more recently in the publication by Kramer and Wang (2015). As discussed in Section 2.3.8.1(b)-(iii), Wang (2003) did not perform any independent analyses to assess σ_{vo}' for his 22 "secondary" cases, and this is one of those cases. Instead, he compiled values of S_r from multiple previous investigators, and averaged these for a best estimate. He also compiled multiple values of S_r/σ_{vo}' from previous investigators, and averaged these for a best estimate. He then used these two best-estimate values of S_r and S_r/σ_{vo}' to infer a resulting representative value of σ_{vo}'. As described in Section 2.3.8.1(b)-(iii), the resulting averaged values of S_r and S_r/σ_{vo}' were incompatible with each other for a number of Wang's "secondary" case histories, and this process produced unreasonable, and in some cases physically infeasible, values of σ_{vo}' for a number of case histories. Accordingly, Wang's value of $\sigma_{vo}' = 1{,}682$ lbs/ft^2 is not considered a useful check here. Agreement between Olson's value, which is well-documented, and the value developed in these current studies, is excellent.

A.6.8 Evaluation of $N_{1,60,CS}$

Figure A.6.8 shows the locations of post-failure SPT borings and SPT tests performed to investigate the failure. Based on the available data and information, it appears most likely that the upstream and downstream slope failures both occurred due to liquefaction-induced sliding within the silty sand upper foundation stratum immediately underlying the dam embankment. Only a limited number of SPT tests are available within this material, so the paucity of useful penetration data is a major source of uncertainty here.

Based on the 2 SPT tests in these upper foundation silty sands on the upstream side, and re-processing these using the relationships and procedures presented in Appendix C, the best estimate mean value of $N_{1,60,CS}$ for the upstream side upper foundation silty sands was found to be $\overline{N_{1,60,CS}} \approx 6.5$ blows/ft. Variance of $\overline{N_{1,60,CS}}$ was estimated primarily on the basis of the perceived uncertainties associated with the (1) the limited number of blowcounts from within the failure zone, and (2) the somewhat higher average values of $N_{1,60,CS}$ in these same upper foundation silty sands on the downstream side. Considering these, the representation of uncertainty in the representative median value of $\overline{N_{1,60,CS}}$ was taken as $\sigma_{\overline{N}} \approx 1.8$ blows/ft.

Table A.1.1(b) shows values of representative $N_{1,60}$ or $N_{1,60,CS}$ values developed by two other teams of investigators, and variance or standard deviations in these representative values if available. Olson and Stark (2001, 2002) developed an estimated representative value of $N_{1,60} = 4.5$ blows/ft for the upstream side, but for this case history they proposed no range. Wang (2003) and Kramer (2008) jointly developed a representative value of $\overline{N_{1,60,CS}} = 6.5$ blows/ft, and their estimated standard deviation of that overall mean value for this case history was $\sigma_{\overline{N}} = 2.8$ blows/ft. Details of the development of this interpretation by Wang and Kramer are not presented. Olson and Stark (2001, 2002) made no fines adjustments, so theirs is an $N_{1,60}$ value rather than an $N_{1,60,CS}$ value. Their value would increase if it was to be adjusted for fines in these silty sand materials. Overall agreement between the three independent assessments of representative $\overline{N_{1,60,CS}}$ values is excellent, and variance or uncertainty in $\overline{N_{1,60,CS}}$ appears to be moderate.

A.6.9 Additional Indices from the Back-Analyses

A number of additional results, and indices, can be extracted from the analyses performed. Some of these are useful in developing some of the over-arching relationships and figures presented in the main text of this report. These values are presented in Table A.6.2.

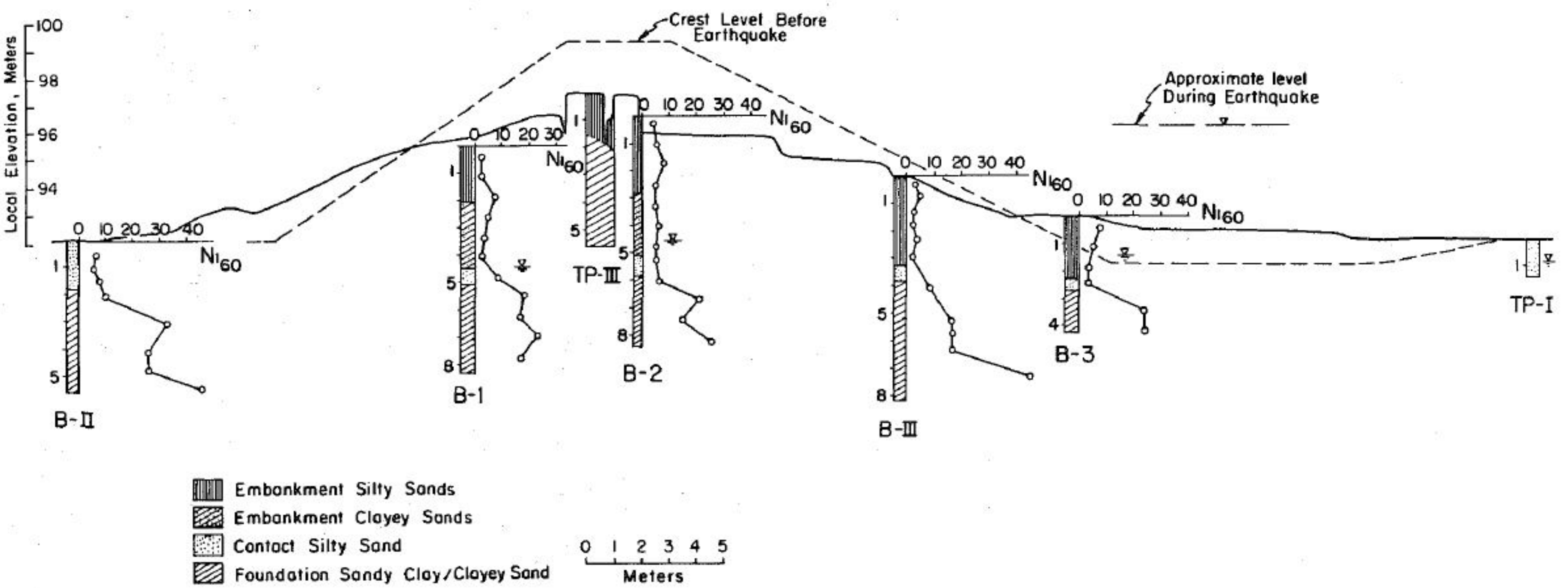

Figure A.6.8: Post-failure cross-section of La Marquesa Dam showing the locations and results of standard penetration tests (de Alba et al., 1987).

Table A.6.1: Representative values for the La Marquesa Dam upstream slope failure case history of: (a) post-liquefaction strength (S_r), (b) initial vertical effective stress (σ_{vo}'), and (c) $N_{1,60,CS}$ developed by various investigation teams, and estimates of variance in each of these indices when available.

(a) Post-Liquefaction Strength:	
Seed and Harder (1990	$S_r \approx 200$ psf(1)
Olson (2001) and Olson and Stark (2002)	$S_r \approx 104$ psf(2)
Wang (2003) and Kramer (2008)	N/A
This Study	$\overline{S_r}$ = 103 psf and $\sigma_{\overline{S}}$ = 31 psf
(b) Representative $N_{1,60}$ or $N_{1,60,CS}$ Value:	
Olson (2001) and Olson and Stark (2002)	$N_{1,60}$ = 4.5 bpf
Wang (2003) and Kramer (2008)	$\overline{N_{1,60,CS}}$ = 6.5 bpf, and $\sigma_{\overline{N}}$ = 2.8 bpf
This Study	$\overline{N_{1,60,CS}}$ = 6.5 bpf, and $\sigma_{\overline{N}}$ = 1.8 bpf
(c) Representative Initial Vertical Effective Stress:	
Olson (2001) and Olson and Stark (2002)	Average $\sigma_{vo}' \approx 960$ psf, with no range provided.
Wang (2003) and Kramer (2008)	Value of $\sigma_{vo}' \approx 1{,}682$ psf is poorly based, and so is not very useful as a basis for comparison. (See Section 2.3.8.1(b) and Table 2.3)
This Study	$\overline{\sigma'_{vo}}$ = 981 psf, and $\sigma_{\overline{\sigma}}$ = 134 psf

[1] This value of S_r was increased to judgmentally incorporate cyclic inertial effects.

[2] See Section A.6.6 for an explanation of this value as presented.

Table A.6.2: Additional results and indices from the analyses of the La Marquesa Dam upstream slope failure case history.

Maximum distance traveled by the center of gravity of the overall failure mass	15.8 ft.
Initial post-liquefaction Factor of Safety prior to displacement initiation, and based on best estimate value of S_r	FS = 0.50
Final post-liquefaction Factor of Safety at final (residual) post-failure geometry, and based on best estimate value of S_r	FS = 1.81

A.7 La Marquesa Dam Downstream Slope (Chile; 1985)

A.7.1 Brief Summary of Case History Characteristics

Name of Structure	La Marquesa Dam, Downstream Slope
Location of Structure	Chile
Type of Structure	Zoned Earthen Dam
Date of Failure	March 3, 1985
Nature of Failure	Seismic, During 1985 Central Chilean Earthquake (M_S = 7.8)
Approx. Maximum Slope Height	26 ft. (D/S side)

A.7.2 Introduction and Description of Failure

The La Marquesa Dam suffered liquefaction-induced slope failures on both its upstream side and its downstream side as a result of the Central Chilean earthquake of March 3, 1985 (M_S = 7.8), and was investigated by de Alba et al. (1987, 1988). This Appendix, Section A.7, will deal primarily with the downstream side failure, though both failures are somewhat interactive with each other. The previous Appendix Section A.6 dealt primarily with the upstream side slope failure, but it also presented a large amount of information, discussion, and figures pertinent to both the upstream and downstream slope failures, and an effort will be made to minimize repetition here.

A.7.3 Initial Yield Stress Analyses

Appendix A.6, Figures A.6.2(a) and A.6.3(a) show the cross-sections used for back-analyses of the post-liquefaction initial yield strength $S_{r,yield}$ that would be required within the liquefied upstream and downstream shell materials to produce a calculated Factor of Safety equal to 1.0. This is not the actual post-liquefaction strength, but it proves to be useful in developing a number of charts and relationships for these overall studies.

As described previously in Appendix A.6, there are two different sets of potential failure surfaces in these two figures, and these correspond to “Scenario A” and “Scenario B”. The central core section of the dam suffered some loss of height, as shown in Figures A.6.1 and A.6.8 from de Alba et al. (1987), and it spread a bit as well becoming a bit wider near its base. As shown in Figure A.6.8, a longitudinal crack occurred roughly along the centerline of the crest, and there was some lateral opening (separation) as well as some shear displacement across this crest crack. There were significantly greater vertical displacements of the two adjacent shell zones, leaving the core (even with its slightly reduced height) protruding upwards like a horst between the two adjacent down-dropped shell zones.

There were two sets of potential failure mechanisms that could potentially explain these features, and the overall observed post-failure geometries of Figures A.6.1 and A.6.6. The first

(Scenario A) involves sliding primarily along the interface between the core zone and the adjacent shell zones, as shown in Figure A.6.2, with some lateral bulging of the core as the level of confinement provided by the adjacent shells reduced somewhat. The second (Scenario B) involves shearing through the lower portions of the core zone, producing both the observed crest settlements of the top of the core zone and also the minor lateral increase in core width. This second Scenario B also serves to directly explain the observed crest crack, and provides a useful explanation for the observed differential vertical displacements across this longitudinal crest crack as well. It was judged that Scenario B provided a better overall explanation of the observed movements, but that Scenario A could not be completely discounted. Accordingly, both scenarios were modeled and analyzed. Modeling of strengths and unit eights, etc. was described previously in Appendix A.6.

Based on the cross-sections shown in Figures A.6.2(a) and A.6.3(a), and the properties and parameters described previously, the best-estimate value of $S_{r,yield}$ for the downstream side failure for Scenario A (Figure A.6.2(a)) was 303 lbs/ft^2, and the best-estimate value for Scenario B (Figure A.6.3(a)) was 324 lbs/ft^2. It was judged that Scenario B was more likely to have occurred than Scenario A, because it appears to better explain the overall observed post-failure geometry and cross-section and geometry details. Accordingly, a weighted average value of $S_{r,yield}$ = 317 lbs/ft^2 was then selected as the overall best estimate value.

Parameters were next varied, as described previously, and alternate potential failure surfaces were also examined for both Scenarios A and B, including failure surfaces passing within the saturated lower portions of the upstream side embankment shell zone. Again weighting the results in favor of Scenario B, it was judged that a reasonable range was $S_{r,yield} \approx$ 245 to 394 lbs/ft^2.

Olson (2001) was the only other investigator who also performed back-analyses to determine $S_{r,yield}$. Failure surfaces analyzed differed somewhat, and so did some of the parameters and other modeling assumptions. Olson reported a best estimate value of $S_{r,yield} \approx$ 12.9 kPa (269 lbs/ft^2), and a range of $S_{r,yield} \approx$ 7.7 to 15.6 kPa (161 to 326 lbs/ft^2).

A.7.4 Residual Strength Analyses Based on Residual Geometry

The calculation of the "apparent" post-liquefaction strength ($S_{r,resid/geom}$) required to produce a calculated Factor of Safety equal to 1.0 based on residual geometry is illustrated in the previous Appendix A.6, Figures A.6.2(b) and A.6.3(b), again representing Scenarios A and B. Modeling parameters and details are as previously described in the preceding sections.

Based on the cross-sections shown in Figures A.6.2(b) and A.6.3(b), and the properties and parameters described above, the best-estimate value of $S_{r,resid/geom}$ for failure on the downstream side based on Scenario A (Figure A.6.2(b)) was 151 lbs/ft^2, and the best-estimate value for Scenario B (Figure A.6.3(b)) was 165 lbs/ft^2. It was again judged that Scenario B was more likely to have occurred than Scenario A, because it appears to better explain the overall observed post-failure geometry and cross-section and geometry details. Accordingly, a weighted average value of $S_{r,resid/geom}$ = 160 lbs/ft^2 was then selected as the overall best estimate value.

Parameters were next varied, as described previously, and alternate potential failure surfaces were also examined for both Scenarios A and B, including failure surfaces passing within the saturated lower portions of the upstream side embankment shell zone. Again weighting the results in favor of Scenario B, it was judged that a reasonable range was $S_{r,resid/geom} \approx 109$ to 214 lbs/ft^2.

Olson (2001) also performed back-analyses to determine $S_{r,yield}$. Failure surfaces analyzed again differed somewhat, and so did some of the parameters and other modeling assumptions. Olson reported a best estimate value of $S_{r,resid/geom} \approx 5.3$ kPa (111 lbs/ft^2) , and a range of $S_{r,resid/geom} \approx 2.2$ to 9.8 kPa (46 to 205 lbs/ft^2).

A.7.5 Incremental Momentum Back-Analyses and Overall Estimates of S_r

Incremental momentum back-analyses were performed using the same sets of properties and geometries (including failure surfaces and phreatic surfaces) as described in the previous sections. Two sets of analyses were again performed, for Scenario A and Scenario B.

Appendix A.6, Figures A.6.4, A.6.5, and A.6.7 show the best-estimate progressive incremental momentum analysis for Scenarios A and B, showing the five stages of geometry evolution modeled as the failure proceeds. The resulting best estimate value of post-liquefaction strength for Scenario A was $S_r = 203$ lbs/ft^2, and the best estimate for Scenario B was $S_r = 215$ lbs/ft^2.

Because Scenario B is judged to better explain the full details of the observed field failure, the overall best estimate value of post-liquefaction strength based on these incremental momentum back-analyses was weighted in favor of Scenario B (and Figures A.6.5 and A.6.7, and the resulting overall best estimate value is $S_r = 211$ lbs/ft^2.

Parameter sensitivity analyses, including modeling of additional potential failure surfaces considered to be "reasonable/feasible" were then performed to investigate the overall range of post-liquefactions strength values. This range was found to be $S_r = 129$ to 299 lbs/ft^2. This was judged to represent approximately +/- 1.5 standard deviations. This range of variance is not symmetrical about the best estimate value, so minor further adjustments were made to produce a representative estimate of S_r suitable for regression analyses.

Overall, based on an assumed normal distribution, it was judged that the (mean and median) best estimate of post-liquefaction strength for this downstream failure case history was judged to be

$$\overline{S_r} = 214 \text{ lbs/ft}^2$$

and that the best estimate of standard deviation of mean overall post-liquefaction strength is

$$\sigma_{\bar{S}} = 57 \text{ lbs/ft}^2$$

The La Marquesa Dam upstream slope failure case history has been back-analyzed by a number of previous investigators, but not with back-analysis methods that reasonably accurately incorporate momentum effects. Seed and Harder (1990) reported a value of $S_r \approx 400$ lbs/ft^2, based on analyses that only approximately accounted for momentum effects, and their reported value included an additional increase in S_r to attempt on a judgmental basis to incorporate cyclic inertial effects. Olson (2001) and Olson and Stark (2002) did not apply their "kinetics" method to this case, and so they did not independently develop an estimate of S_r that incorporated momentum effects. Similarly, Wang (2003) and Wang and Kramer (2008) did not employ their zero inertial force (ZIF) method to incorporate inertial effects in back-analyses of this failure, and so they also did not independently develop an estimate of S_r that incorporated momentum effects.

Approximate comparisons can be made to Olson and Stark's (2001, 2002) values of back-calculated values of $S_{r,yield}$ and $S_{r,resid/geom}$ by means of Equation 4.2, as shown in Tables 4.3 and 4.6, but this is not a very rigorous comparison. As shown in Tables 4.3 and 4.6, the resulting inferred value of S_r for $\xi = 0.8$ would be $S_r \approx 152$ lbs/ft^2, in fairly good agreement with these current studies. A slightly higher value of ξ might be justified by the runout characteristics of this case (see Chapter 4, and Equation 4-1).

A higher value of $S_r = 400$ lbs/ft^2 was developed by Seed and Harder (1990), but that value had a large allowance for cyclic inertial forces, and the current authors now feel that was an over-estimate.

It appears that the values calculated in these current studies are the first set of back-calculated values of post-liquefaction S_r based on analysis methods that formally incorporate momentum effects.

Finally, it should be noted that this case history is one in which (1) a liquefaction-induced slope failure produced moderate displacements and deformations, and (2) levels and duration of strong shaking were high. This is thus a case in which it may be hypothesized that the values back-calculated in these current studies, even with incorporation of momentum effects, may conservatively underestimate the actual values of S_r due to the failure to also incorporate cyclic inertial effects during strong shaking. It is not (yet) analytically possible to reliably quantify this additional potential conservatism. Seed and Harder (1990) had increased their back-estimated value of S_r to judgmentally incorporate incremental inertia effects, but the current engineering team have chosen not to make this type of further adjustment here.

A.7.6 Evaluation of Initial Effective Vertical Stress

Average initial (pre-failure) effective vertical stress was assessed for the liquefied zones of each of the failure surfaces shown in Figures A.6.2(a) and A.6.3(a) of Appendix A.6. Additional sensitivity analyses were then performed for reasonable ranges of variations in (1) the location of the phreatic surface, (2) unit weights, and (3) the precise location of the overall failure surface in order to evaluate uncertainty or variance.

The resulting best estimate of average pre-failure effective stress within the liquefied materials controlling the failure was then $\sigma_{vo}' \approx$ 1,215 lbs/ft^2, with a reasonable range of $\sigma_{vo}' \approx$ 1,011 to 1,423 lbs/ft^2. This range is slightly non-symmetric about the median value, and this range was judged by the engineering team to represent approximately ± 2 standard deviations. Overall, the best characterization of initial (pre-failure) average effective vertical stress was then taken to be represented by a mean value of

$$\overline{\sigma'_{vo}} \approx 1{,}215 \text{ lbs/ft}^2$$

and with a standard deviation of

$$\sigma_{\overline{\sigma}} \approx 103 \text{ lbs/ft}^2$$

An estimate of σ_{vo}' was also calculated by Olson and Stark (2001, 2002) and this is shown in Table A.1.1(c). They reported a weighted average mean value of $\sigma_{vo}' \approx$ 1,073 lbs/ft^2, in good general agreement with these current studies. Average initial vertical effective stresses were not directly reported by Wang (2003) and Kramer (2008), but they were published more recently in the publication by Kramer and Wang (2015). As discussed in Section 2.3.8.1(b)-(iii), Wang (2003) did not perform any independent analyses to assess σ_{vo}' for his 22 "secondary" cases, and this is one of those cases. Instead, he compiled values of S_r from multiple previous investigators, and averaged these for a best estimate. He also compiled multiple values of S_r/σ_{vo}' from previous investigators, and averaged these for a best estimate. He then used these two best-estimate values of "averaged" S_r and "averaged" S_r/σ_{vo}' to infer a resulting representative value of σ_{vo}'. As described in Section 2.3.8.1(b)-(iii), the resulting averaged values of S_r and S_r/σ_{vo}' were incompatible with each other for a number of Wang's "secondary" case histories, and this process produced unreasonable, and in some cases physically infeasible, values of σ_{vo}' for a number of case histories. Accordingly, Wang's value of σ_{vo}' = 1,850 lbs/ft^2 is not considered a useful check here. Agreement between Olson's value, which is well-documented, and the value developed in these current studies is very good, especially considering Olson's apparent propensity to often model and analyze slightly shallower failure surfaces than those considered best estimates in this current study.

A.7.7 Evaluation of $N_{1,60,CS}$

Figure A.6.8 of Appendix A.6 showed the locations of post-failure SPT borings and SPT tests performed to investigate the failure. Based on the available data and information, it appears most likely that the upstream and downstream slope failures both occurred due to liquefaction-induced sliding within the silty sand upper foundation stratum immediately underlying the dam embankment. Only a limited number of SPT tests are available within this material, so the paucity of useful penetration data is a major source of uncertainty here.

Based on the six SPT tests in these upper foundation silty sands on the downstream side, and re-processed using the relationships and procedures presented in Appendix C, the best estimate mean value of $N_{1,60,CS}$ for the downstream side upper foundation silty sands was found to be $\overline{N_{1,60,CS}} \approx 10.5$ blows/ft. Variance of $\overline{N_{1,60,CS}}$ was estimated primarily on the basis of the perceived uncertainties associated with the (1) the limited number of blowcounts from within the failure zone, and (2) the somewhat higher average values of $N_{1,60,CS}$ in these same upper foundation silty sands on the upstream side. Considering these, the representation of uncertainty in the representative median value of $\overline{N_{1,60,CS}}$ was taken as $\sigma_{\overline{N}} \approx 2.2$ blows/ft.

Table A.7.1(b) shows values of representative $N_{1,60}$ or $N_{1,60,CS}$ values developed by two other teams of investigators, and variance or standard deviations in these representative values if available. Olson and Stark (2001, 2002) developed an estimated representative value of $N_{1,60} = 9.0$ blows/ft for the upstream side, but they proposed no range for this case history. Wang (2003) and Kramer (2008) jointly developed a representative value of $\overline{N_{1,60,CS}} = 9.9$ blows/ft, and their estimated standard deviation of that overall mean value for this case history was $\sigma_{\overline{N}} = 3.0$ blows/ft. Details of the development of this interpretation by Wang and Kramer are not presented. Olson and Stark (2001, 2002) made no fines adjustments, so theirs is an $N_{1,60}$ value rather than an $N_{1,60,CS}$ value. Their value would increase if it was to be adjusted for fines in these silty sand materials. Overall agreement between the three independent assessments of representative $\overline{N_{1,60,CS}}$ values is excellent, and variance or uncertainty in $\overline{N_{1,60,CS}}$ appears to be moderate.

A.7.8 Additional Indices from the Back-Analyses

A number of additional results, and indices, can be extracted from the analyses performed. Some of these are useful in developing some of the over-arching relationships and figures presented in the main text of this report. These values are presented in Table A.7.2.

Table A.7.1: Representative values for the La Marquesa Dam downstream slope failure case history of: (a) post-liquefaction strength (S_r), (b) initial vertical effective stress (σ_{vo}'), and (c) $N_{1,60,CS}$ developed by various investigation teams, and estimates of variance in each of these indices when available.

(a) Post-Liquefaction Strength:	
Seed and Harder (1990)	$S_r \approx 400$ psf$^{(1)}$
Olson (2001) and Olson and Stark (2002)	$S_r \approx 152$ psf$^{(2)}$
Wang (2003) and Kramer (2008)	N/A
This Study	$\overline{S_r} = 214$ psf and $\sigma_{\overline{S}} = 57$ psf
(b) Representative $N_{1,60}$ or $N_{1,60,CS}$ Value:	
Olson (2001) and Olson and Stark (2002)	$N_{1,60} = 9.0$ bpf
Wang (2003) and Kramer (2008)	$\overline{N_{1,60,CS}} = 9.9$ bpf, and $\sigma_{\overline{N}} = 3.0$ bpf
This Study	$\overline{N_{1,60,CS}} = 10.5$ bpf, and $\sigma_{\overline{N}} = 2.2$ bpf
(c) Representative Initial Vertical Effective Stress:	
Olson (2001) and Olson and Stark (2002)	Average $\sigma_{vo}' \approx 1{,}063$ psf, no range provided.
Wang (2003) and Kramer (2008)	Value of $\sigma_{vo}' \approx 1{,}850$ psf is poorly based, and so is not very useful as a basis for comparison. (See Section 2.3.8.1(b) and Table 2.3)
This Study	$\overline{\sigma'_{vo}} = 1{,}215$ psf, and $\sigma_{\overline{\sigma}} = 103$ psf

[1] This value of S_r was increased to judgmentally incorporate cyclic inertial effects.

[2] See Section A.7.5 for an explanation of this value as presented.

Table A.7.2: Additional results and indices from the analyses of the La Marquesa Dam downstream slope failure case history.

Maximum distance traveled by the center of gravity of the overall failure mass	6.1 ft.
Initial post-liquefaction Factor of Safety prior to displacement initiation, and based on best estimate value of S_r	FS = 0.73
Final post-liquefaction Factor of Safety at final (residual) post-failure geometry, and based on best estimate value of S_r	FS = 1.51

A.8 La Palma Dam Upstream Slope (Chile; 1985)

A.8.1 Brief Summary of Case History Characteristics

Name of Structure	La Palma Dam, Upstream Slope
Location of Structure	Chile
Type of Structure	Zoned Earthen Dam
Date of Failure	March 3, 1985
Nature of Failure	Seismic, During 1985 Central Chilean Earthquake (M_S = 7.8)
Approx. Maximum Slope Height	25.6 ft. (U/S side)

A.8.2 Introduction and Description of Failure

The La Palma Dam suffered a liquefaction-induced slope failure on its upstream side as a result of the Central Chilean earthquake of March 3, 1985 (M_S = 7.8), and was investigated by de Alba et al. (1987, 1988).

The dam is located near the Chilean coast, approximately 75 km northwest of Santiago, and approximately 55 km north of the La Marquesa Dam which was discussed in Appendices A.7 and A.8. Peak horizontal ground surface accelerations recorded in the general vicinity of the dam during the earthquake were on the order of approximately 0.43 to 0.65 g. (de Alba et al., 1987)

As shown in Figure A.8.1 (from de Alba et al., 1987), the dam suffered liquefaction-induced failure on the upstream side. Maximum displacements were approximately 6 to 8 feet vertically at the crest and upper face, and approximately 17 feet horizontally at the upstream toe.

A.8.3 Geology and Site Conditions

Figure A.8.1 shows conditions both before and after the failure. Borings performed before the earthquake, and additional borings performed after the event, showed the dam foundation to consist primarily of sandy clays and clayey sands, but with shallow surficial deposits of silty sand and sandy silt underlying the upstream two-thirds of the dam. Of particular interest is the relatively thin layer of silty sand Figure A.8.1, as it is primarily within this stratum that liquefaction-induced sliding appears to have occurred. This liquefiable stratum extends from beneath the upstream toe to a point approximately mid-way between the dam's centerline and the downstream toe, but liquefaction appears to have occurred only beneath the upstream side of the dam because on the downstream side this layer was not saturated. The deeper underlying foundation soils were not very much better materials, in terms of material character and SPT penetration resistances, but they were generally somewhat better materials, and it was the judgment of the field investigation that the sliding had occurred primarily within the relatively thin silty sand stratum beneath the upstream side dam embankment shell zone.

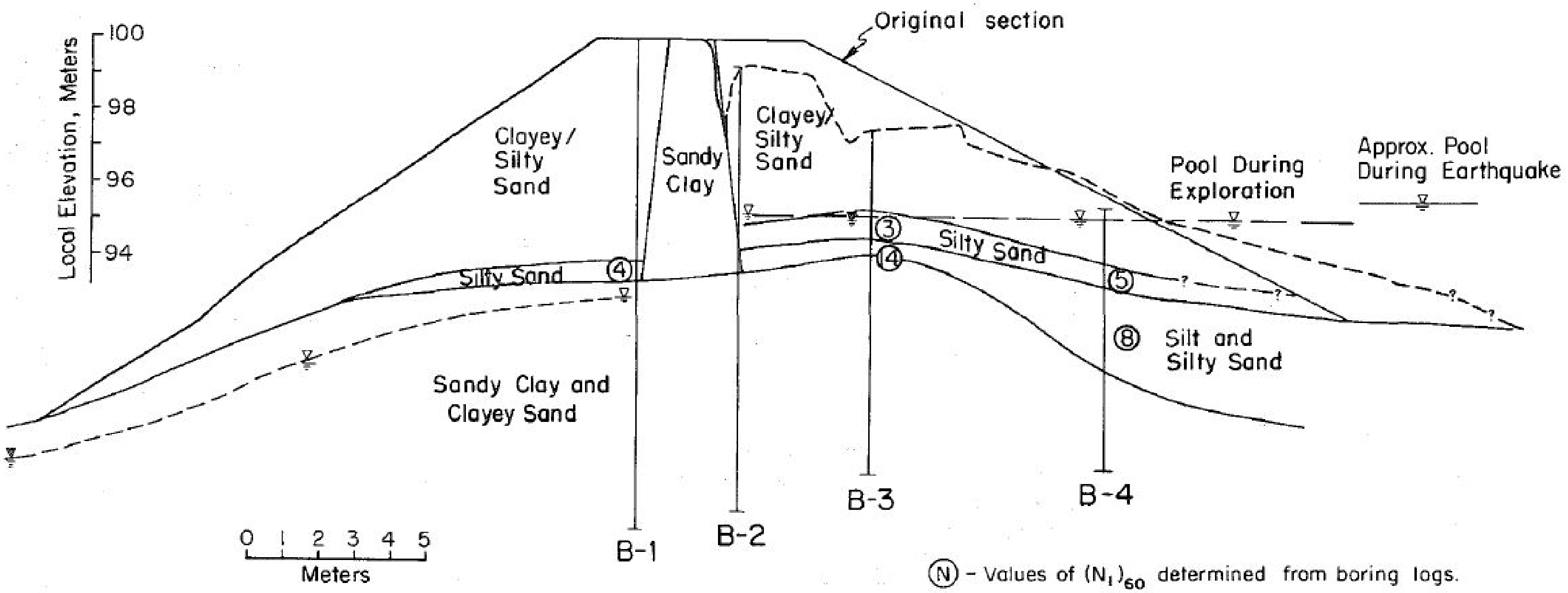

Figure A.8.1: Pre-failure and post-failure cross-sections of the La Palma Dam (from de Alba et. al, 1987).

The dam embankment was constructed with materials excavated locally from the reservoir floor and the abutments, and these consisted primarily of clayey sands and silty sands in the upstream and downstream shell zones, and of sandy clay in the central core zone. A key trench was excavated through the upper silty sand and silt upper foundation strata beneath the core, and this was backfilled with sandy clay fill to key into the deeper sandy clay and clayey sand foundation units at slightly greater depth. Details of embankment fill placement and compaction are not clear, but based on a suite of four post-failure SPT borings, it appears that the embankment fill materials were moderately compacted.

A.8.4 Initial Yield Stress Analyses

Figure A.8.2 shows the cross-sections used for back-analyses of the pre-failure and post-failure conditions associated with calculation of (1) initial yield strength ($S_{r,yield}$) and (2) post-liquefaction residual strength based on final residual geometry ($S_{r,resid/geom}$). Figure A.8.2(a) shows the cross section used for calculation of the value of $S_{r,yield}$ that would be required within the liquefied upstream shell materials to produce a calculated Factor of Safety equal to 1.0. This is not the actual post-liquefaction strength, but it proves to be useful in developing a number of charts and relationships for these overall studies.

Shear strengths of non-saturated silty sand and clayey sand materials in the embankment shells (above the phreatic surface), and above the thin stratum of silty sand foundation material within which the liquefaction-induced sliding appears to have occurred, were modeled as frictional, with a best estimate value of $Ø' = 33°$. This was then varied between 30 to 36° in subsequent sensitivity analyses. Shear strengths in the clayey sand core zone were modeled as cohesive, with residual (large displacement) values of $S_{u,r}/P \approx 0.09$ based on very limited data and information. This was then varied between 0.06 and 0.12 in subsequent sensitivity studies. Shear strengths within the relatively thin stratum of silty sand beneath the base of the upstream shell were modeled with post-liquefaction strength $S_{r,yield}$, and these back-analyses were performed in order to determine this value. Shear strengths in the remaining foundation soils beneath the upper silty sand foundation stratum were not modeled as these did not participate in the failure observed.

Unit weights for the non-saturated shell zones were modeled as γ_m = 120 lbs/ft^3, and the saturated silty sands of the lower upstream shell and the upper foundation stratum were modeled as γ_s = 125 lbs/ft^3. These were varied by +/- 5 lbs/ft^3 in subsequent sensitivity studies. Unit weights of the silty clay core materials were modeled as γ_s = 120 lbs/ft^3 +/- 5 lbs/ft^3.

Based on the cross-section shown in Figures A.8.2(a), and the properties and parameters described above, the best-estimate value of $S_{r,yield}$ was 201 lbs/ft^2. Parameters were next varied, as described above, and the details as to precise depth and shape of the failure surface were also varied, to perform parametric sensitivity analyses. Based on ranges of properties and failure surfaces considered reasonable, the likely range of $S_{r,yield}$ was found to be $S_{r,yield} \approx$ 165 to 238 lbs/ft^2.

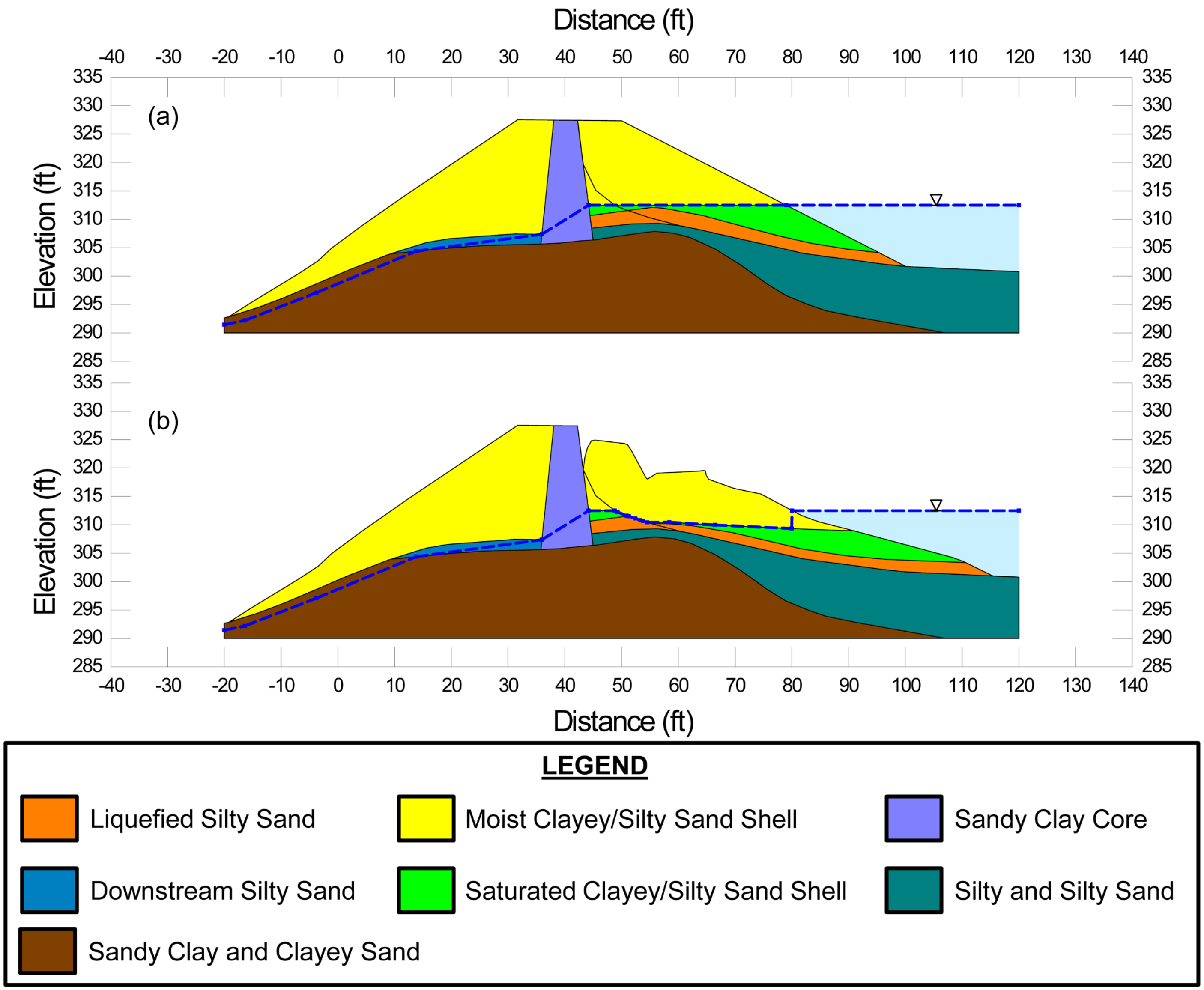

Figure A.8.2: La Palma Dam: (a) pre-failure geometry and failure surface for initial yield stress analyses, and (b) post-failure geometry and failure surface for post-failure residual geometry analyses.

Olson (2001) was the only other investigator who also performed and reported back-analyses to determine $S_{r,yield}$. Failure surfaces analyzed differed somewhat, and so did some of the parameters and other modeling assumptions. Olson reported a best estimate value of $S_{r,yield} \approx 10.1$ kPa (211 lbs/ft^2) , and a range of $S_{r,yield} \approx 9.1$ to 12.2 kPa (190 to 255 lbs/ft^2), in excellent agreement with these current studies.

A.8.5 Residual Strength Analyses Based on Residual Geometry

The calculation of the "apparent" post-liquefaction strength ($S_{r,resid/geom}$) required to produce a calculated Factor of Safety equal to 1.0 based on residual geometry is illustrated in Figure A.8.2(b). Modeling parameters and details are as previously described in the preceding sections. The resulting best-estimate value of $S_{r,resid/geom}$ was found to be $S_{r,resid/geom} = 84$ lbs/ft^2.

Parameters were next varied, as described previously, and alternate potential failure surfaces were also examined. Based on these parametric sensitivity analyses, it was judged that a reasonable range was $S_{r,resid/geom} \approx 68$ to 105 lbs/ft^2.

Olson (2001) also performed back-analyses to determine $S_{r,resid/geom}$. Failure surfaces analyzed differed slightly, and so did some of the parameters and other modeling assumptions. Olson reported a best estimate value of $S_{r,resid/geom} \approx 4.8$ kPa (100 lbs/ft^2) , and a range of $S_{r,resid/geom} \approx 2.4$ to 7.9 kPa (50 to 165 lbs/ft^2), in generally good agreement with these current studies.

A.8.6 Incremental Momentum Back-Analyses and Overall Estimates of S_r

Incremental momentum back-analyses were performed using the same sets of properties and geometries (including failure surfaces and phreatic surfaces) as described in the previous sections. Figure A.8.3 shows the best-estimate progressive incremental momentum analysis for Scenario A, showing the five stages of geometry evolution modeled as the failure proceeds, and Figure A.8.4 shows the associated best estimate calculations of (1) acceleration vs. time, (2) velocity vs. time, and (3) displacement of the overall center of gravity vs. time. The resulting best estimate value of post-liquefaction strength was $S_r = 136$ lbs/ft^2.

Parameter sensitivity analyses, including modeling of additional potential failure surfaces considered to be "reasonable/feasible" were then performed to investigate the overall range of post-liquefactions strength values. This range was found to be $S_r = 103$ to 172 lbs/ft^2. This was judged to represent approximately +/- 1.5 standard deviations. This range was nearly symmetric about the best estimate value of 136 lbs/ft^2, so no significant further adjustments were necessary.

Overall, based on an assumed normal distribution, it was judged that the (mean and median) best estimate of post-liquefaction strength for this case history is

$$\overline{S_r} = 136 \text{ lbs/ft}^2$$

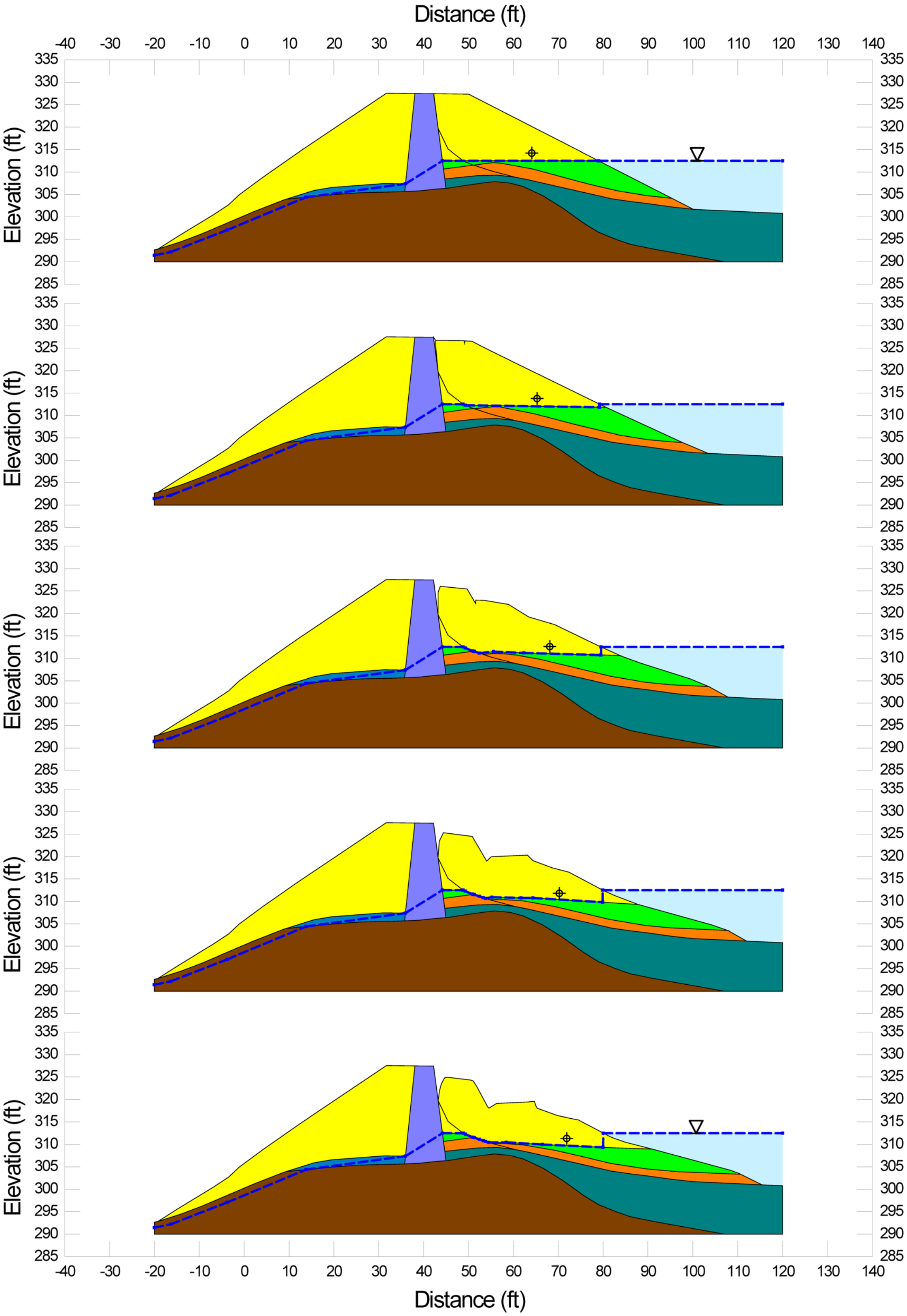

Figure A.8.3: Incremental momentum analysis of the failure of the La Palma Dam, showing progressive evolution of cross-section geometry modeled.

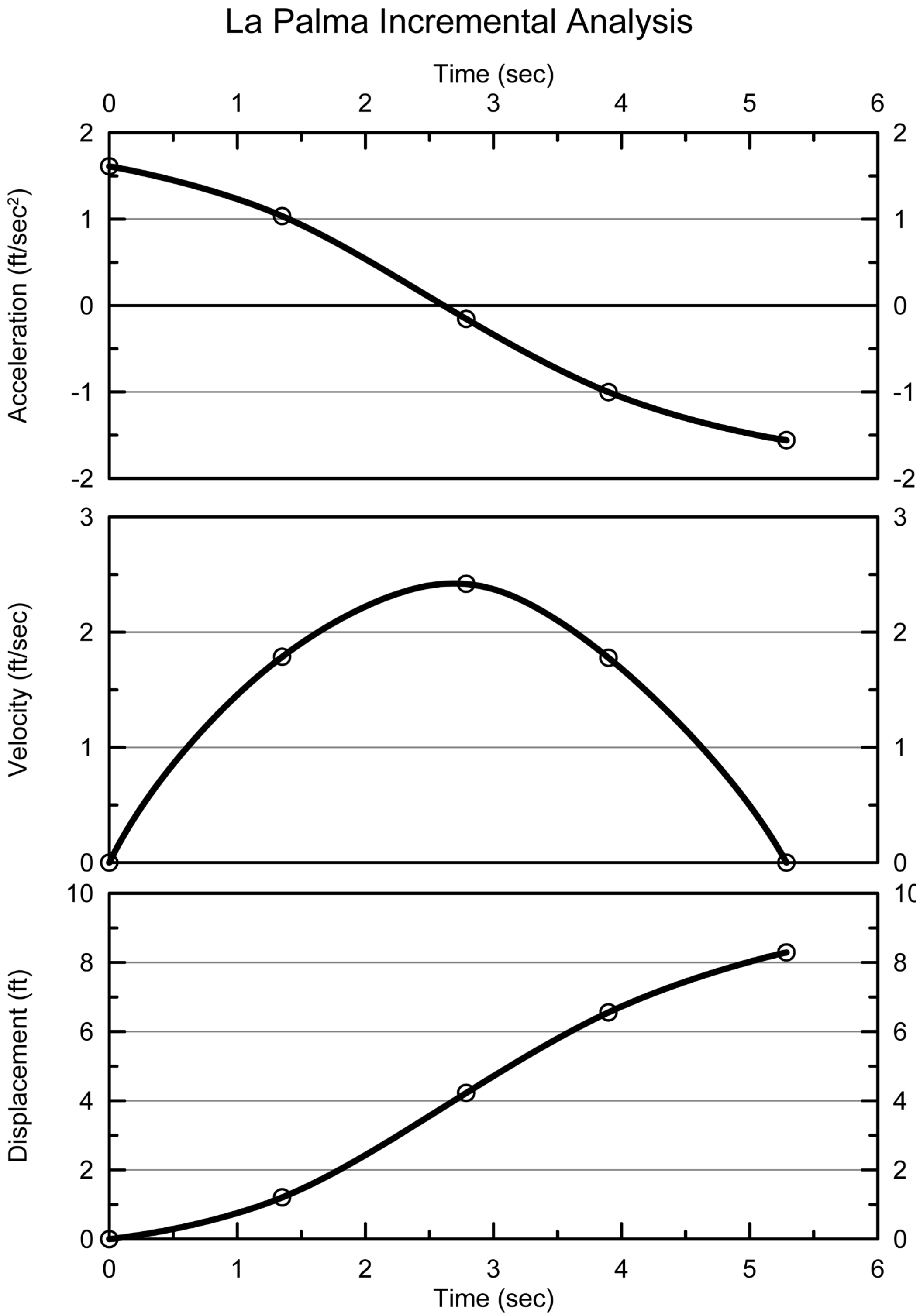

Figure A.8.4: Incremental momentum analysis of the failure of the Upstream Slope of La Palma Dam, showing progressive evolution of: (1) acceleration vs. time, (2) velocity vs. time, and (3) displacement vs. time of the overall center of gravity of the failure mass.

and that the best estimate of standard deviation of mean overall post-liquefaction strength is

$$\sigma_{\bar{S}} = 33 \text{ lbs/ft}^2$$

The La Palma Dam upstream slope failure case history has been back-analyzed by a number of previous investigators, but not with back-analysis methods that reasonably accurately incorporate momentum effects. Seed and Harder (1990) reported a value of $S_r \approx 200$ lbs/ft^2, but this value was judgmentally increased to incorporate cyclic inertial effects. Olson (2001) and Olson and Stark (2002) did not apply their "kinetics" method to this case, and so they did not independently develop an estimate of S_r that incorporated momentum effects. Olson did, however, calculate values of $S_{r,yield}$ and $S_{r,resid/geom}$ (see Sections A.8.3 and A.8.4) for this case, and those two values can be convolved to provide a better estimate of S_r. Based on Equation 4-1 (see Chapter 4), a better estimate for S_r based on calculations performed by Olson (2001) would be $S_r \approx 0.8 \text{ x } [S_{r,yield} + S_{r,resid/geom}] / 2 \approx 0.8 \text{ x } [10.1 \text{ kPa} + 4.8 \text{ kPa}] /2 \approx 6.0$ kPa (125 lbs/ft^2), and this value is more directly comparable with the values of this current study, and so it is the value presented in Table A.8.1(a). This agrees very well with these current studies. Similarly, Wang (2003) and Wang and Kramer (2008) did not employ their zero inertial force (ZIF) method to incorporate inertial effects in back-analyses of this failure, and so they also did not independently develop an estimate of S_r that incorporated momentum effects.

Approximate comparisons can be made to Olson and Stark's (2001, 2002) values of back-calculated values of $S_{r,yield}$ and $S_{r,resid/geom}$ by means of Equation 4.2, as shown in Tables 4.3 and 4.6, but this is not a very rigorous comparison.

It appears that the values calculated in these current studies are the first set of back-calculated values of post-liquefaction S_r for the La Palma Dam upstream slope failure to be based on analysis methods that directly and specifically incorporate momentum effects.

Finally, it should be noted that this case history is one in which (1) a liquefaction-induced slope failure produced moderate displacements and deformations, and (2) levels and duration of strong shaking were high. This is thus a case in which it may be hypothesized that the values back-calculated in these current studies, even with incorporation of momentum effects, may conservatively underestimate the actual values of S_r due to the failure to also incorporate cyclic inertial effects during strong shaking. It is not (yet) analytically possible to reliably quantify this additional potential conservatism. Seed and Harder (1990) had increased their back-estimated value of S_r to attempt to judgmentally incorporate cyclic inertial effects. The current engineering team has elected not to make that further adjustment in these current studies.

A.8.7 Evaluation of Initial Effective Vertical Stress

Average initial (pre-failure) effective vertical stress was assessed for the liquefied zones of the failure surfaces analyzed in the preceding Sections A.8.4 through A.8.6. Sensitivity analyses were performed for reasonable ranges of variations in (1) the location of the phreatic surface, (2) unit weights, and (3) the precise location of the overall failure surface in order to evaluate uncertainty or variance.

The resulting best estimate of average pre-failure effective stress within the liquefied materials along the failure was then $\sigma_{vo}' \approx 767$ lbs/ft^2, with a reasonable range of $\sigma_{vo}' \approx 684$ to 852 lbs/ft^2. This range is slightly non-symmetric about the median value, and this range was judged by the engineering team to represent approximately ± 2 standard deviations. Overall, the best characterization of initial (pre-failure) average effective vertical stress was then taken to be represented by a mean value of

$$\overline{\sigma'_{vo}} \approx 767 \text{ lbs/ft}^2$$

and a standard deviation of

$$\sigma_{\bar{\sigma}} \approx 42 \text{ lbs/ft}^2$$

An estimate of σ_{VO}' was also calculated by Olson and Stark (2001, 2002) and this is shown in Table A.8.1(c). They reported a weighted average mean value of $\sigma_{vo}' \approx 789$ lbs/ft^2, in excellent agreement with these current studies. Average initial vertical effective stresses were not directly reported by Wang (2003) and Kramer (2008), but they were published more recently in the publication by Kramer and Wang (2015). As discussed in Section 2.3.8.1(b)-(iii), Wang (2003) did not perform any independent analyses to assess σ_{vo}' for his 22 "secondary" cases, and this is one of those cases. Instead, he compiled values of S_r from multiple previous investigators, and averaged these for a best estimate. He also compiled multiple values of S_r/σ_{vo}' from previous investigators, and averaged these for a best estimate. He then used these two best-estimate values of S_r and S_r/σ_{vo}' to infer a resulting representative value of σ_{vo}'. As described in Section 2.3.8.1(b)-(iii), the resulting averaged values of S_r and S_r/σ_{vo}' were incompatible with each other for a number of Wang's "secondary" case histories, and this process produced unreasonable, and in some cases physically infeasible, values of σ_{vo}' for a number of case histories. Accordingly, Wang's value of $\sigma_{vo}' = 1{,}577$ is not considered a useful check here. Agreement between Olson's value, which is well-documented, and the value developed in these current studies is excellent.

A.8.8 Evaluation of $N_{1,60,CS}$

Figure A.8.5 shows the locations of post-failure SPT borings, and the results of the SPT tests performed to investigate the failure. Based on the field investigation, it appears that the upstream slope failure occurred due to liquefaction-induced sliding within the silty sand upper foundation stratum immediately underlying the dam embankment. Only a limited number of SPT tests are available within this material, so the paucity of useful penetration data is a major source of uncertainty here.

Based on the 3 SPT tests in these upper foundation silty sands on the upstream side, after re-processing these using the relationships and procedures presented in Appendix C, the best estimate mean value of $N_{1,60,CS}$ for the upstream side upper foundation silty sands was found to be $\overline{N_{1,60,CS}} \approx 5$ blows/ft. Variance of $\overline{N_{1,60,CS}}$ was estimated primarily on the basis of the perceived

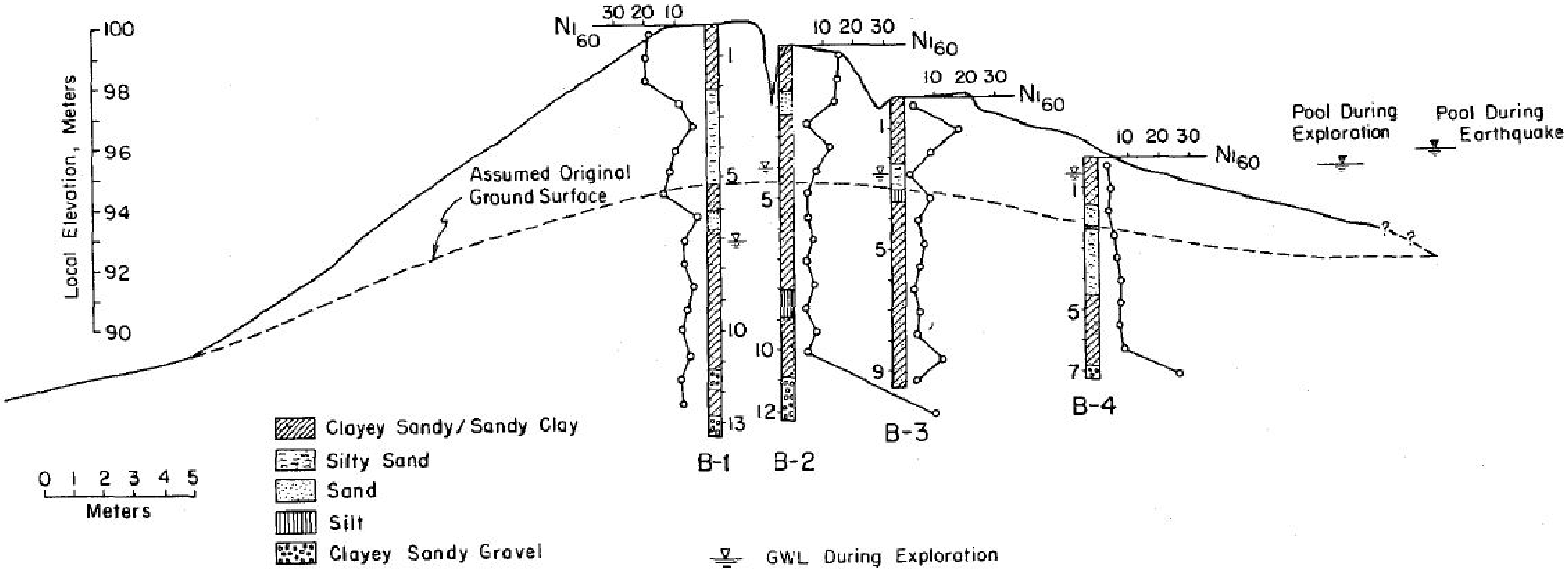

Figure A.8.5: Post-failure cross-section of La Palma Dam showing the locations and results of standard penetration tests (de Alba et al., 1987).

uncertainties associated with the limited number of blowcounts from within the failure zone. Considering this, and the observed variance among the few available data, the representation of uncertainty in the representative median value of $\overline{N_{1,60,CS}}$, based on an assumed normal distribution, was taken as $\sigma_{\overline{N}} \approx 1.2$ blows/ft.

Table A.8.1(b) shows values of representative $N_{1,60}$ or $N_{1,60,CS}$ values developed by three other teams of investigators, and variance or standard deviations in these representative values if available. Olson and Stark (2001, 2002) developed an estimated representative value of $N_{1,60} = 4$ blows/ft, but for this case history they proposed no range. Wang (2003) and Kramer (2008) jointly developed a representative value of $\overline{N_{1,60,CS}} = 4.2$ blows/ft, and their estimated standard deviation of that overall mean value for this case history was $\sigma_{\overline{N}} = 1.8$ blows/ft. Olson and Stark (2001, 2002) made no fines adjustments, so theirs is an $N_{1,60}$ value rather than an $N_{1,60,CS}$ value. Their value would increase if it was to be adjusted for fines in these silty sand materials. Overall agreement between the three independent assessments of representative $\overline{N_{1,60,CS}}$ values is excellent, and variance or uncertainty in $\overline{N_{1,60,CS}}$ appears to be relatively low.

A.8.9 Additional Indices from the Back-Analyses

A number of additional results, and indices, can be extracted from the analyses performed. Some of these are useful in developing some of the over-arching relationships and figures presented in the main text of this report. These values are presented in Table A.8.2.

Table A.8.1: Representative values for the La Palma Dam upstream slope failure case history of: (a) post-liquefaction strength (S_r), (b) initial vertical effective stress (σ_{vo}'), and (c) $N_{1,60,CS}$ developed by various investigation teams, and estimates of variance in each of these indices when available.

(a) Post-Liquefaction Strength:	
Seed and Harder (1990	$S_r \approx 200$ psf$^{(1)}$
Olson (2001) and Olson and Stark (2002)	$S_r \approx 124$ psf$^{(2)}$
Wang (2003) and Kramer (2008)	N/A
This Study	$\overline{S_r} = 136$ psf and $\sigma_{\overline{S}} = 231$ psf
(b) Representative $N_{1,60}$ or $N_{1,60,CS}$ Value:	
Seed and Harder (1990)	$N_{1,60,CS} = 4$ bpf
Olson (2001) and Olson and Stark (2002)	$N_{1,60} = 3.5$ bpf
Wang (2003) and Kramer (2008)	$\overline{N_{1,60,CS}} = 4.2$ bpf, and $\sigma_{\overline{N}} = 1.8$ bpf
This Study	$\overline{N_{1,60,CS}} = 5$ bpf, and $\sigma_{\overline{N}} = 1.2$ bpf
(c) Representative Initial Vertical Effective Stress:	
Olson (2001) and Olson and Stark (2002)	Average $\sigma_{vo}' \approx 789$ psf, with no range provided.
Wang (2003) and Kramer (2008)	Value of $\sigma_{vo}' \approx 1{,}577$ psf is poorly based, and so is not very useful as a basis for comparison. (See Section 2.3.8.1(b) and Table 2.3)
This Study	$\overline{\sigma'_{vo}} = 767$ psf, and $\sigma_{\overline{\sigma}} = 42$ psf

[1] This value of S_r was increased to judgmentally incorporate cyclic inertial effects.

[2] See Section A.8.6 for an explanation of this value as presented.

Table A.8.2: Additional results and indices from the analyses of the La Palma Dam upstream slope failure case history.

Maximum distance traveled by the center of gravity of the overall failure mass	8.3 ft.
Initial post-liquefaction Factor of Safety prior to displacement initiation, and based on best estimate value of S_r	FS = 0.78
Final post-liquefaction Factor of Safety at final (residual) post-failure geometry, and based on best estimate value of S_r	FS = 1.25

A.9 Lake Ackerman Highway Embankment (Michigan, USA; 1987)

A.9.1 Brief Summary of Case History Characteristics

Name of Structure	Lake Ackerman Highway Embankment
Location of Structure	Michigan, USA
Type of Structure	Elevated Highway Embankment Fill
Date of Failure	July 24, 1987
Nature of Failure	Cyclic, due to excitation by large geophysical field exploration shakers
Approx. Maximum Slope Height	25.6 ft.

A.9.2 Introduction and Description of Failure

The liquefaction-induced flow failure of a section of Highway 24 in Michigan's upper peninsula was highly unusual inasmuch as the failure was triggered by shaking from a line of six massive (22-ton) trucks producing coordinated shaking for purposes of deep geophysical investigations (a seismic refraction survey). The six trucks also provided some extra weight (mass) loading the embankment, but it was primarily the strong vibratory shaking that triggered the failure.

Figure A.9.1 is a plan view of the highway embankment showing (a) the locations of the six trucks, and (b) the approximate extent of the failure. Figure A.9.2 presents a photograph taken after the failure, showing (a) the slope failure, and (b) four of the six shaking trucks (one is upright, and the other three are overturned at the left edge this photograph).

The drivers of the trucks all survived, and they provided useful eyewitness observations.

This failure was investigated by Hryciw et al. (1990). The highway embankment was constructed over the northern edge of Lake Ackerman, as shown in Figure A.9.1, in the mid-1950's. Approximately 1.2 m of weak lakebed peaty soils were removed prior to placement of the embankment fill. The embankment fill materials were clean, medium to fine sand with subrounded particles that was borrowed from nearby road cuts. Figure A.9.3 shows the gradation of this material.

Figure A.9.4 shows a reconstructed cross-section through the failure zone (Hryciw et al., 1990), showing the excavation of lakebed peats and muds, and the pre-failure and post-failure embankment cross-sections.

The embankment fill sand was initially end-dumped into the lake, resulting in a very loose and saturated fine sand fill. Fill subsequently placed above the lake water level was reportedly moderately compacted, but the method of compaction was not described. It is the loose, saturated, end-dumped materials that are of primary interest for these back-analyses. The unit weight of

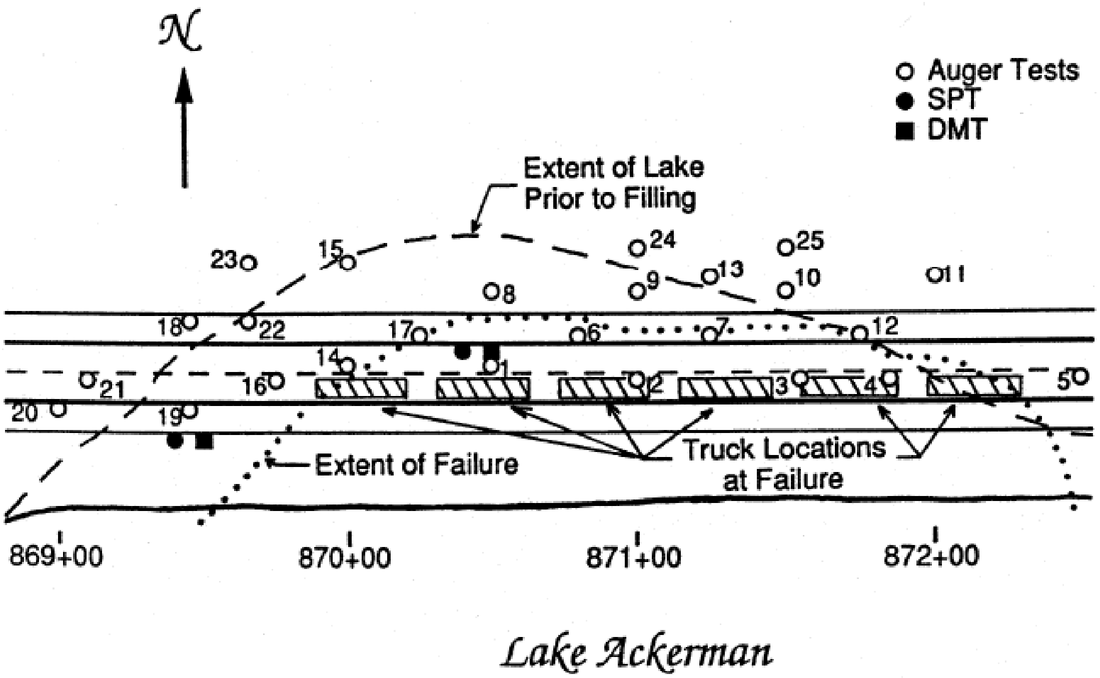

Figure A.9.1: Plan view of the Lake Ackerman slope failure showing (a) the extent of the failure, and (b) the locations of the six geophysical investigation trucks prior to the failure (Hryciw et al., 1990).

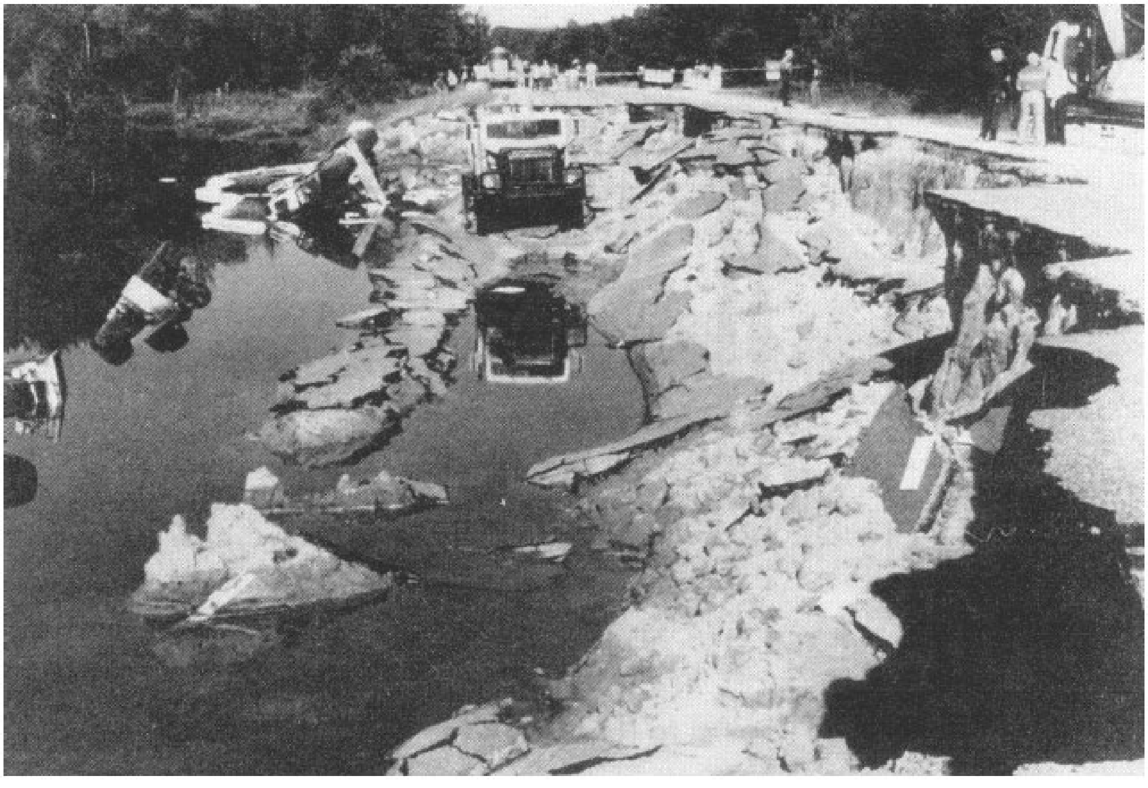

Figure A.9.2: Photograph showing the failed embankment (looking towards the west), showing crest loss and the positions of four of the large geophysical exploration trucks. (Hryciw et al., 1990).

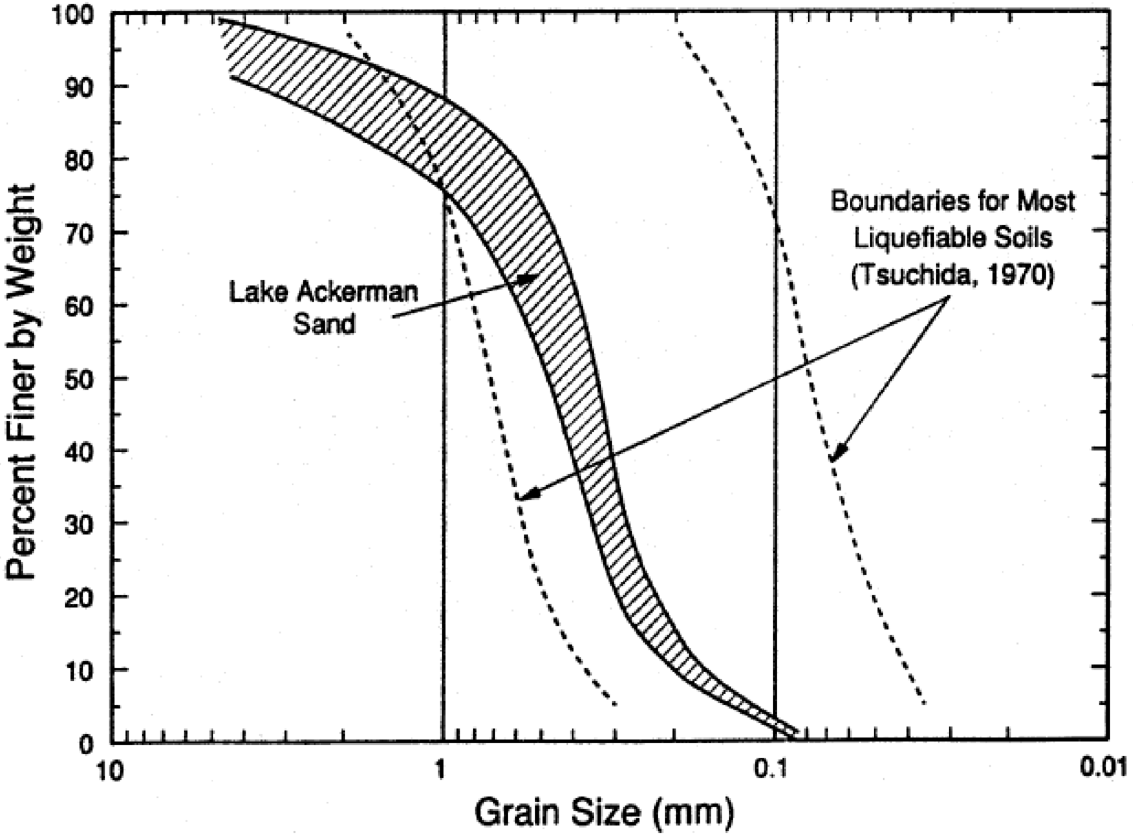

Figure A.9.3: Grain size distribution of the sand used for the Lake Ackerman Highway embankment fill (Hryciw et al., 1990)

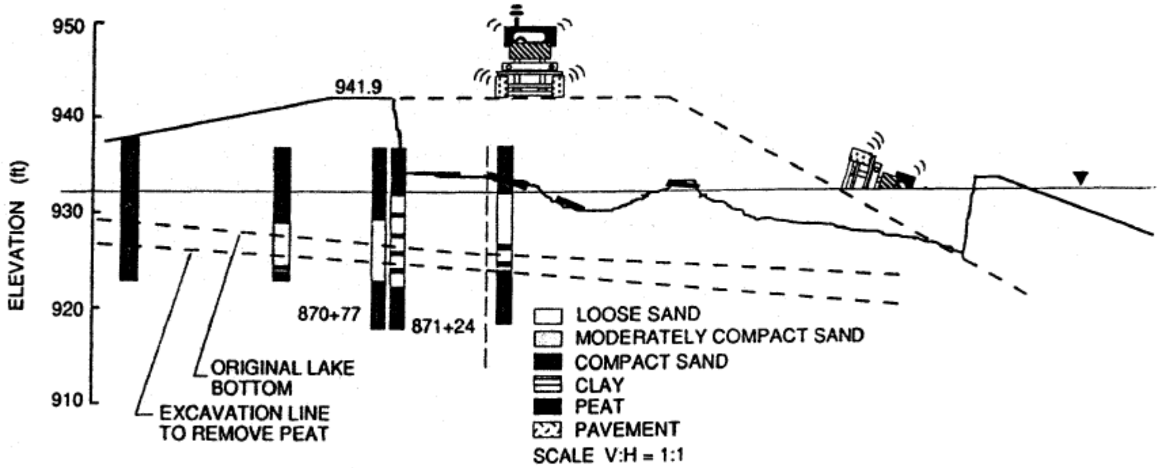

Figure A.9.4: Reconstructed pre-failure and post-failure cross sections (Hryciw et al., 1990) this sand was approximately 19.3 kN/m^3, and Hryciw et al. (1990) estimated the relative density to be as low as approximately 0%.

The presence of the six large trucks, nose-to-tail in a line, added weight to the top of the embankment, but it is felt that the shaking of these six trucks (which could produce high frequency, synchronized shaking at controlled frequencies) was the main cause of the failure. Hryciw at al. (1990) estimated that these trucks produced a high frequency cyclic stress ratio of approximately CSR = 0.12 in the loose, saturated sands at the base of the embankment fill, and this agrees well with studies by Sully et al. (1995). This would have be amply sufficient to trigger liquefaction in these loose, saturated sandy soils.

A.9.3 Initial Yield Strength Analyses

Figure A.9.5 shows the reconstructed pre-failure and post-failure cross-sections used in these current studies. These are based on the cross-sections developed by Hryciw et al. (1990) from Figure A.9.4, and also on the pre-failure and post-failure cross-sections developed and analyzed by Olson (2001). It is similar to Olson's cross-section, except for details regarding the failure surfaces analyzed. Olson's cross-sections were developed by extending the apparent slope of the lakebed to the toe of the failure zone, and by extending the apparent slope of the embankment fill as well. This current investigation team checked these extrapolations, and they appear to be reasonable.

Figure A.9.5(a) shows the pre-failure cross-section used to back-calculate the value of "apparent" initial post-liquefaction yield strength ($S_{r,yield}$) defined as the value that would be required to produce a calculated value of static Factor of Safety equal to 1.0 for pre-failure geometry and conditions assuming that the liquefiable soils have liquefied.

Shear strength of the non-saturated embankment zones above the phreatic surface was modeled as frictional, with a best estimate value of $Ø'_{residual}$ = 30°, based on DMT test results (Hryciw et al, 1990). Shear strength of the loose, saturated embankment zones below the phreatic surface was modeled as "liquefied", with the post-liquefaction strength ($S_{r,yield}$) to be back-calculated. Lakebed soils left in place beneath the embankment fill were assumed to have higher shear strengths than the liquefied strength of the very loose lower embankment fill.

Unit weights of the embankment fill were taken as γ_m = 115 lbs/ft^3 above the phreatic surface, and γ_s = 122.7 lbs/ft^3 below the phreatic surface. The weights of the six geophysical exploration trucks were distributed as a pair of line loads (two parallel sets of wheels) along the alignment.

Figure A.9.5(a) shows the best estimate of the most critical initial failure for this case. It is not known with certitude whether this was a monolithically initiated failure, or a failure that was incrementally progressive, initiating in successive slices retrogressively back to the eventual overall back heel of the failure. Analyses of the initial post-liquefaction cross-section showed that the preferred (most critical) initial failure surfaces would be surfaces deeply plunging towards the base of the liquefiable lower sand fill, and that they would tend to at least approach towards the eventual back heel. So if there was some incremental progression/retrogression, it would likely

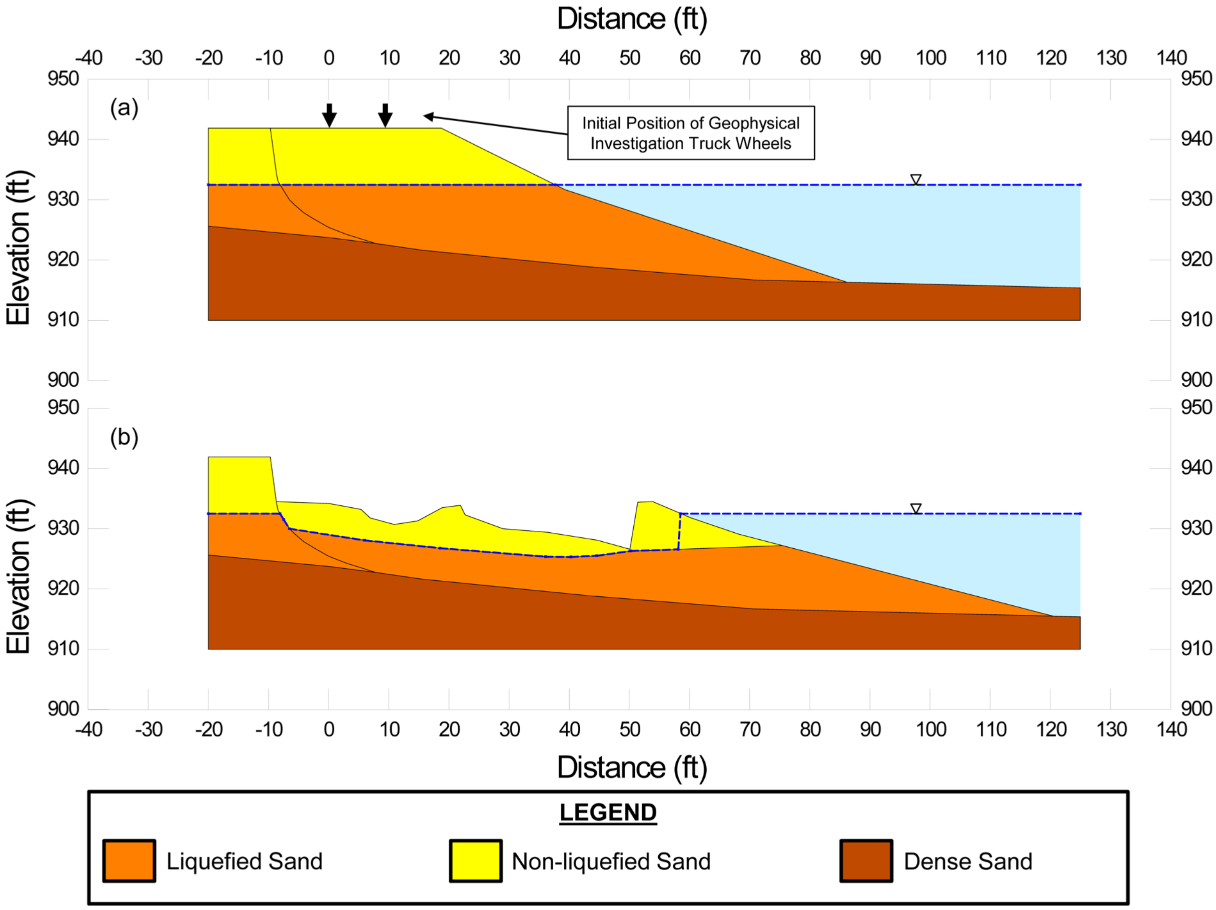

Figure A.9.5: Lake Ackerman Highway Embankment: (a) pre-failure geometry and failure surface for initial yield stress analyses, and (b) post-failure geometry and failure surface for post-failure residual geometry analyses.

have been relatively minor. Accordingly, the best estimate failure mechanism for this case is taken as a monolithically initiating failure that then articulates (or "breaks up") as it travels outwards into the lake.

For the best estimate failure surface shown in Figure A.9.5(a), the back-calculated value of $S_{r,yield}$ is 193 lbs/ft^2. Parameter and assumption sensitivity studies were next performed, varying the location of the initial yield surface (including allowing for partial incremental initiation and then retrogression to the back heel), and varying unit weights and the friction angle of the non-saturated upper embankment fill. For the ranges of conditions considered to be reasonable, the range of resulting values back-calculated was $S_{r,yield}$ = 174 to 205 lbs/ft^2.

Figure A.9.6 shows the pre-failure cross-section used by Olson (2001) to back-calculate $S_{r,yield}$. It also shows a number of the potential failure surfaces that he analyzed. Olson had concluded that because several of the large geophysical investigation trucks had all toppled towards the lake that the initial failure surface had likely had its rear scarp either at or to the lake side of the line of trucks. The current investigation team were aware of this assumption, but concluded that this evidence was inconclusive and that the trucks could have toppled in that direction as a result of a monolithically initiated failure that subsequently broke up and stretched

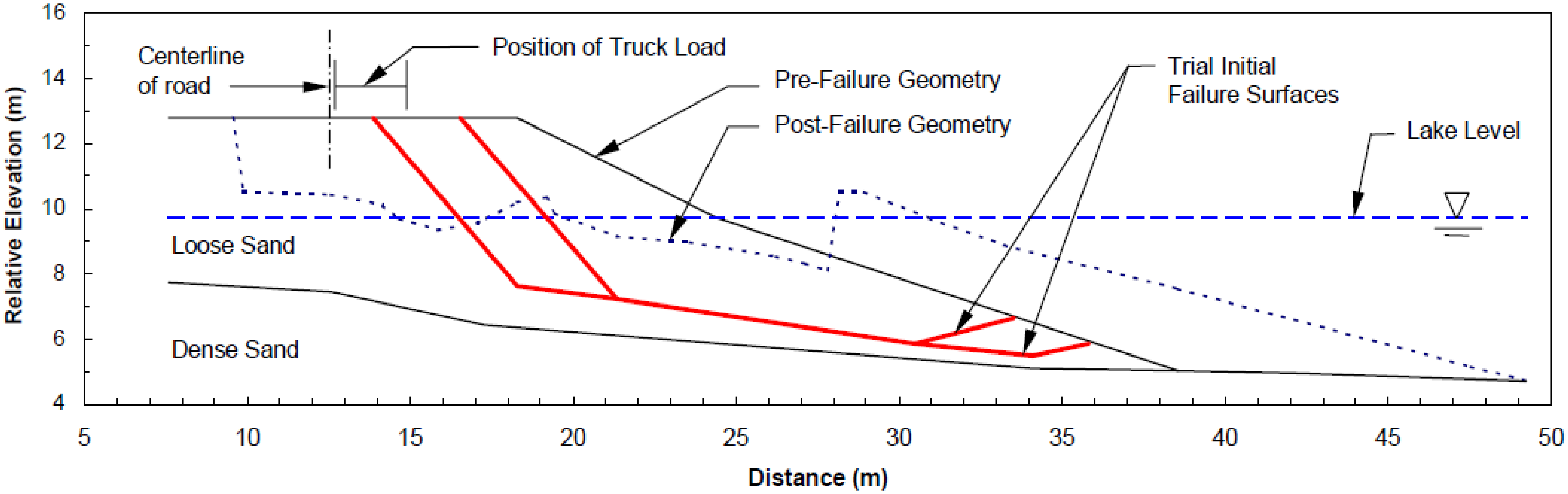

Figure A.9.6: Pre-failure cross-section and trial failure surfaces examined by Olson for purposes of assessing $S_{r,yield}$ (figure from Olson, 2001).

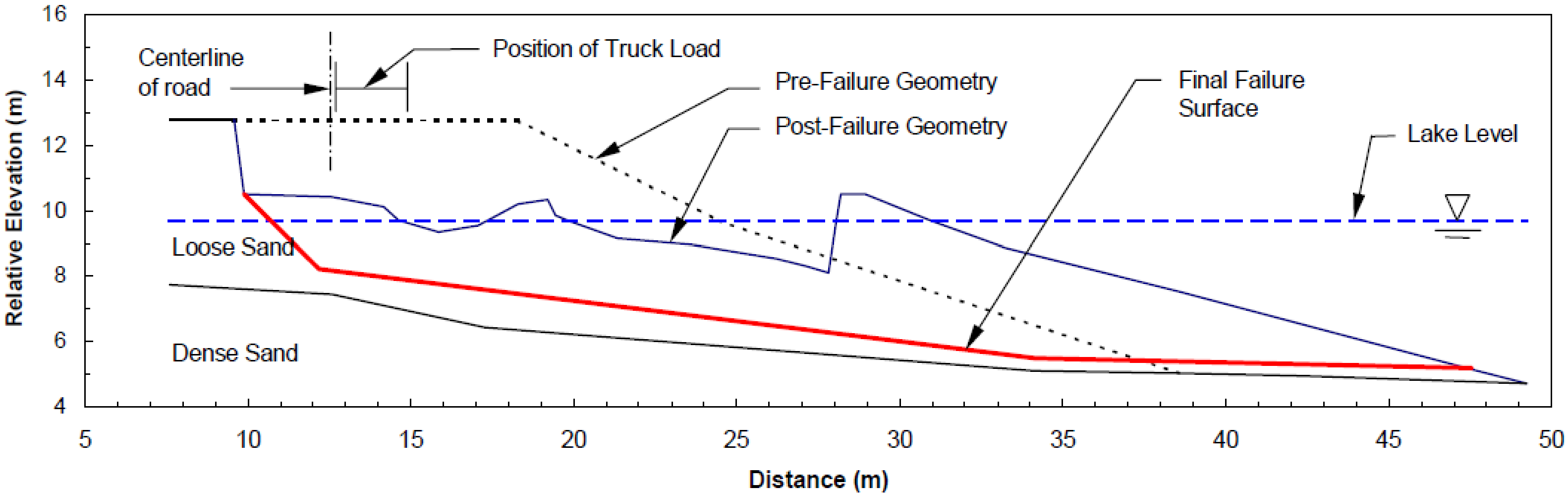

Figure A.9.7: Post-failure cross-section and trial failure surface used by Olson for back-calculation of $S_{r,resid/geom}$ (figure from Olson, 2001).

out as it travelled. Olson also tended to favor slightly shallower failure surfaces than the current investigation team. For this case history, that led Olson (2001) to estimate a slightly smaller initial $S_{r,yield}$ value of 10.1 kPa (211 lbs/ft^2), with a range of 8.6 kPa (180 lbs/ft^2) to 10.5 kPa (219 lbs/ft^2).

A.9.4 Residual Strength Analysis Based on Residual Geometry

The calculation of the "apparent" post-liquefaction strength ($S_{r,resid/geom}$) required to produce a calculated Factor of Safety equal to 1.0 based on residual geometry is illustrated in Figure A.9.5(b). This figure shows the phreatic surface, and the failure surface, used to calculate the best-estimate value of $S_{r,resid/geom}$. The relatively low velocities of this failure (see Section A.9.5) made it unlikely that any significant hydroplaning occurred as the toe of the failure mass entered into the reservoir. It was less easy to determine whether or not the failure mass may have been partially borne along atop weaker reservoir sediments. For the best estimate case it was assumed that strengths at the base of the portion of the failure mass that entered into the reservoir were 90% of the value of the post-liquefaction strength (S_r) of the overlying embankment fill. For the best estimate case, the resulting back-calculated value of $S_{r,resid/geom}$ was 56 lbs/ft^2. This was then varied from 50% to 100% of the value of the post-liquefaction strength (S_r) of the overlying embankment fill in subsequent parameter sensitivity analyses. Variations were then made in parameters, and in location of the pre-failure phreatic surface, as was described in the preceding section in order to evaluate uncertainty or variability. The resulting likely range of post-liquefaction strength required to provide a calculated Factor of Safety equal to 1.0 based on residual geometry was considered to be $S_{r,resid/geom} \approx 46$ to 65 lbs/ft^2.

Olson (2001) also calculated post-liquefaction strength required to produce a calculated Factor of Safety equal to 1.0 based on residual geometry, using the cross-section shown in Figure A.9.7, and reported a range of $S_{r,resid/geom} \approx 3.4$ kPa (71 lbs/ft^2), with a range of 2.9 to 4.8 kPa (61 to 100 lbs/ft^2), in fairly good agreement with the values calculated in these current studies, especially given the differences in critical sliding surfaces chosen by the two investigation teams.

A.9.5 Incremental Momentum Back-Analyses and Overall Estimates of S_r

Incremental momentum back-analyses were performed using the same sets of properties and geometries (including failure surfaces and phreatic surfaces) as described in the previous sections. Figure A.9.8 shows the best-estimate progressive incremental momentum analysis, showing the 5 stages of geometry evolution modeled as the failure proceeds. Figure A.9.9 repeats this figure, at larger scale for clarity, and it also shows the progressive locations of the center of gravity of the overall failure mass. Figure A.9.10 shows the associated calculations of: (1) acceleration vs. time, (2) velocity vs. time, and (3) displacement vs. time of the overall center of gravity. For the geometry and conditions shown in Figures A.9.8 through A.9.10, including assumption of shear strength equal to fully 100% of the liquefied strength S_r at the base of the portion of the toe of the embankment that entered into the reservoir, the best estimate value of post-liquefaction strength was $S_r = 107$ lbs/ft^2.

The main sources of uncertainty, or variability, in back-calculated values of S_r were (1) the precise location of the failure surface, (2) whether or not the failure initiated largely monolithically or retrogressed progressively towards the back heel, (3) unit weights, and (4) strength within the

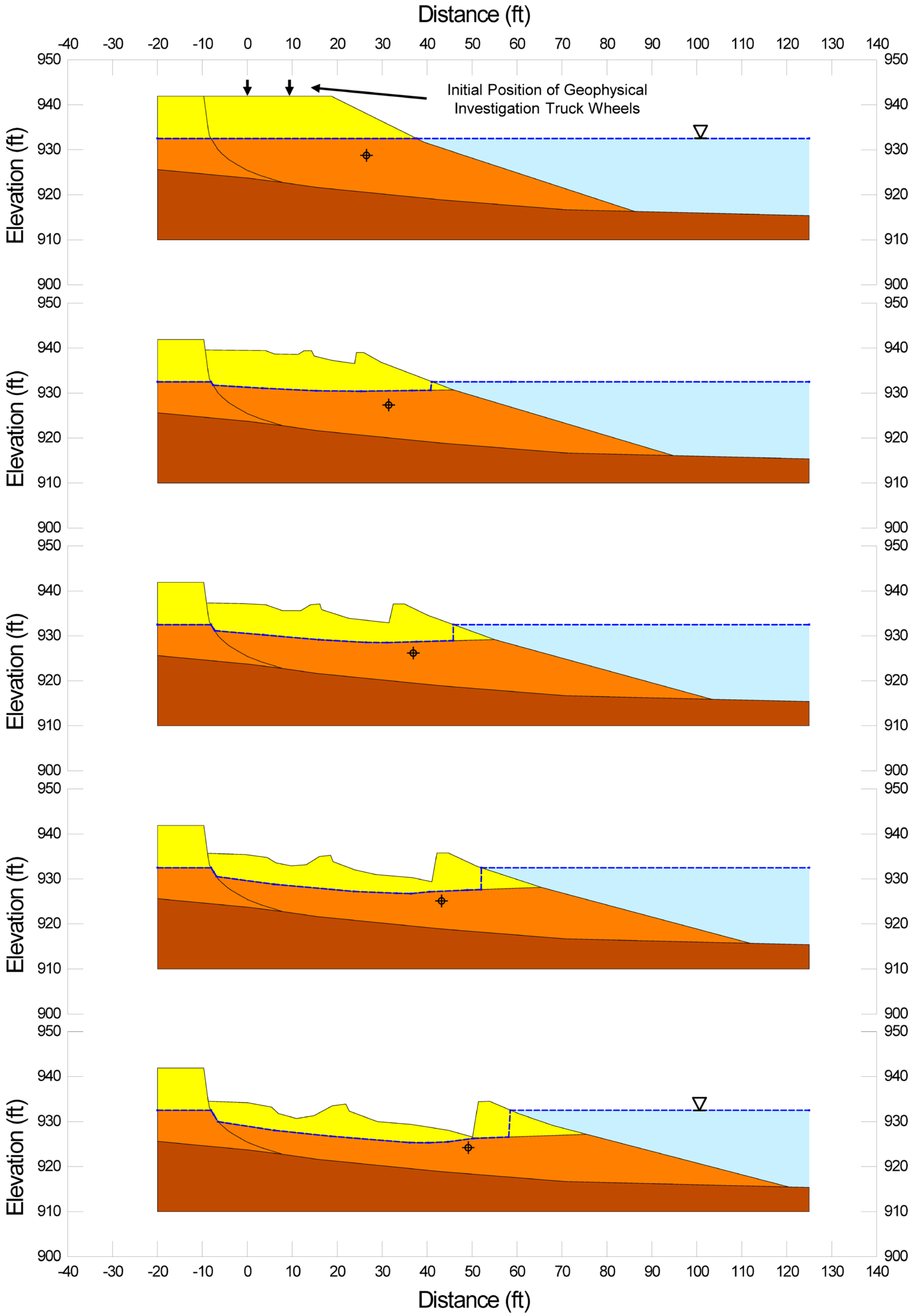

Figure A.9.8: Incremental momentum analysis of the failure of the Lake Ackerman Highway Embankment failure.

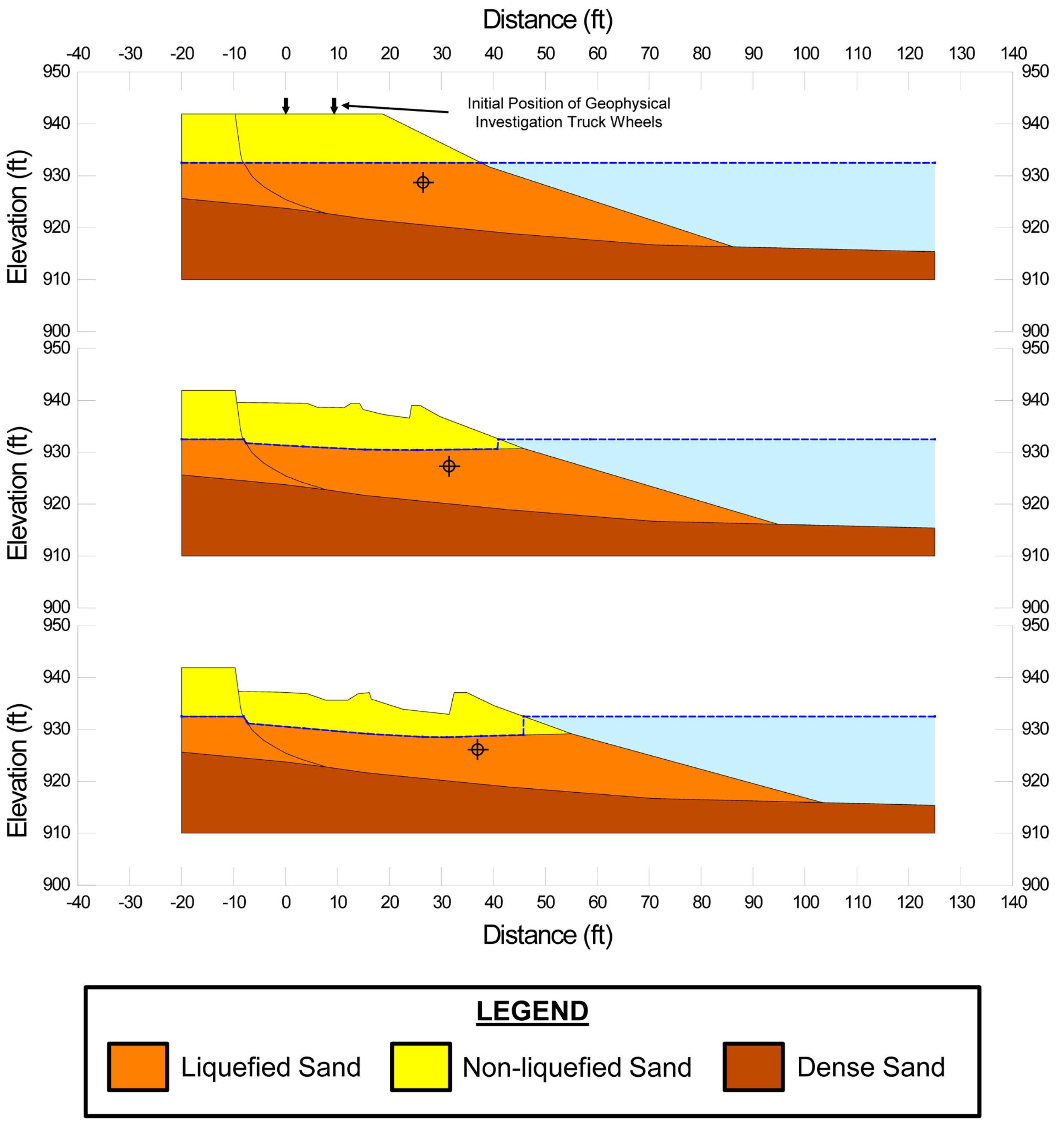

Figure A.9.9: Figure A.9.8 repeated, at larger scale, now also showing the progressive locations of the center of gravity of the overall failure mass.

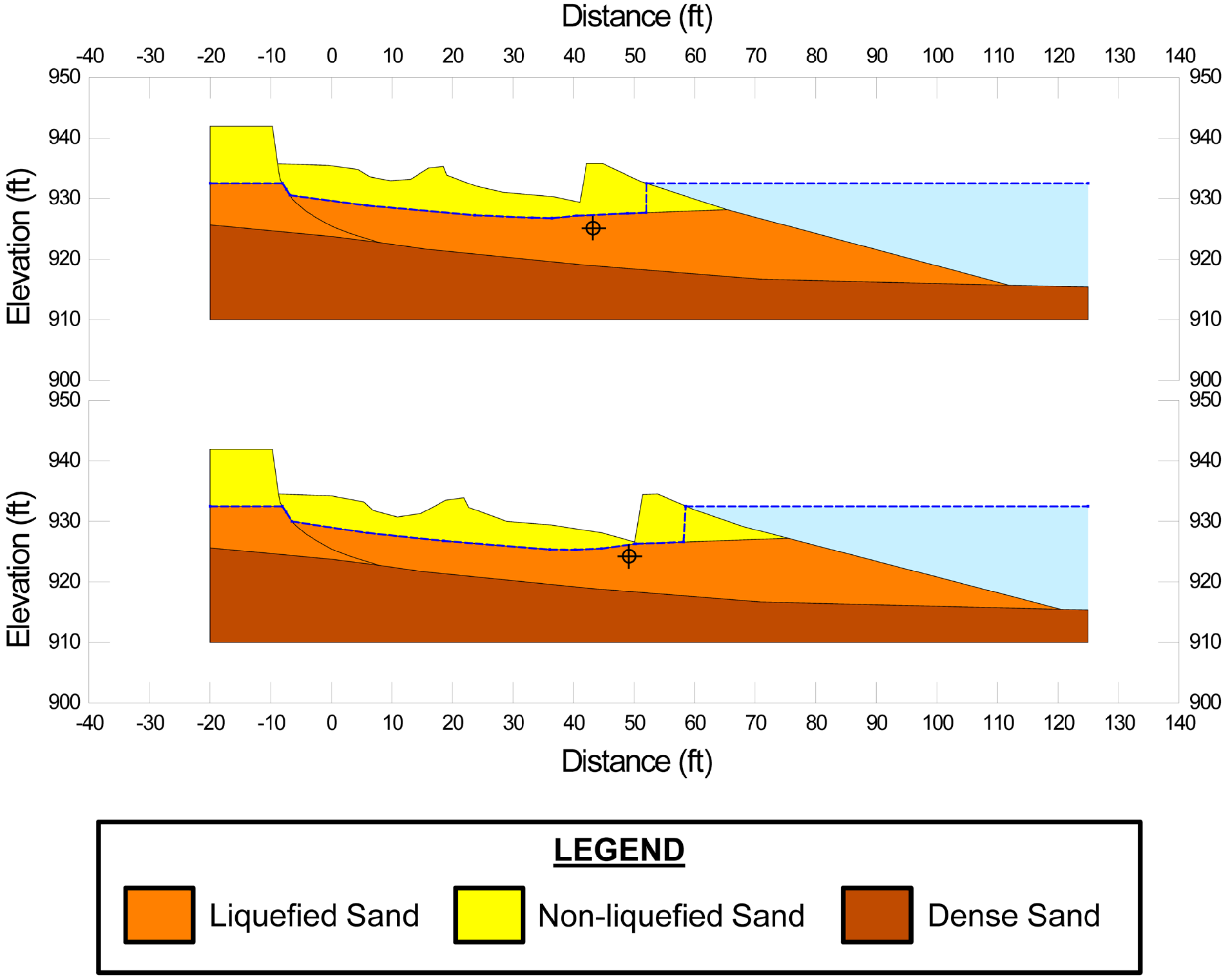

Figure A.9.9 (cont'd): Figure A.9.8 repeated, at larger scale, now also showing the progressive locations of the center of gravity of the overall failure mass.

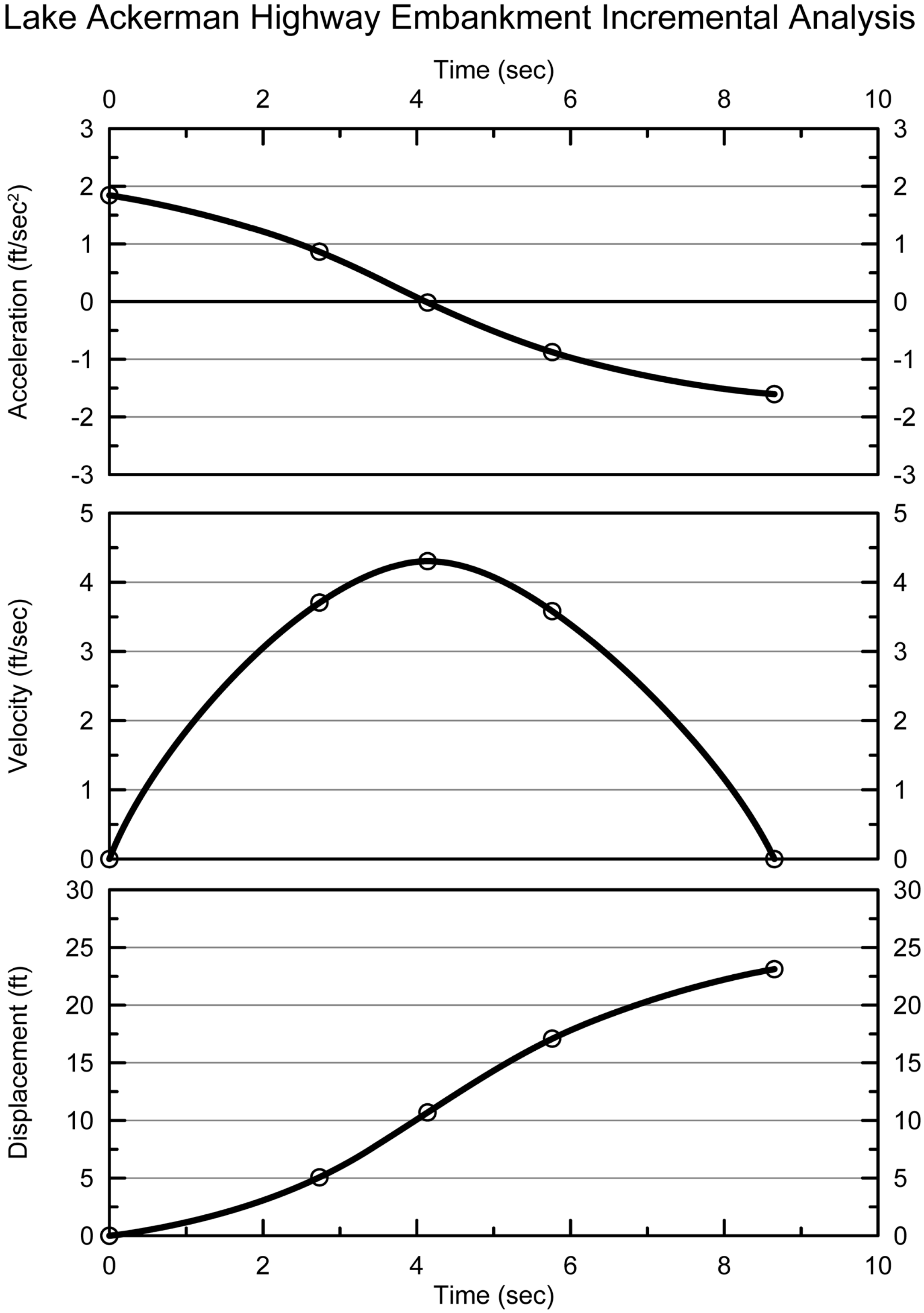

Figure A.9.10: Incremental momentum analysis of the failure of the Lake Ackerman Highway Embankment failure, showing progressive evolution of: (1) acceleration vs. time, (2) velocity vs. time, and (3) displacement vs. time of the overall center of gravity of the failure mass.

non-liquefied materials at the top of the back heel scarp. Parameter sensitivity studies were next performed, varying these parameters and modeling assumptions over the ranges considered reasonable.

Based on all analyses performed, and the considerations discussed herein, the overall best estimate value of post-liquefaction strength for the Lake Ackerman Highway Embankment failure was judged to be $S_r \approx 107$ lbs/ft^2, with a likely range of $S_r \approx 74$ to 150 lbs/ft^2. Based on the factors contributing to uncertainty or variance for this case history, it was the judgment of the investigation team that this range represented approximately +/− 2 standard deviations. This range of variance is not quite symmetrical about the best estimate value, so minor further adjustments were made to produce a representative estimate of S_r suitable for regression analyses.

Overall, based on an assumed normal distribution, it was judged that the (mean and median) best estimate of post-liquefaction strength for this case history is

$$S_r = 107 \text{ lbs/ft}^2$$

and that the best estimate of standard deviation of mean overall post-liquefaction strength is

$$\sigma_{\bar{S}} = 19 \text{ lbs/ft}^2$$

Estimates of S_r were also reported by several other investigation teams, and two sets of these are shown in Table A.9.1(a). Olson (2001) and Olson and Stark (2002), reported a best estimate value of $S_r = 3.9$ kPa (81 lbs/ft^2), based on their inertial displacement analyses that considered kinetics, and a range of $S_r = 3.4$ to 4.7 kPa (71 to 98 lbs/ft^2). Wang (2003) and Wang and Kramer (2008) employed their zero inertial force (ZIF) method to incorporate inertial effects in their back-analyses of this failure, and they also developed estimates of both mean $\overline{S}_r = 98$ lbs/ft^2 as well as the associated standard deviation $\sigma_{\bar{S}} = 20.4$ lbs/ft^2. As discussed previously, Olson favored a slightly shallower failure surface for this case history, and that may have caused him to slightly underestimate S_r. The three studies represented in Table A.9.1(a) each employed different approaches, and different sets of modeling and analysis assumptions. Given this, overall agreement among these three investigations is very good.

A.9.6 Evaluation of Initial Effective Vertical Stress

Average initial (pre-failure) effective vertical stress was assessed for the liquefied zones of the failure surface shown in Figure A.9.8(a). Reasonable variations were then made in (1) unit weights, and (2) the precise location of the overall failure surface.

The resulting best estimate of average pre-failure effective vertical stress within the liquefied materials controlling the failure was then $\sigma_{vo}' \approx 909$ lbs/ft^2, with a reasonable range of $\sigma_{vo}' \approx 787$ to 1,031 lbs/ft^2. This range is slightly non-symmetric abut the median value, and this range was judged by the engineering team to represent approximately +/− 2 standard deviations.

Overall, the best characterization of initial (pre-failure) average effective vertical stress was then taken to be represented by a mean and median value of

$$\sigma_{vo}' \approx 909 \text{ lbs/ft}^2 \text{ (43.5 kPa)}$$

with a standard deviation of

$$\sigma_{\sigma o'} \approx 61 \text{ lbs/ft}^2 \text{ (2.9 kPa)}$$

Estimates of σ_{vo}' were also reported by other investigation teams, and two sets of these are shown in Table A.13.1(c). Average initial vertical effective stresses were reported by Olson (2001) and Olson and Stark (2002) as σ_{vo}' = 1,075 lbs/ft^2. Average initial vertical effective stresses were not directly reported by Wang (2003) and Kramer (2008), but they were published more recently in the publication by Kramer and Wang (2015). As discussed in Section 2.3.8.1(a), the approach taken by Wang (2003) to evaluation of σ_{vo}' for his nine "primary" case histories (this is one of those nine) is not clearly explained, and it is also poorly documented. Wang's value of σ_{vo}' = 838 lbs/ft^2 is in fairly good agreement with the value developed in these current studies, but this is not considered a very rigorous check here. Given the differences in assumptions and in failure surfaces modeled, overall, agreement among these three studies is acceptable here.

A.9.7 Evaluation of $N_{1,60,CS}$

SPT borings were performed after the failure, and the $N_{1,60}$ values varied between 1 to 7 blows/ft in the loosely dumped sand fill at elevations below the lake surface elevation (Hryciw et al., 1990). Hryciw et al. selected a representative value of $N_{1,60}$ = 3 blows/ft, and Olson did the same. These were also $N_{1,60,CS}$ values because the fines adjustment was equal to zero in these clean fine sands. Wang (2002) and Kramer (2008) performed an independent evaluation, and developed a best estimate value of average $\overline{N_{1,60,CS}}$ = 4.8 blows/ft, and a standard deviation of $\sigma_{\overline{N}}$ = 1.2 blows/ft. An independent evaluation was also performed for these current studies, using the corrections and factors discussed in Appendix C, and the resulting characterization of the mean and median value of penetration resistance is $\overline{N_{1,60,CS}}$ = 3.5 blows/ft, with a standard deviation of the value of this mean of $\sigma_{\overline{N}}$ = 0.7 blows/ft. These values are all listed in Table A.9.1(b). Agreement among the three independent teams is very good here.

A.9.8 Other Results and Indices

A number of additional results, and indices, can be extracted from the analyses performed. Some of these are useful in developing some of the over-arching relationships and figures presented in the main text of this report. These values are presented in Table A.9.2.

Table A.9.1: Representative values for the Lake Ackerman Highway Embankment case history of: (a) post-liquefaction strength (S_r), (b) initial vertical effective stress (σ_{vo}'), and (c) $N_{1,60,CS}$ developed by various investigation teams, and estimates of variance in each of these indices when available.

(a) Post-Liquefaction Strength:	
Olson (2001) and Olson and Stark (2002)	S_r = 82 psf, and range = 71 to 98 psf
Wang (2003) and Kramer (2008)	$\overline{S_r}$ = 98 psf, and $\sigma_{\bar{S}}$ = 20.4 psf
This Study	$\overline{S_r}$ = 107 psf, and $\sigma_{\bar{S}}$ = 19 psf
(b) Representative $N_{1,60}$ or $N_{1,60,CS}$ Value:	
Olson (2001) and Olson and Stark (2002)	$N_{1,60}$ = 3 bpf, and range = 1 to 7 bpf
Wang (2003) and Kramer (2008)	$\overline{N_{1,60,CS}}$ = 4.8 bpf, and $\sigma_{\bar{N}}$ = 1.2 bpf
This Study	$\overline{N_{1,60,CS}}$ = 3.5 bpf, and $\sigma_{\bar{N}}$ = 0.7 bpf
(c) Representative Initial Vertical Effective Stress:	
Olson (2001) and Olson and Stark (2002)	σ_{vo}' = 1,076 psf, likely range is not provided.
Wang (2003) and Kramer (2008)	Value of $\sigma_{vo}' \approx$ 838 psf is poorly documented, and so is considered useful only as an approximate comparison. (See Section 2.3.8.1, and Table 2.3.)
This Study	$\overline{\sigma'_{vo}}$ = 909 psf, and $\sigma_{\bar{\sigma}}$ = 61 psf

Table A.9.2: Additional results and indices from the analyses of the Lake Ackerman Highway Embankment failure case history.

Maximum distance traveled by the center of gravity of the overall failure mass	23.1 ft.
Initial post-liquefaction Factor of Safety prior to displacement initiation, and based on best estimate value of S_r	FS = 0.58
Final post-liquefaction Factor of Safety at final (residual) post-failure geometry, and based on best estimate value of S_r	FS = 1.91

A.10 Chonan Middle School (Chiba, Japan; 1987)

A.10.1 Brief Summary of Case History Characteristics

Name of Structure	Chonan Middle School
Location of Structure	Chiba, Japan
Type of Structure	Embankment Fill
Date of Failure	December 17, 1987
Nature of Failure	Seismic, During 1987 Chiba-Toho-Oki Earthquake (M = 6.7)
Approx. Maximum Slope Height	19.3 ft.

A.10.2 Introduction and Description of Failure

The slope of the embankment fill at Chonan Middle School failed during the Chiba-Toho-Oki Earthquake of December 17, 1987 (M = 6.7), and was investigated by Ishihara et al. (1990). The estimated peak ground acceleration at the site was approximately 0.12 g (Olson, 2001).

Figure A.10.1 (from Ishihara et al., 1991) shows a plan view of the Chonan Middle School site and Figure A.10.2 shows a cross section through the failure. Areas where fill material that was excavated from the surrounding hilltops was placed are shown on Figure A.10.1. Fill placement occurred in approximately 1960 and the fill was reportedly placed loosely with no compaction effort (Ishihara, 1993).

Following the failure, Swedish cone penetration tests were performed in the area of the failed slope. Results of these tests are presented in Figure A.10.2. Weak layers can be seen in the results of the Swedish cone tests, and these can be used to infer a reasonable estimate of the likely failure surface. Ishihara et al. (1990) present a reasonable interpretation of a failure surface for the post failure geometry and this is reproduced in Figure A.10.3. Considering the results of the Swedish cone tests and the geometry at the heel and toe of the failure, a failure surface similar to that presented by Ishihara et al. (1990) can be assumed for purposes of back-analyses, and it can be considered to be reasonably well constrained.

Prior to the construction of a building on the school site, four SPT borings had been performed. Only one of these is reported in the available literature, and the location of the boring (Boring B) is shown in Figure A.10.1 to be within the area of fill placement. Figure A.10.4 shows the results of this SPT boring.

A difficulty encountered in performing back-analyses of this failure is that the post-failure volume of the failed slope materials shown in Figure A.10.1 is approximately 17% smaller than the pre-failure volume. This is accommodated in the back-analyses that follow by progressively changing the overall volume of the slide mass as the failure develops. Analyses performed with

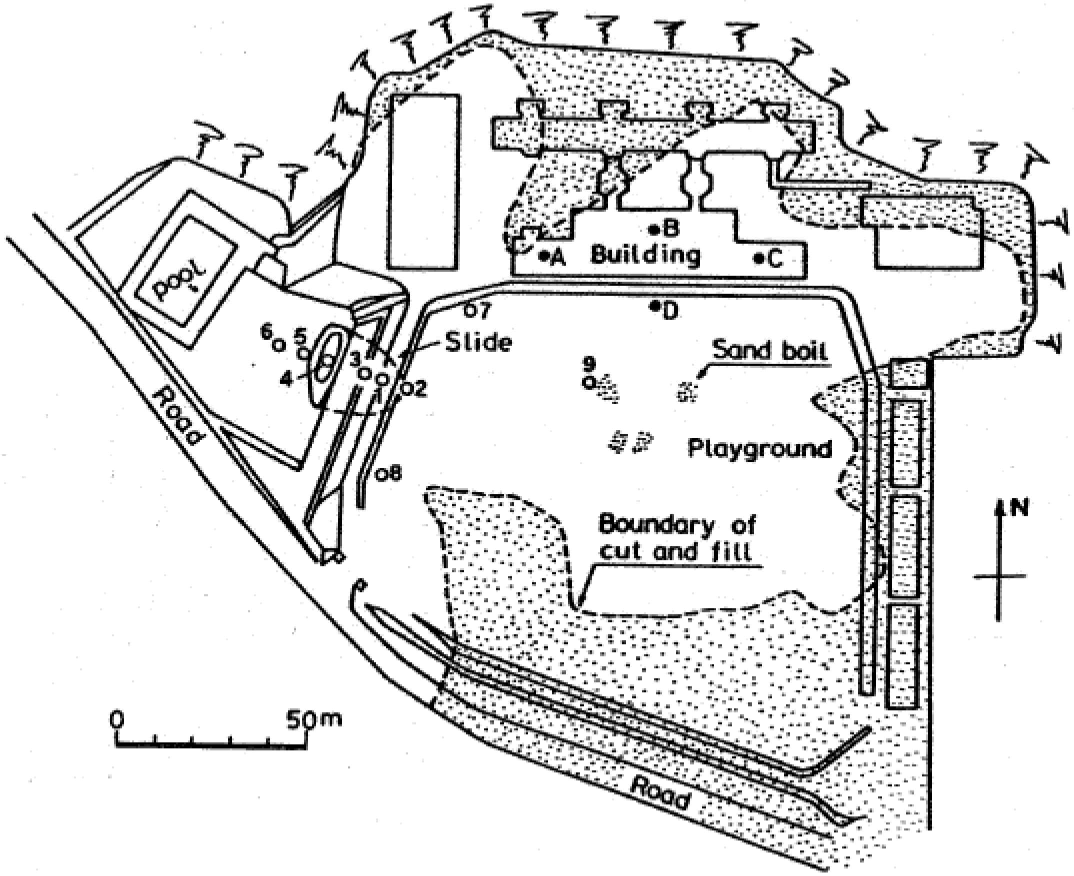

Figure A.10.1: Plan view of the Chonan Middle School site showing the location of the slope failure, locations of penetration tests, and the approximate limits of fill (from Ishihara et al., 1990).

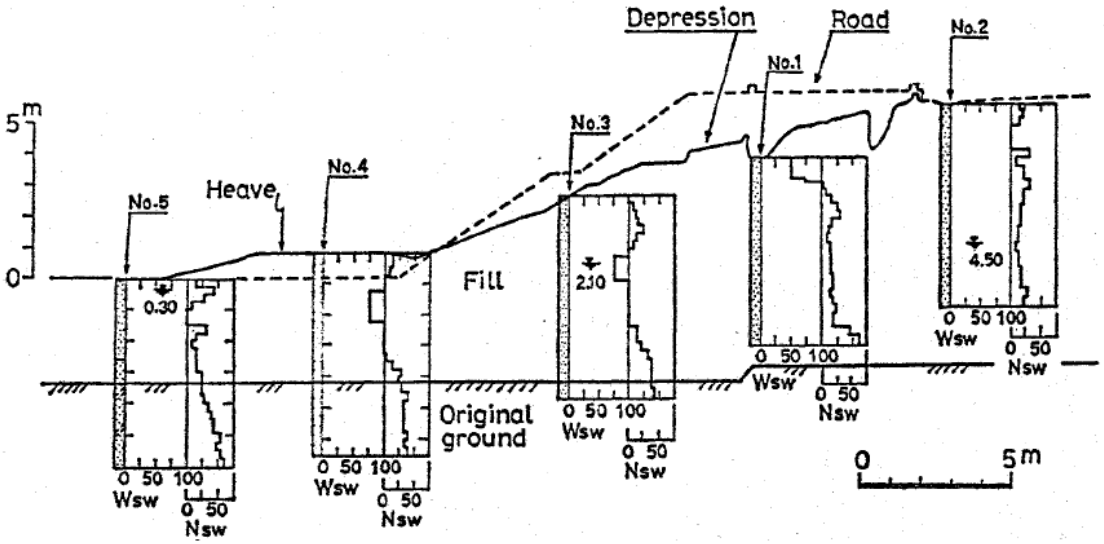

Figure A.10.2: Cross-section of the slope failure at the Chonan Middle School site showing the results of Swedish cone penetration tests and the pre- and post-failure geometry (from Ishihara et al., 1990).

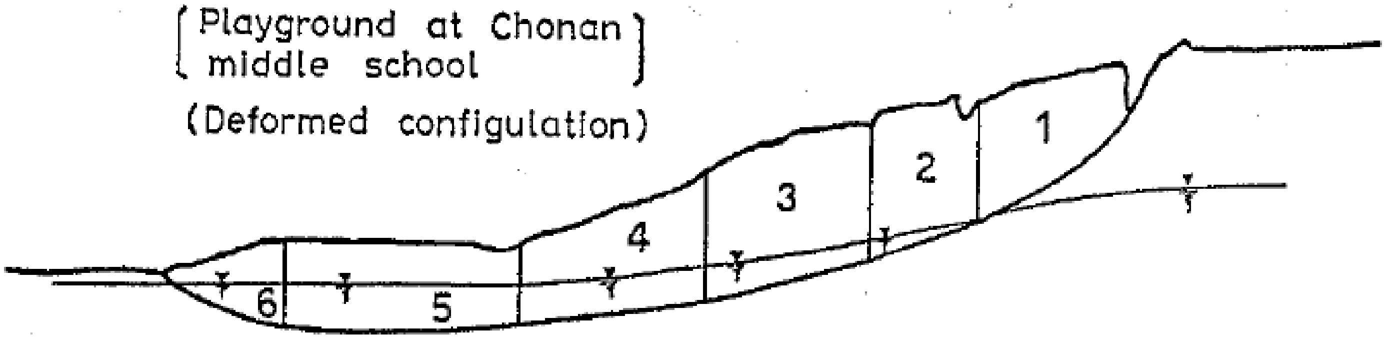

Figure A.10.3: Interpretation of the failure surface and phreatic surface for a limit equilibrium stability analysis of the post failure geometry performed by Ishihara et al. (1990).

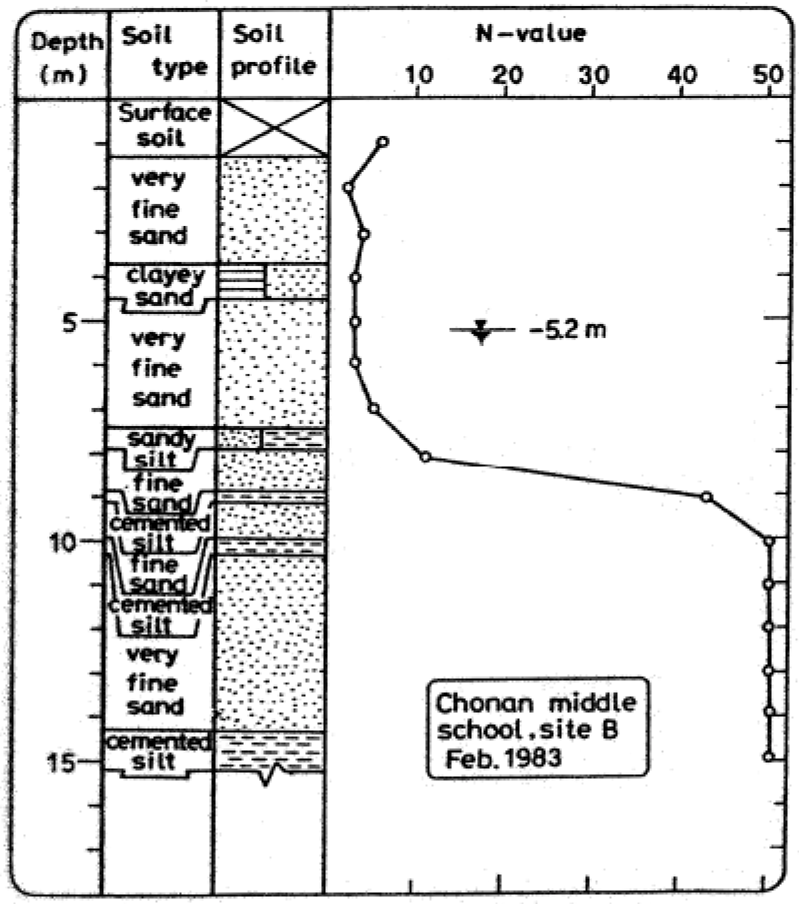

Figure A.10.4: Log of Boring B performed in February of 1983 at the Chonan Middle School site prior to the construction of a school building (from Ishihara, 1993).

different approaches to this variation in slide mass (including using just the initial slide mass without changing it to eventually match the post-failure volume of Figure A.10.1) showed that this volume discrepancy has only a moderate effect on uncertainty, or variance, in back-calculated post-liquefaction strengths for this case history.

A.10.3 Initial Yield Strength Analyses

Figure A.10.5(a) shows the cross-section used in these studies for the best estimate case back-analyses to determine the initial yield stress, defined as the best estimate value of post-liquefaction $S_{r,yield}$ within the liquefiable hydraulic fill required to produce a calculated Factor of Safety equal to 1.0 for pre-failure geometry.

The precise location of the initial failure surface at the base of the failure is uncertain. However, given the geometry of the failure and the reported stratigraphy, the location was fairly well constrained. The best estimate location of the phreatic surface used in the back-analyses

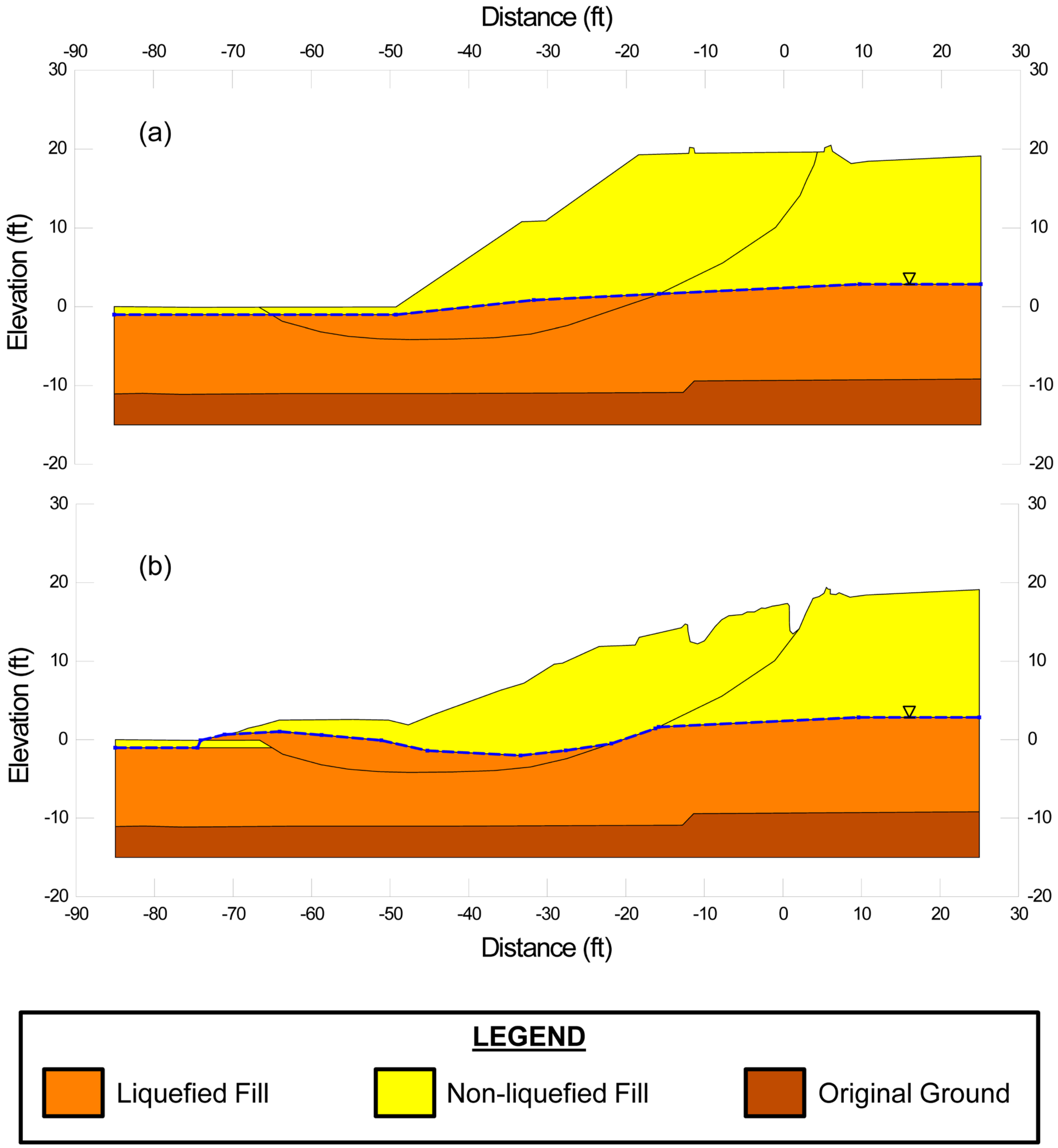

Figure A.10.5: Chonan Middle School cross-sections showing (a) pre-failure geometry of the fill slope and the failure surface used for calculation of post-liquefaction initial yield strength $S_{r,yield}$, and (b) post-failure residual geometry and the failure surface used to calculate $S_{r,resid/geom}$.

was developed considering the reported depths where ground water was encountered during the post-failure investigation reported in Ishihara et al. (1990). The location of the phreatic surface within the fill embankment corresponds well to the location that ground water was encountered during the 1983 investigation for the school building located in the middle of the fill shown in Figure A.10.4.

A search was made for the most critical static failure surface assuming that liquefaction had been "triggered" in all potentially liquefiable materials below the phreatic surface, while constraining the location the failure surface near the toe to match the approximate zone of lower penetration resistance from the Swedish cone tests. Following some minor refinement to the failure surface to better match a surface that would articulate the failed mass as observed, the "best estimate" failure surface is shown in Figure A.10.5(a). This resulting failure surface is in good agreement with the failure surface used for the back-analyses performed by Ishihara et al. (1990). Those earlier analyses neglected seismic inertial forces, however, and they also did not account for likely progressive development of triggering of liquefaction within the slope.

Loose fine sand materials above the phreatic surface were modeled with $Ø' \approx 30°$, and a unit weight of $\gamma_m \approx 115$ lbs/ft^3. Materials below the phreatic surface were considered to liquefy, down to the base of the failure surfaces analyzed, and were assigned an undrained post-liquefaction yield strength of $S_{r,yield}$ that was constant along any given failure surface, and a unit weight of $\gamma_s \approx 120$ lbs/ft^3.

The resulting best-estimate value of $S_{r,yield}$ for the most critical initial failure surface was $S_{r,yield} = 199$ lbs/ft^2.

Parameters and geometry were then varied to examine potentially variability. The location of the phreatic surface was varied, raising it by up by up to 0.5 m (1.5 ft.) across the embankment, and lowering it by up to a similar distance. Unit weights were also varied over the ranges considered likely, and the friction angle of non-liquefied material above the phreatic surface was varied from 28° to 35°. The resulting range of values of $S_{r,yield}$ for the most critical initial failure surface was $S_{r,yield} \approx 165$ to 240 lbs/ft^2.

Olson (2001) also performed back-analyses to determine $S_{r,yield}$. Failure surfaces analyzed were similar, but there were some differences in the details of modeling of the phreatic surface and the failure surface. Olson reported values of $S_{r,yield} \approx 12.0$ to 12.9 kPa (251 to 269 lbs/ft^2), with a best estimate value of 12.2 kPa (255 lbs/ft^2).

A.10.4 Residual Strength Analysis Based on Residual Geometry

The calculation of the "apparent" post-liquefaction strength ($S_{r,resid/geom}$) required to produce a calculated Factor of Safety equal to 1.0 based on residual geometry is illustrated in Figure A.10.5(b).

This figure shows the phreatic surface, and the failure surface, used to calculate the best-estimate value of $S_{r,resid/geom} \approx 102$ lbs/ft^2. Variations were made in parameters, and in location of the pre-failure phreatic surface, as was described in the preceding section. The resulting likely range of post-liquefaction strength required to provide a calculated Factor of Safety equal to 1.0 based on residual geometry was considered to be $S_{r,resid/geom} \approx 86$ to 125 lbs/ft^2.

Olson (2001) also calculated post-liquefaction strength required to produce a calculated Factor of Safety equal to 1.0 based on residual geometry, and reported a best estimate value of $S_{r,resid/geom} \approx 4.8$ kPa (100 lbs/ft^2), with a range of $S_{r,resid/geom} \approx 3.8$ to 6.0 kPa (79 to 125 lbs/ft^2), in exelent agreement with these current studies

A.10.5 Incremental Momentum Back-Analyses and Overall Estimates of S_r

Incremental momentum back-analyses were performed using the same sets of properties and geometries (including failure surfaces and phreatic surfaces) as described in the previous sections.

Figure A.10.6 shows the best-estimate progressive incremental momentum analysis, showing the 5 stages of geometry evolution modeled as the failure proceeds. Figure A.10.7 shows the associated calculations of (1) acceleration vs. time, (2) velocity vs. time, and (3) displacement of the overall center of gravity vs. time. For the geometry and phreatic surface shown in Figure A.10.5, the best estimate value of post-liquefaction strength was $S_r = 141$ lbs/ft^2.

The main sources of uncertainty, or variability, in back-calculated values of S_r were (1) the precise location of the overall failure surface, (2) unit weights, (3) strength within the non-liquefied materials, and (4) the location of the phreatic surface.

The analysis shown in Figure A.10.6 neglects cyclic inertial forces, and so may represent a slightly conservative assessment of actual post-liquefaction strength mobilized.

Based on all analyses performed, and the considerations discussed herein, the overall best estimate value of post-liquefaction strength for the Chonan Middle School slope failure was judged to be $S_r \approx 141$ lbs/ft^2, with a likely range of $S_r \approx 91$ to 196 lbs/ft^2. Based on the factors contributing to uncertainty or variance for this case history, it was the judgment of the investigation team that this range represented approximately +/− 1.5 standard deviations. This range of variance is not quite symmetrical about the best estimate value, so minor further adjustments were made to produce a representative estimate of S_r suitable for regression analyses.

Overall, based on an assumed normal distribution, it was judged that the (mean and median) best estimate of post-liquefaction strength for this case history is

$$S_r = 141 \text{ lbs/ft}^2 \text{ (6.75 kPa)}$$

and that the best estimate of standard deviation of mean overall post-liquefaction strength is

$$\sigma_{\overline{S}} = 35 \text{ lbs/ft}^2 \text{ (1.68 kPa)}$$

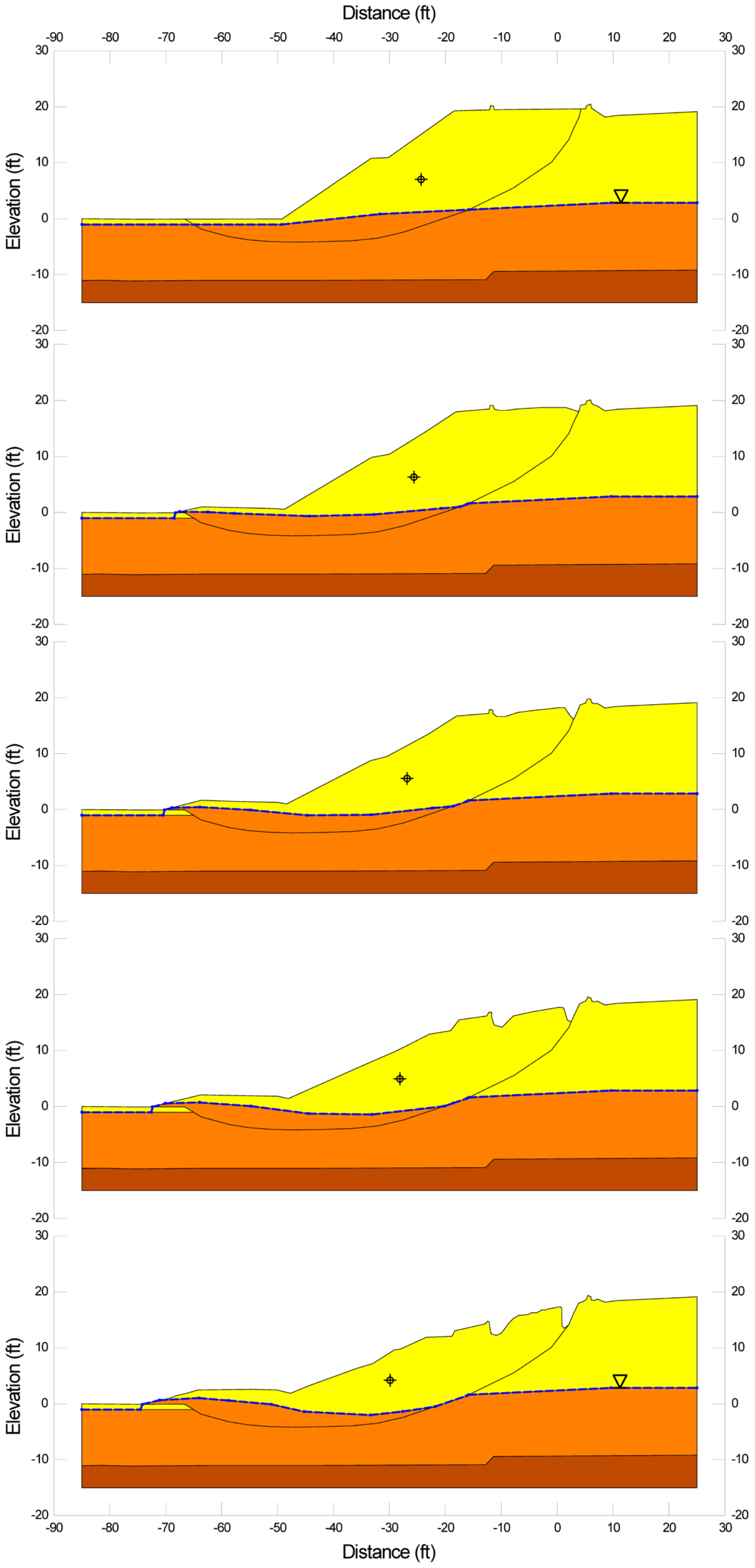

Figure A.10.6: Incremental momentum analysis of the failure of the fill slope at Chonan Middle School, showing progressive evolution of cross-section geometry modeled.

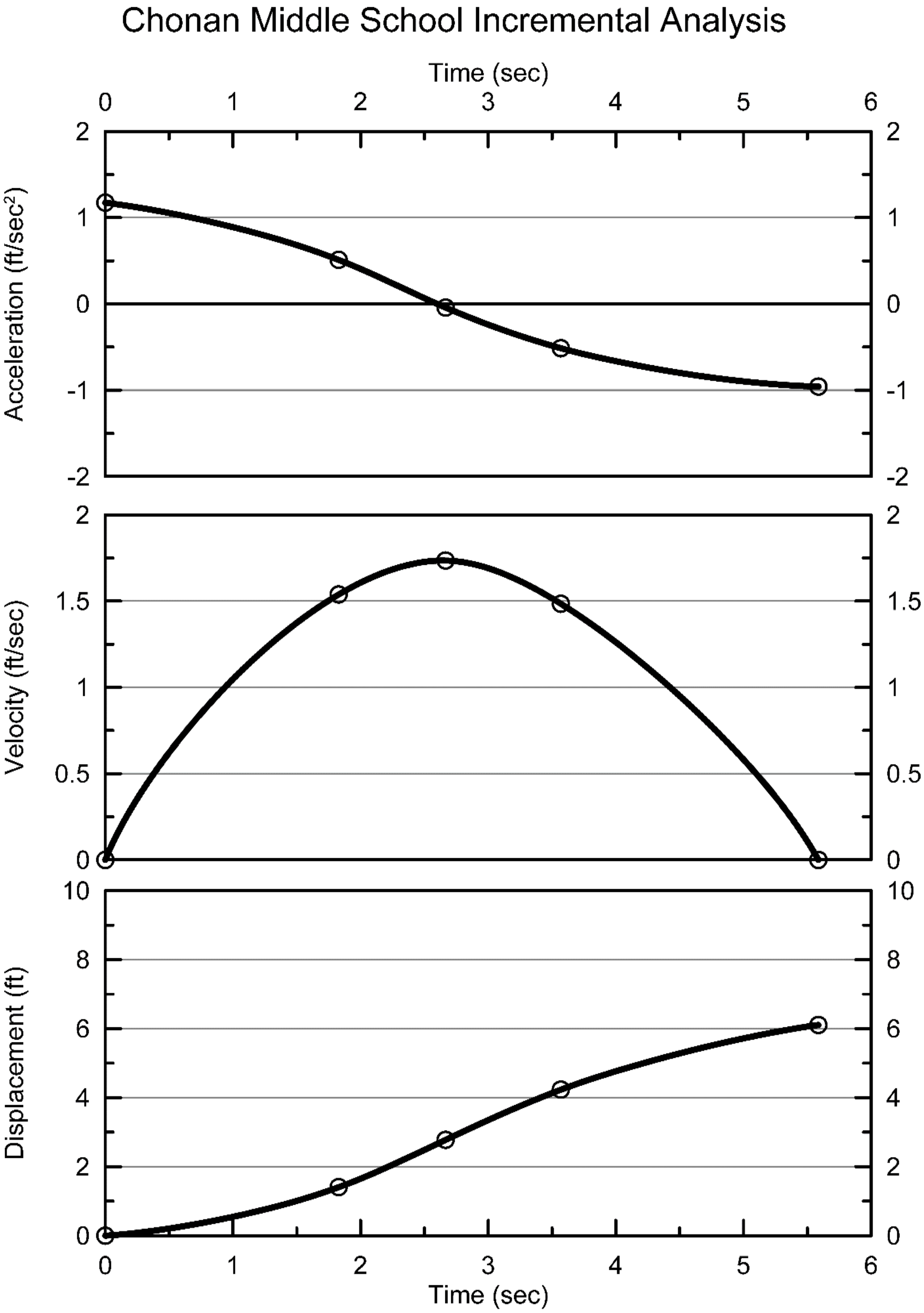

Figure A.10.7: Incremental momentum analysis of the failure of the fill slope a Chonan Middle School showing progressive evolution of: (1) acceleration vs. time, (2) velocity vs. time, and (3) displacement of the overall center of gravity vs. time

Estimates of S_r were also reported by several other investigation teams, and these are shown in Table A.10.1(a). Olson (2001) and Olson and Stark (2002), reported a best estimate value of $S_r = 4.8$ kPa (100 lbs/ft^2), but this was not based on their "kinetics" analyses that considered momentum effects. Instead, it was based on assessment of post-liquefaction residual geometry and it neglected momentum effects. As a result, it will be an overly conservative estimate (the value will be too low). Olson also calculated $S_{r,yield}$ and $S_{r,resid/geom}$ (see Sections A.11.3 and A.11.4) for this case, however, and those two values can be convolved to provide a better estimate of S_r. Based on Equation 4-1 (see Chapter 4), a better estimate for S_r based on calculations performed by Olson (2001) would be $S_r \approx 0.8 \times [S_{r,yield} + S_{r,resid/geom}] / 2 \approx 0.8 \times [12.2 \text{ kPa} + 4.8 \text{ kPa}] / 2 \approx 6.8$ kPa (142 lbs/ft^2), and this value is more directly comparable with the values of this current study, and so it is the value presented in Table A.10.1(a). Wang (2003) and Kramer (2008) developed estimates of both mean $\overline{S_r} = 178.7$ lbs/ft^2 as well as the associated standard deviation $\sigma_{\overline{S}} = 32.0$ lbs/ft^2. Given the differences in approaches among the three studies, overall agreement among these investigations is very good.

A.10.6 Evaluation of Initial Effective Vertical Stress

Average initial (pre-failure) effective vertical stress was assessed for the liquefied zones of the failure surface shown in Figure A.10.5(a). Reasonable variations were then made in (1) the location of the phreatic surface, (2) unit weights, and (3) the precise location of the overall failure surface.

The resulting best estimate of average pre-failure effective stress within the liquefied materials controlling the failure was then $\sigma_{vo}' \approx 1{,}032$ lbs/ft^2, with a reasonable range of $\sigma_{vo}' \approx 911$ to 1,157 lbs/ft^2. This range is slightly non-symmetric about the median value, and this range was judged by the engineering team to represent approximately +/− 1.5 standard deviations. Overall, the best characterization of initial (pre-failure) average effective vertical stress was then taken to be represented by a mean and median value of

$$\sigma_{vo}' \approx 1{,}032 \text{ lbs/ft}^2 \text{ (49.4 kPa)}$$

with a standard deviation of

$$\sigma_{\sigma o'} \approx 82 \text{ lbs/ft}^2 \text{ (3.93 kPa)}$$

Estimates of σ_{vo}' were also reported by other investigation teams, and these are shown in Table A.10.1(c). Olson (2001) and Olson and Stark (2002) report an average initial vertical effective stress on the order of approximately $\sigma_{vo}' \approx 1{,}119$ lbs/ft^2. Average initial vertical effective stresses were not directly reported by Wang (2003) and Kramer (2008), but they were published more recently in the publication by Kramer and Wang (2015). As discussed in Section 2.3.8.1(b)-(iii), Wang (2003) did not perform any independent analyses to assess σ_{vo}' for his 22 "secondary" cases, and this is one of those cases. Instead, he compiled values of S_r from multiple previous investigators, and averaged these for a best estimate. He also compiled multiple values of S_r/σ_{vo}' from previous investigators, and averaged these for a best estimate. He then used these two best-estimate values of S_r and S_r/σ_{vo}' to infer a resulting representative value of σ_{vo}'. As described in

Section 2.3.8.1(b)-(iii), the resulting averaged values of S_r and S_r/σ_{vo}' were incompatible with each other for a number of Wang's "secondary" case histories, and this process produced unreasonable, and in some cases physically infeasible, values of σ_{vo}' for a number of case histories. Accordingly, Wang's value of $\sigma_{vo}' = 1{,}964$ lbs/ft^2 is not considered a useful check here. Agreement between the value calculated by Olson (2001) and the value calculated in these current studies is very good.

A.10.7 Evaluation of $N_{1,60,CS}$

Figure A.10.4 from Ishihara (1993), shows the log of the only boring in available literature with SPT tests performed in the fill material at Chonan Middle School. As a result, lack of numbers of SPT data is a significant contributor to uncertainty or variability with respect to the median or mean $N_{1,60,CS}$ value representative of this material. Olson (2001) utilized an energy ratio of approximately 68%, and this current study does the same. Corrections for effective overburden stress (C_N) were made using the relationships proposed by Deger (2014), as presented and discussed in Appendix C. Corrections for SPT equipment and procedural details, and for fines content, were made based on Cetin et al. (2018a,b) as also presented and explained in Appendix C. The resulting representative $N_{1,60}$ value was between 5 and 5.5 blows/ft. Based on the reported fines content of 18% (Ishihara, 1993), the representative (median) $\overline{N_{1,60,CS}}$ value was determined to be 6.5 blows/ft.

Variance of $\overline{N_{1,60,CS}}$, was only partially determined by variation of $N_{1,60,CS}$ values within this limited data set. Additional factors significantly affecting variance or uncertainty in the median representative $\overline{N_{1,60,CS}}$ value were (1) lack of numbers of SPT data, and (2) uncertainty as to actual SPT equipment and procedural details. Overall, it was the judgment of the investigation team that SPT penetration resistance could be suitably represented with a representative (median) value of $\overline{N_{1,60,CS}}$ = 6.5 blows/ft, and with a standard deviation of the median/representative value of approximately $\sigma_{\overline{N}}$ = 2.1 blows/ft.

Table A.10.1(b) shows values of representative $N_{1,60}$ or $N_{1,60,CS}$ values developed by selected other investigators, and variance or standard deviations in these representative values when available. Olson and Stark (2001, 2002) developed an estimated representative value of $N_{1,60}$ = 5.2 blows/ft, and an estimated range of representative values of $N_{1,60} \approx 2.6$ to 8.8 blows/ft, but did not quantify variance or standard deviation in probabilistic terms. Wang (2003) and Kramer (2008) jointly developed a representative value of $\overline{N_{1,60,CS}}$ = 6.4 blows/ft, and their estimated standard deviation of that overall mean value for this case history was $\sigma_{\overline{N}}$ = 6.9 blows/ft. This standard deviation is larger than the mean value itself, and this is an artifact of the rigidly defined methodology employed by Wang (2003) to develop estimates of $\sigma_{\overline{N}}$. The representative $N_{1,60}$ value of Olson and Stark is about 1 to 1.5 blows/ft lower than the other two sets of values in the table, largely because Olson and Stark did not make a fines correction, which would have served to increase their $N_{1,60}$ values as they became $N_{1,60,CS}$ values in these silty sands. With any reasonable fines correction, agreement between their value and the other values would be very good. Overall, the agreement all three sets of values shown in Table A.10.1(b) is very good.

A.10.8 Other Results and Indices

A number of additional results, and indices, can be extracted from the analyses performed. Some of these are useful in developing some of the over-arching relationships and figures presented in the main text of this report. These values are presented in Table A.10.2.

Table A.10.1: Representative values for the Chonan Middle School case history of: (a) post-liquefaction strength (S_r), (b) initial vertical effective stress (σ_{vo}'), and (c) $N_{1,60,CS}$ developed by various investigation teams, and estimates of variance in each of these indices when available.

(a) Post-Liquefaction Strength:	
Olson (2001) and Olson and Stark (2002)	$S_r \approx 142$ psf*
Wang (2003) and Kramer (2008)	$\overline{S_r}$ = 178.7 psf, and $\sigma_{\overline{S}}$ = 32.0 psf
This Study	$\overline{S_r}$ = 141 psf, and $\sigma_{\overline{S}}$ = 35 psf
(b) Representative $N_{1,60}$ or $N_{1,60,CS}$ Value:	
Olson (2001) and Olson and Stark (2002)	$N_{1,60}$ = 5.2 bpf, and range = 2.6 to 8.8 bpf
Wang (2003) and Kramer (2008)	$\overline{N_{1,60,CS}}$ = 6.4 bpf, and $\sigma_{\overline{N}}$ = 6.9 bpf
This Study	$\overline{N_{1,60,CS}}$ = 6.5 bpf, and $\sigma_{\overline{N}}$ = 2.1 bpf
(c) Representative Initial Vertical Effective Stress:	
Olson (2001) and Olson and Stark (2002)	σ_{vo}' = 1,119 psf. Likely range is not provided.
Wang (2003) and Kramer (2008)	Value of $\sigma_{vo}' \approx$ 1,968 psf is poorly based, and so is not very useful as a basis for comparison. (See Section 2.3.8.1(b) and Table 2.3)
This Study	$\overline{\sigma'_{vo}}$ = 1,032 psf, and $\sigma_{\overline{\sigma}}$ = 82 psf

* Olson (2001) did not employ his "kinetics" back-analysis approach to this case. See the text of Section A.10.5 for an explanation of the value of $S_r \approx 142$ psf attributed here.

Table A.10.2: Additional results and indices from the analyses of the Chonan Middle School failure case history.

Maximum distance traveled by the center of gravity of the overall failure mass	6.1 ft.
Initial post-liquefaction Factor of Safety prior to displacement initiation, and based on best estimate value of S_r	FS = 0.86
Final post-liquefaction Factor of Safety at final (residual) post-failure geometry, and based on best estimate value of S_r	FS = 1.17

A.11 Soviet Tajik May 1 Slope Failure (Tajikistan Republic; 1989)

A.11.1 Brief Summary of Case History Characteristics

Name of Structure	Soviet Tajikistan Slope
Location of Structure	Tajikistan Republic
Type of Structure	Natural Loess Slope
Date of Failure	January 23, 1989
Nature of Failure	Seismic, During the 1989 Soviet Tajik Earthquake (M_L = 5.5)
Approx. Maximum Slope Height	96.8 ft.

A.11.2 Introduction and Description of Failure

The Soviet Tajik Earthquake of January 23, 1989 (M_L = 5.5) produced a number of flow slides in the Gissar area of Tajikistan, USSR. As shown in Figure A.11.1, the Gissar area lies along the Iliakckin Fault, which produced the earthquake. Shaking duration was short (approximately 4 to 5 seconds) and as shown in Figure A.11.1, levels of peak acceleration recorded were relatively low.

Ishihara et al. (1990) describe a series of flow slides that occurred in loessal bluffs overlooking the Gissar area. One of these slides developed into a mud flowslide that travelled approximately 2 km, killing approximately 220 villagers. Another slide, which experienced more limited displacements and deformations, will be studied here.

The "May 1" slide occurred in a loessal hillside overlooking the village of May 1. Figure A.11.2 shows a cross-section through this feature showing the pre-failure and post-failure conditions. This figure is from Olson (2001), and is based on Ishihara et al. (1990), except that the phreatic surfaces shown are inferred by Olson.

This is an interesting case history in several regards. The materials responsible for the failure are fine loessal silts, and they were very loose; at water contents that approximately equaled or exceeded their liquid limits. As a result they were prone to collapse. Earthquake shaking was not very strong, and it was also of short duration, but it was sufficient to "trigger" or initiate this failure. After failure, the materials were not likely subject to much additional shaking, so this was likely a "cyclically initiated" failure that then "flowed" under largely static loading conditions. After initiation of failure, the failure mass travelled only a limited distance, and came to rest with a "pressure ridge" (or bulge) at the toe.

The silt materials responsible were reportedly 100% fines, with approximately 15% clay content based on a hydrometer test (Ishihara et al., 1990). The loess material in the region is reported by Ishihara et al. (1990) to plot near the A-line with a plasticity index of generally PI ≈ 10%.

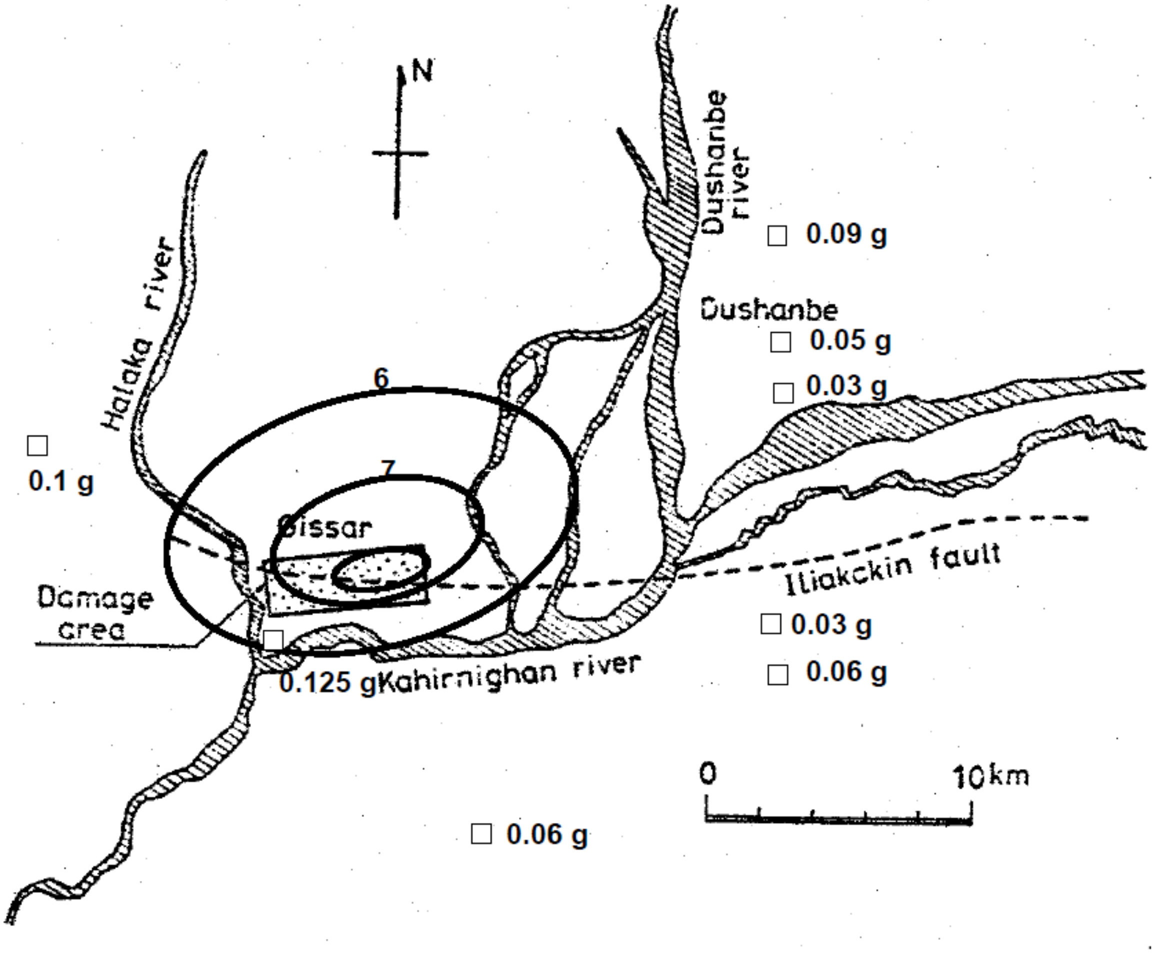

Figure A.11.1: Map of the Gissar area showing the location of the Iliakckin Fault, the damage zone, contours of estimated damage intensity, and recorded peak ground surface accelerations.

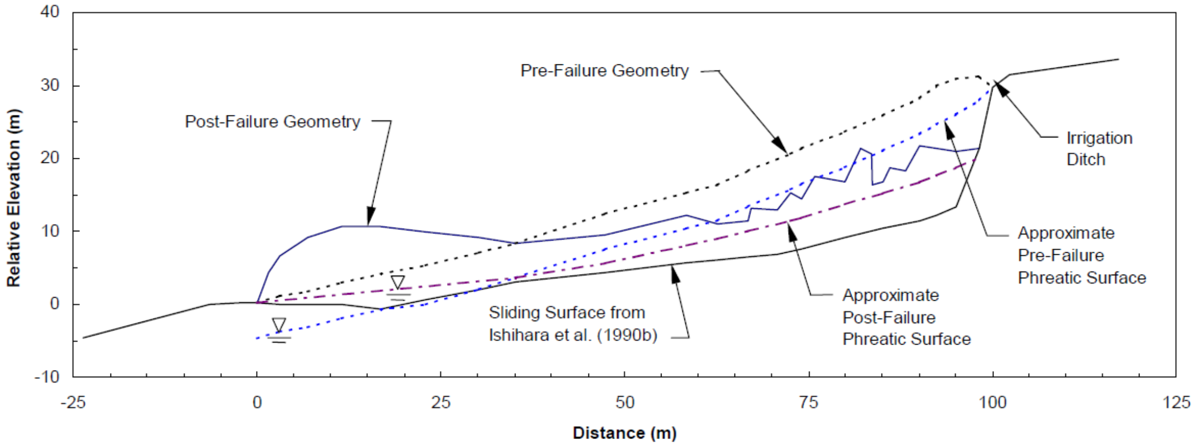

Figure A.11.2: Pre-failure and post-failure cross-sections of the Soviet Tajik May 1 slide (figure from Olson, 2002, after Ishihara et al, 1990)

Constraint as to the likely location of the basal slip surface was conditioned in part on the water content and liquidity indices of the loessal soils. The water contents varied significantly as a function of ground conditions and local irrigation efforts. As shown in Figure A.11.2 (pre-failure cross-section) there was an unlined irrigation ditch present near the crest of the slope. This resulted in elevated water levels within the slope. Ishihara et al. (1990) discuss the likely pre-failure water levels, and also the likelihood that the phreatic surface changed after the failure.

Ishihara et al. (1990) also suggested that the depth of cracking in the loess may play a significant role in its saturation, and in the distribution of differing water contents. Ishihara et al. indicated that the depth of cracking in the loess extended to depths of approximately 15 to 25 m. They also estimated that the pre-failure phreatic surface was located at a depth of approximately 5 m. prior to the failure, but without specificity as to the lateral location to which this assessment corresponds. Ishihara et al. state that the water content increases from a value near to the Plastic Limit at the phreatic surface (at a depth of approximately 5 m.) to water contents higher than the Liquid Limit at depths of between 7 to 17 m. In this range (depth ≈ 7 to 17 m.) with a liquidity index greater than 100%, these silty materials would be expected to be prone to collapse and flow. At slightly greater depths of between approximately 15 to 20m., the permeability of the loess decreases by approximately 4 to 5 orders of magnitude. It is inferred that these deeper loess materials would also be significantly denser and stronger, and that they were not involved in the failure except for their influence on the overlying phreatic conditions.

A.11.3 Initial Yield Strength Analyses

Figure A.11.3(a) shows the cross-section used in these studies for the best estimate case back-analyses to determine the initial yield stress, defined as the best estimate value of post-liquefaction $S_{r,yield}$ within the liquefiable hydraulic fill required to produce a calculated Factor of Safety equal to 1.0 for pre-failure geometry).

Based on the post-failure cross-section, it is assumed that this failure initiated as a monolithic failure, with the collapsible loessal silts that had in situ water contents at or greater than their liquid limits liquefying with the short initial shaking. A key issue here with regard to back-calculated strengths is the location of the phreatic surface at and near to the toe of the failure. Figure A.11.3(a) shows the best estimate cross-section in this regard, and this detail was then varied as part of parameter sensitivity studies.

Silty loess materials above the phreatic surface were modeled with $\text{Ø}' \approx 32°$, and a unit weight of $\gamma_m \approx 105$ lbs/ft^3. Silty loess materials below the phreatic surface were considered to liquefy, down to the base of the failure surfaces analyzed, and were assigned an undrained post-liquefaction yield strength of $S_{r,yield}$ that was constant along any given failure surface, and a unit weight of $\gamma_s \approx 118$ lbs/ft^3. Results for the best estimate conditions shown in Figure A.11.3 were $S_{r,yield} = 580$ lbs/ft^2.

The location of the phreatic surface was reasonably well constrained at the top of the slope by the presence of the operating irrigation ditch at the head of the failure scarp. The phreatic surface within the slope was considered to be approximately 5 m (16 ft) beneath the surface based.

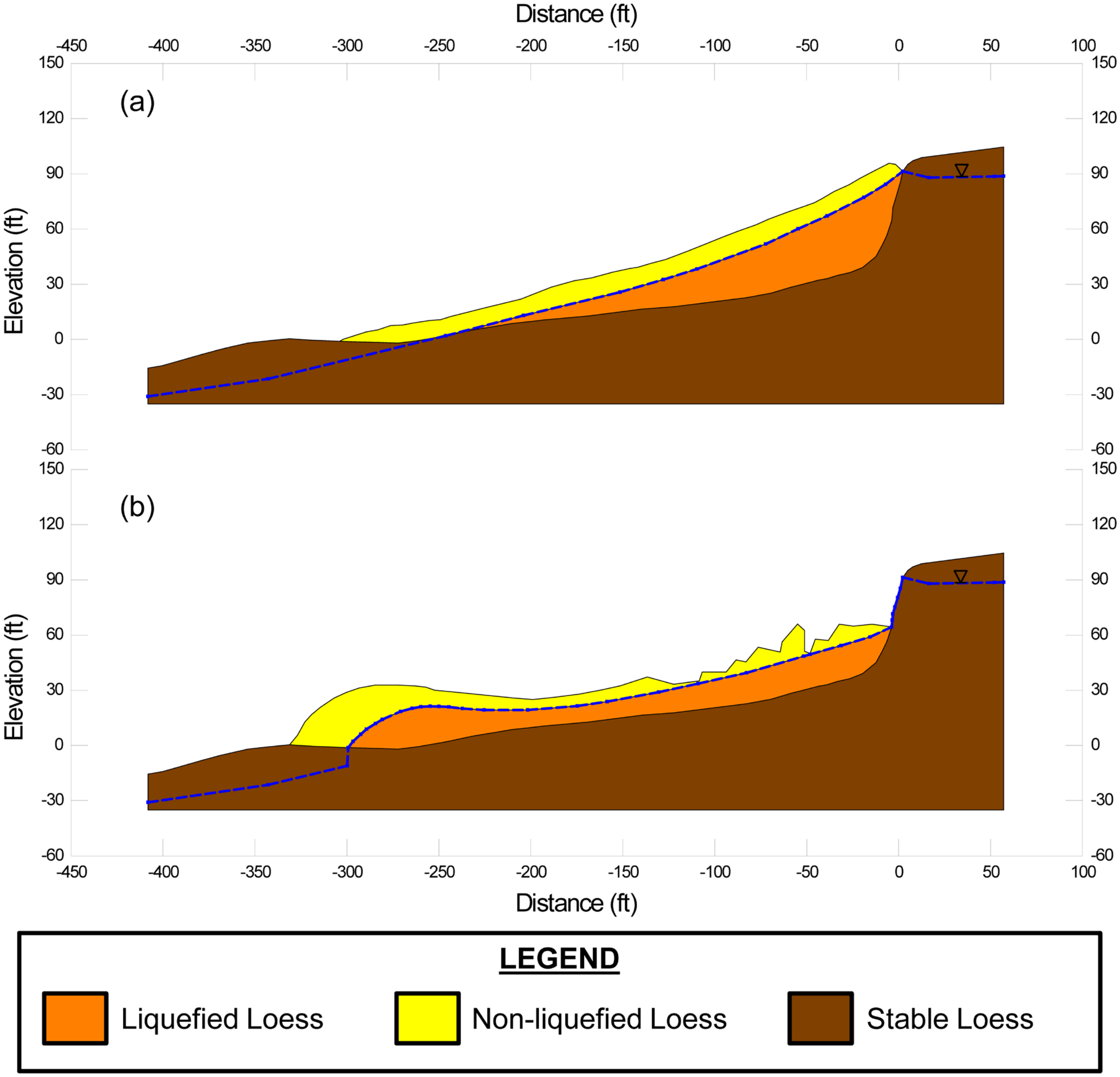

Figure A.11.3: Soviet Tajikistan Slope: (a) pre-failure geometry and failure surface for initial yield stress analyses, and (b) post-failure geometry and failure surface for post-failure residual geometry analyses.

on a general observation by Ishihara et al. (1990) of depth to ground water in the Gissar area. Due to the assumed location of the phreatic surface having a basis in only a general observation of the area, it was found that variations in the details of the phreatic surface at the toe of the slope, where a soil buttress formed during the failure, were a significant source of variance or uncertainty.

Parameters and geometry were then varied to examine parameter sensitivity. The phreatic surface was varied, raising it by up to 1.5 m (5 ft) at about the mid-point of the failure surface, and lowering it by up to a similar distance. Lesser variations in the phreatic surface were applied at the back heel and at the toe. Unit weights were also varied over the ranges considered likely (+/- 5 pcf for the saturated loessial silts), and the friction angle of non-liquefied material above the phreatic surface was varied from 30° to 35°. Searches were made for the most critical initial failure surface for each combination of assumptions and parameters modeled. The resulting range of values of $S_{r,yield}$ for combinations of modeling assumptions and details considered to be reasonable was found to be $S_{r,yield} \approx 545$ to 613 lbs/ft^2.

Olson (2001) also performed back-analyses to determine $S_{r,yield}$. Failure surfaces analyzed were similar, but there were some differences in the details of modeling of the phreatic surface and the failure surface. Olson reported values of $S_{r,yield} \approx 30.4$ to 32.3 kPa (635 to 675 lbs/ft^2), with a best estimate value of 31.6 kPa (660 lbs/ft^2).

A.11.4 Residual Strength Analyses Based on Residual Geometry

The calculation of the "apparent" post-liquefaction strength ($S_{r,resid/geom}$) required to produce a calculated Factor of Safety equal to 1.0 based on residual geometry is illustrated in Figure A.11.3(b). This figure shows the phreatic surface, and the failure surface, used to calculate the best-estimate value of $S_{r,resid/geom} \approx 166$ lbs/ft^2.

Variations were then made in parameters and assumptions, as for the analyses of yield strength as described in the preceding Section A.11.3. Variations were made to all key parameters and to the locations of the post-failure phreatic surface (extrapolated through failure, but not including subsequent drainage and redistribution of pore pressures, and of the failure surface. Considering ranges of variations in modeling details and parameters judged to be reasonable, the resulting likely range of post-liquefaction strength required to provide a calculated Factor of Safety equal to 1.0 based on residual geometry was considered to be $S_{r,resid/geom} \approx 128$ to 206 lbs/ft^2.

Olson (2001) also calculated post-liquefaction strength required to produce a calculated Factor of Safety equal to 1.0 based on residual geometry, and reported a best estimate value of $S_{r,resid/geom} \approx 8.4$ kPa (175 lbs/ft^2), with a range of $S_{r,resid/geom} \approx 2.9$ to 15.6 kPa (61 to 326 lbs/ft^2).

A.11.5 Incremental Momentum Back-Analyses and Overall Estimates of S_r

Incremental momentum back-analyses were performed using the same sets of properties and geometries (including failure surfaces and phreatic surfaces) as described in the previous sections. Strengths at the toe were assumed to be controlled by the post-liquefaction strength S_r, as it was assumed that the underlying materials had higher strengths based on the post-failure geometry observed.

Figure A.11.4 shows the best-estimate progressive incremental momentum analysis, showing the 5 stages of geometry evolution modeled as the failure proceeds. Figure A.11.5 shows the associated calculations of (1) acceleration vs. time, (2) velocity vs. time, and (3) displacement vs. time of the overall center of gravity. For the geometry and phreatic surface shown in Figure A.11.4, the best estimate value of post-liquefaction strength was $S_r = 341$ lbs/ft^2.

The main sources of uncertainty, or variability, in back-calculated values of S_r were (1) the location of the phreatic surface, especially at and near the toe, (2) details of the failure surface near the toe, and (3) unit weights. Considering ranges of variations in modeling details and parameters judged to be reasonable, the resulting likely range of post-liquefaction strength was considered to be $S_r \approx 260$ to 421 lbs/ft^2.

The analysis shown in Figures A.11.4 and A.11.5 neglects cyclic inertial forces, but this is not expected to significantly affect the assessment of actual post-liquefaction strength mobilized for this somewhat unusual case, because cyclic inertial forces appear to have been moderate to minimal during the actual failure movements.

Based on all analyses performed, and the considerations discussed herein, the overall best estimate value of post-liquefaction strength for the Soviet Tajik May 1 slope failure was judged to be $S_r \approx 341$ lbs/ft^2, with a likely range of $S_r \approx 431$ to 260 lbs/ft^2. Based on the factors contributing to uncertainty or variance for this case history, it was the judgment of the investigation team that this range represented approximately +/− 1.5 standard deviations. This range of variance is not symmetrical about the best estimate value, so minor further adjustments were made to produce a representative estimate of S_r suitable for regression analyses.

Overall, based on an assumed normal distribution, it was judged that the (mean and median) best estimate of post-liquefaction strength for this case history is

$$\overline{S_r} = 341 \text{ lbs/ft}^2$$

and that the best estimate of standard deviation of mean overall post-liquefaction strength is

$$\sigma_{\overline{S}} = 57 \text{ lbs/ft}^2$$

Estimates of S_r were also reported by several other investigation teams, and two sets of these are shown in Table A.11.1(a). Olson (2001) and Olson and Stark (2002), reported a best estimate value of $S_r = 8.4$ kPa (178 lbs/ft^2), but this was not based on their "kinetics" analyses that considered momentum effects. Instead, it was based on assessment of the post-liquefaction residual geometry and it neglected momentum effects. As a result, it will be an overly conservative estimate (the value will be much too low). Olson also calculated $S_{r,yield}$ and $S_{r,resid/geom}$ (see Sections A.11.3 and A.11.4) for this case, however, and those two values can be convolved to provide a better estimate of S_r. Based on Equation 4-1, a better estimate for S_r can be developed based on the back-calculations of $S_{r,yield}$ and $S_{r,resid/geom}$ performed by Olson (2001) as $S_r \approx [S_{r,yield} + S_{r,resid/geom}] \times 0.8 \approx [31.6 \text{ kPa} + 8.4 \text{ kPa}] \times 0.8 \approx 16.0$ kPa (334 lbs/ft^2), and this value is more

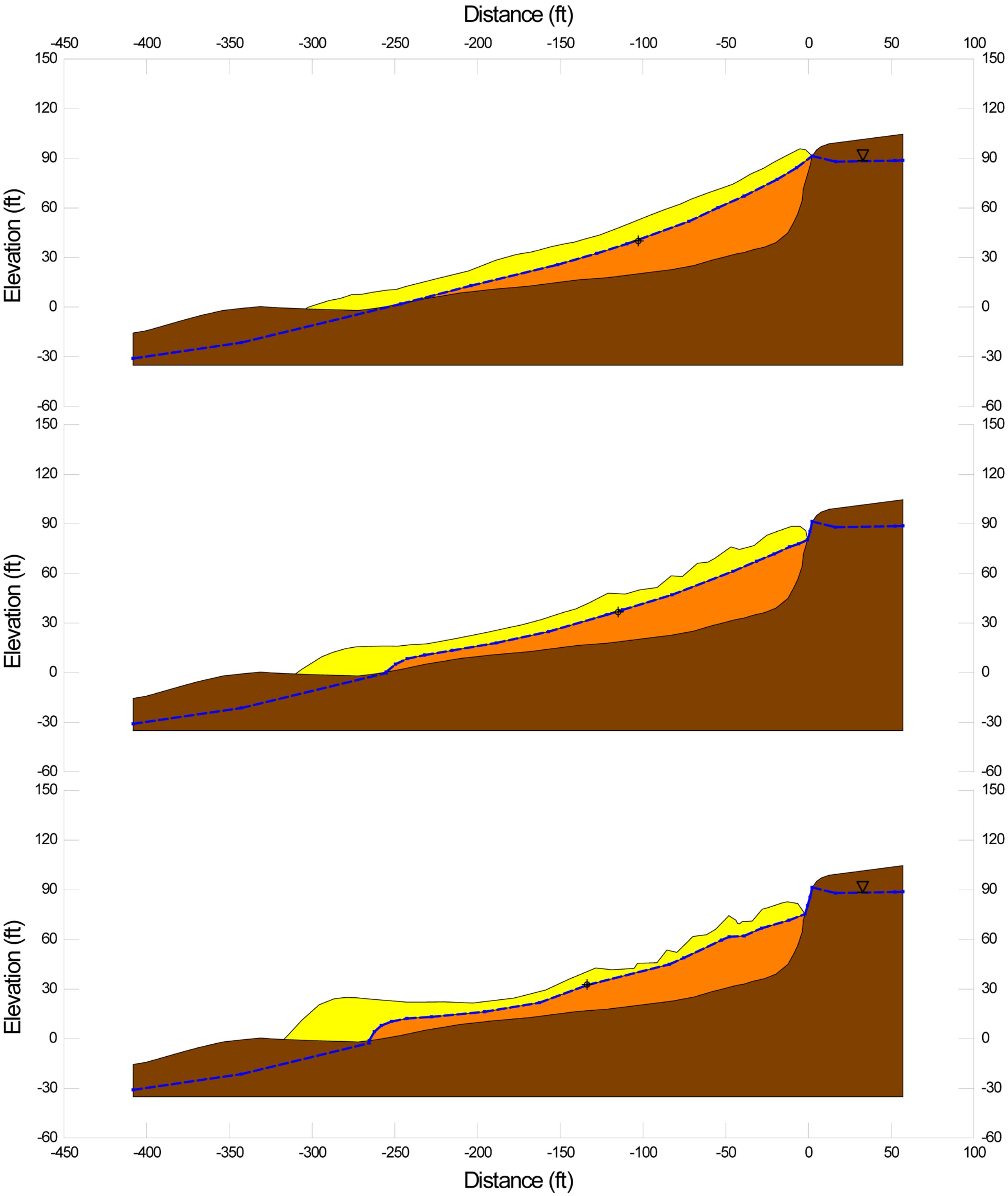

Figure A.11.4(a): Incremental momentum analysis of the failure of the Soviet Tajikistan slope failure, showing the progressive evolution of cross-section geometry modeled (first three cross-sections).

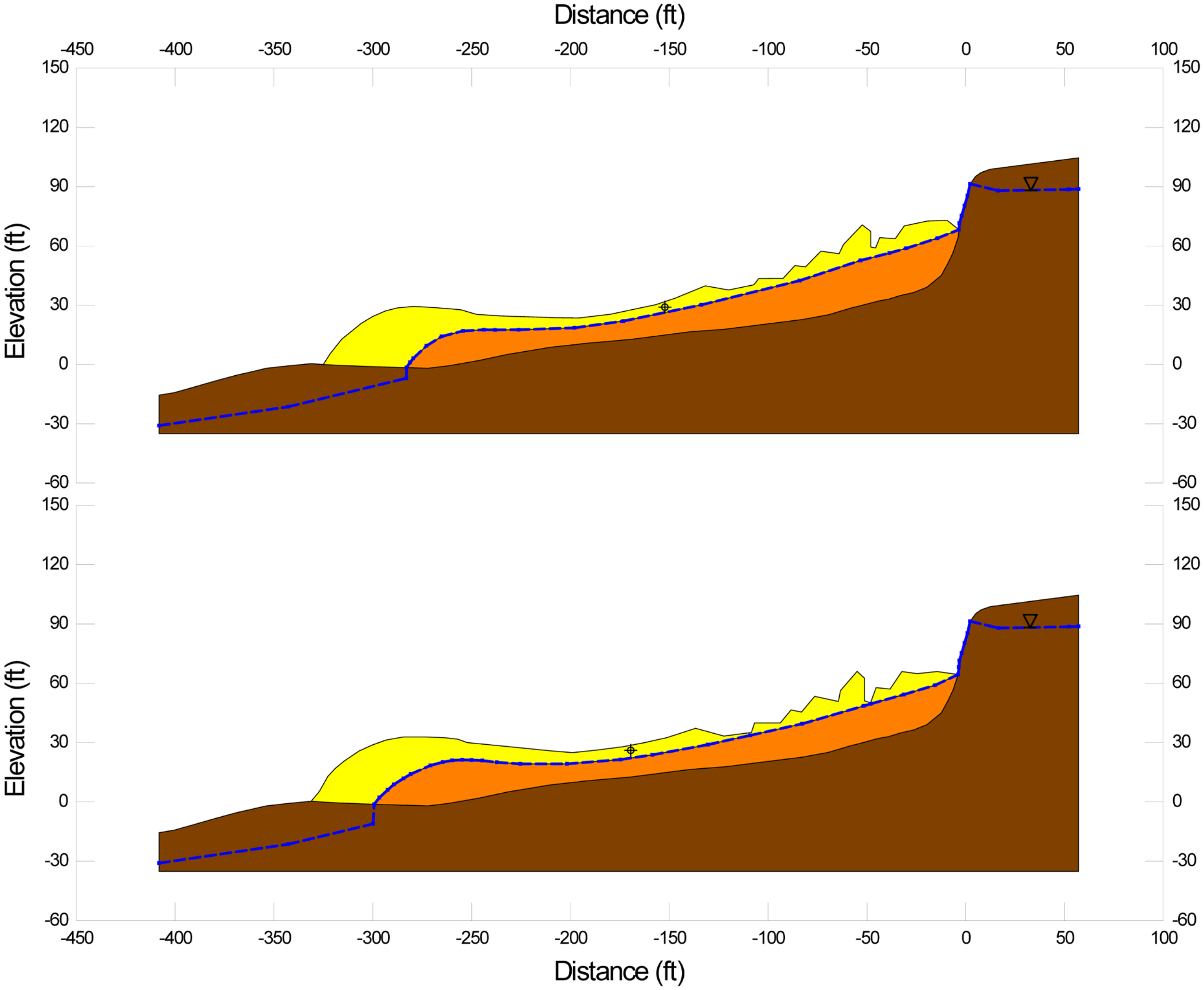

Figure A.11.4(b): Incremental momentum analysis of the failure of the Soviet Tajikistan slope failure, showing the progressive evolution of cross-section geometry modeled (final two cross-sections).

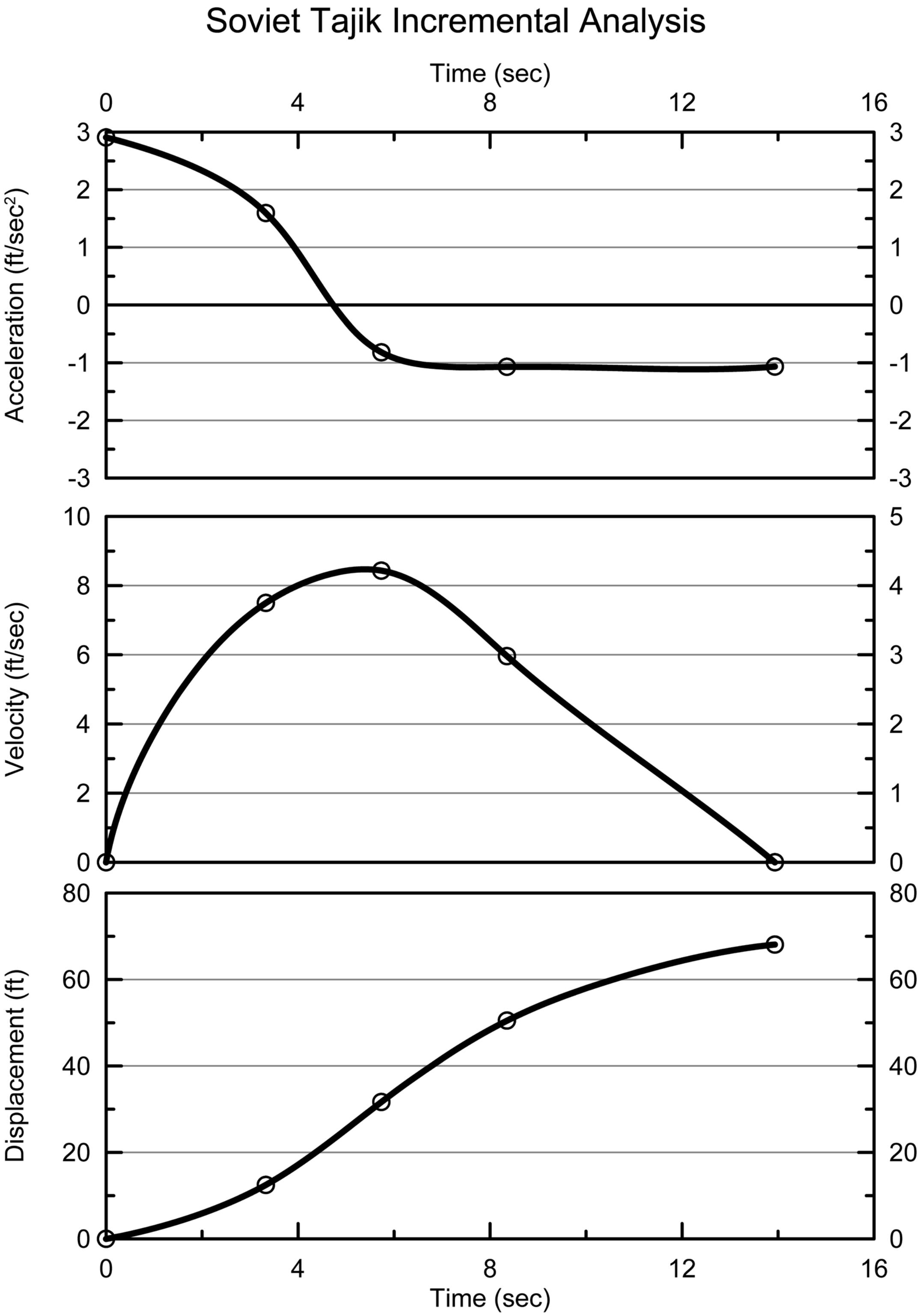

Figure A.11.5: Incremental momentum analysis of the failure of the Soviet Tajik slope failure, showing progressive evolution of: (1) acceleration vs. time, (2) velocity vs. time, and (3) displacement vs. time of the center of gravity of the overall failure mass.

directly comparable with the values of this current study. Accordingly, the value listed in Table A.11.1 for Olson and Stark is $S_r \approx 334$ lbs/ft^2, and this agrees well with these current studies.

Wang (2003) and Wang and Kramer (2008) did not employ their zero inertial force (ZIF) method to incorporate inertial effects in their back-analyses of this failure; instead they developed their estimates of both mean $\overline{S_r}$ = 334 lbs/ft^2 as well as the associated standard deviation $\sigma_{\bar{S}}$ = 111 lbs/ft^2 based on evaluation and consideration of back-analyses performed by other teams of previous investigators. It is not possible to fully back-check these choices and judgments. What is remarkable, is the level of agreement between these three disparate teams of investigators, as the best estimate values of S_r for (1) Olson and Stark, (2) Wang and Kramer, and (3) these current studies are S_r = 334 lbs/ft^2, 334 lbs/ft^2 and 341 lbs/ft^2, respectively. Olson and Stark provide no range or estimate of variance. Wang and Kramer estimate that $\sigma_{\bar{S}}$ = 111 lbs/ft^2, and the value developed in these current studies is $\sigma_{\bar{S}}$ = 57 lbs/ft^2. Overall, agreement between the three investigation teams is excellent here.

A.11.6 Evaluation of Initial Effective Vertical Stress

Average initial (pre-failure) effective vertical stress was assessed for the liquefied zones of each of the initial failure surface shown in Figure A.11.4(a). The resulting best estimate of average pre-failure effective stress within the liquefied materials controlling the failure was then $\sigma_{vo}' \approx$ 1,907 lbs/ft^2, with a reasonable range of $\sigma_{vo}' \approx$ 2,263 to 1,555 lbs/ft^2. This range is slightly non-symmetric about the median value, and this range was judged by the engineering team to represent approximately +/− 2 standard deviations. Overall, the best characterization of initial (pre-failure) average effective vertical stress was then taken to be represented by a mean value of

$$\overline{\sigma'_{vo}} \approx 1{,}907 \text{ lbs/ft}^2$$

and with a standard deviation of

$$\sigma_{\bar{\sigma}} \approx 177 \text{ lbs/ft}^2$$

Estimates of σ_{vo}' were also reported by other investigation teams, and two sets of these are shown in Table A.11.1(c). Olson (2001) calculated an average initial effective vertical stress of σ_{vo}' = 106 kPa (2,214 lbs/ft^2). Average initial vertical effective stresses were not directly reported by Wang (2003) and Kramer (2008), but they were published more recently in the publication by Kramer and Wang (2015). As discussed in Section 2.3.8.1(b)-(iii), Wang (2003) did not perform any independent analyses to assess σ_{vo}' for his 22 "secondary" cases, and this is one of those cases. Instead, he compiled values of S_r from multiple previous investigators, and averaged these for a best estimate. He also compiled multiple values of S_r/σ_{vo}' from previous investigators, and averaged these for a best estimate. He then used these two best-estimate values of S_r and S_r/σ_{vo}' to infer a resulting representative value of σ_{vo}'. As described in Section 2.3.8.1(b)-(iii), the resulting averaged values of S_r and S_r/σ_{vo}' were incompatible with each other for a number of Wang's "secondary" case histories, and this process produced unreasonable, and in some cases physically infeasible, values of σ_{vo}' for a number of case histories. Accordingly, Wang's value of $\sigma_{vo}' = 4{,}122$ lbs/ft^2 is not considered a useful check here. Agreement between the values of (1) Olson and Stark (2001, 2002) and (2) these current studies is very good.

A.11.7 Evaluation of $N_{1,60,CS}$

Only very limited data and information was available as a basis for evaluation of representative penetration resistances for the silty loessial soils. As a result, this is a case history in which back-calculated values of S_r and σ_{vo}' are well constrained, but there is large uncertainty regarding $N_{1,60,CS}$.

No SPT data are available for this case history. Instead, a portable cone penetrometer was used to evaluate penetration resistance (Ishihara et al, 1990). The penetration tests were performed from the bottom of a crack in the post-slide failure zone, and extended downwards to the approximate depth of the apparent sliding surface. At that depth, the value of qc1 ranged from approximately 1.1 to 2.4 MPa. Olson (2001) selected a "representative" value of 1.9 MPa, and the current investigation team did the same. Using $q_{c1}/N_{1,60} \approx 2.5$, the current investigation team estimated $N_{1,60} \approx 7.6$ blows/ft. This was further adjusted for fines content (FC = 100%, all silt) as per Appendix C, to develop a best estimate value of $\overline{N_{1,60,CS}} \approx 10.5$ blows/ft. A significant range of uncertainty was then inferred due to (1) paucity of data, and (2) uncertainty regarding transformation of q_{c1} to $N_{1,60}$ for the portable CPT. Overall, the assessment of the current investigation team was that penetration resistance would be characterized as

$$\overline{N_{1,60,CS}} = 10.5 \text{ blows/ft}, \quad \text{and} \quad \sigma_{\overline{N}} = 2.7 \text{ blows/ft}.$$

Values were also developed by other investigation teams, and two sets of these are presented in Table A.11.1(b). Olson and Stark (2001, 2002) employed values of $N_{1,60} = 7.6$ blows/ft, with a range of 4.4 to 9.6 blows/ft. Wang and Kramer (2003, 2008) selected values of $\overline{N_{1,60,CS}} = 8.9$ blows/ft, and $\sigma_{\overline{N}} = 5.7$ blows/ft. The value of Olson and Stark is somewhat lower than those of (1) Wang and Kramer, and (2) these current studies because Olson and Stark did not make a fines adjustment, so theirs is an $N_{1,60}$ value rather than an $N_{1,60,CS}$ value. Given that the loessial soils of interest here are entirely silts, the fines adjustment by any recent approach would raise their value to an $N_{1,60,CS}$ value equal to or higher than those of (1) Wang and Kramer, or (2) these current studies. Overall, agreement between the three investigation teams is very good here.

A.11.8 Additional Indices from the Back-Analyses

A number of additional results, and indices, can be extracted from the analyses performed. Some of these are useful in developing some of the over-arching relationships and figures presented in the main text of this report. These values are presented in Table A.11.2.

Table A.11.1: Representative values for the Soviet Tajik May 1 slope failure case history of: (a) post-liquefaction strength (S_r), (b) initial vertical effective stress (σ_{vo}'), and (c) $N_{1,60,CS}$ developed by various investigation teams, and estimates of variance in each of these indices when available.

(a) Post-Liquefaction Strength:	
Olson (2001) and Olson and Stark (2002)*	$S_r \approx$ 334 psf*
Wang (2003) and Kramer (2008)	$\overline{S_r}$ = 334 psf, and $\sigma_{\bar{S}}$ = 111 psf
This Study	$\overline{S_r}$ = 341 psf and $\sigma_{\bar{S}}$ = 57 psf
(b) Representative $N_{1,60}$ or $N_{1,60,CS}$ Value:	
Olson (2001) and Olson and Stark (2002)	$N_{1,60}$ = 7.6 bpf, and range = 4.4 to 9.6 bpf
Wang (2003) and Kramer (2008)	$\overline{N_{1,60,CS}}$ = 8.9 bpf, and $\sigma_{\bar{N}}$ = 5.7 bpf
This Study	$\overline{N_{1,60,CS}}$ = 10.5 bpf, and $\sigma_{\bar{N}}$ = 2.7 bpf
(c) Representative Initial Vertical Effective Stress:	
Olson (2001) and Olson and Stark (2002)	σ'_{vo} = 2,270 psf, with no range given.
Wang (2003) and Kramer (2008)	Value of $\sigma_{vo}' \approx$ 4,122 psf is poorly based, and so is not useful as a basis for comparison. (See Section 2.3.8.1(b) and Table 2.3)
This Study	$\overline{\sigma'_{vo}}$ = 1,907 psf, and $\sigma_{\bar{\sigma}}$ = 177 psf

* Olson (2001) did not employ his "kinetics" back-analysis approach to this case. See the text of Section A.11.5 for an explanation of the value and so his residual geometry based value of $S_r \approx$ 334 psf attributed here.

Table A.11.2: Additional results and indices from the analyses of the Soviet Tajik May 1 Slope failure case history.

Maximum distance traveled by the center of gravity of the overall failure mass	68.1 ft.
Initial post-liquefaction Factor of Safety prior to displacement initiation, and based on best estimate value of S_r	FS = 0.60
Final post-liquefaction Factor of Safety at final (residual) post-failure geometry, and based on best estimate value of S_r	FS = 1.45

A.12 Shibecha-Cho Embankment (Hokkaido, Japan; 1993)

A.12.1 Brief Summary of Case History Characteristics

Name of Structure	Shibecha-Cho Embankment
Location of Structure	Hokkaido, Japan
Type of Structure	Side Hill Structural Fill Pad
Date of Failure	September 22, 1933
Nature of Failure	Seismic, During the 1993 Kushiro-Oki Earthquake (M_L = 7.8)
Approx. Maximum Slope Height	33.7 ft.

A.12.2 Introduction and Description of Failure

The Shibecha-Cho Embankment failed during Kushiro-Oki Earthquake of January 15, 1993 (M_L = 7.8), and was initially investigated by Miura et al. (1995, 1998). Miura et al. estimated that the peak ground acceleration at this site was approximately 0.38 g.

Figure A.12.1 (from Miura et al., 1998) shows a plan view of the large embankment fill, and the resort development which was developed atop this fill platform. The embankment was constructed of fill taken from cut and fill operations on the adjacent slopes. Figure A.12.1 shows the locations in plan view of four cross-sections developed with pre-failure and post-failure geometries, and Figure A.12.2 shows these four cross-sections. Movements were only minor to moderate at cross-sections A, C and D, and it was judged here that these cross-sections were not suitable for the types of back-analyses performed in these current studies to evaluate post-liquefaction strengths because the scales of these movements could likely be explained to some significant degree by cyclic lurching displacements, so that accurate calculation of fully developed post-liquefaction S_r would be difficult. Cross-section B, on the other hand, experienced a flow-type of failure with large displacements, and it is this cross-section that will be analyzed here.

Post-failure geotechnical investigation for this case history was performed mainly by means of Swedish cone soundings, and the locations of these soundings are shown in Figure A.12.2 (from Miura et al., 1998). These soundings reasonably well constrain the key ground conditions at the base of the failure, especially beneath the main body of the failure zone and at the rear heel, as there is a relatively distinct increase in penetration resistance at the interface between the base of the fill and the “harder” underlying native soils. Figures A.12.3(a) and A.12.3(b) show the interpretations of cross-section geometry and stratigraphy for the pre-failure and post-failure cross-section at Cross-Section B made by Olson (2001). These are reasonable interpretations, and the topographic and stratigraphic interpretations employed in these current studies were in good agreement with these interpretations of Olson for the “best estimate” analyses performed here, although some alternate modeling of additional potential failure surfaces was performed for these current studies.

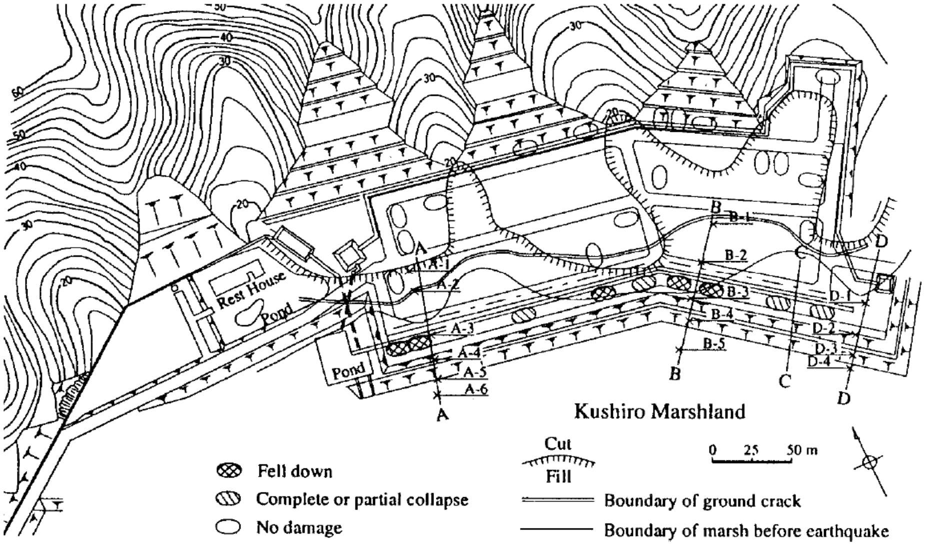

Figure A.12.1: Plan view of the Shibecha-Cho Embankment fill and the resort development atop the fill, showing the locations of four post-failure cross-sections (from Miura et al., 1998)

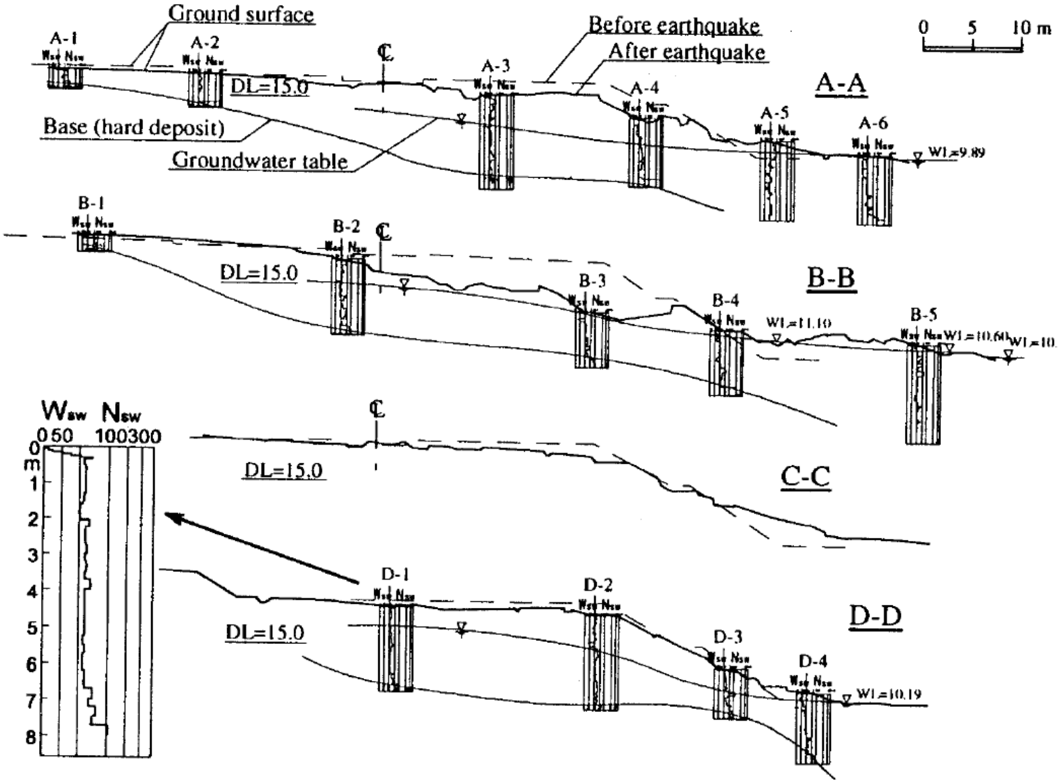

Figure A.12.2: Cross-sections A-A, B-B, C-C and D-D from Figure A.12.1 above (from Miura et al, 1998)

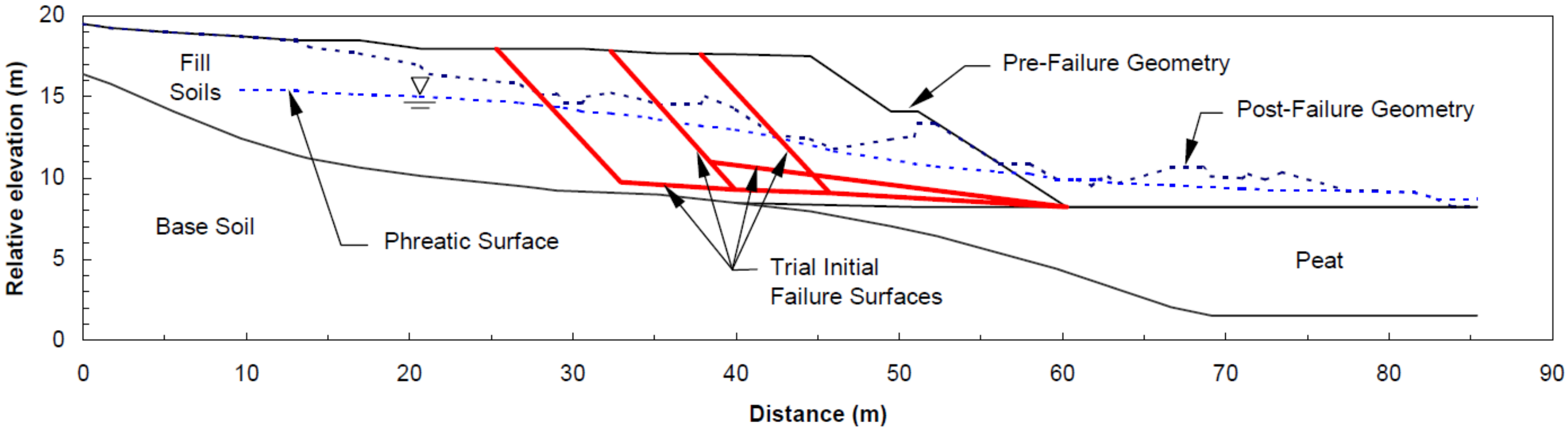

Figure A.12.3(a): Pre-failure geometry of the Shibecha-Cho Embankment showing failure surfaces used by Olson (2001) for calculation of post-liquefaction initial yield strength $S_{r,yield}$ (Figure from Olson, 2001).

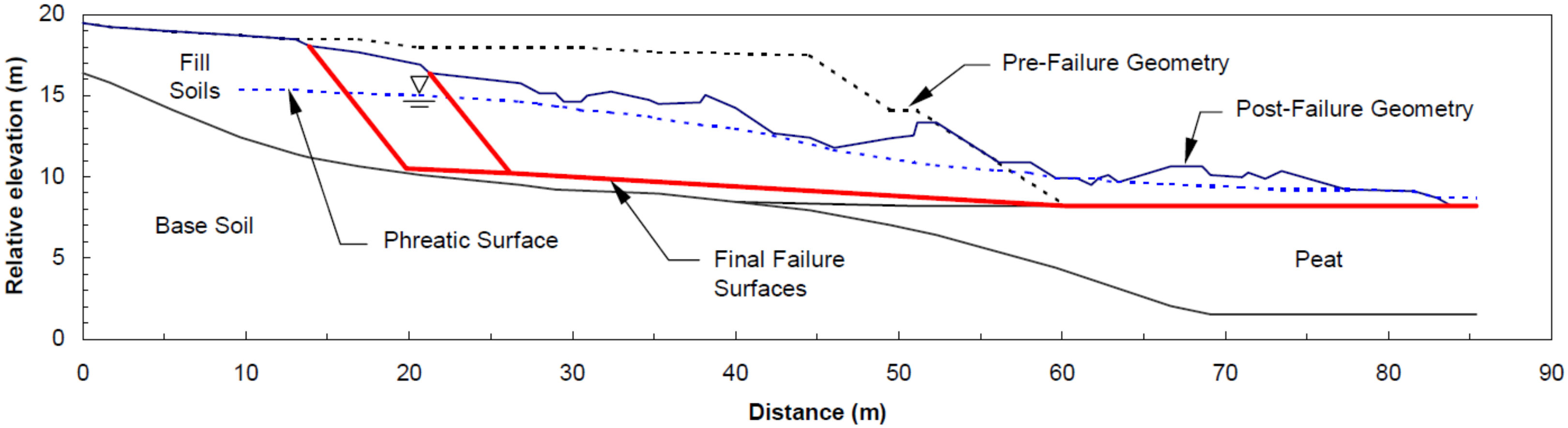

Figure A.12.3(b): Pre-failure geometry of the Shibecha-Cho Embankment showing failure surfaces used by Olson (2001) for calculation of post-liquefaction strength $S_{r,resid/geom}$ (Figure from Olson, 2001).

The embankment fill was comprised of the same volcanic silty sand ash deposits as the adjacent and underlying materials comprising the natural hills. This material had a fines content that varied between approximately 12% to 33%, with a representative value of approximately 20% (Yasuda et al, 1993; Saito et al., 1993 and Mori, 1993), but some of these gradations are taken from sampled boil ejecta and may have segregated somewhat during transport and ejection. The embankment fill was placed without formal, controlled engineering compaction and so was only lightly and variably compacted by random construction traffic.

As shown in Figure A.12.3(a), a unit of peaty marsh deposits (the adjacent Kushiro Marshland) occurs beneath the toe of the pre-failure embankment, and this peat extends farther out from the toe. Two uncertainties in performing back-analyses of this case history are (1) whether or not the failure extended into the peaty marsh deposits beneath the embankment toe and (2) peat shear strengths as the toe of the embankment translated outwards further onto the peats during the failure. Lack of reported upwards bulging beyond the toe suggests that the failure did not extend into the peaty deposits at the toe. But there are other possibilities, and this will be discussed further.

Another uncertainty is the location of the phreatic surface at the time of the failure.

A.12.3 Initial Yield Strength Analyses

Figure A.12.4(a) shows the cross-section used in these studies for the best estimate case back-analyses to determine the initial yield stress, defined as the best estimate value of post-liquefaction $S_{r,yield}$ within the liquefiable hydraulic fill required to produce a calculated Factor of Safety equal to 1.0 for pre-failure geometry.

It is not known whether this failure initiated as a monolithic failure, or as an incrementally progressive failure that retrogressed backwards towards the back heel in incrementally progressive slices. Based on an assumed phreatic surface that passes approximately through the mid-height of the slope, and exits at the toe, a search was made for the most critical static failure surface assuming that liquefaction had been "triggered" in all potentially liquefiable embankment materials below the phreatic surface. This exercise showed that the most critical potential failure surfaces for this set of assumptions would have been for a failure initially closer to the slope face than the final rear scarp shown in Figure A.12.1.

Figure A.12.4(a) shows two potential failure surfaces analyzed. The rear-most surface is the eventual "final" underlying (or bounding) failure surface, which is reasonably well constrained by the data available. The other failure surface is the surface that was found to be a more critical initial yield surface (requiring a higher value of post-liquefaction yield strength in order to produce a calculated static Factor of Safety = 1.0). Silty sand embankment fill materials above the phreatic surface were modeled with $Ø' \approx 35°$, and a unit weight of $\gamma_m \approx 90$ lbs/ft^3. Materials below the phreatic surface were considered to liquefy, down to the base of the failure surfaces analyzed, and were assigned an undrained post-liquefaction yield strength of $S_{r,yield}$ that was constant along any given failure surface, and a unit weight of $\gamma_s \approx 95$ lbs/ft^3. Results for the most critical initial yield surface (near to the front face of the embankment) were $S_{r,yield} = 415$ lbs/ft^2.

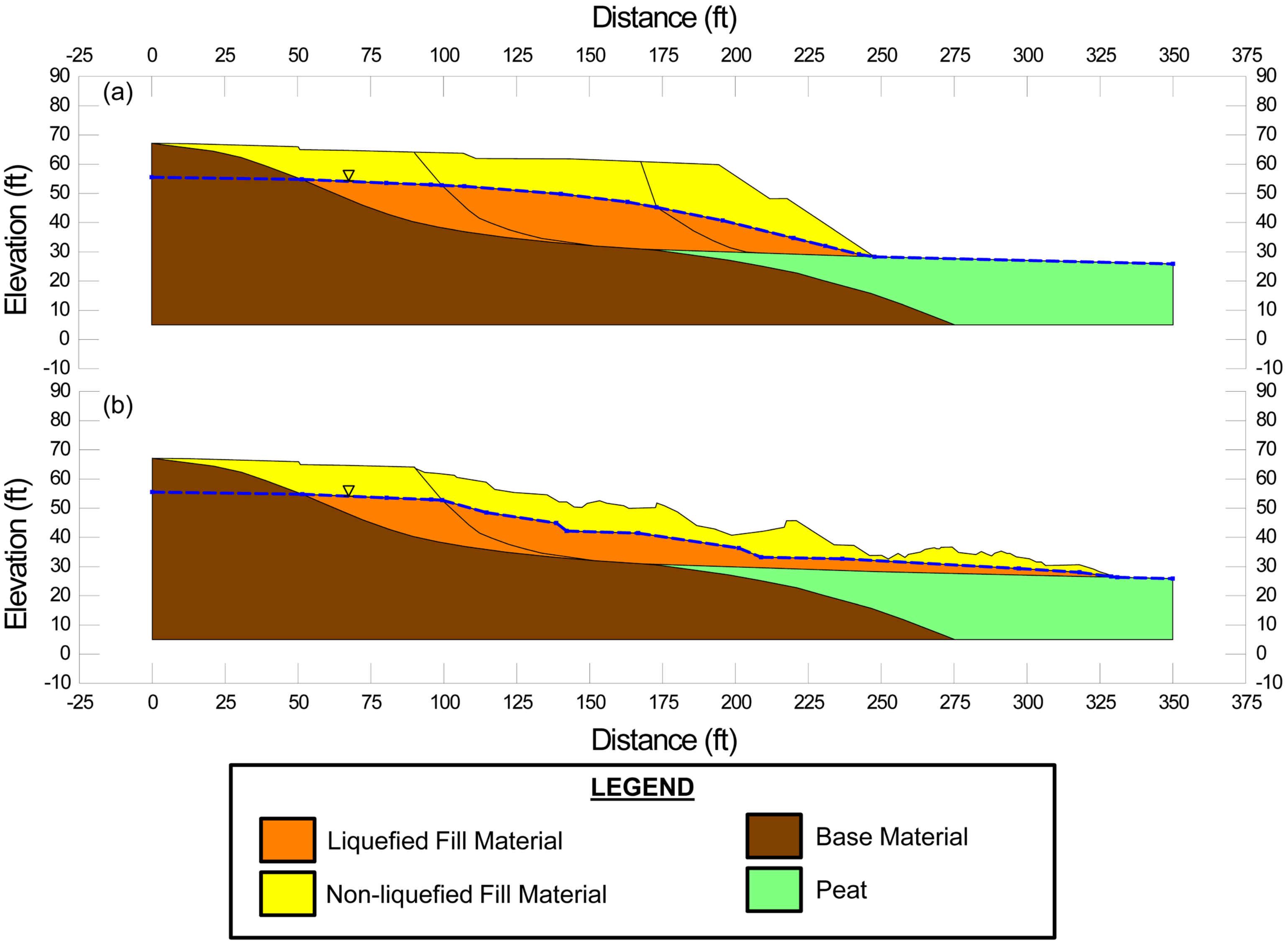

Figure A.12.4: Shibecha-Cho Embankment cross-section showing (a) pre-failure geometry showing failure surfaces used for initial yield stress analyses, and (b) post-failure geometry and best-estimate failure surface for post-failure residual geometry analyses.

Parameters and geometry were then varied to examine potentially variability. The location of the phreatic surface was varied, raising it by up to 1.5 m (5 ft) at the back heel of the final failure surface, and lowering it by up to a similar distance. The phreatic surface was considered to exit at or near the toe of the slope, based on the observed failure (and post-failure geometry), while the location of the phreatic surface within the embankment was varied. Unit weights were also varied over the ranges considered likely, and the friction angle of non-liquefied material above the phreatic surface was varied from 30° to 37°. Searches were made for the most critical initial failure surface for each combination of assumptions and parameters modeled. The resulting range of values of $S_{r,yield}$ for combinations of modeling assumptions and details considered to be reasonable was found to be $S_{r,yield} \approx 367$ to 467 lbs/ft^2.

Olson (2001) also performed back-analyses to determine $S_{r,yield}$. Failure surfaces analyzed were similar, but did not appear to include surfaces extending fully back to the rear heel of the eventual "final" yield surface for the evaluation of $S_{r,\ yield}$. Olson reported values of $S_{r,yield} \approx 14.8$ to 18.7 kPa (309 to 391 lbs/ft^2).

A.12.4 Residual Strength Analyses Based on Residual Geometry

The calculation of the "apparent" post-liquefaction strength ($S_{r,resid/geom}$) required to produce a calculated Factor of Safety equal to 1.0 based on residual geometry is illustrated in Figure A.12.4(b). This figure shows the phreatic surface, and the failure surface, used to calculate the best-estimate value of $S_{r,resid/geom} \approx 147$ lbs/ft^2. Variations were then made in parameters. One key parameter here was the strength in the underlying peaty marsh deposits outside the toe. Strength outside the toe was varied, with the minimum toe strength assumption being that shear strength within the underlying peaty marsh deposits was less than that of the liquefied embankment fill, and a minimum shear strength of 50% of that of the calculated initial yield strength of the overlying embankment fill was employed. This case was judged to be of low likelihood, however, based on the lack of (a) observed compression wrinkles in the peaty marsh deposits just beyond the toe, and (b) lack of vertical heave in this same area. The upper bound toe strength condition assumed at the base of the toe section was the full post-liquefaction strength (S_r) of the liquefied embankment fill, and this was also the best estimate case. Variations were also made to other parameters and to the location of the pre-failure phreatic surface, as was described in the preceding section in order to evaluate uncertainty or variability, except that all analyses assumed that the failure surface defining the boundaries of the eventual full failure mass controlled $S_{r,resid/geom}$. Considering ranges of variations in modeling details and parameters considered to be reasonable, the resulting likely range of post-liquefaction strength required to provide a calculated Factor of Safety equal to 1.0 based on residual geometry was considered to be $S_{r,resid/geom} \approx 126$ to 172 lbs/ft^2.

Olson (2001) also calculated post-liquefaction strength required to produce a calculated Factor of Safety equal to 1.0 based on residual geometry, and reported a best estimate value of $S_{r,resid/geom} \approx 5.0$ kPa (104 lbs/ft^2), with a range of $S_{r,resid/geom} \approx 4.1$ to 6.2 kPa (86 to 130lbs/ft^2).

A.12.5 Incremental Momentum Back-Analyses and Overall Estimates of S_r

Incremental momentum back-analyses were performed using the same sets of properties and geometries (including failure surfaces and phreatic surfaces) as described in the previous sections. Strengths at the toe, both beneath the original embankment toe, and beneath the toe section as it translated outwards over the peaty marsh deposits, were modeled as 100% of S_r for the liquefiable embankment fill for the case illustrated in Figures A.12.5 and A.12.6.

Figure A.12.5 shows the best-estimate progressive incremental momentum analysis, showing the 5 stages of geometry evolution modeled as the failure proceeds. Figure A.12.6 shows the associated calculations of (1) acceleration vs. time, (2) velocity vs. time, and (3) displacement of the overall center of gravity vs. time. For the geometry and phreatic surface shown in Figure A.13.3, the best estimate value of post-liquefaction strength was $S_r = 224$ lbs/ft^2.

Based on the initial yield strength analyses described previously, and the observed pre- and post-failure field geometry, failure was modeled as proceeding in a progressive series of slices retrogressing back towards the back heel. This required some judicious juggling of progressively changing overall failure surface mass, momentum and velocity as successive slices began to join in the failure. The incremental momentum analyses for this case history are a bit more approximate than for most other cases as a result.

The main sources of uncertainty, or variability, in back-calculated values of S_r were (1) the location of the phreatic surface, (2) whether or not the failure initiated largely monolithically or retrogressed progressively towards the back heel in a series of “slices”, and the discretization and timing of successive slice initiation, (3) unit weights, (4) whether the failure surface at and near the toe the ran along within the base of the liquefiable embankment fill or passed into the underling peaty marsh deposits, and (5) the precise location of the overall failure surface.

The analysis shown in Figures A.12.5 and A.12.6 neglects cyclic inertial forces, and so may represent a slightly conservative assessment of actual post-liquefaction strength mobilized, but this minor conservatism was neglected.

Based on all analyses performed, and the considerations discussed herein, the overall best estimate value of post-liquefaction strength for the Shibecha-Cho Embankment failure was judged to be $S_r \approx 224$ lbs/ft^2, with a likely range of $S_r \approx 166$ to 277 lbs/ft^2. Based on the factors contributing to uncertainty or variance for this case history, it was the judgment of the investigation team that this range represented approximately +/− 1.5 standard deviations. This range of variance is not symmetrical about the best estimate value, so minor further adjustments were made to produce a representative estimate of S_r suitable for regression analyses.

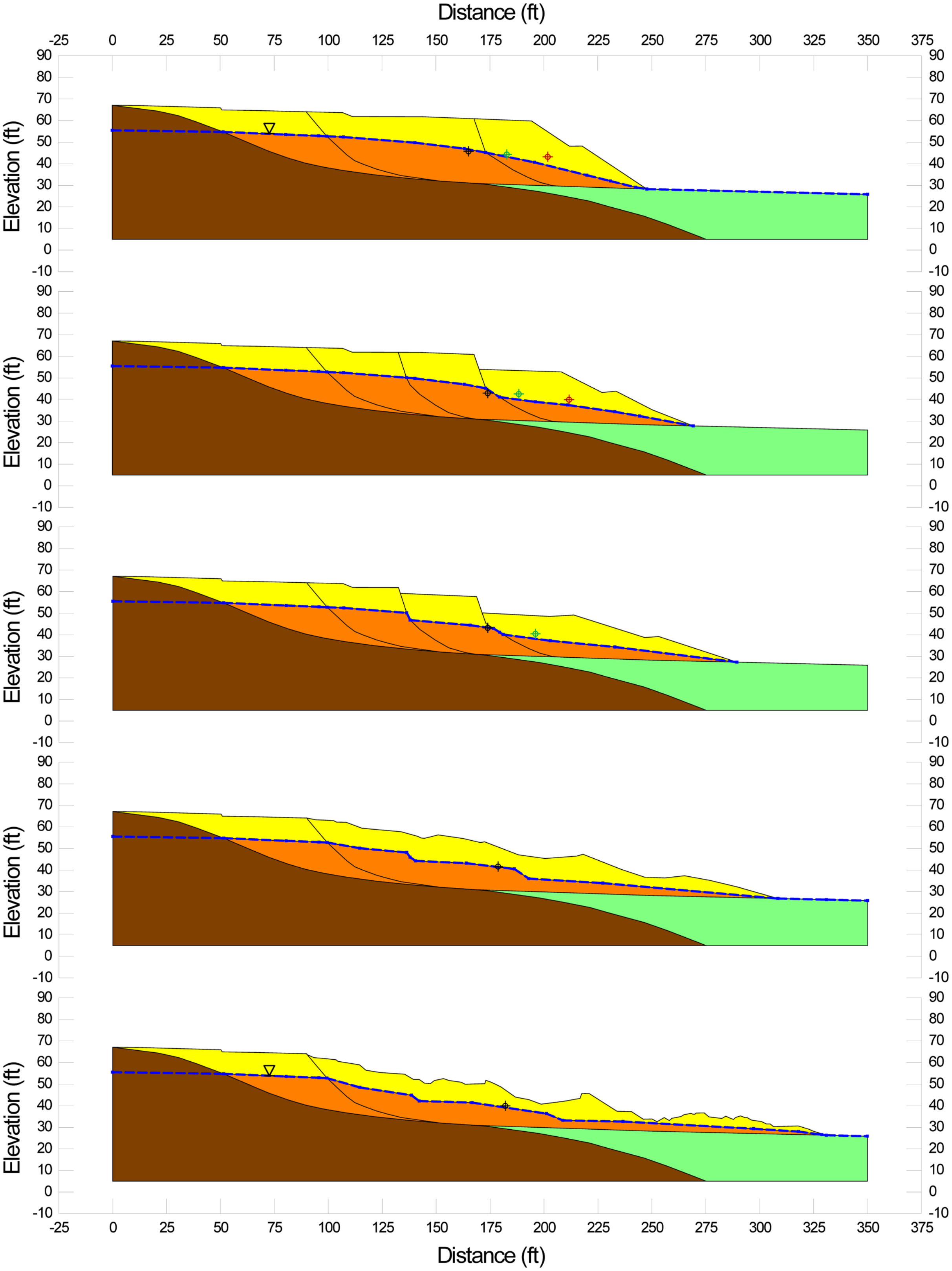

Figure A.12.5: Incremental momentum analysis of the failure of the Shibecha-Cho Embankment, showing progressive evolution of cross-section geometry modeled.

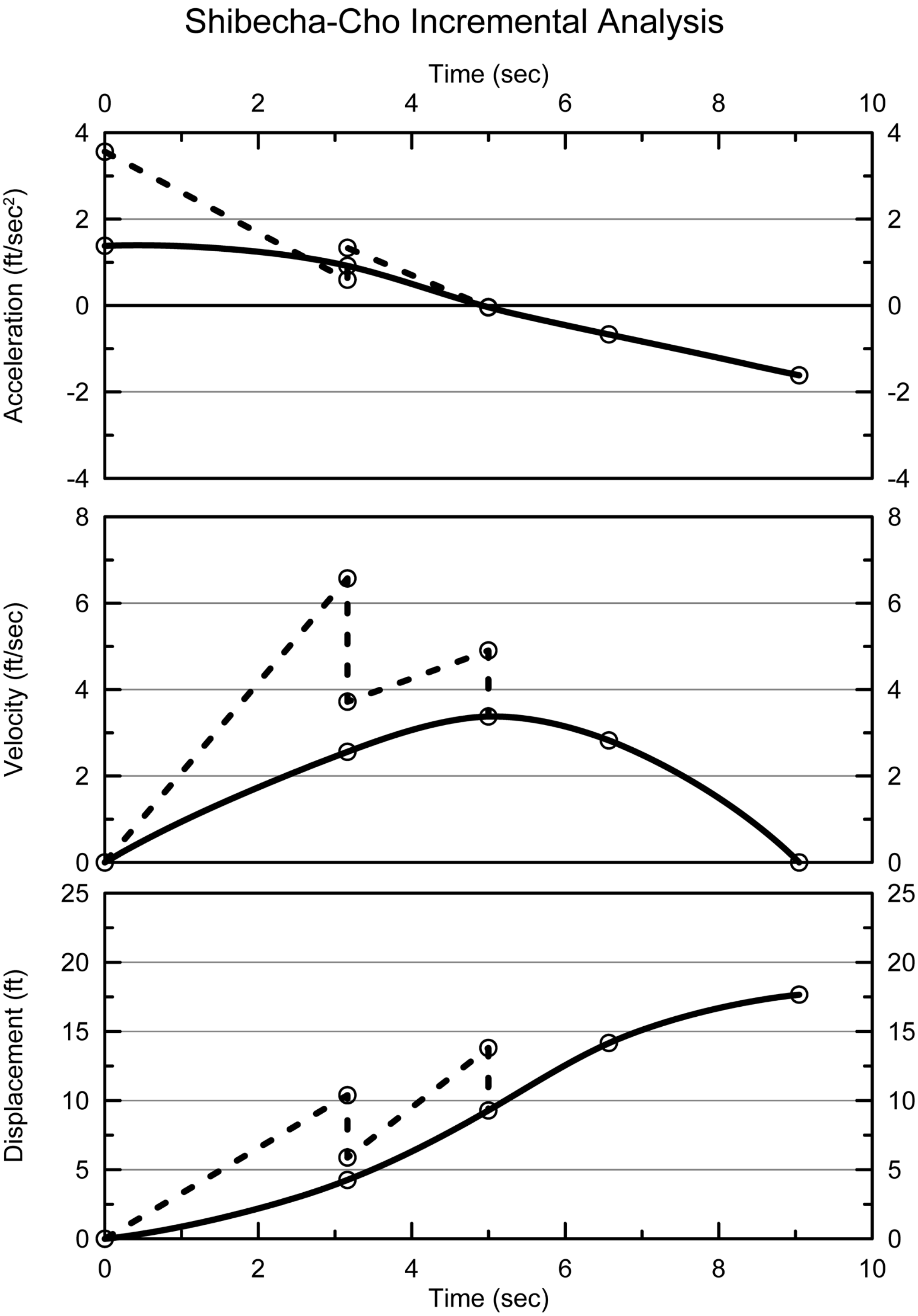

Figure A.12.6: Incremental momentum analysis of the failure of the Shibecha-Cho Embankment, showing progressive evolution of: (1) acceleration vs. time, (2) velocity vs. time, and (3) displacement vs. time of the overall center of gravity of the failure mass

Overall, based on an assumed normal distribution, it was judged that the (mean and median) best estimate of post-liquefaction strength for this case history is

$$\overline{S_r} = 224 \text{ lbs/ft}^2$$

and that the best estimate of standard deviation of mean overall post-liquefaction strength is

$$\sigma_{\overline{S}} = 37 \text{ lbs/ft}^2$$

Estimates of S_r were also reported by several other investigation teams, and these are shown in Table A.13.1(a). Olson (2001), and Olson and Stark (2002), reported a best estimate value of S_r = 5.6 kPa (117 lbs/ft^2), based on their inertial displacement analyses that considered kinetics, and a range of S_r = 3.9 to 8.3 kPa (81 to 174 lbs/ft^2). Their kinetics analysis, however, only tracked the movements of the centroid of a failure mass corresponding to a smaller "initial" toe failure, rather than the overall eventual failure mass. It appears that this resulted in a conservative underestimate of S_r. Wang (2003) and Wang and Kramer (2008) employed their zero inertial force (ZIF) method to incorporate inertial effects in their back-analyses of this failure, and they also developed estimates of both mean $\overline{S_r}$ = 208.9 lbs/ft^2 as well as the associated standard deviation $\sigma_{\overline{S}}$ = 38.6 lbs/ft^2. The details of their analyses, and the cross-sections and failure mass assumptions employed, are not presented and so cannot be checked. But this is yet another case history in which the "ZIF" calculations of Wang (2003), which account for inertial effects, produced S_r values in generally good agreement with the results of these current studies.

A.12.6 Evaluation of Initial Effective Vertical Stress

Average initial (pre-failure) effective vertical stress was assessed for the liquefied zones of each of the two failure surfaces shown in Figure A.12.4(a). The best estimate of the overall average initial vertical effective stress was then taken as the average of these two averages. Reasonable variations were then made in (1) the location of the phreatic surface, (2) unit weights, and (3) the precise location of the overall failure surface.

The resulting best estimate of average pre-failure effective stress within the liquefied materials controlling the failure was then $\sigma_{vo}' \approx$ 1,416 lbs/ft^2, with a reasonable range of $\sigma_{vo}' \approx$ 1,234 to 1,614 lbs/ft^2. This range is slightly non-symmetric about the median value, and this range was judged by the engineering team to represent approximately +/− 2 standard deviations. Overall, the best characterization of initial (pre-failure) average effective vertical stress was then taken to be represented by a mean value of

$$\overline{\sigma'_{vo}} \approx 1{,}416 \text{ lbs/ft}^2$$

and with a standard deviation of

$$\sigma_{\overline{\sigma}} \approx 95 \text{ lbs/ft}^2$$

Estimates of σ_{vo}' were also reported by other investigation teams, and two sets of these are shown in Table A.12.1(c). Olson (2001) and Olson and Stark (2002) reported a value of $\overline{\sigma'_{vo}}$ = 1,351 lbs/ft^2, in good agreement with these current studies. Average initial vertical effective stresses were not directly reported by Wang (2003) and Kramer (2008), but they were published more recently in the publication by Kramer and Wang (2015). As discussed in Section 2.3.8.1(a), the approach taken by Wang (2003) to evaluation of σ_{vo}' for his nine "primary" case histories (this is one of those nine) is not clearly explained, and it is also poorly documented. Wang's value of σ_{vo}' = 1,048 lbs/ft^2 is somewhat lower than the values of Olson (2001) and these current studies, but this is not considered a very rigorous check here. Wang (2003) presents no detailed cross-section for his analyses, so it is not possible to know why his estimated value of σ_{vo}' is lower than the values calculated (1) by Olson (2001) and (2) in these current studies.

A.12.7 Evaluation of $N_{1,60,CS}$

Only Swedish cone (penetration) test data were performed within the liquefiable embankment fill materials. Conversion of these to equivalent SPT N-values was made using the relationship recommended by Ishihara et al. (1990). There is considerable uncertainty in this relationship, and this is a significant contributor to uncertainty or variability with respect to the median $\overline{N_{1,60,CS}}$ value representative of this material. Corrections for effective overburden stress (C_N) were made using the relationships proposed by Deger (2014), as presented and discussed in Appendix C. Corrections for fines content were made using the relationship propose by Cetin et al. (2018a,b), and a representative fines content of approximately 20%. The resulting best estimate median $N_{1,60,CS}$ value for these current studies is $\overline{N_{1,60,CS}} \approx 7.5$ blows/ft. Variance of $\overline{N_{1,60,CS}}$ was estimated primarily on the basis of the perceived uncertainty associated with conversion for Swedish cone penetration resistances to equivalent SPT penetration resistances, and was taken as being represented by a standard deviation of $\sigma_{\overline{N}} \approx 1.7$ blows/ft.

Table A.12.1(b) shows values of representative $N_{1,60}$ or $N_{1,60,CS}$ values developed by two other teams of investigators, and variance or standard deviations in these representative values. Olson and Stark (2001, 2002) developed an estimated representative value of $N_{1,60} = 5.6$ blows/ft, and an estimated range of representative values of $N_{1,60} \approx 2.9$ to 10.7 blows/ft, but did not quantify variance or standard deviation in probabilistic terms. This value is a bit lower than the $N_{1,60,CS}$ value from these current studies because it is uncorrected for fines, and so is not an $N_{1,60,CS}$ value. If a similar fines correction were to be made, the resulting $N_{1,60,CS}$ value of Olson and Stark would be in closer agreement with these current studies. Wang (2003) and Kramer (2008) jointly developed a representative value of $\overline{N_{1,60,CS}} = 5.6$ blows/ft, and their estimated standard deviation of that overall mean value for this case history was $\sigma_{\overline{N}} = 2.2$ blows/ft. Details of the development of this interpretation by Wang and Kramer are not presented, so it is not known why their $\overline{N_{1,60,CS}}$ value is a bit lower than the corresponding value developed in these current studies. As relationships between $N_{1,60,CS}$ and S_r have relatively low slopes, this difference is relatively modest with regard to impact on subsequent development of SPT-based predictive relationships for evaluation of S_r.

A.12.8 Additional Indices from the Back-Analyses

A number of additional results, and indices, can be extracted from the analyses performed. Some of these are useful in developing some of the over-arching relationships and figures presented in the main text of this report. These values are presented in Table A.12.2.

Table A.12.1: Representative values for the Shibecha-Cho Embankment case history of: (a) post-liquefaction strength (S_r), (b) initial vertical effective stress (σ_{vo}'), and (c) $N_{1,60,CS}$ developed by various investigation teams, and estimates of variance in each of these indices when available.

(a) Post-Liquefaction Strength:	
Olson (2001) and Olson and Stark (2002)	S_r = 117 psf, and range = 81 to 174 psf
Wang (2003) and Kramer (2008)	$\bar{S}_r$ = 208.9 psf, and $\sigma_{\bar{S}}$ = 38.6 psf
This Study	$\bar{S}_r$ = 214 psf and $\sigma_{\bar{S}}$ = 37 psf
(b) Representative $N_{1,60}$ or $N_{1,60,CS}$ Value:	
Olson (2001) and Olson and Stark (2002)	$N_{1,60}$ = 6.3 bpf, and range = 2.4 to 10.0 bpf
Wang (2003) and Kramer (2008)	$\overline{N_{1,60,CS}}$ = 8.5 bpf, and $\sigma_{\bar{N}}$ = 2.6 bpf
This Study	$\overline{N_{1,60,CS}}$ = 8.1 bpf, and $\sigma_{\bar{N}}$ = 1.6 bpf
(c) Representative Initial Vertical Effective Stress:	
Olson (2001) and Olson and Stark (2002)	σ'_{vo} = 1,351 psf, likely range is not provided.
Wang (2003) and Kramer (2008)	Value of $\sigma_{vo}' \approx$ 2,558 psf is poorly documented, and so is considered useful only as an approximate comparison. (See Section 2.3.8.1, and Table 2.3.)
This Study	$\overline{\sigma'_{vo}}$ = 1,285 psf, and $\sigma_{\bar{\sigma}}$ = 104 psf

Table A.12.2: Additional results and indices from the analyses of the Shibecha-Cho Embankment failure case history.

Maximum distance traveled by the center of gravity of the overall failure mass	17.9 ft.
Initial post-liquefaction Factor of Safety prior to displacement initiation, and based on best estimate value of S_r	FS = 0.79
Final post-liquefaction Factor of Safety at final (residual) post-failure geometry, and based on best estimate value of S_r	FS = 1.36

A.13 Route 272 Embankment (Higashiarekinai, Japan; 1993)

A.13.1 Brief Summary of Case History Characteristics

Name of Structure	Route 272 Embankment
Location of Structure	Higashiarekinai, Japan
Type of Structure	Sidehill Highway Embankment
Date of Failure	September 22, 1933
Nature of Failure	Seismic, During 1993 Kushiro-Oki Earthquake (M_L = 7.8)
Approx. Maximum Slope Height	26 ft.

A.13.2 Introduction and Description of Failure

The Route 272 Highway Embankment failed during Kushiro-Oki Earthquake of January 15, 1993 (M_L = 7.8), and was investigated by Sasaki et al. (1994). Sasaki et al. developed an event-specific acceleration attenuation relationship for the Kushiro-Oki Earthquake, and estimated that the peak ground acceleration at this site was approximately 0.38 g.

Figure A.13.1 shows a cross-section through the failure. The highway embankment was a sidehill fill underlain by pumice bearing volcanic sands and silts, and by partially pumice tuff.

After the failure, two SPT borings were performed and these are shown in Figure A.13.1 (from Sasaki et al., 1994). These two borings reasonably well constrain the key ground conditions at the base of the failure. Construction details are not reported, and it is assumed that the sandy fill was locally sourced, and that it received minimal compaction effort. This embankment is not far from the Shibecha-Cho Embankment discussed previously in Section A.12, and fill material is assumed to have been locally available volcanic sands and silty sands.

Close inspection of the two borings shown in Figure A.13.1 shows that the transition from fill to underlying native soils appears to be relatively clearly demarcated by a transition from very low SPT blowcounts within the fill to slightly higher penetration resistances in the immediately underlying pumice bearing volcanic sand. The back heel of the final failure surface is also well constrained. As a result, the approximate location of the overall bounding failure surface is relatively well constrained for this case by the clear heel scarp, and by the transition to firmer materials at the base of the liquefiable fill. The location of the phreatic surface at the time of the earthquake was not so well constrained, but potential variability with regard to location of the phreatic surface was at least reasonably bounded.

A difficulty encountered in performing back-analyses of this failure is that the post-failure volume of the failed slope materials shown in Figure A.13.1 is approximately 27% larger than the pre-failure volume. This is accommodated in the back-analyses that follow, and it is found that this volume discrepancy has only a moderate effect on uncertainty, or variance, in back-calculated post-liquefaction strengths for this case history.

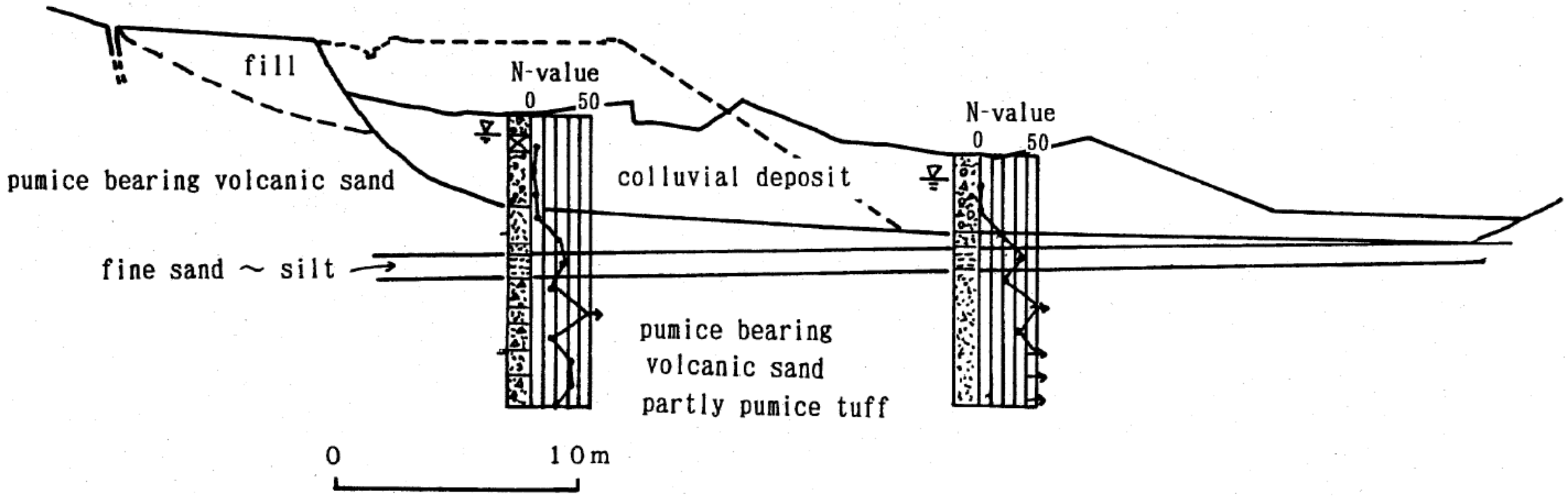

Figure A.13.1: Cross-section through the Route 272 Highway Embankment showing pre-failure and post-failure geometry and the available SPT boring logs (from Sasaki et al., 1994)

A.13.3 Initial Yield Strength Analyses

It is not known whether this failure initiated as a monolithic failure, or as an incrementally progressive failure that retrogressed towards the back heel in progressive slices. Based on an assumed phreatic surface that passes approximately through the mid-height of the slope, and exits at the toe, a search was made for the most critical static failure surface assuming liquefaction had been "triggered" in all potentially liquefiable materials below the phreatic surface. This exercise showed that the most critical potential failure surfaces for this set of assumptions would have been for a failure initially closer to the slope face than the final rear scarp shown in Figure A.13.1. These analyses neglected seismic inertial forces, however, and they also did not account for likely progressive development of triggering of liquefaction within the slope.

The post-failure geometry shown in Figure A.13.1 is suggestive, on the other hand, of a more monolithic initiation of failure, likely articulating itself into sub-sections as it progressed.

Figure A.13.2(a) shows two potential failure surfaces analyzed. The rear-most surface is the eventual "final" underlying (or bounding) failure surface, which is reasonably well constrained by the data provided by Sasaki et al. (1994). The other failure surface is the surface that was found to be the most critical initial yield surface (requiring the highest value of post-liquefaction yield strength in order to produce a calculated static Factor of Safety = 1.0). Silty sand materials above the phreatic surface were modeled with $\text{Ø}' \approx 32°$, and a unit weight of $\gamma_m \approx 103$ lbs/ft^3. Materials below the phreatic surface were considered to liquefy, down to the base of the failure surfaces analyzed, and were assigned an undrained post-liquefaction yield strength of $S_{r,yield}$ that was constant along any given failure surface, and a unit weight of $\gamma_s \approx 108$ lbs/ft^3.

The resulting best-estimated value of $S_{r,yield}$ for the most critical initial (smaller) failure surface was $S_{r,yield} = 374$ lbs/ft^2, and the best-estimated value for the eventual "final" larger failure surface was $S_{r,yield} = 307$ lbs/ft^2.

Parameters and geometry were then varied to examine potentially variability. The location of the phreatic surface was varied, raising it by up to 1.5 m (5 ft) at the back heel of the final failure surface, and lowering it by up to a similar distance. The phreatic surface was considered to exit at or near the toe of the slope, based on the observed failure (and post-failure geometry). Unit weights were also varied over the ranges considered likely, and the friction angle of non-liquefied material above the phreatic surface was varied from 28° to 36°. The resulting range of values of $S_{r,yield}$ for the most critical initial failure surface was $S_{r,yield} \approx 360$ to 391 lbs/ft^2, and the best-estimated range for the eventual "final" larger failure surface (which would be pertinent if the failure initiated monolithically) was $S_{r,yield} \approx 286$ to 319 lbs/ft^2.

Given the uncertainty as to whether or not this failure was initiated largely monolithically, or was progressively retrogressive towards the back heel, the overall best estimate value of post-liquefaction initial yield strength was developed by considering both sets of possible mechanisms and then taking a middle position with regard to the median value, and then considering the full range of variability for both mechanisms, again averaged for the two potential failure surfaces. The resulting best estimate (median) value was found to be on the order of $S_{r,yield} \approx 341$ lbs/ft^2, with a likely range of $S_{r,yield} \approx 302$ to 380 lbs/ft^2.

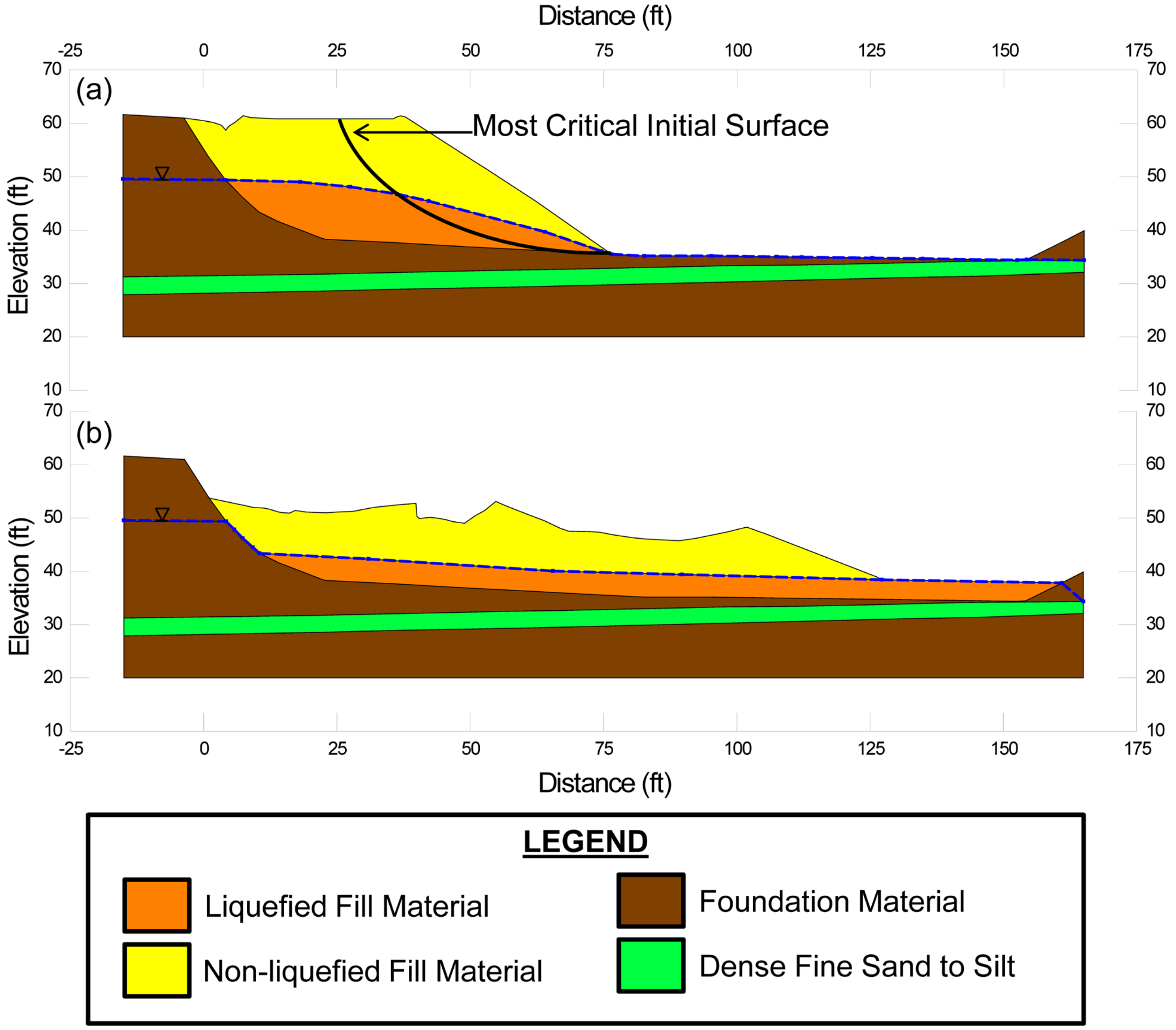

Figure A.13.2: Route 272 Embankment cross-sections showing (a) pre-failure geometry of the embankment and the failure surfaces used for calculation of post-liquefaction initial yield strength $S_{r,yield}$, and (b) post-failure residual geometry and the failure surface used to calculate $S_{r,resid/geom}$.

Olson (2001) also performed back-analyses to determine $S_{r,yield}$. Failure surfaces analyzed were similar, but did not appear to include surfaces extending fully back to the rear heel of the eventual "final" yield surface. Olson reported values of $S_{r,yield}$ ≈ 13.0 to 13.4 kPa (272 to 280 lbs/ft^2).

A.13.4 Residual Strength Analyses Based on Residual Geometry

The calculation of the "apparent" post-liquefaction strength ($S_{r,resid/geom}$) required to produce a calculated Factor of Safety equal to 1.0 based on residual geometry is illustrated in Figure A.13.2(b). This figure shows the phreatic surface, and the failure surface, used to calculate the best-estimate value of $S_{r,resid/geom} \approx 69$ lbs/ft^2. Variations were then made in parameters, and in location of the pre-failure phreatic surface, as was described in the preceding section in order to evaluate uncertainty or variability. The resulting likely range of post-liquefaction strength required to provide a calculated Factor of Safety equal to 1.0 based on residual geometry was considered to be $S_{r,resid/geom} \approx 65$ to 74 lbs/ft^2.

Olson (2001) also calculated post-liquefaction strength required to produce a calculated Factor of Safety equal to 1.0 based on residual geometry, and reported a range of $S_{r,resid/geom} \approx 2.9$ to 3.0 kPa (61 to 63 lbs/ft^2), in good agreement with the values calculated in these current studies.

A.13.5 Incremental Momentum Back-Analyses and Overall Estimates of S_r

Incremental momentum back-analyses were performed using the same sets of properties and geometries (including failure surfaces and phreatic surfaces) as described in the previous sections. Overall volume of the failure mass was subtly increased progressively throughout the increments because, as discussed previously, the post-failure geometry shown in Figure A.13.1 (Sasaki et al., 1994) shows an increase in the volume of the failure mass of approximately 27% from pre-failure to post-failure geometry. This anomalous volume discrepancy was progressively shared relatively equally from inception of failure to cessation of movements in the incremental momentum analyses.

Figure A.13.3 shows the best-estimate progressive incremental momentum analysis, showing the 5 stages of geometry evolution modeled as the failure proceeds. Figure A.13.4 shows the associated calculations of (1) acceleration vs. time, (2) velocity vs. time, and (3) displacement of the overall center of gravity vs. time. For the geometry and phreatic surface shown in Figure A.13.3, and the monolithic initiation of failure modeled in Figures A.13.3 through A.13.5, the best estimate value of post-liquefaction strength was $S_r = 138$ lbs/ft^2.

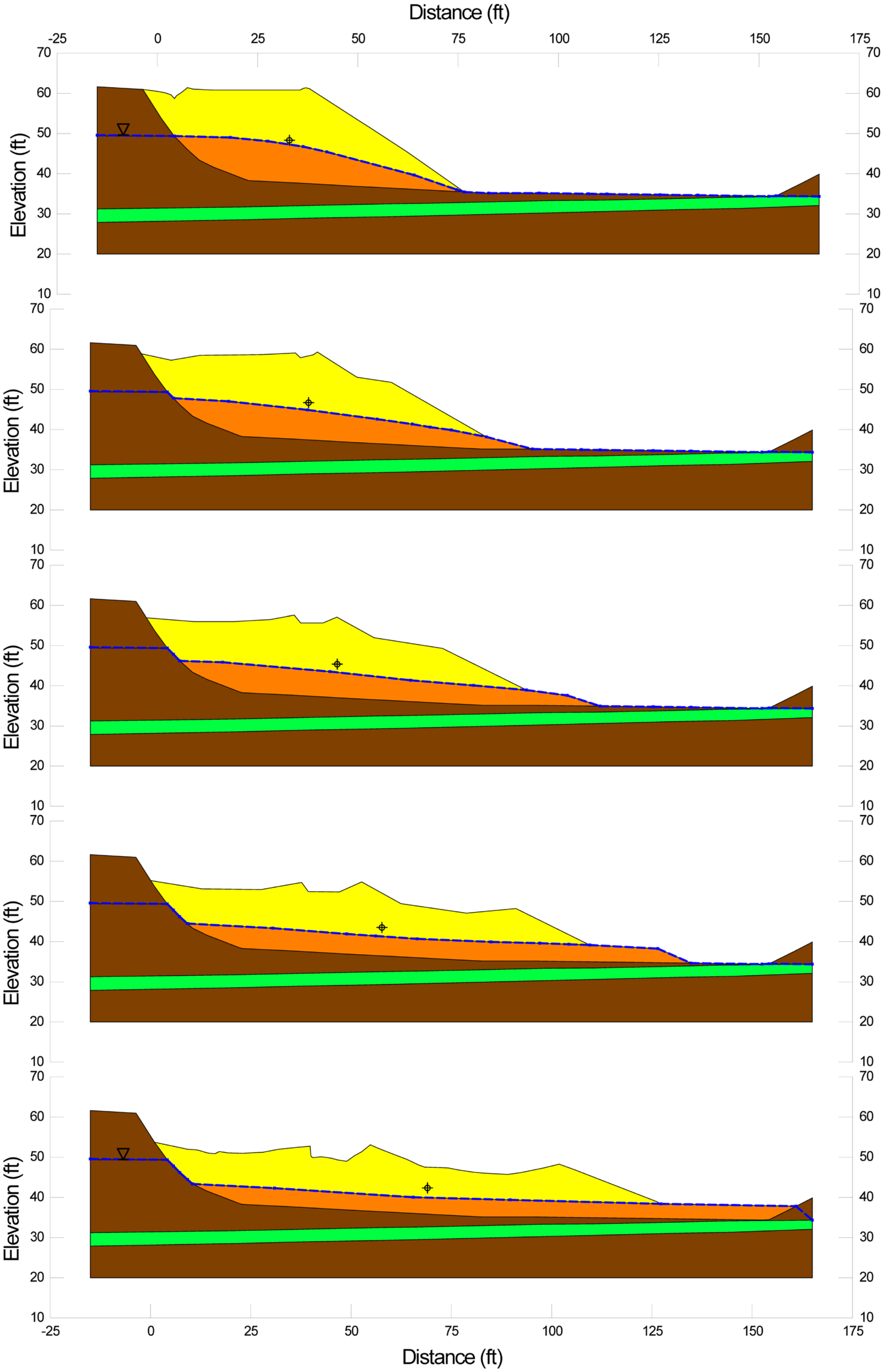

Figure A.13.3: Incremental momentum analysis of the failure of the Route 272 Embankment, showing progressive evolution of cross-section geometry modeled

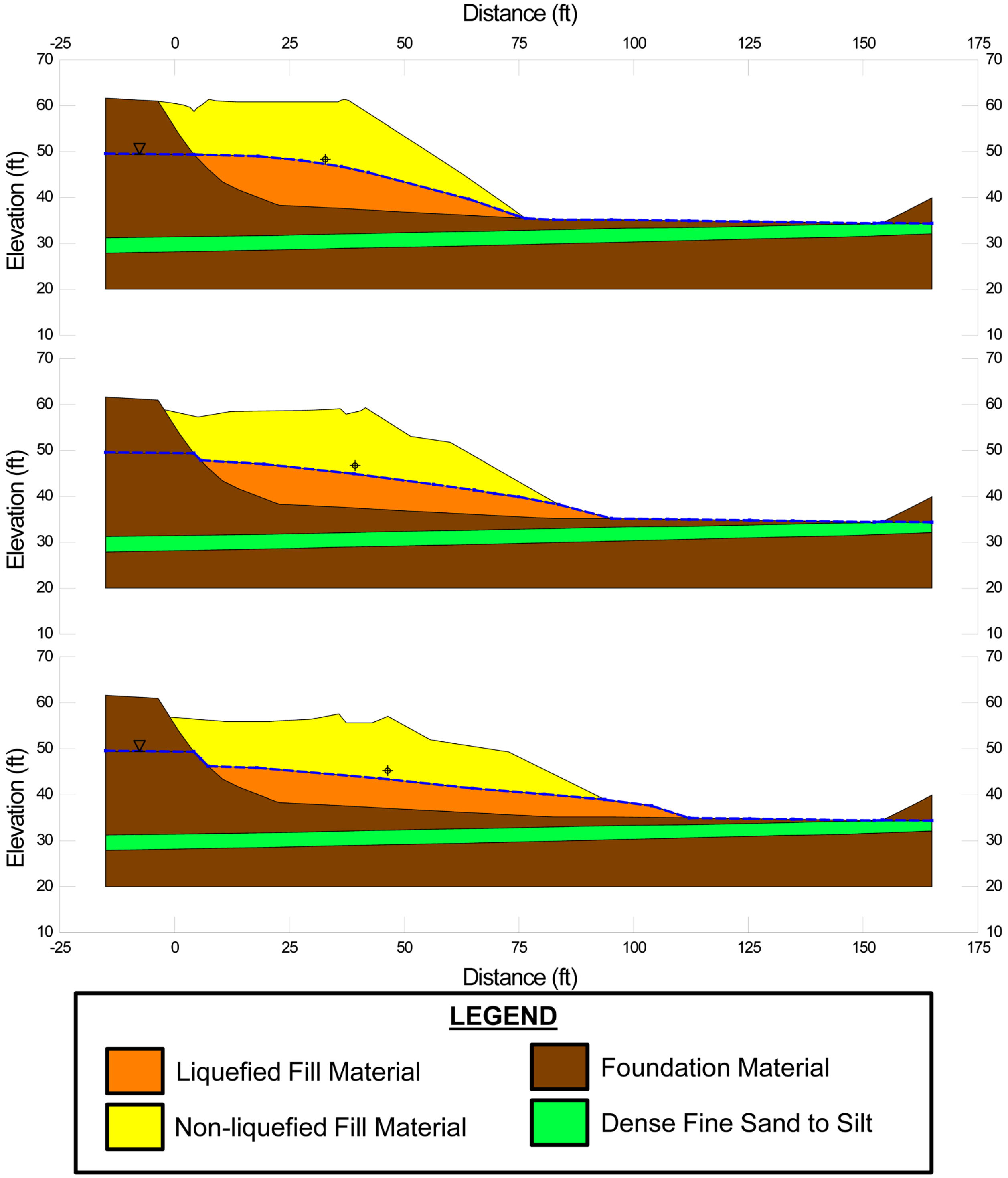

Figure A.13.4: Figure A.13.3 repeated, at larger scale, now also showing the progressive locations of the center of gravity of the overall failure mass.

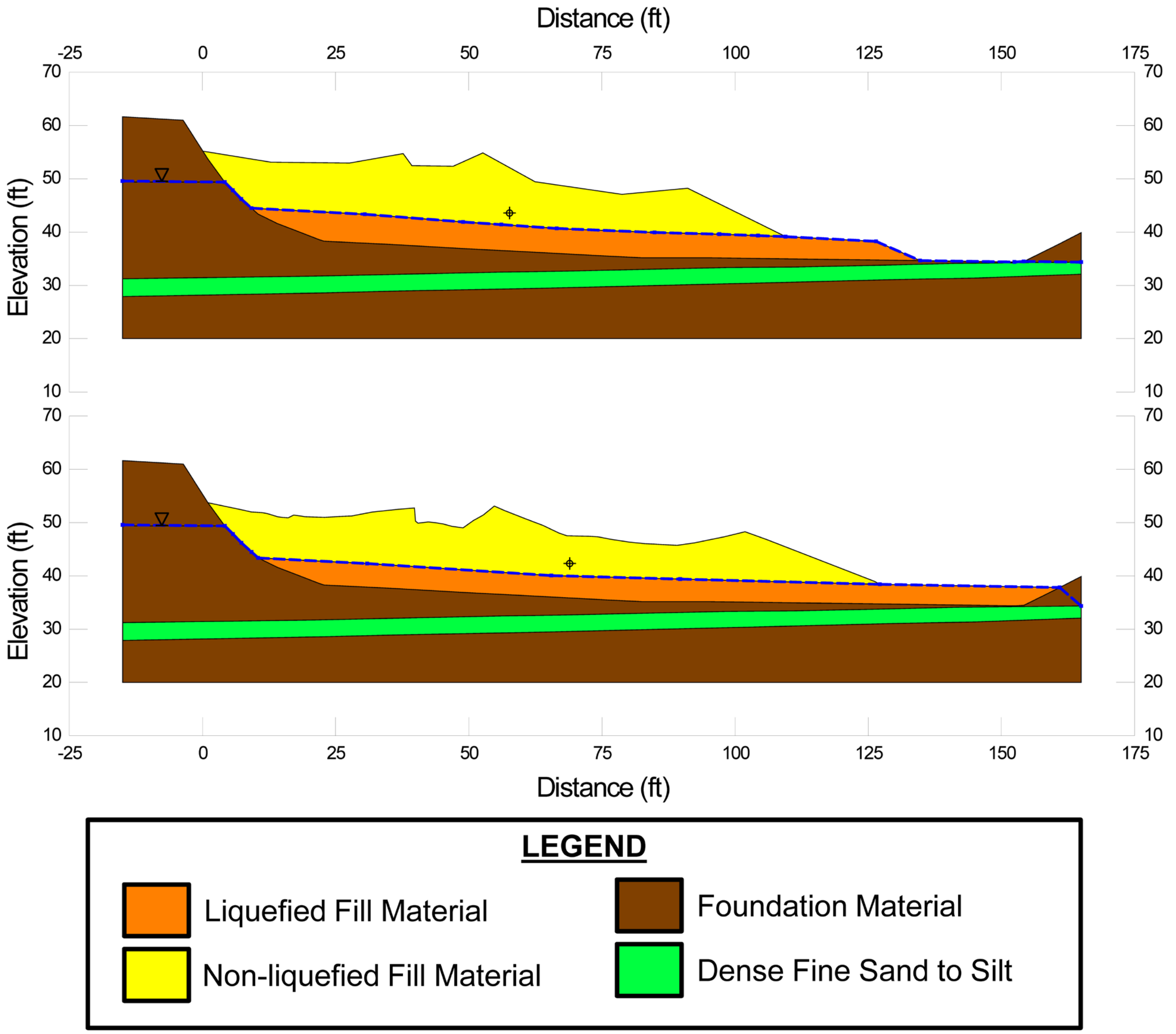

Figure A.13.4 (Cont'd): Figure A.13.3 repeated, at larger scale, now also showing the progressive locations of the center of gravity of the overall failure mass.

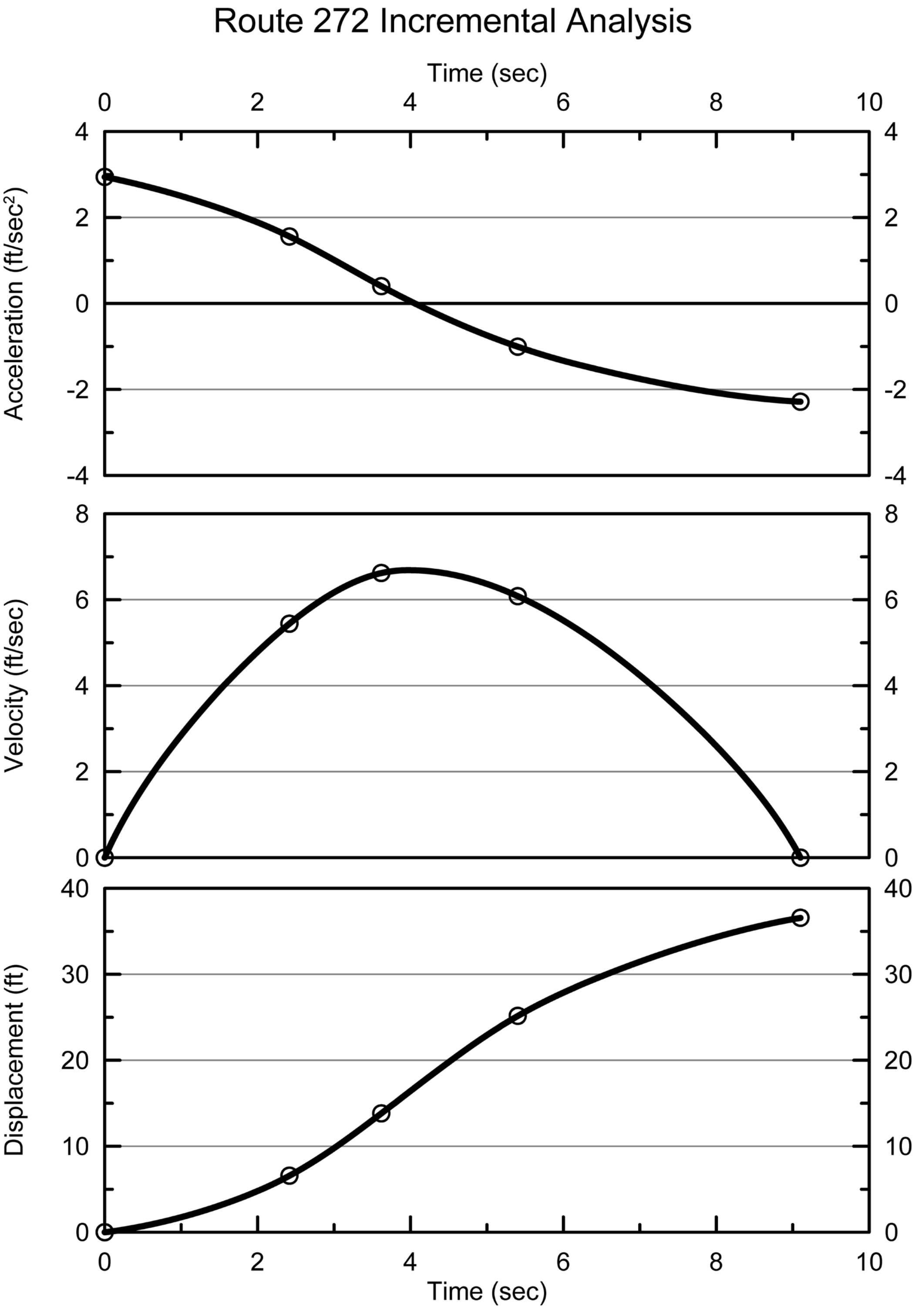

Figure A.13.5: Incremental momentum analysis of the failure of the Route 272 Embankment, showing progressive evolution of: (1) acceleration vs. time, (2) velocity vs. time, and (3) displacement of the overall center of gravity vs. time

The main sources of uncertainty, or variability, in back-calculated values of S_r were (1) the location of the phreatic surface, (2) whether or not the failure initiated largely monolithically or retrogressed progressively towards the back heel, (3) unit weights, (4) strength within the non-liquefied materials at the top of the back heel scarp, and (5) the precise location of the overall failure surface.

Because the location of the overall final failure surface was relatively well constrained in this case history, the two main sources of uncertainty, or variability, were (1) the location of the phreatic surface, and (2) the question as to whether the actual failure initiated largely monolithically, or progressed retrogressively towards the back heel.

The analysis shown in Figures A.13.3 through A.13.5 neglects cyclic inertial forces, and so may represent a slightly conservative assessment of actual post-liquefaction strength mobilized. Incremental momentum back-analyses assuming that failure initiates with a failure surface similar to the forward-most initial failure surface shown in Figure A.13.2(a) and then retrogresses back towards the eventual back heel scarp develop somewhat lower overall calculated values of S_r, with the amount of decrease being dependent upon the rate at which subsequent progression of retrogressive failure towards the back heel initiates. It is not feasible to produce the final post-failure geometry actually documented in the field by Sasaki et al. (1994) if an initial yield surface from the forward section of the eventual failure mass is allowed to "run out" too very far before a subsequent second failure extending further rearwards towards the eventual final back heel of the failure initiates. There may have been only a single monolithic inception of failure, or there may have been multiple retrogressive initiations (two or more). But the additional analyses performed suggest that retrogressive progressive failures would only have reduced the S_r values from those calculated based on the largely monolithic failure shown in Figures A.13.3 and A.13.4 by on the order of approximately 5 to 12%. It was then judged that the best-estimate value of post-liquefaction strength would have been intermediate between a monolithic initiation of failure and a progressively retrogressive initiation.

Based on all analyses performed, and the considerations discussed herein, the overall best estimate value of post-liquefaction strength for the Route 272 Embankment failure was judged to be $S_r \approx 138$ lbs/ft^2, with a likely range of $S_r \approx 107$ to 175 lbs/ft^2. Based on the factors contributing to uncertainty or variance for this case history, it was the judgment of the investigation team that this range represented approximately +/− 2 standard deviations. This range of variance is not quite symmetrical about the best estimate value, so minor further adjustments were made to produce a representative estimate of S_r suitable for regression analyses.

Overall, based on an assumed normal distribution, it was judged that the (mean and median) best estimate of post-liquefaction strength for this case history is

$$S_r = 138 \text{ lbs/ft}^2 \text{ (6.61 kPa)}$$

and that the best estimate of standard deviation of mean overall post-liquefaction strength is

$$\sigma_{\overline{S}} = 17 \text{ lbs/ft}^2 \text{ (0.81 kPa)}$$

Estimates of S_r were also reported by several other investigation teams, and these are shown in Table A.13.1(a). Olson (2001) and Olson and Stark (2002), reported a best estimate value of $S_r = 4.8$ kPa (100 lbs/ft^2), based on their inertial displacement analyses that considered kinetics, and a range of $S_r = 3.0$ to 5.7 kPa (63 to 119 lbs/ft^2). Wang (2003) and Wang and Kramer (2008) employed their zero inertial force (ZIF) method to incorporate inertial effects in their back-analyses of this failure, and they also developed estimates of both mean $\overline{S_r} = 130.5$ lbs/ft^2 as well as the associated standard deviation $\sigma_{\overline{S}} = 33.5$ lbs/ft^2. These other studies each employed different approaches, and different sets of modeling and analysis assumptions. Given this, overall agreement among these investigations is very good.

A.13.6 Evaluation of Initial Effective Vertical Stress

Average initial (pre-failure) effective vertical stress was assessed for the liquefied zones of each of the two failure surfaces shown in Figure A.13.2(a). The best estimate of the overall average initial vertical effective stress was then taken as the average of these two averages. Reasonable variations were then made in (1) the location of the phreatic surface, (2) unit weights, and (3) the precise location of the overall failure surface.

The resulting best estimate of average pre-failure effective stress within the liquefied materials controlling the failure was then $\sigma_{vo}' \approx 1{,}285$ lbs/ft^2, with a reasonable range of $\sigma_{vo}' \approx 1097$ to 1512 lbs/ft^2. This range is slightly non-symmetric about the median value, and this range was judged by the engineering team to represent approximately +/− 2 standard deviations. Overall, the best characterization of initial (pre-failure) average effective vertical stress was then taken to be represented by a mean and median value of

$$\sigma_{VO}' \approx 1{,}285 \text{ lbs/ft}^2 \text{ (61.5 kPa)}$$

with a standard deviation of

$$\sigma_{\sigma O'} \approx 104 \text{ lbs/ft}^2 \text{ (4.98 kPa)}$$

Estimates of σ_{VO}' were also reported by other investigation teams, and these are shown in Table A.13.1(c). Average initial vertical effective stresses were reported by Olson (2001) and Olson and Stark (2002) as $\sigma_{vo}' = 1{,}030$ lbs/ft^2. Average initial vertical effective stresses were not directly reported by Wang (2003) and Kramer (2008), but they were published more recently in the publication by Kramer and Wang (2015). As discussed in Section 2.3.8.1(a), the approach taken by Wang (2003) to evaluation of σ_{vo}' for his nine "primary" case histories (this is one of those nine) is not clearly explained, and it is also poorly documented. Wang's value of $\sigma_{vo}' = 1{,}043$ lbs/ft^2 is in good agreement with the value of Olson (2003), and in fair agreement with the value developed in these current studies. Overall, agreement among these three studies is acceptable here.

A.13.7 Evaluation of $N_{1,60,CS}$

As shown in Figure A.13.1, only 5 SPT were performed within the liquefiable upper stratum. As a result, lack of numbers of SPT data is a significant contributor to uncertainty or variability with respect to the median or mean value representative of this material. Seed et al. (1985) and Ishihara (1993) assumed an energy ratio of approximately 72%, and this current study does the same. Corrections for effective overburden stress (C_N) were made using the relationships proposed by Deger (2014), as presented and discussed in Appendix C. Corrections for SPT equipment and procedural details, and for fines content, were made based on Cetin et al. (2018a,b). The resulting median $\overline{N_{1,60,CS}}$ value was 8.1 blows/ft.

Variance of $N_{1,60,CS}$ within this limited data set was used to calculate the associated variance in the mean (and thus approximately the median) value of $\overline{N_{1,60,CS}}$, but this under-estimated the actual variance or uncertainty. Additional factors significantly affecting variance or uncertainty in the median representative $\overline{N_{1,60,CS}}$ value were (1) lack of numbers of SPT data, and (2) uncertainty as to actual SPT equipment and procedural details. Overall, it was the judgment of the investigation team that SPT penetration resistance could be suitably represented with a representative (median) value of $\overline{N_{1,60,CS}}$ = 8.1 blows/ft, and with a standard deviation of the median/representative value of approximately $\sigma_{\overline{N}}$ = 1.6 blows/ft.

Table A.13.1(b) shows values of representative $N_{1,60}$ or $N_{1,60,CS}$ values developed by other investigators, and variance or standard deviations in these representative values when available. Olson and Stark (2001, 2002) developed an estimated representative value of $N_{1,60}$ = 6.3 blows/ft, and an estimated range of representative values of $N_{1,60} \approx 2.4$ to 10 blows/ft, but did not quantify variance or standard deviation in probabilistic terms. Wang (2003) and Kramer (2008) jointly developed a representative value of $\overline{N_{1,60,CS}}$ = 8.5 blows/ft, and their estimated standard deviation of that overall mean value for this case history was $\sigma_{\overline{N}}$ = 2.6 blows/ft. The representative $N_{1,60}$ value of Olson and Stark is about 2 to 2.5 blows/ft lower than the other two sets of values in the table, in part because Olson and Stark did not make a fines correction, which would have served to increase their $N_{1,60}$ values as they became $N_{1,60,CS}$ values in these silty sands.

The investigation teams whose results are presented in Table A.13.1(c) each employed slightly different approaches with regard to corrections for effective overburden stress, fines content, and SPT equipment and procedural details. Given this, the agreement with the value employed in this current study is good. Wride, McRoberts and Robertson (1999) developed a somewhat lower estimate of representative $N_{1,60,CS}$ for this case history, but their approach targeted determination of a more nearly lower bound value, and so is this lower value is to be expected and is not directly comparable with the others shown.

A.13.8 Other Results and Indices

A number of additional results, and indices, can be extracted from the analyses performed. Some of these are useful in developing some of the over-arching relationships and figures presented in the main text of this report. These values are presented in Table A.13.2.

Table A.13.1: Representative values for the Route 272 Highway Embankment case history of: (a) post-liquefaction strength (S_r), (b) initial vertical effective stress (σ_{vo}'), and (c) $N_{1,60,CS}$ developed by various investigation teams, and estimates of variance in each of these indices when available.

(a) Post-Liquefaction Strength:	
Olson (2001) and Olson and Stark (2002)	S_r = 100 psf, and range = 63 to 211 psf
Wang (2003) and Kramer (2008)	$\overline{S_r}$ = 130.5 psf, and $\sigma_{\overline{S}}$ = 33.5 psf
This Study	$\overline{S_r}$ = 138 psf, and $\sigma_{\overline{S}}$ = 17 psf
(b) Representative $N_{1,60}$ or $N_{1,60,CS}$ Value:	
Olson (2001) and Olson and Stark (2002)	$N_{1,60}$ = 6.3 bpf, and range = 2.4 to 10.0 bpf
Wang (2003) and Kramer (2008)	$\overline{N_{1,60,CS}}$ = 8.5 bpf, and $\sigma_{\overline{N}}$ = 2.6 bpf
This Study	$\overline{N_{1,60,CS}}$ = 8.0 bpf, and $\sigma_{\overline{N}}$ = 1.6 bpf
(c) Representative Initial Vertical Effective Stress:	
Olson (2001) and Olson and Stark (2002)	σ_{vo}' = 1,030 psf, likely range is not provided.
Wang (2003) and Kramer (2008)	Value of $\sigma_{vo}' \approx$ 1,043 psf is poorly documented, and so is considered useful only as an approximate comparison. (See Section 2.3.8.1, and Table 2.3.)
This Study	$\overline{\sigma'_{vo}}$ = 1,285 psf, and $\sigma_{\overline{\sigma}}$ = 104 psf

Table A.13.2: Additional results and indices from the analyses of the Route 272 Highway Embankment failure case history.

Maximum distance traveled by the center of gravity of the overall failure mass	36.6 ft.
Initial post-liquefaction Factor of Safety prior to displacement initiation, and based on best estimate value of S_r	FS = 0.50
Final post-liquefaction Factor of Safety at final (residual) post-failure geometry, and based on best estimate value of S_r	FS = 1.90

A.14 Calaveras Dam (California, USA, 1918)

A.14.1 Brief Summary of Case History Characteristics

Name of Structure	Calaveras Dam
Location of Structure	San Francisco Bay Area, California, USA
Type of Structure	Hydraulic Fill Dam
Date of Failure	March 24, 1918
Nature of Failure	Static, During Construction
Approx. Maximum Slope Height	201 ft.

A.14.2 Introduction

The Calaveras Dam embankment failed during construction on March 24, 1918, suffering a massive flowslide on its upstream side. The dam was being constructed by the ponded hydraulic fill method, and was nearing completion at the time of the failure. The nearly completed embankment had a maximum crest height of approximately 200 feet at the tallest section, and the reservoir was partially filled, with a reservoir surface elevation of approximately 75 feet above the base of the lowest point of the embankment; approximately 35 to 40% of the way up towards the still uncompleted dam crest.

Figure A.14.1 shows a photograph of the failure, with the failure mass having moved upstream (towards the upper right hand corner of the photograph). Figure A.14.2 shows a complicated set of super-imposed cross-sections (Hazen, 1920). The lower portion of the cross-section shows the post-failure cross-section geometry. The dashed lines (which can be difficult to see) show the pre-failure geometry, and the remainder of the figure shows the final cross-section after reconstruction and then completion of the dam. Figure A.14.3 shows pre-failure and post-failure cross-sections as interpreted by Olsen (2001) based on Hazen (1920) and the information available in 2001. This interpretation is essentially identical to the cross-sections employed in these current studies.

This failure was well investigated for its time, and Hazen and Metcalf (1918), Hazen (1918) and Hazen (1920) provide good descriptions of the failure, and of the construction of the dam up to the time of the failure.

There had been partial movements on the upstream side of the dam for at least nine months prior to the eventual failure. On June 18, 1917 horizontal displacements of approximately 0.5 m had been measured at one location on the upstream face, and additional horizontal movements of approximately 0.15 m occurred over the next day, eventually opening a crack along approximately 650 feet of the upstream side concrete facing. Fill placement was stopped, and the movements quickly ceased. So fill placement resumed. Two additional, similar, incidents of observed movements and temporary stoppage of fill placement then occurred prior to the eventual failure. Finally, on the day before the failure, approximately 4 feet of horizontal movement was measured on the upstream face.

Figure A.14.1: Oblique aerial photograph of the March 24, 1918 upstream slope failure (the failure mass moved towards the upper right hand corner of this photograph). [Photo from Hazen, 1920 (with arrow and notation from Olson, 2001)]

The failure itself was observed by witnesses. According to Hazen (1918): "The men who saw the dam go state that at first the whole mass seemed to move forward as a unit. Afterward it seemed to separate, and the parts that were farthest back stopped, while those that were further advanced continued to move forward… The material was carried forward on a good lubricant, and that lubricant first became used up or expelled near the center of the dam and left the higher parts of the dam on solid bottom while there was still lubricant to carry forward the lower and more advanced portions."

This was thus a slide that was monotonically initiated, and it then subsequently elongated as it travelled upstream into the partially filled reservoir.

Soil liquefaction was not well understood at the time of the failure, and Hazen (1918) and others were surprised that the failure mass was "hard and solid" soon after the failure when test piles were driven to qualitatively asses the consistency and apparent density of the massively displaced slide mass. It was initially suspected that clayey materials from the puddled core might have been present as horizontal lenses extending well into the upstream shell zone, and that these weak clay strata might have been responsible for the observed failure. Post-failure investigations were unable, however, to find any significant amounts of clay-dominated strata within the displaced failure mass.

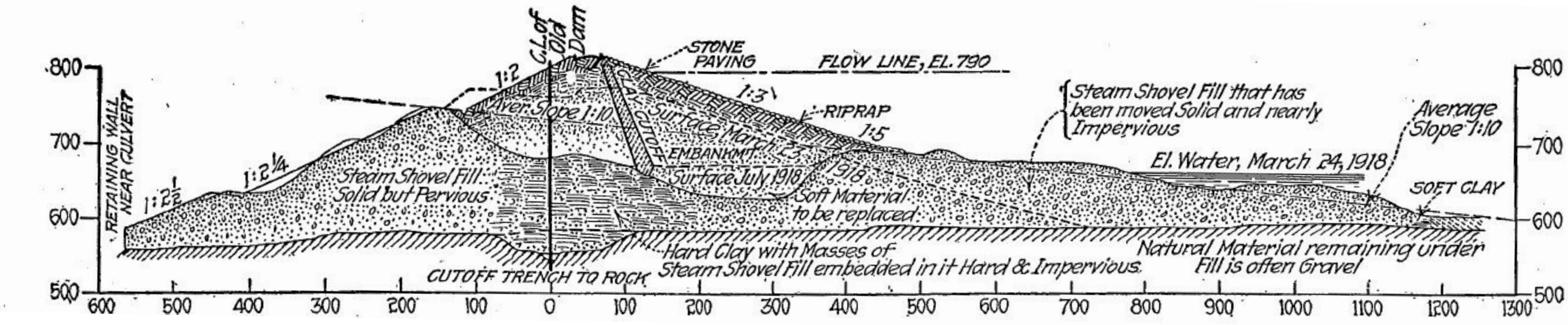

Fig. A.14.2: Cross-section from Hazen, 1920 showing both pre-failure and post-failure conditions, as well as the re-constructed and completed dam.

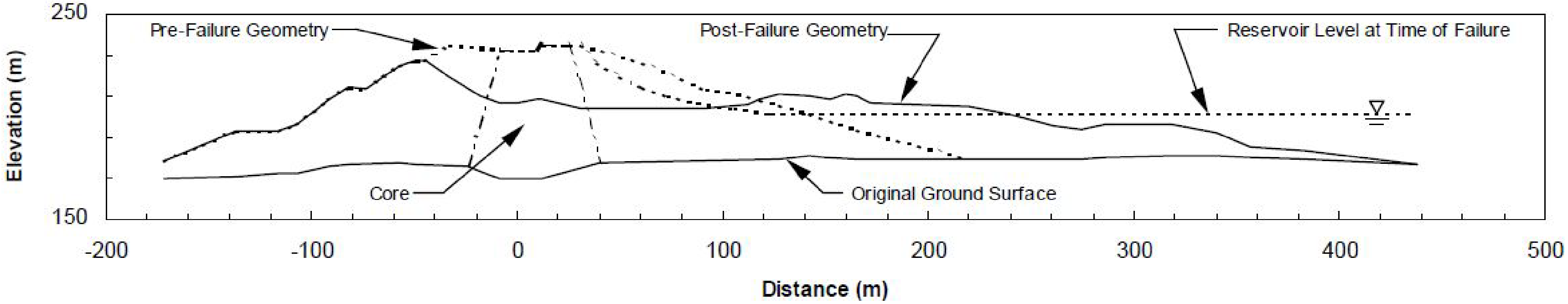

Fig. A.14.3: Pre-failure and post-failure cross-sections as interpreted by Olsen (2001) based on Hazen (1918).

.

As a result, Hazen (1920) suggested instead that: "As water pressure increased, the pressure on the edges is reduced and the friction resistance of the material becomes less. If the pressure of the water is great enough to carry all the load, it will have the effect of holding the particles apart and of producing a condition that is practically equivalent to that of quicksand. A sharp blow, as with a foot, however liquefies a certain volume and makes quicksand…. The condition of quicksand lasts only for a few seconds until the surplus water can find its way out. When this happens the grains again come to solid bearings and stability is restored. During the few seconds after the sand is struck, however, it is almost liquid, and is capable of moving or flowing or of transmitting pressure in the same measure as a liquid…. The conditions that control stability or lack of stability in quicksand may also control the stability or lack of stability in dams…. It may be that after the first movement there was some readjustment of the material in the toe which resulted in producing temporarily this condition of quicksand, and which destroyed for a moment the stability of the material and facilitated the movement that took place."

That was a brilliantly insightful early description of the mechanisms involved in this type of liquefaction-induced flow failure, and it stands as one of the earliest useful engineering descriptions of soil liquefaction and resulting stability failure.

A.14.3 Geology and Site Conditions

The base of the dam appears to have been constructed with little or no excavation of existing foundation materials. The valley floor and side slopes were covered with weathered colluvium, and with alluvium sourced from the weathered colluvium. Relatively clean gravelly fill was placed both by sluicing and by steam shovels to initially level the deepest portions of the foundation prior to construction of the main embankment. The gravel used was locally available material from the existing creek bed, and had few fines. Neither these gravels, nor the underlying foundation soils, appear to have been involved in the eventual failure.

The dam was being constructed by the hydraulic fill method, with starter dikes on the upstream and downstream sides to contain the arriving hydraulic fill. Figure A.14.4 gives a good idea of the complexity of the evolving internal geometry as the embankment was raised. Hydraulic fill was simultaneously deposited from pipes on both the upstream and downstream edges of the dam, so that coarser materials would settle out and form "shell" zones while finer materials would travel towards the center of the pool (and thus the center of the rising embankment) producing a clayey "puddled core". The hydraulic fill material was excavated from the surrounding hills, and consisted of variably weathered sandstone materials that were easily broken down by excavation and transport. Gradation, and clay content, were variable within these weathered materials. As a result, the hydraulic material actually emplaced was also highly variable as to gradation and fines content. Fines tended to be low to moderate plasticity CL materials (Olivia Chen Consultants, 2003).

The materials placed as starter dikes were also excavated from the surrounding hillsides, and had the same general characteristics. The starter dikes were unusually thick, as illustrated in Figure A.14.4, and these were placed primarily by steam shovels. This steam shovel fill of the "starter dikes" was placed in large lifts of approximately 4 to 6 feet, and was not compacted.

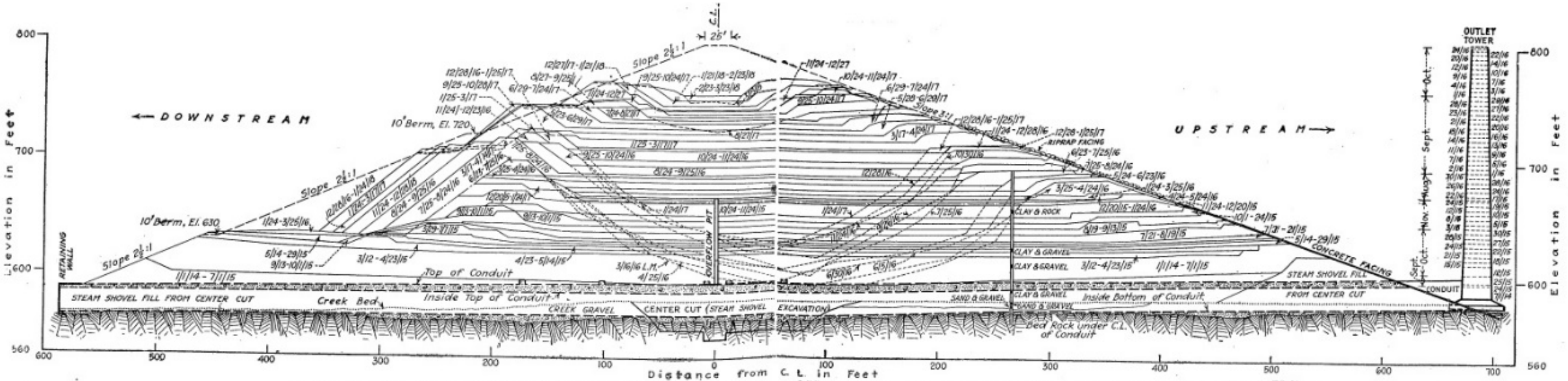

FIG. 1. PROGRESS OF CONSTRUCTION OF THE CALAVERA S DAM UNTIL THE OCCURRENCE OF THE SLIP IN MARCH, 1918, SHOWING METHOD OF FILL EMPLOYED

Fig. A.14.4: Cross-section by Hazen (1920) showing the progressive evolution of the Calaveras Dam embankment as a series of starter dikes and hydraulic fill beaches and puddled core ponds were used to raise the embankment up to the time of the failure on March 24, 1918.

Subsequent modern investigations were performed from 2000 to 2003 (Olivia Chen Consultants, 2003) to assess seismic stability of the repaired and completed dam, and these newer studies served to usefully further characterize the materials and approximate zonation within the dam, as will be discussed further. These more recent seismic studies concluded that the dam was seismically unsafe, and this resulted in emptying of the reservoir and removal of the dam. As this is being written, an entirely new dam is currently under construction so that this important reservoir can be re-established.

The modern (2000 to 2003) investigations provided significantly improved insight regarding the nature and character of the materials comprising the main embankment, including (a) the starter dikes, (b) the original hydraulic fill shells, and (c) the central "puddled" clayey core. Figures A.14.5(a) and (b) show the pre-failure and post-failure cross-sections, respectively, as analyzed in these current studies. No internal stratigraphy or zonation is shown in these figures, and this will be discussed further.

Figure A.14.6 shows the internal zonation developed by Olivia Chen Consultants (2003) for the recent seismic stability investigations. Multiple zones and sub-zones were employed to characterize the highly variable conditions within this complex embankment. Table A.14.1 presents summaries of estimated equivalent SPT $N_{1,60,CS}$ values for the principal zones shown in Figure A.14.6, as developed in the 2002-2003 studies.

Most of the embankment shell materials, including both hydraulically placed fill and also fill placed (largely uncompacted) with steam shovels, were comprised of weathered and fractured sandstone excavated from local hillsides. These materials were weathered and friable, and the resulting fill materials were broadly well-graded, with highly variable fines contents ranging from only a few percent fines to as much as 90% fines, and with relatively random variations in fines content locally within even the multiple zones shown in Figure A.14.6 and in Table A.14.1. Fines tended to be low to moderate plasticity CL materials. These "shell" materials also had significant gravel and cobble contents, also highly variable, and maximum particle sizes were often up to approximately 8-inches or greater, with gravel or coarser contents of between 15% to 60% and more being relatively common. The central "core" materials tended to have higher fines contents, but there were layers and stringers of cleaner material that appeared to penetrate into what was characterized as the puddled core zone.

To deal with these very broadly graded, and highly variable, materials the principal characterizations of seismic soil liquefaction potential were developed by means of (1) large diameter Becker Penetrometer tests (BPT), and (b) "short interval" SPT in which blowcounts were measured per each inch of penetration so that corrections could be made for apparent interference from larger particles (gravels and cobbles). Special steps were taken to deal with significant casing adhesion/friction on the Becker Penetrometer tests as the penetrometer passed through these broadly well-graded and variably cohesive to non-cohesive materials.

As a result of these recent investigations, it was the conclusion of this current investigation team, with unanimous concurrence from the informal advisory panel, that (1) the soils were more randomly variable than had been previously understood, (2) there were (variably) higher fines contents in many of the "shell" materials including both the hydraulically placed materials and

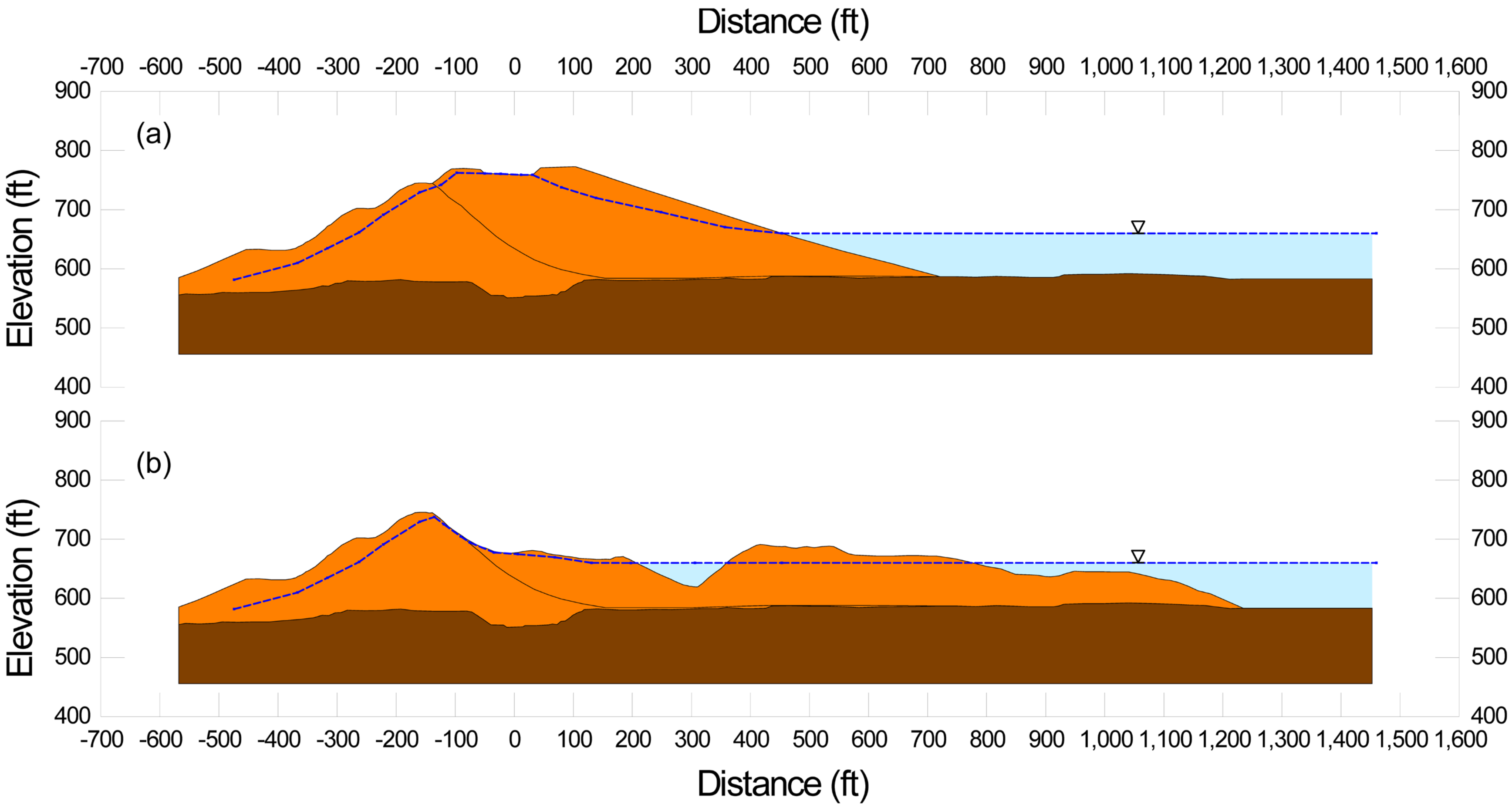

Figure A.14.5: Calaveras Dam: (a) Pre-failure and (b) post-failure cross-sections as analyzed in these current studies.

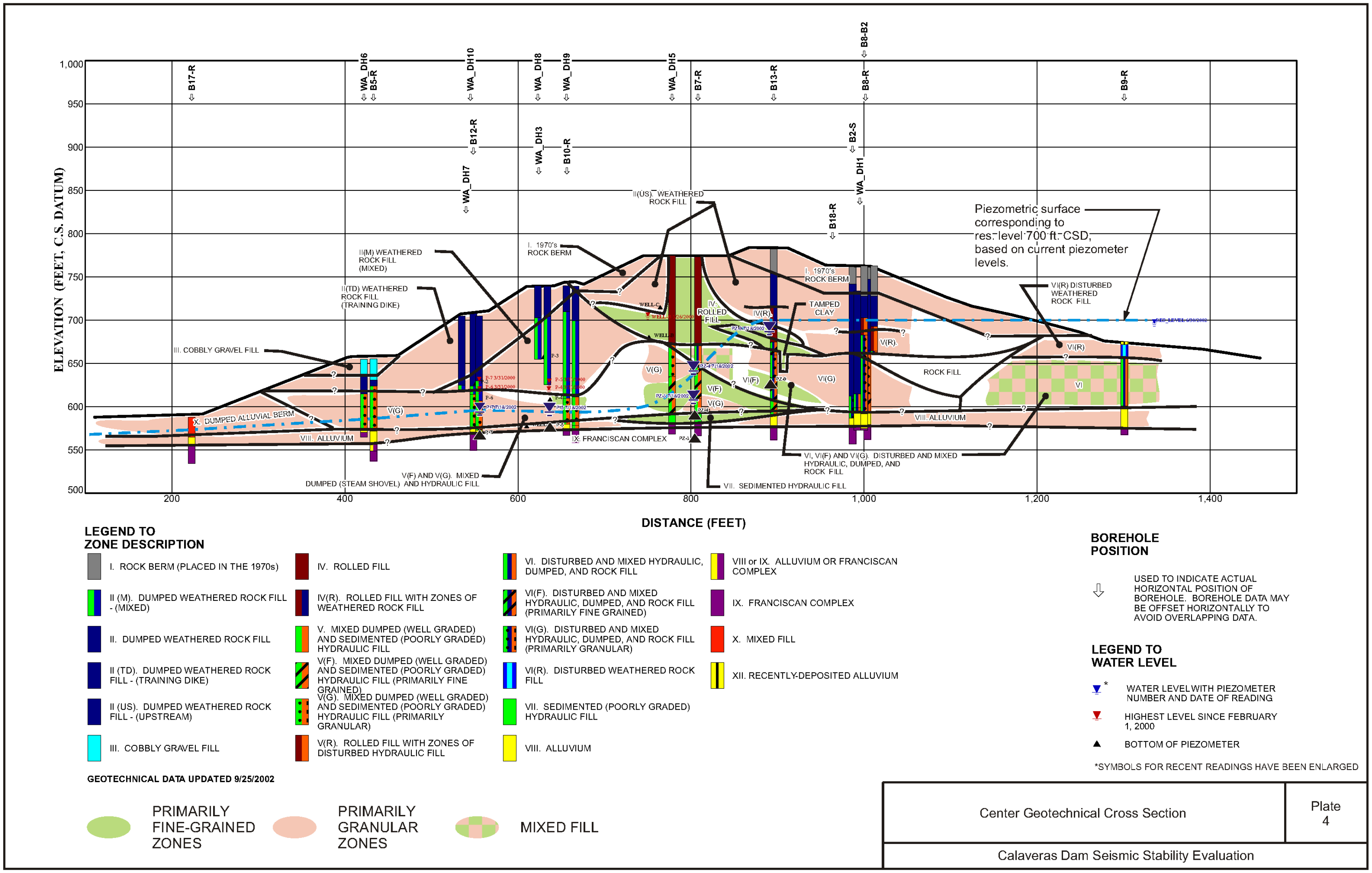

Fig. A.14.6: Cross-section developed by Olivia Chen Consultants (2003) for seismic stability analyses of Calaveras dam.

Table A.14.1: Characterizations of equivalent (and representative) $N_{1,60,CS}$ values for zones within the reconstructed Calaveras Dam (from Seed et al., 2003 based on Olivia Chen Consultants, 2003).

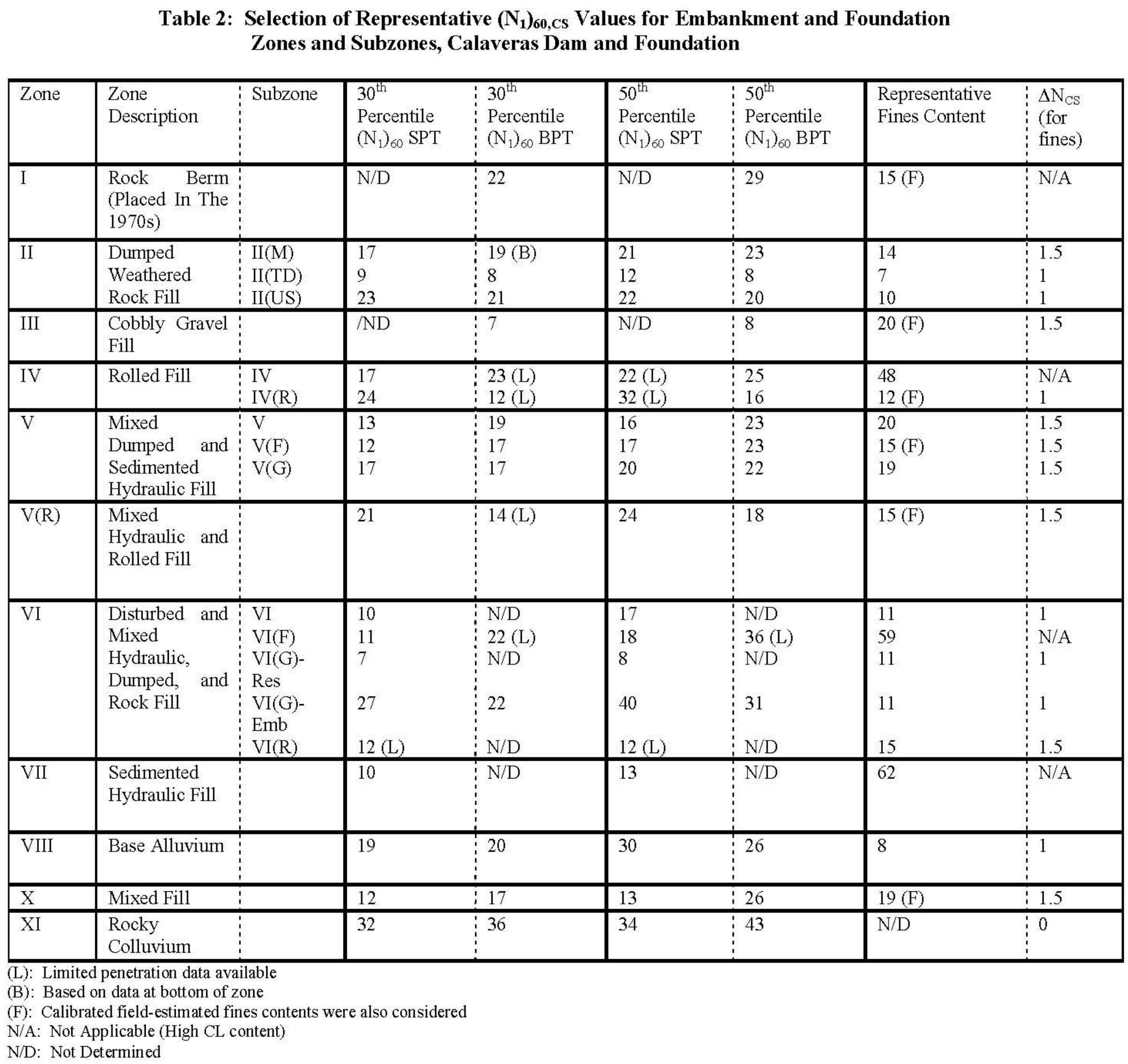

Table 2: Selection of Representative $(N_1)_{60,CS}$ Values for Embankment and Foundation Zones and Subzones, Calaveras Dam and Foundation

Zone	Zone Description	Subzone	30th Percentile $(N_1)_{60}$ SPT	30th Percentile $(N_1)_{60}$ BPT	50th Percentile $(N_1)_{60}$ SPT	50th Percentile $(N_1)_{60}$ BPT	Representative Fines Content	ΔN_{CS} (for fines)
I	Rock Berm (Placed In The 1970s)		N/D	22	N/D	29	15 (F)	N/A
II	Dumped Weathered Rock Fill	II(M) II(TD) II(US)	17 9 23	19 (B) 8 21	21 12 22	23 8 20	14 7 10	1.5 1 1
III	Cobbly Gravel Fill		/ND	7	N/D	8	20 (F)	1.5
IV	Rolled Fill	IV IV(R)	17 24	23 (L) 12 (L)	22 (L) 32 (L)	25 16	48 12 (F)	N/A 1
V	Mixed Dumped and Sedimented Hydraulic Fill	V V(F) V(G)	13 12 17	19 17 17	16 17 20	23 23 22	20 15 (F) 19	1.5 1.5 1.5
V(R)	Mixed Hydraulic and Rolled Fill		21	14 (L)	24	18	15 (F)	1.5
VI	Disturbed and Mixed Hydraulic, Dumped, and Rock Fill	VI VI(F) VI(G)-Res VI(G)-Emb VI(R)	10 11 7 27 12 (L)	N/D 22 (L) N/D 22 N/D	17 18 8 40 12 (L)	N/D 36 (L) N/D 31 N/D	11 59 11 11 15	1 N/A 1 1 1.5
VII	Sedimented Hydraulic Fill		10	N/D	13	N/D	62	N/A
VIII	Base Alluvium		19	20	30	26	8	1
X	Mixed Fill		12	17	13	26	19 (F)	1.5
XI	Rocky Colluvium		32	36	34	43	N/D	0

(L): Limited penetration data available
(B): Based on data at bottom of zone
(F): Calibrated field-estimated fines contents were also considered
N/A: Not Applicable (High CL content)
N/D: Not Determined

those placed by steam shovels, and (3) it would not be possible to suitably infer equivalent penetration resistance for conditions as they existed at the time of the 1918 slope failure in these complex materials that would provide a suitable basis for the current development of correlations between penetration resistance and post-liquefaction strength. Issues here include the observation that some portions of the "shell" zones were actually fines dominated, and that it would be exceedingly difficult to infer strengths in materials that would have been underconsolidated at the time of the failure, and that would also require very significant adjustments in penetrations resistances measured in the 2000 – 2003 studies in order to develop suitable characterizations compatible with conditions associated with a failure that had occurred eight decades prior.

Accordingly, with great reluctance, it was determined that this classic case history would not be employed in development of predictive correlations in these current studies.

That does not mean that this case history is not of value to these current studies, however, and so this case is the single "Class C" case in these current studies.

This case history provides an excellent opportunity to perform both incremental momentum analyses, as well as more simplistic $S_{r,yield}$ and $S_{r,resid/geom}$ analyses, and by doing so to develop useful information and back-analysis results that can be employed in development of relationships for characterization of post-liquefaction strengths as a function of failure and runout characteristics.

The recent (2000 – 2003) studies confirmed previous assessments that the materials comprising the uncompacted steam shovel fill forming the starter dikes, and those comprising the hydraulic fill "shell" zones, were generally similar with regard to material types and variability of materials, and that they were also generally similar in density. As a result, the upstream shell zones comprised of steam shovel fill and those comprised of hydraulic fill will be treated as essentially similar materials in these current studies.

The central puddled core materials would have been underconsolidated at the time of the 1918 failure, and it is difficult to estimate exactly what their strength characteristics would have been. They would have been mainly cohesive dominated materials, with CL fines, and they would have had high liquidity indices. Accordingly they would have (a) had relatively low ratios of Su/P, and (b) they would also have been sensitive and so would have suffered strength reduction when sheared to large strains.

Fortunately, as this case history will not be sued in development of correlations between penetration resistance and post-liquefaction strength (S_r), it is not necessary to closely characterize these puddled "core" materials here. Instead, these materials will not be differentiated from the adjacent "shell" materials (including both hydraulically placed materials and materials loosely placed by steam shovels), and the entire length of the apparent failure surface will simply be characterized by an undrained strength "S_r". As shown in Figure A.14.5, the phreatic surface created jointly by the "pond" atop the rising hydraulic fill and by the partially filled reservoir led to a situation in which essentially all of the failure surface was saturated.

A.14.4 Evaluation of Representative Post-Liquefaction Residual Strength

A.14.4(a) Initial Yield Stress Analyses

The pre-failure and post-failure cross-sections utilized for back analyses were based in large part on the cross-sections presented by Hazen (1918), and these are shown in Figure A.14.7. Figure A.14.7(a) shows the pre-failure cross-section geometry modelled as the best estimate case. This figure also shows the best estimate failure surface for these initial yield stress analyses. Initial yield stress ($S_{r,yield}$) is defined as the theoretical post-liquefaction strength within liquefiable materials on the eventual failure surface that would be necessary to develop a calculated Factor of Safety equal to 1.0 for the pre-failure geometry.

The unit weights of the hydraulic fill materials at the time of failure above and below the phreatic surface were estimated considering the recent time since placement, the nature of the hydraulic fill materials that comprised the dam, the values used by other investigators, and data developed by available field studies. Unit weights for saturated embankment materials were taken as $\gamma_s \approx 128$ lbs/ft^2. Because all materials involved in the stability analyses were saturated, this is the only unit weight required.

Similarly, as discussed in the previous section, all materials along the eventual failure surface were assigned a strength of $S_{r,yield}$.

The location of the failure surface was well-constrained by the observed field failure and by the post-failure investigations.

Based on these conditions and geometry, the best-estimate value of $S_{r,yield}$ was found to be $S_{r,yield}$ = 1,790 lbs/ft^2. Parameter sensitivity studies were then performed, including varying the unit weights of the materials (and also varying the distribution of unit weights, employing slightly lower unit weights in the "core" zone and slightly higher unit weights in the "shell" zone). Sensitivity studies also analyzed a suite of slightly different failure surfaces, but these variations in details of the failure surface were minor. Based on these sensitivity studies, a reasonable range of back-calculated values was judged to be $S_{r,yield} \approx$ 1,445 to 2,133 lbs/ft^2.

Olsen (2001) also calculated values of $S_{r,yield}$ in his studies, but his values were targeted specifically at the materials of the "shell" zones and so they are not directly comparable.

A.14.4(b) Residual Strength Analyses Based on Residual Geometry

Similar "static" stability analyses were performed to evaluate the "apparent" shear strength within the liquefiable hydraulic fill (S_r) that would result in a calculated Factor of Safety equal to 1.0 for the post-failure residual geometry of Figure A.14.7(b). Assumptions and modeling details were largely the same as described in the previous Section A.14.7(a), and sensitivity analyses with varying combinations of modeling and parameter details were performed here as well.

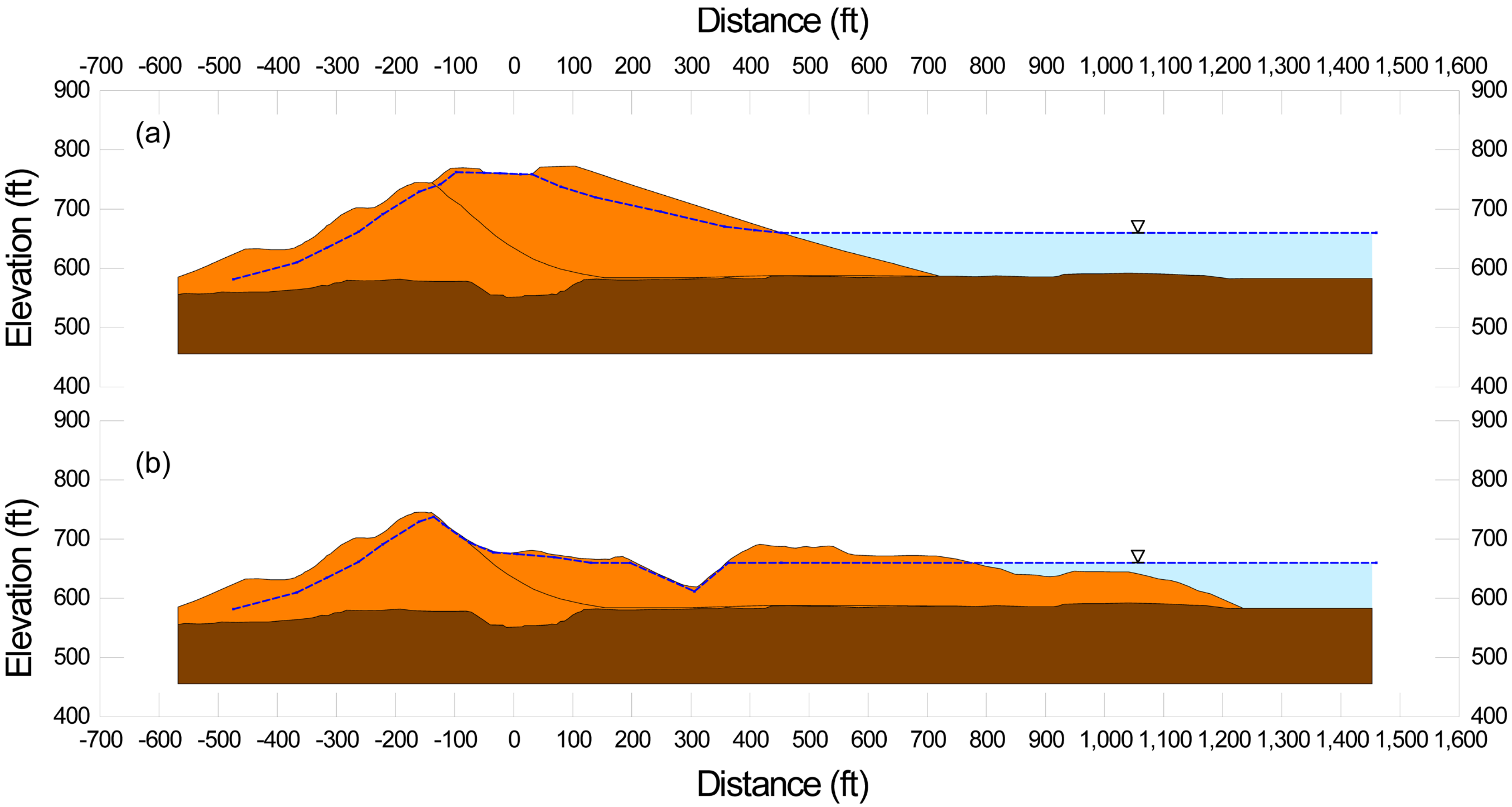

Figure A.14.7: Calaveras Dam: (a) Pre-failure geometry and best-estimate failure surface for initial yield stress analyses, and (b) post-failure geometry and best-estimate failure surface for post-failure residual geometry analyses.

Based on the modeling conditions and assumptions described above, the resulting best estimate value of the post-liquefaction shear strength required for FS = 1.0 with residual geometry is $S_{r,resid/geom} \approx 255$ lbs/ft^2. The approximate range, based on reasonable variations in parameters and modeling details, is $S_{r,resid/geom} \approx 207$ to 313 lbs/ft^2.

Olsen (2001) also calculated $S_{r,resid/geom}$ for this case history, but because his values specifically targeted the "shell" zone materials, they are not directly comparable here.

A.14.4(c) Incremental Momentum and Displacement Analyses and Overall Evaluation of Post-Liquefaction Strength

Full incremental momentum and displacement analyses were performed using similar modeling assumptions and details as described in the preceding Sections. Figures A.14.8 and A.14.9 show the best estimate case analysis. The modeled geometric failure progression can be seen in Figure A.14.9. A total of eight cross-sections were modeled for this large-displacement case. Figure A.14.10 then shows the associated plots of (1) acceleration vs. time, (2) velocity vs. time and (3) displacement vs. time for the center of gravity of the failure mass.

The resulting best estimate value of post-liquefaction strength for this case was $S_r = 749$ lbs/ft^2. Based on sensitivity analyses, a reasonable range of Sr was judged to be $S_r \approx 622$ to 900 lbs/ft^2.

A.14.5 Evaluation of Representative Penetration Resistance

No significant effort was expended to develop a well-refined characterization of representative penetration resistance for this case history because, as discussed previously in Section A.14.3, it will not be feasible to attempt to cross-correlate penetration resistance in materials that were underconsolidated (and sometimes fines dominated) at the time of the 1918 with penetration resistances measured eight decades later.

Accordingly, as a proxy, the penetration resistance assigned for this case will be the value developed by the 2000 to 2003 studies of Olivia Chen Consultants for the zones considered, as an ensemble, to best represent the zones that controlled the 1918 failure. This value is judged to be $N_{1,60,CS} \approx 15$ blows/ft.

It should be noted that this value is similar to values employed in a number of previous studies, which <u>did</u> employ this case history in development of correlations between Sr and $N_{1,60,CS}$ or similar. <u>If</u> this penetration was to be used in such an effort, it would be necessary to make significant adjustments for both ageing and consolidation effects over the past eight decades, and to employ a number far lower than 15 blows/ft.

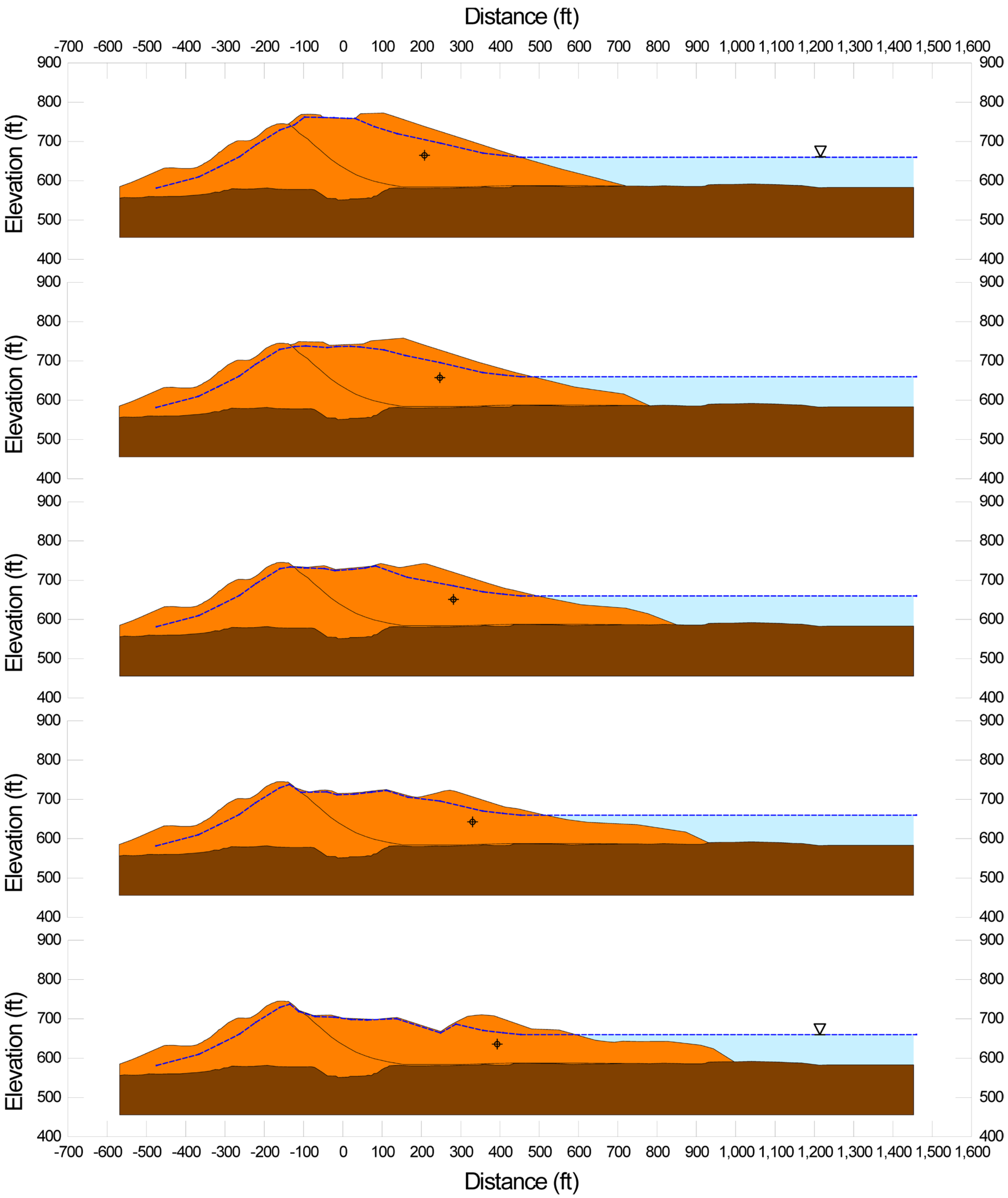

Figure A.14.8: Incremental inertial analysis of the failure of the Calaveras, showing the progressive evolution of cross-section geometry modeled (first five of eight cross-sections).

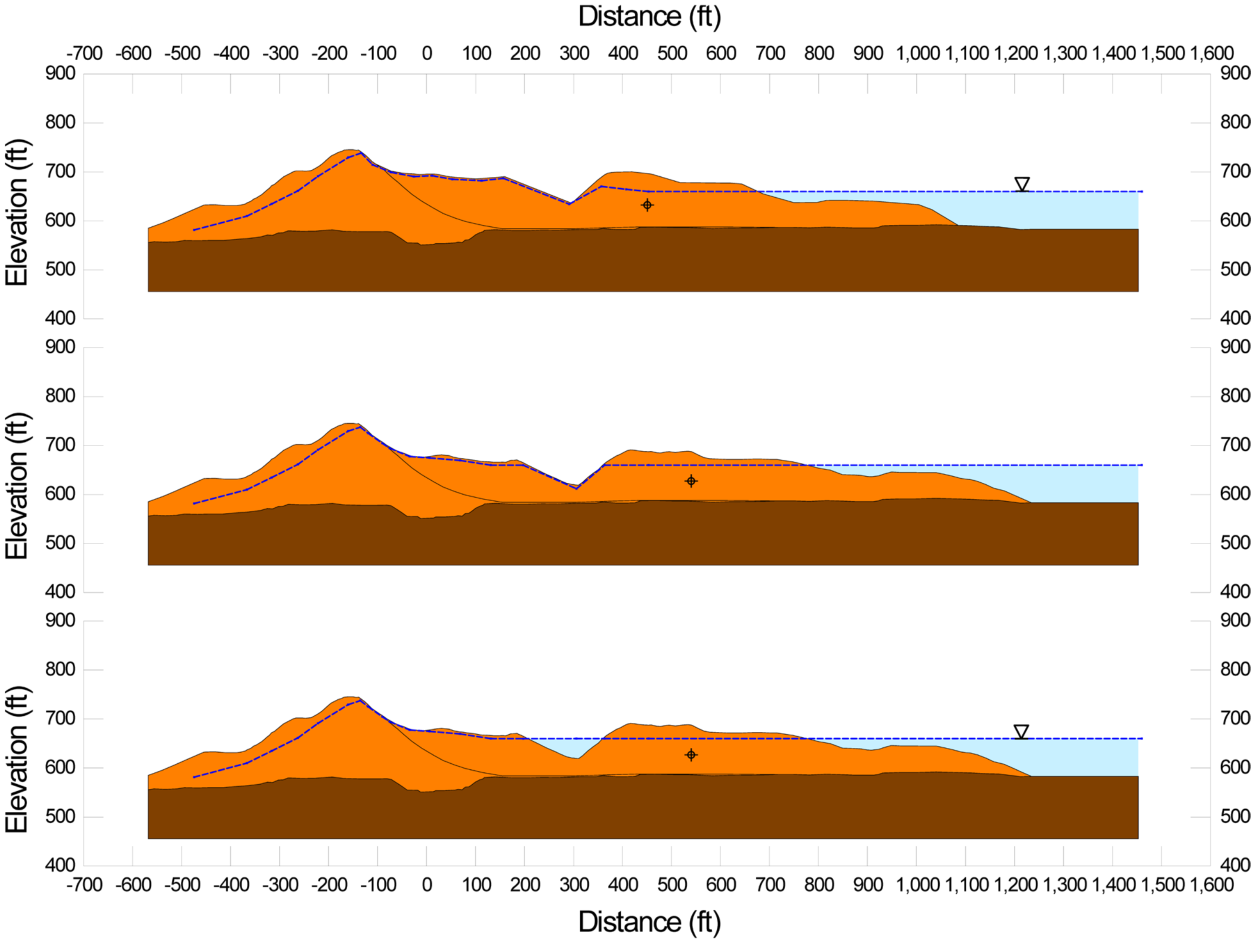

Figure A.14.8(cont'd): Incremental inertial analysis of the failure of the Calaveras Dam, showing the progressive evolution of cross-section geometry modeled (last three of eight cross-sections).

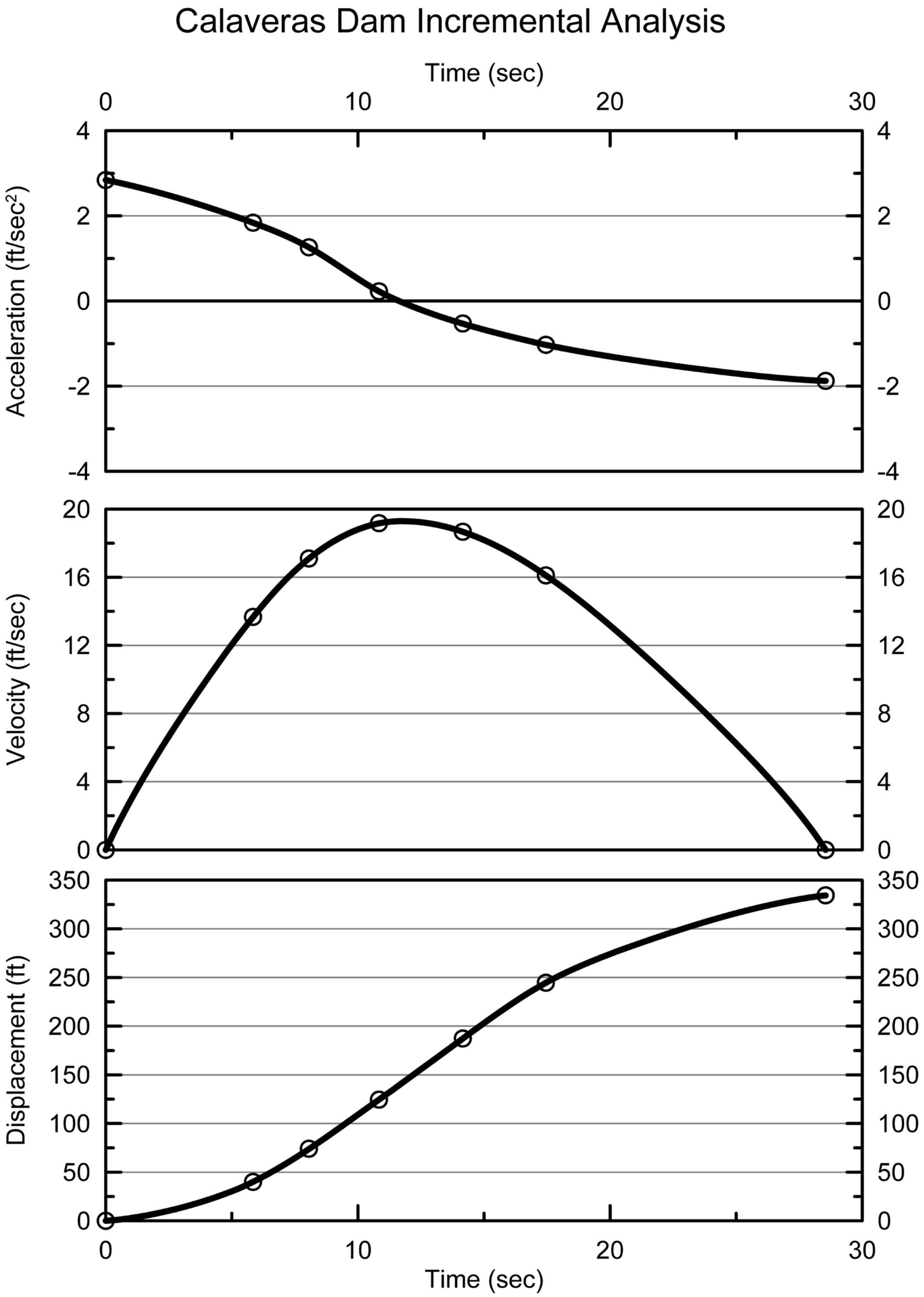

Fig. A.14.9: Incremental inertial analysis of the failure of the Upstream Slope of Calaveras Dam, showing progressive evolution of: (1) acceleration vs. time, (2) velocity vs. time, and (3) displacement vs. time of the overall center of gravity of the failure mass.

A.14.6 Evaluation of Representative Initial Effective Vertical Stress

The overall best estimate value of the average initial effective vertical effective stress on the eventual failure surface was calculated to be $\sigma_{vo}' = 7{,}097$ lbs/ft^2, with a range of $\sigma_{vo}' \approx 5{,}500$ to 8,650 lbs/ft^2.

Olsen (2001) also calculated initial effective vertical stresses, but his values specifically targeted the "shell" zone materials, and so they are not directly comparable here.

A.14.7 Additional Indices from the Back-Analyses

A number of additional results, and indices, can be extracted from the analyses performed. Some of these are useful in developing some of the over-arching relationships and figures presented in the main text of this report. These values are presented in Table A.14.1 below.

Table A.14.1: Additional results and indices from the analyses of the Calaveras Dam embankment failure case history.

Maximum distance traveled by the center of gravity of the overall failure mass	334 ft.
Initial post-liquefaction Factor of Safety prior to displacement initiation, and based on best estimate value of S_r	FS = 0.41
Final post-liquefaction Factor of Safety at final (residual) post-failure geometry, and based on best estimate value of S_r	FS = 2.62